2022

# A Multidisciplinary Characterization of the Enzymology and Biology of Reversible Glucan Phosphorylation in *Toxoplasma gondii*

Robert Murphy
rdmurphy89@gmail.com
Author ORCID Identifier:
https://orcid.org/0000-0003-1057-4078
Digital Object Identifier: https://doi.org/10.13023/etd.2022.56

STUDENT AGREEMENT:

I represent that my thesis or dissertation and abstract are my original work. Proper attribution has been given to all outside sources. I understand that I am solely responsible for obtaining any needed copyright permissions. I have obtained needed written permission statement(s) from the owner(s) of each third-party copyrighted matter to be included in my work, allowing electronic distribution (if such use is not permitted by the fair use doctrine) which will be submitted to UKnowledge as Additional File.

I hereby grant to The University of Kentucky and its agents the irrevocable, non-exclusive, and royalty-free license to archive and make accessible my work in whole or in part in all forms of media, now or hereafter known. I agree that the document mentioned above may be made available immediately for worldwide access unless an embargo applies.

I retain all other ownership rights to the copyright of my work. I also retain the right to use in future works (such as articles or books) all or part of my work. I understand that I am free to register the copyright to my work.

REVIEW, APPROVAL AND ACCEPTANCE

The document mentioned above has been reviewed and accepted by the student's advisor, on behalf of the advisory committee, and by the Director of Graduate Studies (DGS), on behalf of the program; we verify that this is the final, approved version of the student's thesis including all changes required by the advisory committee. The undersigned agree to abide by the statements above.

Robert Murphy, Student

Dr. Matthew S. Gentry, Major Professor

Dr. Trevor P. Creamer, Director of Graduate Studies

# A MULTIDISCIPLINARY CHARACTERIZATION OF THE ENZYMOLOGY AND BIOLOGY OF REVERSIBLE GLUCAN PHOSPHORYLATION IN *TOXOPLASMA GONDII*

---

DISSERTATION

---

A dissertation submitted in partial fulfillment of the
requirements for the degree of Doctor of Philosophy in the
College of Medicine
at the University of Kentucky

By
Robert Daniel Murphy
Lexington, Kentucky
Co- Directors: Dr. Matthew S. Gentry, Professor of Molecular and Cellular Biochemistry
and Dr. Anthony P. Sinai, Professor of Microbiology, Immunology, and Molecular Genetics
Lexington, Kentucky
2022


https://orcid.org/0000-0003-1057-4078

ABSTRACT OF DISSERTATION

A MULTIDISCIPLINARY CHARACTERIZATION OF THE ENZYMOLOGY AND BIOLOGY OF REVERSIBLE GLUCAN PHOSPHORYLATION IN *TOXOPLASMA GONDII*

*Toxoplasma gondii* is an opportunistic, protozoan parasite of all warm-blooded animals, infecting roughly one-third of humans worldwide. Humans acquire infections by consuming *T. gondii* tissue cysts in undercooked meat or from oocysts shed in cat feces. Encysted parasites convert into rapidly growing tachyzoites that disseminate throughout the body, defining the acute phase of infection. Under host immune pressure, tachyzoites convert into bradyzoites that populate tissue cysts found in CNS or muscle tissue and persist for the lifetime of the host, defining the chronic phase of infection. Tissue cysts are responsible for transmission via carnivory, but also possess the ability to reactivate into tachyzoites within their current host. In the context of immunosuppression, reactivation manifests primarily as toxoplasmic encephalitis. Current therapeutic options are poorly tolerated by many and effective only against tachyzoites. Thus, there is a need for a better understanding of the chronic infection to develop new treatments that eliminate tissue cysts or prevent reactivation.

The present work therefore examines the parasite's utilization of amylopectin granules (AGs), a morphological feature found in bradyzoites that distinguishes them from tachyzoites. AGs, much like plant starch, are insoluble storage molecules composed of branched chains of glucose and believed to fuel bradyzoite replication, transmission, and reactivation. In plants, insoluble starch is made enzymatically accessible by a cycle of direct, reversible glucan phosphorylation. The addition of phosphate by a glucan kinase solubilizes the starch surface to facilitate enzymatic glucose release, and the subsequent removal of phosphate by a glucan phosphatase prevents hyperphosphorylation that would obstruct enzyme access. The *T. gondii* genome encodes these opposing enzymatic activities: the glucan, water dikinase, "TgGWD," and the glucan phosphatase, "TgLaforin."

The work herein, along with recent studies, strongly suggests that the historical understanding of AGs is lacking. There is mounting evidence that tachyzoites

contain small and rapidly metabolized glucans that are key to *T. gondii* biology. Thus, an understanding of how *T. gondii* accesses its glucose stores throughout the asexual cycle is needed. Perturbations of glucan phosphatase activity in plants and animals result in significant defects in metabolism and glucan morphology, suggesting the need to investigate reversible phosphorylation of *T. gondii* AGs. To date, little has been done to characterize the enzymology or relevance of reversible glucan phosphorylation in *T. gondii*.

Herein, the functions and unique structures of TgLaforin and TgGWD were characterized using a wide range of biochemical and biophysical techniques. Additionally, a role for TgLaforin in *T. gondii* was elucidated using protein localization and knockout approaches. With these tools, it was demonstrated that TgLaforin plays a vital role in both tachyzoites and bradyzoites, linking TgLaforin to parasite metabolism, virulence, and development across the asexual cycle. The data here suggests that the tachyzoite glucan may play a previously unappreciated role in *T. gondii*. Thus, this work provides a unique window into the role of AGs through the first multi-disciplinary characterization of reversible glucan phosphorylation in *T. gondii* and establishes a framework for the development of future therapeutic approaches.

KEYWORDS: *Toxoplasma gondii*, amylopectin granules, glucan phosphatase, glucan dikinase, reversible glucan phosphorylation.

Robert Daniel Murphy

April 21, 2022

Date

# A MULTIDISCIPLINARY CHARACTERIZATION OF THE ENZYMOLOGY AND BIOLOGY OF REVERSIBLE GLUCAN PHOSPHORYLATION IN *TOXOPLASMA GONDII*

By
Robert Daniel Murphy

Dr. Matthew S. Gentry
Co-Director of Dissertation

Dr. Anthony P. Sinai
Co-Director of Dissertation

Dr. Trevor Creamer
Director of Graduate Studies

April 21, 2022
Date

DEDICATION

*To all those who supported me all these years.*

## ACKNOWLEDGMENTS

I must begin by acknowledging my incredible mentors, Dr. Matthew Gentry and Dr. Anthony Sinai. Both have modeled not only scientific rigor, but generosity, caring, and kindness. I have been uniquely fortunate in benefitting from their distinct approaches to mentorship. I thank Dr. Gentry for providing a laboratory environment with limitless scientific opportunities, and his trust in allowing all members of his lab the complete freedom to explore. I know that I would not have learned to trust my own scientific instincts without such autonomy. I thank Dr. Sinai for endlessly offering his own time, intellect, and enthusiasm in supporting all aspects of my scientific and personal endeavors. He pushed me to attend national and international conferences at least yearly and introduced me to the incredible *Toxoplasma* community. Under the mentorship of Dr. Sinai, I learned to be curious, intellectually open yet self-critical, and appreciative of surprises. I must also acknowledge my previous mentors. Dr. Mary Huff, my undergraduate advisor, first encouraged to me to consider a career in biochemistry. Dr. Kristen Reynolds and Dr. Mark Borgman at PGXL trained me in clinical lab techniques and operations, and they also encouraged me to consider going to graduate school.

I would also like to thank the rest of my dissertation committee members and outside examiner for monitoring my scientific progress for many years. Dr. Tianyan Gao and Dr. Sabire Ozcan have both challenged me with insightful questions, and both have graciously served as mentors for my departmental seminars. Additionally, Dr. Gao, as the newly appointed acting chair, has continued the work of improving the Biochemistry department in very tangible ways that I benefit from

as a graduate student. Dr. Ken Fields, my outside examiner, through his leadership roles in the Department of Microbiology, Immunology, and Molecular Genetics (MIMG) shaped an environment in which I found a great graduate student community. I am incredibly honored and grateful to him for agreeing to participate in my final steps toward obtaining a PhD.

In addition to those that formally mentored me, I am also grateful for the guidance and advice of Dr. Craig Vander Kooi. His door was frequently open for questions and quick chats about science that were vital to me over the years. He was always generous with his time, even coming in late at night to set up experiments with me. Dr. Vander Kooi and his lab transformed aspects of my dissertation project that are mentioned throughout this work. As such, I must also acknowledge members of his lab: Tiantian Chen, Dr. Savita Sharma, Dr. Carl Vander Kooi, and Caden Pearson, who all provided help at key points in my projects and enabled the submission of my first first-authored manuscript, co-authored with Tiantian. I especially enjoyed conversations with Tiantian whose expertise in structural biology was invaluable.

During the first years of my graduate training, my technical skills and critical thinking as a scientist blossomed working with Dr. Corey Brizzee, Dr. Animesh Dhara, Dr. Madushi Raththagala, Dr. Ramon Sun, and Dr. Katy Brewer. Each taught me foundational aspects of biochemistry, molecular biology, and cellular biology without which I would be lost today. In particular, conversations with Corey Brizzee resulted in several scientific and personal breakthroughs over the course of working toward this dissertation for which I am deeply thankful.

Additionally, I always look forward to talking with Lyndsay Young, Kia Markussen, Dr. Ron Bruntz, Kit Donohue, Anna Juras, Tara Hawkinson, Annette Mestas, and Dr. Andrea Kuchtova every day that I enter the Biochemistry department. I will miss laughing and chatting with each of them, including previous lab members Dr. Zoe Simmons, Dr. Jessica Macedo, and Dr. Shane Emanuelle. I was also fortunate to have been surrounded by equally great lab mates in the Sinai lab: Cortni Troublefield, Seth McConnell, and Joy Miracle who each have been a delight to work with. I must mention that without the daily support of Cortni, certain aspects of this dissertation would have not been possible. I am grateful for her generosity and honesty, both of which improved my science.

The core facilities and services at the University of Kentucky have been instrumental in enabling this work. I want to thank each for their contributions to this work: Dr. Martin Chow in the Protein Core, Dr. Carole Moncman in the Microscopy Core, Dr. Jennifer Strange in the Flow Cytometry Facility, Jim Begley in the Imaging Center, Jillian Cramer in the Electron Microscopy Center, Dr. Jing Chen in the Proteomics Core, and Dana Napier in the Biospecimen Procurement and Translational Pathology Facility. Outside of the University of Kentucky, a collaboration with Dr. Zhong-Yin Zhang at Purdue University is also gratefully acknowledged.

Science is not possible without administrative personnel working behind the scenes to ensure we have what we need. For that reason, I thank Rachel Putty, Brenda Woods, Tonya Knox, and Phil Dickson who keep the Biochemistry department running, and Cheylene Plummer and Brian Goodley have kept the

Gentry lab afloat during my tenure as a graduate student. I also thank the previous administrative associate, Melissa Hollifield, who served as an exceptional resource and friend in the MIMG department.

I must finally thank my support system outside of the lab. My friends Karen Kenney, Margaret Hamilton, Joanna Englert, and Brittany Voll provided strong shoulders to lean upon, and they provided understanding of how personally challenging these years have been. My rock-climbing partners and friends Dr. Tyler Kinder, Doug Martin, Kia Markussen, Marissa and Isaac Cook, and Sveta Zamakhaeva each challenged me to keep climbing, especially during the stressful times (even if I didn't always listen). My parents, Beth and Dan Murphy, have also supported me throughout this journey and never ceased to give me strength by reminding me how proud they are. My brothers, Nick, Thomas, and Lucas, remind me to never take myself too seriously. Finally, I am deeply grateful to Gabdiel Yulfo-Soto, my partner, a fellow scientist, and my closest friend who has supported through all the ups and downs since we met.

## TABLE OF CONTENTS

## LIST OF TABLES

## LIST OF FIGURES

# CHAPTER 1. THE TURNOVER AND METABOLISM OF AMYLOPECTIN GRANULES IN *TOXOPLASMA GONDII*

## 1.1 Introduction to *T. gondii* and its morphology

### 1.1.1 *T. gondii*, the model Apicomplexan

*Toxoplasma gondii* is an opportunistic, protozoan pathogen of humans and all warm-blooded animals. It was first discovered in 1908 in two separate labs, one in Tunisia and the other in Brazil, that each found this parasite in either gundis (from which the parasite takes its name) or rabbits, respectively (1,2), immediately suggesting its global distribution. Its ubiquity is now well recognized, as roughly one-third of humans worldwide are estimated to be seropositive for *T. gondii* (3).

*T. gondii* is a member of the large Apicomplexan phylum, a collection of intracellular pathogens with medical and veterinary significance such as *Plasmodium*, *Crytosporidium*, *Eimeria*, *Neospora,* and *Sarcocystis*. Of these pathogens, *T. gondii* is the most easily studied due to its ability to be propagated indefinitely in cell culture, the establishment of animal models used to study both parasite virulence *in vivo* and immune responses to its presence, and the availability of a wide variety of cell markers and standard assays by which to evaluate parasite fitness (4).

The *T. gondii* haploid genome also allows for ease of genetic manipulation using well-established transfection protocols in generating mutants for which a variety of selectable markers have been identified (5-7). Several conditional knockdown systems have been developed in *T. gondii* including Cre-LoxP, Tet, and, most recently, an auxin-inducible degron (8,9). Exciting new technologies have also been adapted to *T. gondii* enabling a genome wide knockout screen using CRISPR/Cas9 technology (10), subcellular localization of the entire *T. gondii* proteome using hyperLOPIT (11), and single-cell transcriptomics that defined gene expression profiles across both the cell cycle and asexual developmental stages (12).

Importantly, the *T. gondii* research community has assembled these complex data sets, alongside entire genome sequences and gene annotations, into ToxoDB.org. Genes in *T. gondii* are easily identified using several strategies including a BLAST functionality, common gene name queries, or specific accession numbers. Within gene pages, all available genomic, transcriptomic, proteomic, and localization data are displayed, along with many more gene features and link-outs to common database with more information such as UniProt, NCBI, etc. Moreover, the *T. gondii* community has collaborated on multiple books such as *Toxoplasma gondii: The Model Apicomplexan – Perspectives and Methods* that has served as a unified source of current *T. gondii* knowledge that is now in its third edition (13). An invaluable collection of some of the most important

methodologies in the field was also recently assembled in *Toxoplasma gondii: Methods and Protocols* (14).

This chapter will serve as an introduction to the parasite that has motivated such a dedicated community to undertake these herculean efforts to understand its biology. As such, the basic biology of *T. gondii* first presented will then be used as the context by which to present key discoveries in glucan composition, turnover, and metabolism across life stages in *T. gondii*. Finally, the motivation for studying the regulation of glucan degradation via reversible glucan phosphorylation in *T. gondii* will be presented.

### 1.1.2 Basic biology and morphology of *T. gondii*

The *T. gondii* life cycle is complex and consists of many stages. Broadly speaking, three stages within this cycle are considered transmissible: the tachyzoite, the bradyzoite, and the sporozoite. Even though these forms of the parasite are found in physically distinct locations (both within and outside of the host) and at distinct stages of infection, their overall morphology is strikingly similar. These stages are all commonly described as bow, crescent, or banana shaped (contributing to the parasite's name, from Greek: *Toxon* = arc/bow*, plasma* = shape), and each is approximately 2-3 μm wide and 7-9 μm in length (15) (**Figure 1.1a**).

With regards to its ultrastructure, it has been known since the first EM studies of *T. gondii* tachyzoites that it possesses standard eukaryotic organelles including a nucleus, a single mitochondrion, a Golgi apparatus, an endoplasmic reticulum, and ribosomes, as revealed in the first electron micrograph study of this parasite (16). Follow up studies then expounded upon and detailed several unique organelles that had been previously unknown (17). These organelles included micronemes, rhoptries, and dense granules (18) (each of these unique organelles is highlighted in **Figure 1.1b**). Since their discovery, these three organelles have been characterized as possessing secretory functions (19), and the protein cargo of each organelle has been extensively dissected and attributed to key stages in the lytic cycle.

The small, rod-shaped micronemes (*micro* = tiny, *neme* = hairs) function primarily in host cell egress, gliding motility, and host cell attachment through secretion of perforins, adhesins, and proteases (20). The club-shaped rhoptries (*rhopos* = club) secrete proteins that enable early moving junction formation between the parasite and host cell, facilitating parasite invasion (21). Many of the secreted rhoptry proteins also act as effector proteins that are injected directly into the host cell for early manipulation by the parasite, and also decorate the outer side of the parasitophorous vacuole membrane (PVM), the replicative niche of the parasite (**Figure 1.1a**) (22). Finally, the dense granules secrete a wide variety of proteins found throughout the infected cell: 1) found within the PVM lumen, 2) anchored on the host cytosolic side of the PVM, and 3) released within the host

cell cytosol and nucleus where they alter host transcription and halt cell cycle progression (21,23,24). Perhaps most dramatically, proteins secreted from the dense granules have been shown to be involved in recruiting the host cell's mitochondria to the PVM (25) where it makes very extensive contact (26). A role for the rhoptry protein ROP2 has also been proposed to mediate PVM-mitochondrial association (27).

The organization of the parasite's plasma membrane and cytoskeleton are also unique. *T. gondii* is a member of the alveolate superphylum, and thus contains an intermembrane complex (IMC) composed of alveoli (flattened vesicles) stitched together into a patchwork like network by suture components (28). The IMC underlies the parasite's plasma membrane, and this combination of alveoli + plasma membrane is referred to as the "pellicle." Underlying the pellicle are 22 microtubules that radiate out from an apical polar ring (APR) extending about 2/3 of the way down the parasite body, lending the parasite its distinctive shape (29). Above the APR is a tubulin-based structure resembling a spring called the "conoid" that rapidly extrudes and retracts during extracellular parasite motility and is believed to be the gateway for invasion factor secretion (30). The rhoptries and micronemes are commonly seen being docked in the conoid (**Figure 1.1b**), and the combination of these organelles and cytoskeletal elements form the "apical complex" from which the Apicomplexan phylum gets its name.

Other notable organelles in *T. gondii* have also been described, and include the plant like vacuole that appears to act as a lysosomal compartment (31), the acidocalcisome where calcium is stored (32), and, most notably, the apicoplast (33). This distinctive four-membraned structure was recognized by TEM in both *T. gondii* and *Eimeria* in 1965 and given the name "große Vakuole mit kräftiger Wandung" (German for "large vacuole with thick walls") long before its evolutionary history was untangled (34). Over the course of the next several decades, many more names were proposed for this structure, including "hohlzylinder" (German for "hollow cylinder") and "Golgi adjunct" (35). It was eventually recognized that *T. gondii* and other apicomplexans contain a 35 kb segment of extrachromosomal DNA outside of its mitochondrial genome (6-7 kb), and that this 35 kb segment shared significant similarities with chloroplast genomes (36,37). Two studies published in 1996 and 1997 utilized variations on *in situ* hybridization with portions of this 35 kb DNA, one in conjunction with TEM in both *T. gondii* and *Plasmodium* (33) and the other by fluorescence microscopy in *T. gondii* only (38). Both studies showed localization of this DNA to the four-membraned structure. Thus, the final name of this structure recognized its evolutionary past in calling it the "apicomplexan plastid" or "apicoplast."

Because the apicoplast is contained by four membranes, secondary endosymbiosis of a red or green algal chloroplast was suspected (39). Interestingly, the mystery surrounding its origin was unshrouded in studies that sought to characterize the nature of starch-like amylopectin granule (AG) metabolism in *T. gondii* (40). Due to the biochemical similarities of AGs in *T. gondii*

to “floridean starch” in red alga (discussed in section 1.5.6), this study suggested that *T. gondii* was of red algal origin.

In summary, it is now known that the apicoplast contains a highly reduced 35 kb genome, is no longer photosynthetic, and was responsible for lateral gene transfer of algal/plant-like metabolic enzymes into the *T. gondii* genome (discussed in section 1.5.6) (41,42). The apicoplast houses pathways for short-chain fatty acid synthesis (primarily C14:0 and C16:0) via a FASII pathway, isoprenoid synthesis, iron-sulfur cluster synthesis, and heme synthesis (43,44). Moreover, the apicoplast is an essential organelle, as loss of the apicoplast genome results in parasites that are ultimately unable to survive (45). Thus, the apicoplast has received targeted focus for drug development, and some drugs such as clindamycin and doxycycline specifically target the apicoplast (46,47).

Despite the presence of the aforementioned organelles throughout the invasive stages of *T. gondii,* the stages also display key differences from one another. Tachyzoites (tachos, from Greek = speed) replicate quickly during the acute phase of a new infection (48) and reside within a non-fusogenic vacuole inside of the host cell called the parasitophorous vacuole (PV) that is enclosed by the PVM (49). The speed of tachyzoite replication enables efficient establishment of a new infection and dissemination throughout a new host. Depending on the strain, tachyzoites double in number through synchronous replication every 5-9 hours (50). This rapid growth rate results in host cell egress roughly 24-48 hours after invasion (51). The tachyzoite life stage is the most amenable to study, as it naturally propagates under standard cell culture conditions at 37$^{o}$C and 5% $CO_2$, and is easily cryogenically stored in glycerol or 10% DMSO (52).

Bradyzoites (brady, from Greek = slow) are the persistent form of *T. gondii* that define the chronic phase of infection and are result from tachyzoite conversion under immune pressure from the host (discussed in more detail in section 1.3.2.). Bradyzoites reside in tissue cysts that are contained by a modified PVM known as the cyst wall. Tissue cysts are typically found in the CNS (**Figure 1.1c-d**) or muscle tissue of the host (most notably cardiac and skeletal muscle). These tissue cysts vary in size, ranging from 10-100 μm and contain hundreds or even thousands of parasites (**Figure 1.1e**). Bradyzoites replicate more slowly than tachyzoites (53) due to slowed progression through the cell cycle (54), but their asynchronous and sporadic replication patterns preclude a precise determination of overall replication rate (55). Bradyzoites are also morphologically distinct from tachyzoites as they are typically slimmer, their nuclei are located at the posterior end of the cell, they contain many more micronemes, and they contain numerous starch-like polysaccharides known as amylopectin granules (AGs) in their cytoplasm (**Figure 1.1f**) (discussed extensively in sections 1.4, and 1.5.4.-1.5.6.).

Finally, *T. gondii* sporozoites, like bradyzoites, are organized in an environmental cyst known as the oocyst and also contain AGs. Each oocyst contains two sporocysts, each in turn containing four sporozoites (eight total sporozoites per oocyst) (56). The oocyst is the product of sexual recombination

within felids that is shed in cat feces. Oocysts are notable for their persistence in the environment as they can survive for a year or more under suitable conditions (57).

## 1.2 Key discoveries in *T. gondii* transmission and lifecycle

The involvement of these infectious stages in the life cycle of *T. gondii* was worked out over the course of the 20th century and is presented in **Figure 1.2** (58). The first documented clinical case in a human in 1937 was a case of vertical transmission of the parasite from mother to fetus, the least common but often most devastating mode of transmission that can result in either spontaneous abortion or severe ocular and mental defects in the newborn. Because vertical (i.e. congenital) transmission results in such devastating consequences, these initial discoveries motivated the intense research into *T. gondii* that has since followed (59). Interest in the parasite has never waned due to the HIV/AIDS epidemic in the United States that resulted in high rates of toxoplasmic encephalitis in immunocompromised individuals (discussed in section 1.3.3.), and the increasing spotlight on areas around the world in which infection with so-called “atypical strains” of *T. gondii* results in a much higher disease burden than in the United States (60,61).

### 1.2.1 The discovery and initial characterization of *T. gondii* tissue cysts and their transmission via carnivory

The first documented *T. gondii* tissue cysts were found in the brains of mice and rabbits in the late 1920s (62). They were soon suspected as a latent form of the parasite after asymptomatic, pregnant mothers gave birth to children infected with *T. gondii* (63), ultimately leading to the hypothesis that mothers, and asymptomatic individuals, could be carriers of the parasite. By 1939, several cases of *T. gondii* infections in newborns were compiled and described (63). Notably, all the described infants suffered seizures, and several presented with hydrocephaly at birth. None of them lived longer than 7 weeks, and evidence of *T. gondii* tachyzoites and encysted bradyzoites was found in necrotic tissue in the brain and sometimes in the retina upon autopsy. While it is true that individuals can carry the parasite for an indefinite amount of time, we now know that pregnant individuals typically only transmit *T. gondii* to a developing fetus if acutely infected during the course of pregnancy (64), not from a latent infection. For this reason, public health officials often recommend pregnant individuals refrain from cleaning cat litter boxes (CDC.gov).

More evidence supporting the theory that humans could asymptomatically carry *T. gondii* accumulated in the 1940s when carriers of *T. gondii* were discovered upon routine autopsies of deaths unrelated to toxoplasmosis. After a 14 year old boy died from an ailment described as “liver atrophy,” researchers examined various tissues from his body during a routine autopsy, and they found

what appeared to be a 48x20 μm mass in his myocardial tissue that was described as a tissue cyst (65). Following this report, another asymptomatic carrier who died in a drowning accident was discovered by U.S. Army officials in Panama. Upon his autopsy, *T. gondii* tissue cysts were also found in his myocardium (66). A few years later, it was demonstrated that the brains of *T. gondii* infected rats retained their infectivity for the entire length of a two year study, and together with the discovery of asymptomatic humans with *T. gondii* infections, this evidence suggested the parasite's ability to establish asymptomatic infection and its ability to persist indefinitely (67).

The development of a *T. gondii* complement-based serological test by Sabin and Feldman in 1948 enabled researchers to survey a much wider number of living people and animals for evidence of a latent *T. gondii* infection (68). In a survey of 1,747 people from around the world in 1956 using the Sabin-Feldman serological test, researchers realized how prevalent asymptomatic carriers were with 31% of tested individuals found to be seropositive for *T. gondii* (69). There were wide ranges of seropositivity among different groups in this study ranging from 0% in one geographic group up to 68% in another.

Around the same time, anti-*Toxoplasma* antibodies were being discovered in many of the animals that humans consume including cows, pigs, goats, and sheep, leading to the theory that meat might indeed be a major reservoir of *T. gondii* infection (70). This hypothesis was demonstrated to be true in a study that found *T. gondii* could be transmitted from rodent to pig, and from pig to humans through carnivory (71,72). All of these discoveries were put into perspective by key experiments demonstrating that tissue cyst walls are easily ruptured in artificial digestive fluid containing pepsin, liberating the bradyzoites within (73). Importantly, bradyzoites were shown to be pepsin resistant, retaining their infectivity after pepsin exposure, whereas tachyzoites did not. Tissue cysts have also been demonstrated to survive in meat several weeks at 4 $^{o}$C (74).

Thus, with these early observations, the ability of *T. gondii* to be carried in livestock, persist for long periods in the same host, and transmit via carnivory from one host to another were established. The chain of transmission was thus far demonstrated as (and summarized in the "carnivory"-labeled portions of **Figure 1.2**): a rodent infected with bradyzoites could be consumed by a pig, which, in turn, would become infected itself and develop *T. gondii* tissue cysts in its skeletal muscle that might persist for the lifetime of the animal. This undercooked muscle in which cysts could survive for several weeks, when consumed by humans, could then result in their subsequent infection.

### 1.2.2 The discovery and initial characterization of *T. gondii* oocysts and their transmission through the environment

At this point, another major mystery remained to be solved related to the life cycle—how did herbivores and vegetarians contract the parasite? Either arthropod

or fecal transmission was suspected, but not until 1965 was it discovered that cat feces contains an infectious form of *T. gondii* that retains its infectivity for at least a year, although the infectious form of the parasite was not visualized upon first being discovered (75). Interestingly, it was suggested in this study that *T. gondii* passed into cat feces protected in the eggs of *Toxocara cati* (a feline roundworm), which was not an unreasonable suggestion at the time considering that tissue cysts could only survive a matter of days or weeks after death of the host, not an entire year as seen in cat feces (73). Over the next several years, the infectious material in cat feces was extensively characterized, and finally named the “oocyst” once it was finally visualized due to its resemblance to *Isospora bigemina* oocysts (76,77). Importantly to the elucidation of the *T. gondii* life cycle, oocysts retained their infectivity in mice after separation from roundworm eggs by centrifugation through a sucrose gradient. Moreover, kittens that had never been infected with *T. cati* (and thus were incapable of containing their eggs) were shown to shed infective oocysts after *T. gondii* infection in the lab, thus dispensing with the roundworm co-transmission theory.

Continued characterization of oocysts revealed basic facts about their biology: excretion begins 3-5 days after a cat consumes a tissue cyst, and they require 2-3 days at 24 $^{o}$C to mature into fully sporulated oocysts that could then cause infection (78) as mice that consumed oocysts before the sporulation point did not contract *T. gondii* infections. Shortly after these seminal discoveries, the developmental stages of the parasite within the cat intestinal epithelia were characterized (79). These stages, distinct from the transmissible stages, were named “merozoites” (mero, from Greek = partial or intermediate) and display more similarity to tachyzoites than any of the other stages. After several days of development through multiple morphological steps, merozoites convert into the male and female gametocytes that ultimately recombine and produce oocysts shed in cat feces, establishing felids as the definitive host of *T. gondii* (80). Why *T. gondii* only undergoes sexual recombination in felids long remained a mystery in the field after this discovery. Recently, however, it was determined that an excess of linoleic acid in the felid gut triggers sexual development (81). Felids are the only mammal that lack intestinal delta-6-desaturase activity, which is required for linoleic acid metabolism, thus explaining why *T. gondii* restricts its sexual cycle to cats.

### 1.2.3 A description of *T. gondii* life cycle

The key aspects of the *T. gondii* life cycle are presented in **Figure 1.2** and summarized here: shortly after cyst-induced infection, cats (the definitive host) shed *T. gondii* oocysts (the product of sexual recombination) in their feces. After sporulation, *T. gondii* oocysts are infectious to all warm-blooded wildlife and humans (the intermediate hosts) for up to a year. If humans consume unwashed produce or scoop cat litter without washing their hands, oocysts can be consumed directly from the environment. Common livestock also consume oocysts, become

chronically infected, and then become a source of tissue cysts for human consumption in raw or undercooked meat. Humans can also obtain *T. gondii* infections via vertical transmission or organ transplant from an infected donor (82). The *T. gondii* lifecycle is completed when a cat consumes a chronically infected rodent and then generates new oocysts.

## 1.3 The role of the asexual stages in human infection and disease

Due to the wide variety of transmission options available to *T. gondii* and its ability to infect any warm-blooded animal, it is estimated that one-third of humans worldwide harbor this parasite (83). The prevalence of human infection is uneven across the globe as was hinted at in early studies, with some countries having a seroprevalence of <10%, and others reaching >70% (84). As the early transmission studies revealed, horizontal transmission of the parasite occurs most frequently through the consumption of raw or undercooked meat (tissue cysts), and through the consumption of contaminated fruits, vegetables, and untreated water (oocysts) (85). In rare instances, transmission of tachyzoites has been suggested as possible through the consumption of raw milk (86). This section will describe the asexual life stages after transmission of the parasite that define the acute and chronic phases of infection and their role in toxoplasmosis. Of note, *T. gondii* tachyzoites replicate rapidly by a specialized internal budding process known as endodyogeny (18,87).

### 1.3.1 The acute phase of infection

Of particular concern to humans are the asexual stages of *T. gondii* that drive the disease manifestations of toxoplasmosis in intermediate hosts: the tachyzoite that defines the acute phase of infection, and the bradyzoite that defines the chronic phase of infection. After ingestion of the parasite, most commonly an oocyst (sporozoites) or tissue cyst (bradyzoites), the acidic environment of the host's digestive system rapidly releases the encysted parasite that is then able to invade the epithelial cells lining the intestine (88). Once inside the epithelial cells, the liberated sporozoite or bradyzoite then differentiates into a tachyzoite, initiating the acute phase of infection (89). These early stages of infection in a new host are not completely defined, but it is known that tachyzoites begin rapidly replicating after conversion and will ultimately cross the intestinal epithelia. This process occurs by a combination of three routes: 1) tachyzoites invade epithelial cells and then exit into the lamina propria where immune cells are recruited, 2) tachyzoites migrate between epithelial cell tight junctions without ever entering a cell, or 3) immune cells migrate into the intestinal lumen where they are infected by tachyzoites and then transport the parasites into the blood for subsequent dissemination (90). Regardless of how the parasite encounters the immune system, these immune cells are then used as Trojan horses for dissemination

throughout the body of the host (91). In the early stages, the parasite can be identified in many organs of the new host and throughout its blood flow (92,93). It is also by this Trojan horse mechanism that *T. gondii* has been shown to cross the blood brain barrier (94).

Repeated rounds of replication, host-cell egress, motility, and invasion define the lytic cycle of the tachyzoite (48,95), and the dissemination of the tachyzoite is greatly aided by its ability to invade any nucleated host cell. If a naïve mother is infected during pregnancy, vertical transmission at this point of infection is possible in which tachyzoites can cross the placenta and infect the fetus (64). Depending on the trimester of gestation in which this occurs, the results of congenital infection can range from mild/unnoticeable (typically third trimester) to premature termination of pregnancy (often first trimester) with symptoms of varying severity caused by a second trimester infection (3). Children that are infected congenitally display a wide variety of neurological symptoms ranging from asymptomatic to hydrocephaly, seizures, and mental deficits. Another major clinical manifestation of congenital transmission is retinochoroiditis in which toxoplasmic lesions develop within the eyes of children approximately 4-8 years after birth (3). In immunocompetent hosts, outside of complications regarding vertical transmission, the acute phase of infection typically causes very low to mild disease manifestations that are self-limited.

### 1.3.2 The chronic phase of infection

As immune pressure mounts against the tachyzoite, it begins the process of conversion into the slower-growing, persistent bradyzoite (96). The exact process by which this occurs is still being defined, but a wide range of stresses induce tachyzoite to bradyzoite conversion *in vitro* including alkaline or acidic stress, interferon-$\gamma$ and other cytokines, and nitric oxide (96,97). Additionally, cell type and host metabolic state appear to play a role in bradyzoite induction *in vivo*—even though *T. gondii* tachyzoites invade most cell types, bradyzoites within tissue cysts are typically found only in long-lived cells such as muscle cells and neurons (98). A study examining *T. gondii* conversion in muscle cells demonstrated that a host cell that is withdrawn from the cell cycle, as is often seen in fully differentiated neurons and muscle cells, results in stage conversion, although it is not yet clear how parasites sense that they are in a terminally differentiated cell (99).

Upon bradyzoite conversion, morphological changes within the parasite occur that are highlighted in section 1.1.2, including the accumulation of crystalline starch-like amylopectin granules (AGs). In addition to these internal morphological changes, the PVM surrounding the dividing tachyzoites develops into the tissue cyst wall, becoming heavily glycosylated and studded with glycoproteins (100). Within the cyst, bradyzoites are present in random assortments of numbers, indicating that they no longer divide synchronously (55). While the view of bradyzoites has traditionally been that they are inert and largely quiescent, recent

data has indicated that bradyzoites do indeed replicate with evidence for varying patterns of synchronous, clustered, and sporadic replication (55,101). Occasionally, tissue cysts rupture, and bradyzoites can reinvade surrounding cells and establish new tissue cysts. It is this process of tissue cyst rupture that is believed to keep the immune system alert and primed to their presence, but also presents no danger in an immunocompetent host (102).

In addition to morphological changes, significant molecular and metabolic changes also occur during the conversion. Classically, conversion has been monitored with a set of molecular markers (103). For example, tachyzoites express a major GPI-anchored protein on their surface known as “surface antigen 1” (SAG1) that is downregulated during tachyzoite to bradyzoite conversion concurrent with the upregulation of “SAG1-related sequence 9” (SRS9), and there are many more such markers that have been extensively described (104). One of the major glycosylation markers on the surface of the tissue cyst wall, N-acetylgalactosamine, has classically been detected with the lectin *Dolichos biflorus* agglutinin (DBA) (100). Additionally, several glycolytic enzymes are encoded by multiple isoforms that are differentially regulated in these two stages: lactate dehydrogenase 1 (LDH1) and enolase 2 (ENO2) are highly expressed in tachyzoites whereas LDH2 and ENO1 are found in bradyzoites (105). Underlying the changes in these classical molecular markers are massive transcriptional and metabolic changes that are themselves regulated by Apicomplexan specific, plant-like ApiAP2 transcription factors (106). More recently, a Myb-like transcription factor, bradyzoite formation deficient1 (BFD1), was identified as the master regulator of differentiation in *T. gondii*, being both necessary and sufficient for conversion (107). While BFD1 was shown to interact with many stage-specific genes, its interaction with the AP2 transcription factors remains to be elucidated (108).

### 1.3.3 Bradyzoite reactivation in acquired toxoplasmosis

In immunocompromised hosts, *T. gondii* bradyzoites can reactivate into tachyzoites resulting in significant damage to the host’s CNS tissue that often manifests as toxoplasmic encephalitis (TE) (109). Such damage is the result of an uncontrolled tachyzoite lytic cycle in places where quiescent bradyzoites used to reside. Early studies of this process first observed these reactivation events in the context of cancer treatments (110). Case studies noted changes in patient demeanor, speech, and behavior alongside seizures and symptoms of encephalitis that began after chemotherapy and steroid treatment, all consistent with significant neurological damage. Upon autopsy of patients that presumably died from complications related to toxplasmosis, examination of their brains often revealed large areas of total necrosis (in one case, a 4 cm clearing was observed). In each of these brains, *T. gondii* tachyzoites were observed surrounding necrotic areas, sometimes alongside tissue cysts that had not yet ruptured. Indeed, imaging

of such lesions by either magnetic resonance imaging (MRI) or computer tomography (CT) is a key diagnostic of cerebral toxoplasmosis in living patients (111). Importantly, a study using retrospective analyses suggested that immunosuppression was the driver of reactivation and not the various cancers these patients had, as non-cancer patients treated with immunosuppressants also developed toxoplasmosis (112).

At the beginning of the HIV epidemic in the early 1980s, cases of TE increased dramatically in people living with HIV/AIDS (113). In the United States, between 10-40% of people living with HIV/AIDS were chronically infected with *T. gondii*. Thus, the combination of plummeting immune protection and a latent parasitic infection presented a situation akin to carrying ticking time bombs in which cyst rupture events were not able to be controlled, allowing for reactivation. Indeed, almost 100% of toxoplasmosis in people living with HIV/AIDS was due to tissue cyst reactivation, as it was very rarely associated with a new infection (114). Overall, it was estimated that about 25-50% of patients with AIDS who were seropositive for *T. gondii* would go on to develop TE. By the end of the first decade of the epidemic, *T. gondii* was recognized as being one of the most common opportunistic pathogens with clinical manifestations in people living with HIV/AIDS (113). While anti-*Toxoplasma* therapeutics were available during this time, fatality rates were still incredibly high for hospitalized patients that received these drugs (113). Therefore, significant declines in TE were seen only after anti-HIV combined antiretroviral therapy (cART) became available in the mid-1990s. However, it was estimated as recently as 2017 that over 13 million people around the world are currently co-infected with HIV and *T. gondii* (115).

### 1.3.4 Anti-*Toxoplasma* therapeutic options

Treatment of toxoplasmosis has historically relied on targeting parasite folate synthesis in cases of both acquired and congenital infection (116). The most well-known *T. gondii* anti-folate was recognized as an anti-parasitic almost seventy years ago and relies on the synergistic effects of combining pyrimethamine and sulfadiazine (P/S) (117). Pyrimethamine inhibits dihydrofolate reductase (DHFR), and sulfadiazine inhibits dihydropteroate synthetase (DHPS). The combination of these two drugs ultimately blocks DNA synthesis in the parasite, but this combination also targets metabolically active host tissue. To circumvent this, P/S is commonly given with folate supplementation without any decrease the antiparasitic effects of P/S (118). Alternatives to this regimen include cotrimoxazole as a monotherapy (another antifolate), pyrimethamine in combination with various protein synthesis inhibitors (spiramycin, clindamycin, clarithromycin, and azithromycin) or in combination with a *T. gondii*-specific electron transport chain inhibitor (atovaquone) (116). None of these regimens, however, have been demonstrated to be more effective than P/S as it is still considered the gold standard by which all other anti-*Toxoplasma* therapeutics are judged (119).

Spiramycin is an incredibly important option in the clinic for pregnant individuals. Because pyrimethamine has been demonstrated to be teratogenic, an acute infection that is acquired during pregnancy is instead treated with spiramycin which uniquely accumulates in the placenta without crossing it, thus providing a difficult barrier for *T. gondii* to overcome (120). If, however, the fetus itself should become infected at any time during pregnancy, it is recommended that the newborn remain on P/S for the 1-2 years after birth (121).

While P/S is currently the first-line option, it also has the potential to result in severe toxicity in patients related to its ability to cause bone marrow suppression and dermatologic complications. Moreover, sulfonamides occasionally result in allergic reactions. In fact, adverse events related to these drugs result in high rates of discontinuation (up to 32% in some studies) and the need to switch to drugs that have been considered as less effective (113). All of this taken together indicates that the current options for treating toxoplasmosis are toxic and old. Moreover, they are only effective against tachyzoites. There are currently no approved drugs that target bradyzoites or prevent their reactivation (122), although there is an ongoing and considerable effort to develop them (123). Clearly, there is a continued need for the exploration of drug development against *T. gondii* as the only drugs developed against this parasite are least useful in those who need them the most.

## 1.4 Amylopectin granules (AGs): a mysterious *T. gondii* polysaccharide

Based on the function of polysaccharides elsewhere throughout nature, AGs are believed to play a role in energy storage that can be tapped into for bradyzoite replication, persistence, transmission, and reactivation into tachyzoites. A complete understanding of AGs and their utilization across the asexual cycle still awaits a complete characterization. This section will describe the first observations of this glucan, and the following sections will describe the modern understanding of AGs.

### 1.4.1 The early years

The first studies documenting a glucan in *T. gondii* bradyzoites were actually studies characterizing the tissue cyst wall. At this time, there was a debate surrounding the nature of the cyst wall, and if *T. gondii* formed true cysts (i.e., a cyst generated wholly by the parasite) or “pseudocysts” (i.e., a cyst derived from host cell components). One study, in fact, proposed avoiding this debate altogether by naming the cyst a “terminal colony” (124). Thus, the first studies noting the glucan within the bradyzoites were focused on demonstrating that the cyst wall is a distinct structure by showing that it is argyrophilic (staining with silver) and that it stains faintly with periodic acid-Schiff (PAS), and it was also noted that the bradyzoites within are PAS+ as well (containing a polysaccharide) (125,126). This was the first time a glucan had been described in bradyzoites, and it was termed

“glycogen” at the time (126). In 1958, a study used these characteristics to definitively distinguish *T. gondii* tachyzoites in their “pseudocysts” (the term PV was not in use yet) from bradyzoites that occupied a true cyst (127).

The first electron micrographs of *T. gondii* tissue cysts allowed visualization of the glucan within bradyzoites [seen in studies (128,129)]. It is important to note, however, that in these two studies, there was no mention of the glucan within bradyzoites. In the context of discussion in the field with regards to pseudocysts versus true cysts, these studies were more concerned with highlighting the unique nature of the cyst wall. In fact, structures that appear to be a glucan within bradyzoites were either not recognized at all (129), or described as “polygonal inclusions” and termed either “vacuoles” or “precursor vacuoles” (128). Indeed, studies on another Apicomplexan parasite were needed to characterize this glucan within the encysted parasites.

### 1.4.2 Recognition of amylopectin granules in another coccidian parasite

In parallel with discoveries being made in *T. gondii*, a detailed characterization of *Eimeria tenella*, a closely related parasite that causes coccidiosis in chickens, was also occurring. Of note, *E. tenella* gametocytes were recognized in the 1940s as containing a glucan that was then also described as glycogen by iodine staining (130). However, 25 years later the polysaccharide from *E. tenella* sporozoites and merozoites was more thoroughly characterized using biochemical and PAS-adapted electron microscopy techniques (131). The polysaccharide was isolated using the Pflüger method—parasites were boiled in 30% KOH and then the glucan was precipitated using ethanol. Acid hydrolysis of the isolated polysaccharide revealed that it contained only glucose, and β-amylase/debranching enzyme treatment demonstrated the presence of α-1,6-glycosidic bonds. Using the products of these enzymatic digests, it was estimated that the average glucan chain length was 12-17 glucose units, slightly longer than glycogen and more similar to amylopectin (these enzymes, glucans, and their linkages are described in detail in section 1.5).

While such a study was not conducted in *T. gondii* at the time, electron-lucent inclusions seen in electron micrographs of *T. gondii* within both sporozoites (132,133) and bradyzoites (134) were beginning to be labeled as polysaccharide granules (PGs). Ultimately, by the end of the 20$^{th}$ century, these PGs were labeled as amylopectin granules (AGs) even without a proper biochemical characterization (15). The first study that verified the polysaccharide nature of these inclusions was performed in 2003 using a TEM technique in which ultra-thin sections of resin-embedded *T. gondii* tissue cysts were stained with a PAS-based techniques compatible with EM (135). These studies demonstrated that the electron lucent structures that had long been visualized in *T. gondii* were indeed a polysaccharide by their dark gray staining.

## 1.5 Structure, synthesis, and degradation of glucose-storage molecules

More recently, AGs in *T. gondii* have been described biochemically and much of their enzymology is beginning to be dissected. This section will first provide a brief overview of two of the major storage glucans found across the plant and animal kingdoms: starch and glycogen, respectively. The structure, synthesis, and degradation of each will also be described. Finally, the first biochemical studies of AGs in *T. gondii* will be described in the context of these two major storage macromolecules alongside a description of the specific enzymology related to AG turnover.

### 1.5.1 Biochemical structure of starch and glycogen

*Starch*—Despite its seemingly simple composition as a homopolymer of glucose, starch is an incredibly complex energy storage molecule synthesized primarily by plants, algae, and some protists. Its complex and highly regulated structure results in its characteristic semicrystalline nature [thoroughly reviewed in ref. (136)]. Starch is practically unlimited in size, ranging from 500 nm up to 100 μm in some roots (137). In fact, the size of starch granules appears limited only by the physical constraints imposed by the organelle in which it resides and the number of starch granules surrounding it (138). Fundamentally, glucose units within starch are linked through either α-1,4 or α-1,6 glycosidic bonds to form both linear and branched glucose connections, respectively (**Figure 1.3a**).

Starch is composed of two types of glucans: amylose and amylopectin (139). Amylose, the simpler molecule of the two, is primarily linear with many fewer branchpoints and thought to serve more of a space-filling role within the starch granule (140). Amylopectin, on the other hand, is a moderately branched glucan that is the primary constituent of starch, making up approximately 70-90% of the granule (141). The α-1,6 branchpoints within amylopectin make up approximately 5% of its glycosidic bonds, which are placed non-randomly throughout the molecule and tend to be found in clusters (142). This clustered pattern allows for long uninterrupted chains, with an average length of 20-25 glucose units, to wind around their neighbors, forming helices that exclude water and contribute to the crystallinity of starch (140) (**Figure 1.3b**). The chains themselves also pack with each other in parallel, and their arrangements (also known as “allomorphs”) are usually one of two types: A-allomorphs that are composed of densely packed helices and exclude more water, and B-allomorphs that are arranged in a hexagonal lattice, creating space for more water between the neighboring helices (143) (**Figure 1.3b**). Importantly, A-allomorphs are more often associated with “storage starch” that is found in non-photosynthetic plant tissue, and B-allomorphs are more frequently found in the “transitory starch” of leaves and other photosynthetic tissue (144).

*Glycogen*—Like starch, glycogen found in animals is a branched glucan connected through α-1,4 and α-1,6 glycosidic bonds. Unlike starch, however, glycogen contains shorter glucan chains (an average of 13 glucose units per chain) and is more frequently branched with α-1,6 branchpoints making up approximately 8% of total glycosidic bonds (145). Moreover, these branches are evenly distributed throughout the molecule, preventing extensive glucan helix formation as seen in starch (146). Combined, these properties result in the increased water-solubility of glycogen relative to amylopectin (147). Additionally, the evenly distributed branching pattern of glycogen results in a molecule that is organized into tiers defined by each new set of branches on each chain (**Figure 1.3c**) [modeled in (148) based on the crystal structure of maltoheptaose, and reviewed alongside other competing models in (149)]. This tiered structure imposes a physical limit on the size of glycogen of 12 tiers (roughly 55,000 glucose units), or about 44 nm in diameter. This limit is due to an exponential increase in glucan chains within each tier that would lead to eventual molecular overcrowding and subsequent enzyme inaccessibility in a theoretical 13$^{th}$ tier (150,151). These 44 nm glycogen molecules are referred to as β-particles and can aggregate into larger units known as α-particles that are seen primarily in the liver (152). It has been speculated that these differing organizations of glycogen result in either slower (α-particle) or faster (β-particle) degradation due to their surface area differences (153). A recent study found that glycogen contains covalently bound glucosamine as well (154). Strikingly, glucosamine levels varied depending on the source of the glycogen, with glycogen from liver, muscle, and brain tissue containing 0.1%, 1%, and 25% glucosamine, respectively. The source of glucosamine in glycogen was demonstrated to be glycogen synthase itself, as it was demonstrated to be capable of incorporating glucosamine, in addition to glucose, into glycogen.

### 1.5.2 Glucan synthesis

*Starch*—In plants and green algae, starch synthesis occurs entirely in the chloroplast and begins with the synthesis of ADP-glucose. First, phosphoglucomutase (PGM) converts glucose-6-phosphate (G6P) to glucose-1-phospahte (G1P). G1P is then a combined with ATP by ADP-glucose pyrophosphorylase (AGPase) to form the activated sugar nucleotide, ADP-glucose (155) (**Figure 1.4, right side**). This reaction is made effectively irreversible by the simultaneous release of pyrophosphate that is rapidly hydrolyzed within the cell, preventing the reverse reaction from occurring (156). The formation of ADP-glucose, therefore, considered the committed step in starch synthesis under physiological conditions (157).

To synthesize amylopectin, starch synthase (SS) adds the glucose moiety from ADP-glucose onto the non-reducing end of an existing glucan chain by forming an α-1,4 glycosidic bond (157). Branching enzymes (BEs) work along SS, creating branch points by removing α-1,4 linked chains and reattaching them at C6

positions to form α-1,6 glycosidic bonds, maintaining the branching pattern characteristic of amylopectin (158). Finally, debranching enzymes (DBEs) participate in perfecting the amylopectin structure by removing excess branches (159). Careful curation of these branchpoint locations results in their clustering such that the long, unbranched chains can wind around each other (summarized **Figure 1.4, right side**). The synthesis of linear amylose relies solely on the action of granule-bound starch synthase (GBSS) that also utilized ADP-glucose (160). In plants, many of these enzyme activities (SS, BE, and DBE) are encoded by multiple isoforms such that they each have subtly, and sometimes dramatically, different functions.

*Glycogen*—In animals and fungi, glycogen synthesis is initiated in the cytosol by the protein glycogenin (161). Glycogenin functions as a dimer and first glycosylates itself before extending a glucose chain of about 8 glucoses from this initial O-linked glucose (162). Glycogenin uses a different sugar nucleotide, UDP-glucose that is generated by UDP-glucose pyrophosphorylase (UGPase) for both autoglycosylation and glucan chain synthesis (163). This initial protein-linked chain acts as a primer for glycogen synthase (GYS), a highly regulated protein with two isoforms found either in the muscle/brain (GYS1) or liver (GYS2), that elongates glucan chains by forming additional α-1,4 glycosidic bonds using UDP-glucose as a substrate (164). Much like starch synthesis, a glycogen branching enzyme (GBE) is required to curate the structure of the macromolecule by cleaving α-1,4 glycosidic bonds and attaching the cleaved chain (a minimum of six glucose units) at the C6 of a nearby chain forming an α-1,6 glycosidic bond (165). It is worth noting that branching enzymes, through their role in creating distinct branching patterns, are believed to be largely responsible for the crystallinity and solubility of starch and glycogen, respectively (166).

### 1.5.3 Glucan degradation

*Starch*—insoluble starch degradation is facilitated by a cycle of direct, reversible glucan phosphorylation. Phosphate is directly esterified to the C6 and C3 hydroxyl groups of glucosyl moieties within glucan chains by the glucan, water dikinase (GWD) and the phosphoglucan, water dikinase (PWD), respectively (167,168) (**Figure 1.4**, **left side**). The addition of phosphate disrupts the crystalline helices on the starch surface, allowing further enzyme access (169,170). Estimates of starch phosphate content ranges from one phosphate group per 100 or 1000 glucosyl units in *Arabidopsis* leaf starch and potato tuber starch, respectively (171). After the addition of phosphate, endo- and exo-acting amylases (α- and β-amylases, respectively) are then more easily able to cleave α-1,4 glycosidic bonds, releasing maltose (β-amylase) and longer, branched oligosaccharides (α-amylase) (172). Eventually, the phosphate groups added by GWD and PWD becomes a steric hindrance to these amylases, and a glucan

phosphatase is required to remove the phosphate to allow for further rounds of degradation (173).

In plants, these glucan phosphatases are known as starch excess4 (SEX4) (174) and like sex four2 (LSF2) (175). Glucan phosphatases employ a wide variety of glucan binding platforms that are discussed extensively in section 3.1. As a result of their unique binding platforms, SEX4 dephosphorylates both the C6 and C3 positions (176), but prefers C6, while LSF2 exclusively dephosphorylates the C3 position (177). Branch points in addition to phosphate groups also inhibit the actions of amylases, so DBEs are also needed in starch degradation to cleave $\alpha$-1,6 glycosidic bonds in addition to their role in synthesis (summarized in **Figure 1.4, left side**). In starch degradation, these are typically *direct* debranching enzymes, such as isoamylase, that remove an entire branch in one step. Other enzymes can also act on starch, such as starch phosphorylase ($\alpha$-glucan phosphorylase) that releases G1P, and disproportionating enzyme (D-enzyme) that can transfer maltosyl units from one $\alpha$-1,4 glycosidic linkage to another, potentially creating better substrates for enzymes in both synthesis and degradation (178).

*Glycogen*—Like its synthesis, glycogen degradation can occur in the cytosol, but also occurs through autophagy in the lysosome (termed “glycophagy”) (146). In the cytosol, degradation occurs by phosphorolysis through the actions of glycogen phosphorylase. There are three isoforms of phosphorylase throughout the body, wish muscle, liver, and brain isoforms represented highly in their namesake tissue (179). Glycogen phosphorylase transfers glucose from glycogen to inorganic phosphate, forming G1P. In the reverse pathway to synthesis, G1P can then be funneled into glycolysis through the action of PGM that converts G1P into the glycolytic intermediate G6P. Glycogen phosphorylase can also catalyze the reverse reaction by adding the glucose group from G1P back into glycogen when G1P concentrations are high (180). Importantly, glycogen phosphorylase is unable to release glucose from glycogen within 4 glucosyl residues of a branchpoint, so glycogen debranching enzyme (GDE) is required to transfer a glucan chain from a branchpoint onto the reducing end of a linear chain, extending the substrate for phosphorylase to act upon (181). GDEs first transfer a chain consisting of three glucosyl units using its transferase activity, leaving a single glucose attached at the branchpoint. It then releases a free glucose by hydrolyzing using amylo-$\alpha$-1,6-glucosidase activity, and is thus known as an *indirect* debranching enzyme (182).

Like starch, glycogen also contains covalently bound phosphate, ranging from one phosphate per 500-5000 glucosyl units depending on the glycogen source (183). The function of the phosphate in glycogen is not entirely clear, and its origins are also unclear as no glucan kinase has been identified in animals. Regardless, animals contain one glucan phosphatase known as laforin, encoded by the *EPM2A* gene (184). Mutations in *EPM2A* have been extensively classified and result in the neurodegenerative childhood dementia and progressive epilepsy, Lafora disease

(LD; discussed more below) (185), in which a defining characteristic is hyperphosphorylated glycogen containing much longer glucan chains than normal glycogen (186). These aberrant glycogen molecules are known as lafora bodies (LBs) and are more like amylopectin in size and their insolubility (187). Curiously, mutations in another gene, *EPM2B* that encodes the E3 ubiquitin ligase known as malin, also leads to LB formation (188). Malin appears to play a role in glycogen metabolism by forming a complex with laforin that targets other enzymes involved in glycogen metabolism for ubiquitination (189,190). However, the precise functions of laforin and malin, their role in glycogen metabolism, and the relationship between phosphate content and chain length all remain open questions.

It has more recently been suggested that phosphate is occasionally incorporated into glycogen through a rare glycogen synthase side reaction (191), although this claim has been the subject of debate (183,192). Regardless, phosphate may serve as a molecular method by which to date glycogen that has been broken down and resynthesized several times, resulting in longer chains (193). Thus, a role for glycogen-bound phosphate has been proposed in the second major glycogen degradation pathway: glycophagy. Such a mechanism was elegantly detailed in a recent review (194) and is briefly summarized here: as an older glycogen molecule accumulates more phosphate from repeated rounds of synthesis and develops longer glucan branches (which laforin has been shown to prefer), laforin recruits malin to those glycogen molecules nearing their point of precipitation into LBs, malin ubiquitinates nearby proteins via K63 linkages, this attracts autophagy machinery, and glycogen is targeted for the lysosomal compartment. Within the lysosome, lysosomal acid $\alpha$-glucosidase (GAA) hydrolyzes both $\alpha$-1,4 and $\alpha$-1,6 glycosidic bonds, rapidly releasing free glucose (195).

### 1.5.4 *T. gondii* glucan structure

The first biochemical characterizations of the glucan within *T. gondii* were performed by Dr. Stanislas Tomavo's lab (40,196,197). Importantly, generation of the *T. gondii* glucan in each of these studies utilized acid stress on the RH strain of *T. gondii* by growing it in HepG2 cells that naturally acidify their own cell culture media. It was demonstrated by TEM that parasites under acid stress were producing polysaccharides in their cytoplasm (197), but revealed by western blot analysis that these acid-stress parasites retained their tachyzoite identify, i.e., these parasites had not converted to bradyzoites. RH parasites have a low bradyzoite conversion rate, so this finding was not surprising. The presence of an abundance of crystalline AGs in tachyzoites, however, was not something that had been previously demonstrated. At this point, this set of studies diverged in how the polysaccharide was purified and subsequently analyzed.

In the first two studies (40,196), the polysaccharide was purified under mild conditions by disrupting the tachyzoites with a French press, centrifuging the lysate to pellet insoluble material containing the glucan, and then isolating the glucan by passing the insoluble material over a 90% Percoll gradient. Only something like starch would be able to pellet through such a dense gradient, as water-soluble glycogen requires ultra-centrifugation for pelleting even in the absence of Percoll (198). Both studies then examined the chain lengths of the uncharacterized polysaccharide by first treating the glucan with isoamylase that cleaves $\alpha$-1,6 glycosidic bonds, only leaving linear chains of glucose. The lengths of these chains were then analyzed utilizing high performance anion-exchange chromatography coupled with pulsed amperometric detection (HPAEC-PAD) that relies on the increasingly negative charge of successively longer glucose chains to separate them for detection, or by using capillary electrophoresis (CE), another gel-filtration based technique that separates glucan chains on the basis of charge. In both cases, the chain length distributions (CLDs) were found to be more similar to plant amylopectin than to animal glycogen with the average chain length being 8-12 glucosyl units but ranging up to 36. X-ray analysis revealed that this glucan was also the more hydrated B-type allomorph, a characteristic typical of transitory starch found in leaves. Moreover, NMR and size-exclusion analysis of the undigested glucan demonstrated that no amylose (unbranched chains of glucose) was present in these molecules. Thus, the *T. gondii* glucan had been characterized as true amylopectin, finally warranting the name “amylopectin granules.”

In a follow up study from the same lab (197), AGs were purified from *T. gondii* tachyzoites using a harsher method—parasites were lysed in hot water, contaminants were removed by repeated phenol and chloroform/methanol washes, and AGs were once again analyzed using HPAEC-PAD. Interestingly, the CLD shifted toward shorter chain lengths in this study, with the majority of chains falling into the shorter (DP$\leq$7) category. However, there were still a large number of long chains (8-16). These differences were attributed to the harsher purification technique that might have resulted in a disruption of the longer glucan chains. Importantly, there was a very low proportion of $\alpha$-1,6 linkages (<4%) relative to the linear $\alpha$-1,4 glycosidic bonds as determined by methylation analysis, thus confirming the amylopectin nature of this glucan.

### 1.5.5 Synthesis and degradation of AGs in *T. gondii*

Since the first biochemical characterization of AGs in *T. gondii*, most enzymes related to AG synthesis and degradation have been identified, and are summarized in **Table 1.1** and visualized in **Figure 1.4** (199). Notably, many of these enzymes are expressed in tachyzoites, where AGs have not been observed by EM (ToxoDB.org). This section will serve to highlight these *T. gondii* enzymes in the context of the enzymes previously introduced in starch/glycogen synthesis and degradation. All enzymes involved in AG synthesis and degradation were

determined to be “dispensable” by a genome wide CRISPR knockout screen, meaning that loss of any one of these genes does not impose an appreciable fitness defect on the parasite (10). It should be noted, however, that this screen was conducted under ideal, nutrient-replete cell culture conditions in tachyzoites only, and following its publication, many of these AG-related genes have been demonstrated to be critical virulence and cyst-forming factors in mice.

*Synthesis—T. gondii* encodes the enzymes needed to produce UDP-glucose: two PGM isoforms (PGM1/2) and a UGPase (ToxoDB.org). PGM1/2 in *T. gondii* have been characterized for their parafusin-related activity in calcium signaling and secretion, and PGM1 was ultimately renamed parafusin-related protein 1 (PRP1) (200). It was shown the PGM1/2 were truly dispensable and simultaneous deletion of both genes had no effect on parasite virulence in mice. Deletion of PRP1 did, however, result in defective microneme secretion in response to the calcium ionophore A23187, suggesting a potential link between amylopectin metabolism, calcium signaling, and egress-related secretion. The UGPase has not been studied, but it has been confirmed that *T. gondii* primarily incorporates glucose from UDP-glucose into AGs (40). Despite synthesizing crystalline amylopectin, *T. gondii* also expresses a glycogenin orthologue that was also characterized outside of the glucan synthesis pathway in its role as a glycosyltransferase that acts on Skp1 [(201) that was originally published under a different title (202)].

The glucan synthase (TgSS) in *T. gondii* is referred to interchangeably as “starch synthase” and “glycogen synthase” in the literature, and its knockout resulted in loss of glucan synthesis in *T. gondii* tachyzoites and bradyzoites, verifying its function (203). ΔTgSS parasites also displayed a mild growth defect in cell culture tachyzoites, lower tissue cyst numbers in mouse brains, and a decreased ability to reactivate from bradyzoites back into tachyzoites *in vitro*. Moreover, SS is only found in other coccidian parasites that synthesize starch-like polysaccharides such as *Neospora* and *Eimeria*. The role of TgSS and what it reveals about the role of AGs in central carbon metabolism will be discussed in section 1.6.3. *T. gondii* also encodes two putative branching enzymes (ToxoDB.org), but how they specifically remodel the branchpoints in AGs remains to be determined. Finally, as would be expected, *T. gondii* does not encode a granule-bound starch synthase (GBSS), an amylose synthesizing enzyme, which is consistent with the observation that it synthesizes a true amylopectin containing no amylose.

*Degradation—T. gondii* encodes all the enzymes needed in AG degradation alongside the cycle of reversible phosphorylation that facilitates degradation with some key differences. As in plants, *T. gondii* encodes both a glucan phosphatase and a glucan, water dikinase. The glucan phosphatase was previously named TgLaforin based on its domain orientation (204,205) (**Figure 1.5**). Mammalian laforin contains a carbohydrate binding module (CBM) N-terminal to its dual-specificity phosphatase (DSP) domain, while the plant glucan phosphatase SEX4 is arranged in the opposite orientation with a DSP N-terminal to its CBM (**Figure**

**1.5**). Moreover, the CBMs found in laforin and SEX4 are from different families, with laforin possessing a CBM20 and SEX4 possessing a CBM48. Accordingly, *T. gondii* laforin, or TgLaforin, contains a unique CBM20 N-terminal to its DSP domain like human laforin (this CBM20 is dissected extensively in section 3.2.3 and 3.2.4). Opposing TgLaforin activity is a GWD orthologue, TgGWD, containing at least two CBM45 domains and a PPDK domain (discussed in section 4.1 and 4.2). Neither of these proteins had been characterized *in vivo*, or extensively *in vitro*, until the writing of this dissertation. *T. gondii* does not possess orthologues to the other plant-like glucan phosphatase, LSF2, to the C3-specific glucan dikinase PWD, or to the E3 ubiquitin ligase, malin, found in humans.

In addition to the enzymes involved in reversible phosphorylation, *T. gondii* also encodes the enzymes needed to release glucose from AGs. Debranching enzyme was characterized in *T. gondii* (named "Aa16GL") in two ΔAa16GL lines of parasites—one in Type I parasites (RH strain) and one in Type II parasites (Pru strain). In both cases, parasites displayed significantly slower growth as evidenced by plaque assays with tachyzoites but appeared to have no obvious morphological defects related to AGs. Moreover, ΔAa16GL parasites displayed no acute virulence defect in mice but did form significantly fewer cysts.

*T. gondii* also contains two classes of enzymes that cleave glycosidic bonds: α-amylases (endo-acting) and a glycogen phosphorylase ortholog, but *T. gondii* does not contain β-amylases (exo-acting). Interestingly, loss of either α-amylase or glycogen phosphorylase (TgGP) activity resulted in overaccumulation of AGs in both tachyzoites and bradyzoites, and, once again, lower cyst formation in mice while not affecting the acute phase of infection (206). Interestingly, the post-translational regulation of TgGP via phosphorylation was determined by mutating a phospho-site, S25, to either an alanine (S25A; unable to be phosphorylated) or a glutamate (S25E; constitutively "phosphorylated"). The phosphomimetic S25E displayed no AG accumulation or cyst formation penalty compared to WT, but the S25A mutant resulted in both AG-excess and a significantly lower cyst burden mice, demonstrating the importance of this phosphorylation site, possibly by the kinase CDPK2 (discussed below), in the regulation of AG metabolism.

### 1.5.6 The hybrid nature of *T. gondii* AG metabolism and its red algal lineage

It is worth noting that enzymes involved in *T. gondii* AG metabolism are either plant- or animal-like (**Figure 1.6**). *T. gondii* utilizes UDP-glucose (not ADP-glucose) to synthesize AGs in its cytoplasm (not in its plastid), which are both features of animals. The end product, however, is a crystalline AG with low branching frequency, which is plant-like. With regards to enzymology, the cycle of reversible phosphorylation includes a glucan, water dikinase (plant-like) opposing a laforin-like glucan phosphatase (animal-like). *T. gondii* also encodes a glycogenin ortholog (animal-like) whose activity relative to AG metabolism has not been established. It does not appear that *T. gondii* possesses the glycogen-

degrading lysosomal enzyme GAA (animal-like), which implies that glycophagy may not occur in this parasite.

This unique combination of characteristics from different kingdoms of life provides evidence for its red algal ancestry. A *T. gondii* ancestor is believed to have participated in a secondary endosymbiotic event that resulted in its obtainment of the apicoplast. While the cytoplasm of the ancestral red alga was lost, its plastid remained in the form of the four-membraned apicoplast, a result of the original double-membraned chloroplast obtaining two additional membrane leaflets upon its engulfment. Thus, like *T. gondii*, red algae, such as *Cyanidioschyzon merolae*, also display characteristics of a plant/animal hybrid starch machinery as they also synthesize an amylopectin-like molecule in their cytoplasm with UDP-glucose, not in their plastids with ADP-glucose (207). In addition, *C. merolae* and *T. gondii* share the similarity that both of have highly simplified mechanisms of starch synthesis and degradation when compared to plants or green algae where 30-40 genes have been identified in starch turnover (199). *C. merolae* and *T. gondii* each contain 15 or fewer genes in synthesis and degradation combined. As an example of the simplification of starch synthesis in these unicellular organisms, *Arabidopsis thaliana* (representative of land plants) and *Chlamydomonas reinhardtii* (representative of green algae) contain 5 and 7 starch synthases, respectively, whereas *C. merolae* and *T. gondii* only contain 1 starch synthase each. Moreover, land plants and green algae also contain GWD and PWD along with SEX4, whereas both *C. merolae* and *T. gondii* contain only GWD opposing a laforin orthologue.

## 1.6 A new role for AGs in *T. gondii* tachyzoite metabolism

Until recently, a role for AGs in tachyzoites had not been considered. References to AGs in early literature typically note their abundance in bradyzoites by TEM, and typically noted their relative absence/rarity in tachyzoites, despite the fact that tachyzoites were observed to stain with the PAS, the glucan stain, as early as 1956 (125). This section will serve to highlight the recent recognition that AGs play a role in tachyzoite central carbon metabolism. As such, an overview of *T. gondii* metabolic concepts will first be presented, followed by a recent understanding of AGs in tachyzoite metabolism.

### 1.6.1 General metabolic themes in *T. gondii*

*T. gondii* central carbon metabolism is largely intact as it encodes a complete set of enzymes needed to fuel glycolysis (208), gluconeogenesis (209-211), the pentose phosphate pathway (PPP) (212), the TCA cycle (ToxoDB.org), and oxidative phosphorylation (OX-PHOS) (213). Major metabolites and enzymes in these pathways discussed in this section are illustrated in **Figure 1.7.** Several enzymes that participate in these pathways are encoded by multiple genes that

are regulated in a stage specific manner such as lactate dehydrogenase (214-216) and enolase (217,218). Moreover, while tachyzoites utilize glycolysis and the TCA cycle, there is evidence that bradyzoites downregulate mitochondrial metabolic pathways such as the TCA cycle and OX-PHOS, and therefore depend more on glycolysis (105,219). The evidence for this, however, is largely based on *in vitro* bradyzoite conversion that results from treatment with oligomycin, a mitochondrial ATP synthase inhibitor (53). Tachyzoites, on the other hand, have been shown to be dependent on a functional TCA cycle, as inhibition of aconitase with sodium fluroacetate (NaFAc) results in complete inhibition of tachyzoite growth (220).

There are key differences, however, in *T. gondii* central carbon pathways from conventional pathways. For example, *T. gondii* encodes a pyruvate dehydrogenase (PDH) complex that resides in its apicoplast, but does not encode a *mitochondrial* PDH isoform for the conversion of pyruvate to acetyl-CoA to enter the TCA cycle. Only relatively recently was it discovered that the mitochondrial branched chain ketoacid dehydrogenase (BCKDH; **Figure 1.7**) could perform this function, allowing for glucose-derived carbon to flow from glycolysis into the TCA cycle (221). *T. gondii* also encodes a plant-like sedoheptulose bisphosphatase not found in mammals that provides an alternative route for incorporation of glycolytic carbon into the PPP (222). Finally, *T. gondii* does not encode a standard OX-PHOS pathway found in mammals as it lacks a Type I proton-pumping NADH dehydrogenase (complex I), instead encoding for two non-proton pumping Type II NADH dehydrogenases (223). Such differences between pathways make for attractive drug targets (224).

### 1.6.2 Glucose and glutamine metabolism

*T. gondii* is both flexible with its utilization of the carbon backbones of glucose and glutamine and also dependent on these two molecules to fuel its central carbon pathways. This was first demonstrated by the knockout of the only plasma-membrane glucose transporter in *T. gondii*, TgGT1 (**Figure 1.7**) (225). Surprisingly, ΔTgGT1 tachyzoites only demonstrated a moderate growth penalty, forming plaques in a host-cell monolayer ~70% the size of WT parasites. This was shown to be both the result of a slower replication rate and almost completely abolished extracellular motility that was ~10% of the WT level. Importantly, these defects could be replicated in WT parasites by starving them of glucose. The motility defect could be rescued in ΔTgGT1 parasites with glutamine supplementation, suggesting that *T. gondii* can utilize glutamine to substitute for glucose in times of nutrient starvation.

These observations were expanded upon in a follow-up study that used stable isotope labeling of ΔTgGT1 parasites with both $^{13}$C-glucose and $^{13}$C-glutamine to tease out the precise metabolic contributions of glucose and glutamine (226). In ΔTgGT1 parasites, incorporation of exogenous glucose into glycolytic, PPP, and TCA pathways was significantly decreased as would be expected. Importantly,

incorporation of $^{13}$C-glutamine was highly elevated in ΔTgGT1 parasites throughout all of the aforementioned pathways, suggesting that *T. gondii* increases flux of glutamine into central carbon metabolism through glutaminolysis and gluconeogenesis (**Figure 1.7; red arrows**) (209,220). Glutaminolysis in *T. gondii* was shown to be unique in that it can utilize a GABA shunt whereby glutamine is converted into GABA and ultimately incorporated into the TCA cycle by conversion into succinate, providing a two routes including the conventional funneling of glutamine into α-ketoglutarate (**Figure 1.7**) (220). Depletion of glutamine from ΔTgGT1 tachyzoites resulted in highly attenuated growth, the inability to survive extracellularly for any extended period, and an impaired ability to invade host cells. A complementary study was performed in which loss of the mitochondrial gluconeogenic enzyme, phosphoenolpyruvate carboxykinase (TgPEPCK) that converts oxaloacetate into phosphoenolpyruvate, was examined (**Figure 1.7**) (210). Tachyzoites tolerated loss of TgPEPCK with no gross growth defects in cell culture, but knockdown of TgPEPCK resulted in a decreased flux of $^{13}$C-glutamine through gluconeogenesis. Consistent with this, ΔTgGT1 parasites were unable to tolerate simultaneous knockdown of TgPEPCK, as this results in a complete loss of carbon flow through both glycolysis and gluconeogenesis.

Because ΔTgGT1 parasites could theoretically retain the ability to operate glycolysis, another study examined “glycolysis deficient” parasites by knocking out hexokinase, “Tghk” (**Figure 1.7**) (211). ΔTghk parasites largely recapitulated the phenotypes seen in the ΔTgGT1 strain—a moderate growth defect, upregulation of gluconeogenesis, and an increased dependence on glutamine. While the previous studies did not show how loss of glycolysis might impact virulence in mice, this study demonstrated that ΔTghk mutants remained virulent in mice, but only at a high parasite inoculum. Moreover, they were severely compromised in their ability to form cysts. Interestingly, this study also demonstrated that inhibition of glutaminolysis with a glutamine analogue, azaserine, was detrimental not only to ΔTghk mutants, but also to WT parasites. Thus, glutamine appears to be an essential nutrient, even in the presence of glucose.

Similar models have been proposed in these studies regarding parasite utilization of glucose and glutamine (210,211). Under normal conditions, *T. gondii* utilizes glucose to fuel glycolysis and the first reactions of the TCA cycle, and glutamine-derived-carbon to fuel the remainder of the TCA cycle (**Figure 1.7; glucose fueled reactions: blue; glutamine fueled reactions: red**). However, if deprived of either nutrient, the parasite demonstrates plasticity in its nutrient utilization. Under glutamine deprivation, the parasite funnels glucose-derived carbon through glycolysis into the TCA cycle to make up for the loss of glutamine. Under glucose deprivation, *T. gondii* utilizes glutaminolysis to fuel the TCA cycle through glutamine conversion to either α-ketoglutarate or succinate via the GABA shunt to then supply carbon to the glycolytic reactions via gluconeogenesis through functional PEPCK, pyruvate carboxylase (TgPyC), and fructose-6-phosphate

bisphosphatase (FBPase). Moreover, *T. gondii* growth is severely impacted in the absence of both nutrients, but not completely ablated.

Interestingly, it appears that while *T. gondii* can tolerate absolute glucose starvation (as evidenced by ΔTgGT1 parasites), it cannot tolerate total glutamine starvation via pharmacological methods (211). This suggests that host cells generate glutamine when it is removed from the media in "glutamine starvation experiments" that the parasites are ultimately able to scavenge, explaining their ability to survive without supplemented glutamine. The reason underlying this is unclear, but could be due to nitrogen deprivation in glutamine's absence or its importance in protein synthesis as demonstrated by glutamine-derived carbon's incorporation into protein by $^{14}$C-labeling (226). Notably, a glutamine transporter in *T. gondii* has not yet been identified (227).

### 1.6.3 A new understanding of AGs in *T. gondii* metabolism

Outside of applying acid stress, the presence of AGs or functional AG metabolism in tachyzoites had not been significantly discussed until recent exploration of the role of plant-like calcium-dependent protein kinase2, CDPK2 (228). CDPKs regulate a wide variety of processes in *T. gondii* related to calcium signaling such as egress (CDPK1 and 3) (229,230), invasion (CDPK1) (231), and replication (CDPK7) (232). Each CDPK contains a kinase domain, a calmodulin-like domain composed of multiple EF-hands for calcium binding, and a variable N-terminal region (233). In the case of CDPK2, its N-terminus contains a CBM20, immediately suggesting its involvement with polysaccharides. Indeed, it was demonstrated that CDPK2 targets to multiple, small puncta within the *T. gondii* cytoplasm via its CBM as this localization disappears with the mutation of key carbohydrate binding residues in the CBM (228). This CDPK2 study was the first modern study to demonstrate small punctate AG staining within tachyzoites by PAS. The deletion of any of the three domains in CDPK2 resulted in parasites containing large AG accumulations on their basal end and within their residual bodies (a remnant from replication), strongly suggesting a link between calcium signaling and carbohydrate metabolism, as did the PGM1/2 knockout (section 1.5.5).

In the ΔCDPK2 study, pulse-chase analysis of $^{13}$C-glucose into and out of amylopectin in tachyzoites indicated that the WT parasites rapidly synthesize and degrade AGs, and ΔCDPK2 parasites synthesized AGs at a faster rate and degraded them at a slower rate than WT parasites, thus resulting in an AG excess phenotype (228). This demonstrated that CDPK2 has roles in regulation of both AG synthesis and degradation. The metabolic profile of the parasites was altered as well with an upregulation of glucose incorporation into glycolysis, although the reasons underlying this are unclear. Moreover, several putative targets of CDPK2's kinase activity related to AG metabolism were demonstrated including TgGWD, Aa16GL (debranching enzyme), TgGP, a branching enzyme, and an α-amylase.

Finally, ΔCDPK2 parasites were less virulent in mice and resulted in the formation of no tissue cysts.

After this report, a number of studies were subsequently published examining some of the putative targets of CDPK2. Thus far, the only two enzyme knock outs that resulted in a similar AG-excess phenotype and a decreased cyst burden in mice were TgGP (206) and α-amylase (234), but neither of these studies examined parasite central carbon metabolism. α-amylase mutants were much less virulent in mice, and further explored as a potential vaccine candidate as infection with these mutants protected mice against further challenges with WT parasites. While the mechanism is not understood, inducible knockdown of pyruvate kinase (PYK) (**Figure 1.7**) is the only other mutant that has demonstrated an overaccumulation of AGs in tachyzoites at the time of writing this dissertation (235). A remarkable observation from this study demonstrated that AG excess remained under glucose-starved conditions while PYK was knocked down, suggesting that AGs can be synthesized from glutamine-derived carbon.

Studies of starch synthase (TgSS) in *T. gondii* demonstrate the role of AGs in central carbon metabolism most clearly (203). Loss of TgSS resulted in loss of AGs in tachyzoites and bradyzoites by PAS staining, no virulence defect in mice, and a slightly lower cyst burden. Curiously, loss of TgSS resulted in higher bradyzoite conversion efficiency *in vitro*, and larger cysts *in vivo*. This study also provided the first direct evidence of AG involvement in bradyzoite reactivation by demonstrating that ΔTgSS parasites were impaired in turning off bradyzoite markers in an *in vitro* reactivation assay. Importantly, flux of glucose-derived carbon through glycolysis, the TCA cycle, and the PPP in ΔTgSS parasites was significantly decreased. While it was not examined here, decreased glucose flux through central carbon metabolism implies the simultaneous upregulation of glutamine metabolism. This study therefore provided significant evidence that AGs play a role in glucose allocation in *T. gondii* tachyzoites, that the effective removal of AGs results in dysregulation of glucose allocation, and that AGs are needed in bradyzoite reactivation.

## 1.7 Regulation of AG metabolism in *T. gondii*

As the importance of AGs in tachyzoites is currently being elucidated, the regulatory mechanisms underlying their usage is still unknown. The critical regulatory role of reversible phosphorylation of both starch and glycogen has been recognized over the past 25 years by two distinct fields, plant biologists and neurobiologists, whose findings often complemented and informed each other during the early days of discovery (236).

### 1.7.1 The importance of direct, reversible glucan phosphorylation in plants in animals

While the presence of covalently bound phosphate has been recognized in both glycogen and starch, it was treated as either a contaminant or a curiosity (237) until knockdown of GWD (then known as “R1 protein”) in 1998 resulted in a starch-excess phenotype alongside reduced phosphate content in *A. thaliana* leaves (238). Following this, it was soon recognized that R1 was a glucan, water dikinase (GWD) (167), and predicted that direct phosphorylation of starch facilitated its breakdown by other enzymes (237). Simultaneous to the discovery of the importance of starch-bound phosphate, an *A. thaliana* mutant that displayed a striking *starch-excess* (SEX) phenotype was characterized, and the gene related to this phenotype was named *SEX4* (239). Notably, the ∆*SEX4* line of plants displayed no decrease in enzymatic activity of other starch degrading enzymes (239), and it was demonstrated that the SEX phenotype developed progressively as plant leaves aged (240). Independent of this study, the protein encoded by this gene was identified in an *A. thaliana* phosphatase screen and classified as a protein tyrosine phosphatase (PTP) due to the presence of its catalytic $CX_5R$ motif in its phosphatase domain (241). This study also classified a domain downstream of the PTP domain as a “kinase interaction sequence (KIS).” Several years later, a study mapped the *SEX4* locus to this protein, identified that the KIS was indeed a CBM, and demonstrated that recombinant SEX4 could bind glycogen (242).

Prior to these studies in plants, scientists were grappling with the molecular underpinnings of Lafora disease (LD) in humans. LD was first described in 1911 by Dr. Gonzalo Lafora who discovered amyloid-like deposits in the brains of young patients with a neurodegenerative epilepsy at autopsy (243). These deposits were subsequently shown to be glucose-based polymers that were amylopectin-like in nature and termed “Lafora bodies” (LBs) (244,245). In 1998, mutations in one of two genes causing LD (*EPM2A*) was identified and classified as a protein-tyrosine-phosphatase (the family to which DSPs belong) (184). Subsequently, laforin’s CBM was identified, and the CBM was shown to target laforin to glycogen (246), making it the only human phosphatase to possess a CBM (236).

Notably, the study that demonstrated the ability of SEX4 to bind carbohydrates also recognized the similarities between SEX4 and mammalian laforin, speculating that their shared functions allowed them to bind carbohydrates and dephosphorylate proteins related to carbohydrate metabolism (242). That same year, a study was published demonstrating that laforin could instead dephosphorylate amylopectin *in vitro*, possessing a target and function that had not yet been predicted—namely, that laforin is a glucan phosphatase (247). Studies immediately followed demonstrating that loss of laforin in *epm2a*$^{-/-}$ mice resulted in hyperphosphorylated glycogen, speculating that hyperphosphorylation is what lead to the aberrant branching characteristic of LBs (186). It was then confirmed that laforin and SEX4 were functional equivalents, as complementation of laforin into ∆*SEX4* plants resulted in rescue of the SEX phenotype; this was both visualized by iodine staining and quantified in total starch content in the leaves (204). These complementary fields describing glucan phosphorylation came full

circle by demonstrating that SEX4 also behaved as a glucan phosphatase *in vitro* and *in vivo*, as Δ*SEX4* plants accumulated hyperphosphorylated starch breakdown intermediates (174). Following these foundational findings in the LD field, it has been shown that loss of laforin has an impact beyond the glycogen molecule, extending into metabolism (248) and glycosylation defects (154).

### 1.7.2 Laforin in protists and motivation for the project

At the same time that glucan phosphatase activity was described and established in both plants and animals, laforin orthologues were recognized in many Apicomplexan protists of red algal descent including *T. gondii*, *Neospora*, *Sarcosystis*, and *Eimeria* among others (204,205). Indeed, *a priori* criteria to determine if protists contain laforin were developed: the protist must 1) contain an insoluble glucan, 2) contain a true mitochondrion, and 3) be of red algal descent. Importantly, all the identified protists in these studies also encyst for some portion of their life cycle, implying the importance of glucan storage, and thus its regulation via reversible phosphorylation, in each protist's life cycle.

Given the importance of direct reversible phosphorylation across kingdoms of life in proper glucan degradation and central carbon metabolism, and the clear roles of AGs in metabolism and energy storage across asexual (tachyzoite and bradyzoite) and sexual (sporozoite) life stages of *T. gondii*, we sought to further characterize the enzymes involved in AG regulation via an understanding of reversible glucan phosphorylation in *T. gondii*.

In **Chapter 3**, to accomplish this task, we first provide a detailed characterization of recombinant TgLaforin by 1) elucidating the organization of its unique CBM, 2) providing evidence for its DSP-mediated dimerization, 3) demonstrating its activity as a glucan phosphatase that dephosphorylates amylopectin *in vitro* with preference for the C3 position, and 4) developing a glucan phosphatase inhibitor with specificity to TgLaforin.

In **Chapter 4**, we next characterized TgGWD *in vitro* as a true glucan, dikinase that 1) utilizes the β-phosphate from ATP to autophosphorylate itself before, 2) phosphorylating amylopectin on the C6 position, and 3) releasing AMP that we detected using a novel capillary electrophoresis-based assay to detect.

In **Chapter 5**, we finally demonstrate that TgLaforin does indeed play a critical role in AG metabolism in *T. gondii* tachyzoites and bradyzoites using CRISPR/Cas9 to both tag and knockout TgLaforin. We demonstrate that 1) TgLaforin localizes to AGs in tachyzoites, 2) that loss of TgLaforin results in a dependence on glutamine, decreased virulence in mice, and decreased cyst-forming ability, and 4) loss of TgLaforin results in the selective over-accumulation of AGs in bradyzoites and not tachyzoites.

The impact of each of these studies will be discussed in the chapter in which it is presented, and a discussion regarding where these studies push our

understanding of AGs and their role throughout the *T. gondii* asexual life stages will be presented in **Chapter 6**.

**Table 1.1 Enzymes required for AG synthesis and degradation.**
All identified enzymes in AG turnover are listed in this table, alongside ToxoDB.org accession numbers.

| Starch Synthesis | Accession No. |
|---|---|
| Hexokinase | 265450 |
| Phosphoglucomutase 1/2 | 285980/38580 |
| UDP-glucose pyrophosphorylase | 218200 |
| Glycogen Synthase | 222800 |
| Branching Enzymes | 316520/209960 |
| **Starch Degradation** | |
| Glucan, Water Di-kinase (GWD) | 214260 |
| α-Amylases | 246690/283490 |
| TgLaforin | 205290 |
| Glycogen phosphorylase | 310670 |
| **Both** | |
| Disproportionating enzyme | 271210 |
| Debranching enyzme | 226910 |

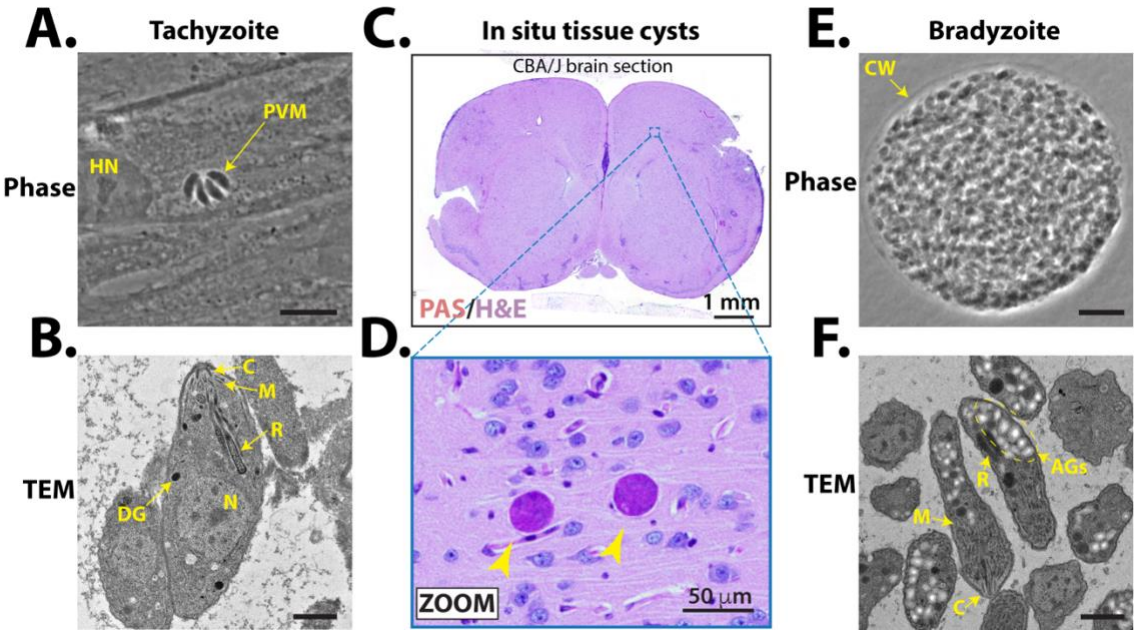


**Figure 1.1 Morphology of asexual stages of *T. gondii* tachyzoites and bradyzoites.**

**A,** Phase image of four *T. gondii* tachyzoites in human foreskin fibroblasts (HFFs), demonstrating their overall arc-like morphology. The parasitophorous vacuole membrane (PVM) that contains tachyzoites is highlighted. Scale bar = 10 μm. **B**, TEM of tachyzoite with secretory organelles labeled. Scale bar = 1 μm. **C,** Coronal slice of CBA/J infected brain. **D,** Zoom of blue box from (C), PAS+ tissue cysts indicated with arrowheads. **E**, Phase image of *T. gondii* tissue cyst isolated from the brain of a mouse containing hundreds of individual bradyzoites; cyst wall (CW) labeled. Scale bar = 10 μm. **F**, TEM of bradyzoites within tissue cysts from brain of infected mouse containing amylopectin granules (AGs) and an increased number of micronemes (M). Scale bar = 1 μm. *Abbreviations:* AG = amylopectin granule; C = conoid; CW = cyst wall; DG = dense granule; HN = host nucleus; N = parasite nucleus; M = micronemes; PAS = periodic acid-Schiff; R = rhoptries.

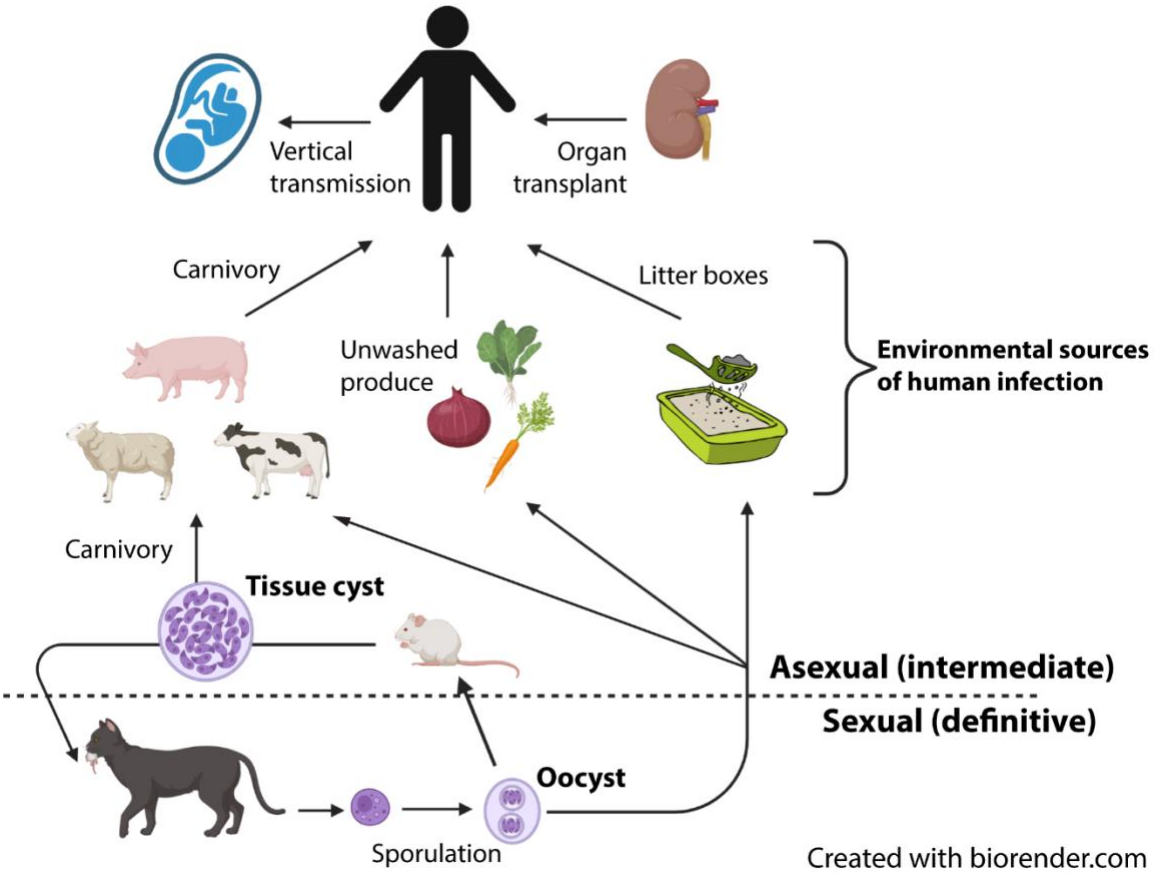


**Figure 1.2 The *T. gondii* life cycle and common sources of human infection.** Evidence for each mode of transmission is presented in section 1.2.1 and 1.2.2. A compact description of the entire lifecycle is presented in section 1.2.3.

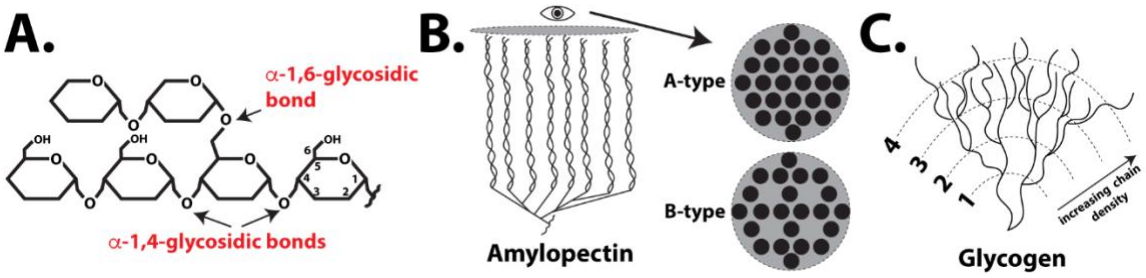


**Figure 1.3 The molecular underpinnings of amylopectin and glycogen organization.**

**A**, Both amylopectin and glycogen are composed of glucose joined by α-1,4- and α-1,6-glycosidic bonds that result in linear bonds and branchpoints, respectively. **B**, The low frequency and clustered arrangement of branchpoints in amylopectin allows glucan chains to wind around each other, excluding water. The top-down view of chains demonstrates their packing beside one another, resulting in either A-type amylopectin (excluding more water) or B-type (incorporating more water). **C**, The increased frequency of branching in combination with evenly distributed branchpoints in glycogen results in a tiered structure that exponentially increases in glucose content with each tier. This arrangement prevents extensive chain-winding, resulting in a water-soluble glucan.

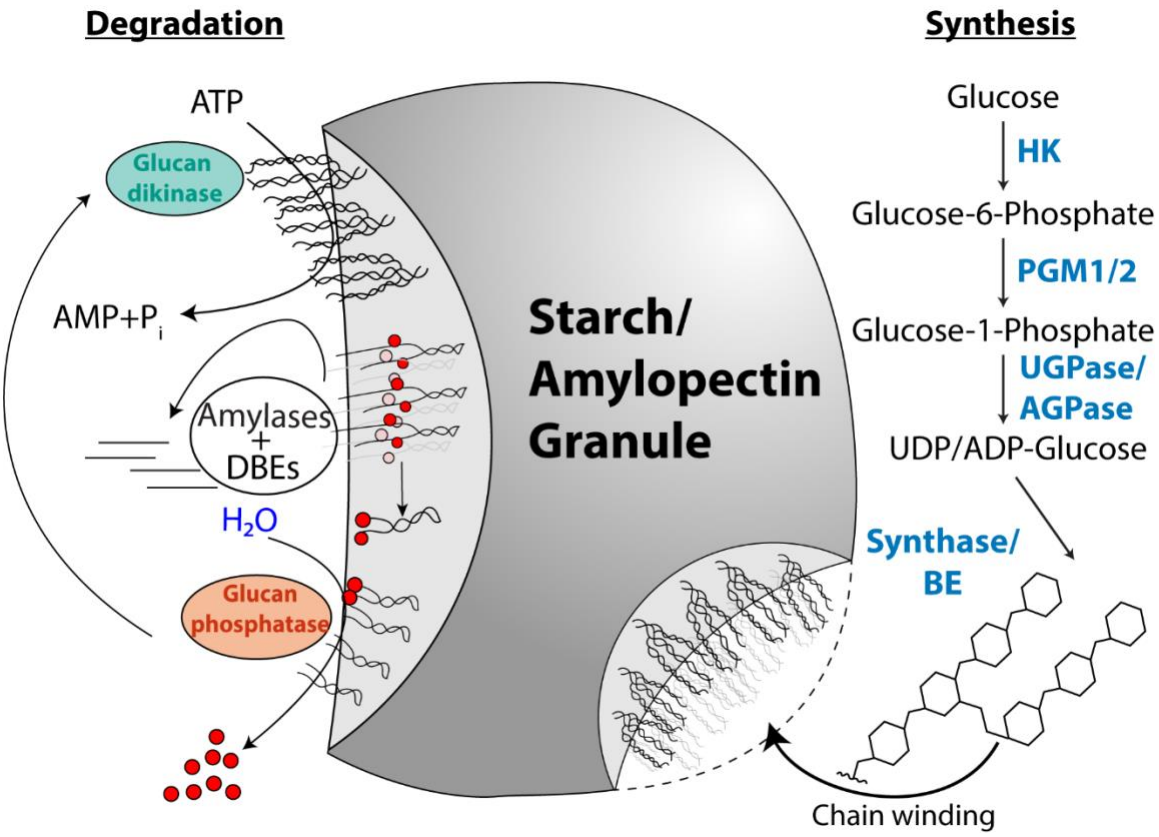


**Figure 1.4 The enzymology of insoluble glucan synthesis/degradation.**
The right side depicts the generation of the substrate for starch synthesis, an activated sugar-nucleotide, and its incorporation into growing glucan chains that ultimately wind around each other excluding water. The left side depicts starch degradation via a cycle of reversible glucan phosphorylation. Red circles symbolize phosphate. *Abbreviations:* AGPase = ADP-glucose pyrophosphorylase; BE = branching enzyme; DBE = debranching enzyme; HK = hexokinase; PGM = phosphoglucomutase; UGPase = UDP-glucose pyrophosphorylase.

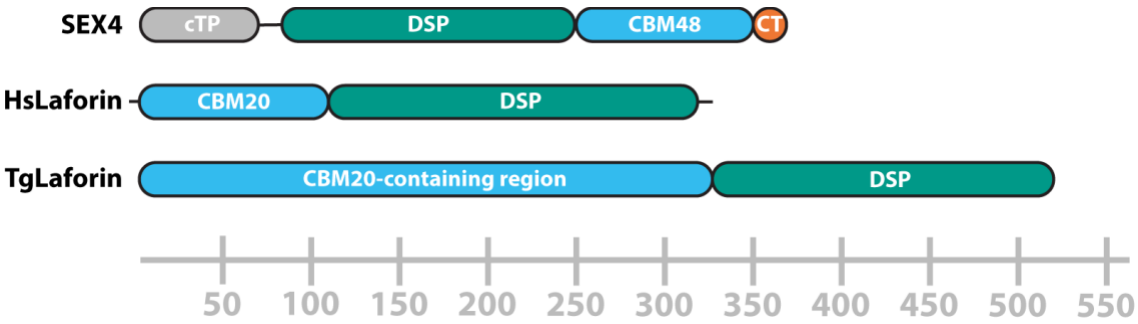


**Figure 1.5 Domain composition and orientation of glucan phosphatases.** Ruler below corresponds to the amino acid length of each protein/domain. *Abbreviations:* CBM = carbohydrate binding module; CT = C-terminal domain; cTP = chloroplast Targeting Peptide; DSP = dual specificity phosphatase domain.

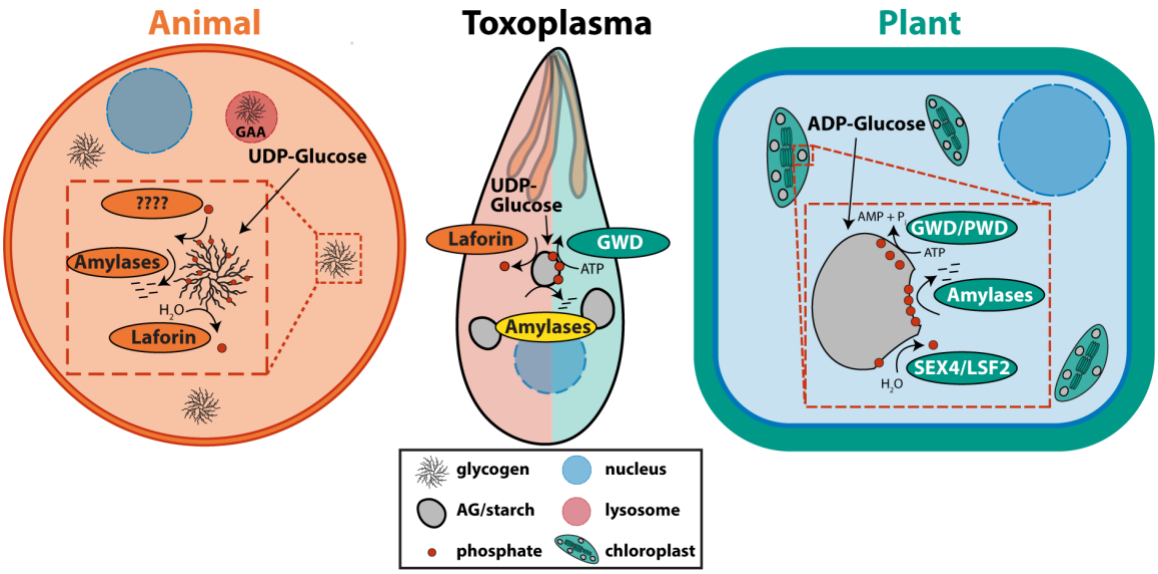


**Figure 1.6 *T. gondii* AG metabolism combines animal glycogen and plant starch characteristics.**
Schematic of both animal and plant glucan localization, synthesis, and degradation, and the properties of each that are found in *T. gondii. Abbreviations:* ADP = adenosine di-phosphate; GAA = acid-α-glucosidase; GWD = glucan, water dikinase; PWD = phosphoglucan, water dikinase; UDP = uridine di-phosphate.

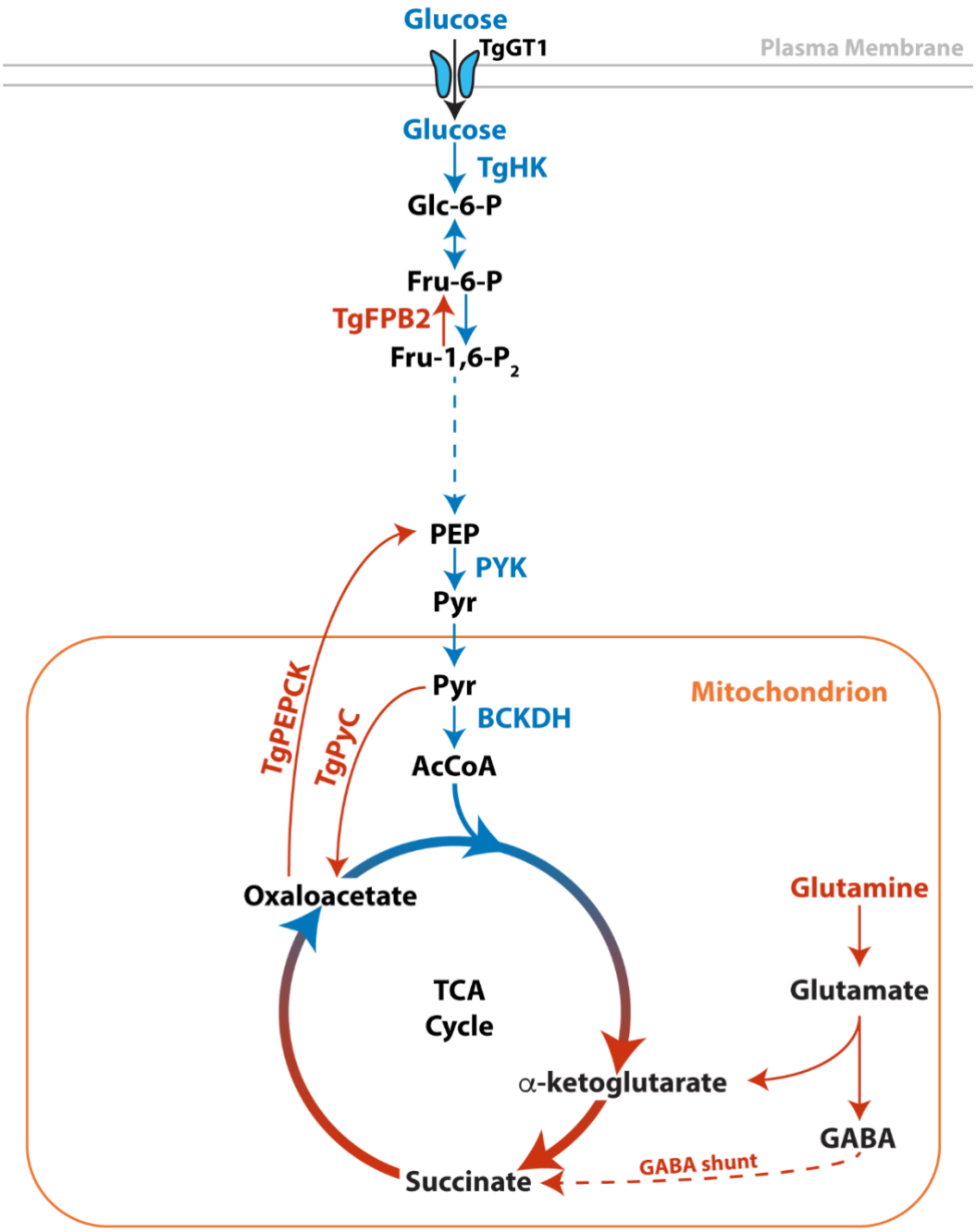


**Figure 1.7 Glycolysis, gluconeogenesis, and the TCA cycle in *T. gondii*.** Reactions typically filled by glucose are depicted with blue arrows, and those filled by glutamine are depicted with red arrows. Similarly, glycolytic enzymes are in blue font, and glutaminolytic/gluconeogenic reactions are in red font. *Abbreviations:* BCKDH = branched-chain ketoacid dehydrogenase; Fru-6-P = fructose-6-phosphate; Fru-1,6-$P_2$ = fructose 1,6-bisphosphate; Glc-6-P = glucose-6-phosphate; PEPCK = phosphoenolpyruvate carboxykinase; PYK = pyruvate kinase; TgFBP2 = fructose-1,6-bisphosphatase; TgGT1 = glucose transporter 1; Tghk = hexokinase; TgPyC = pyruvate carboxylase.

# CHAPTER 2. MATERIALS AND METHODS

## 2.1 Biochemical, biophysical, and structural studies of TgLaforin and TgGWD

### 2.1.1 Sequence alignments, secondary structure predictions, and transcriptomics

The amino acid sequences of TgLaforin (TGME49_205290) and TgGWD (TGME49_214260) were obtained using ToxoDB.org. The sequences of other glucan phosphatases and glucan dikinases were obtained from UniProt (249). Domain boundaries of proteins were defined using a combination of previously published literature (250-254), the "Family and Domains" section in UniProt, and/or the NCBI's Conserved Domain Database (255). UniProt accession numbers and amino acid numbering corresponding to each glucan phosphatase domain are listed in **Table 2.1**. UniProt accession numbers of glucan, water dikinases and domain boundaries are listed in **Table 2.2.** Amino acid sequences of the CBM domains, DSP domains, and His-domains within each were aligned separately from each other using ClustalW with default settings (Gonnet Matrix, Open Gap Penalty: 10, Extend Gap Penalty: 0.2, Delay Divergent: 30%) and prepared using MacVector 18. Secondary structure predictions of TgLaforin were obtained using the Jpred 4 server (256) and compared to HsLaforin secondary structures (253).

Transcriptomics datasets were obtained from ToxoDB.org for TgLaforin, TgGWD, and SRS9 (TGME49_320190). $Log_2$(RMA) values were plotted in Prism 9 (GraphPad) along with their reported standard deviations.

### 2.1.2 AlphaFold2 modeling of TgLaforin

The three-dimensional models for TgLaforin were obtained by running AlphaFold2 via the DeepMind official Colab server using AlphaFold v2.1.0 (https://colab.research.google.com/github/deepmind/alphafold/blob/main/notebooks/AlphaFold.ipynb) (257,258). For the TgLaforin monomer structure prediction, model confidence was assessed by the predicted Local Distance Difference Test (pLDDT) score (258), whereas a weighed combination of predicted TM-score (pTM) and interface pTM score (ipTM) was used to assess the reliability of the TgLaforin dimer model (257). In both cases, top ranked models were used for subsequent analysis. Structural models were analyzed, and figures were made using PyMOL 2.2.3 (Schrodinger).

### 2.1.3 Cloning and expression of TgLaforin and TgGWD

*Cloning*: The cDNA sequences of TgLaforin (TGME49_205290) and TgGWD (TGME49_214260) were obtained from ToxoDB.org. The sequences were then codon optimized, synthesized, and cloned into pET28b+ using NdeI/XhoI digest

sites by GenScript. The catalytically inactive mutants [TgLaforin-FL C452S (C/S) and the TgGWD-FL H1241A (H/A)] and all CBM constructs were also generated by GenScript using site-directed mutagenesis. TgLaforin was further subcloned into ppSUMO, a vector containing a small ubiquitin-like modifier (SUMO) that fused TgLaforin-FL to an N-terminal $His_6$-SUMO tag, and into pFastBac-HTA (Invitrogen) using NdeI/XhoI restriction digest sites (New England Biolabs). All plasmids used in this study are listed in **Table 2.3.**

*For BL21 E. coli expression:* 50 ng each plasmid was transformed into chemically competent BL21 (DE3) *E. coli* cells (New England Biolabs). *E. coli* was next plated on LB agar plates containing kanamycin and chloramphenicol, and single colonies were selected for protein expression the next day. Colonies were suspended in 7 mL LB containing kanamycin (50 μg/mL) and chloramphenicol (25 μg/mL) and rotated at 225 rpm for ~16 hr at 37 ºC. Saturated cultures were then directly added to 1 L 2xYT media each in a 4 L flask, rotated at 180 rpm at 37 ºC, and induced to produce protein with 400 μM isopropyl β-D-1-thiogalactopyranoside (IPTG; GoldBio) when the $OD_{600}$ of the culture reached 0.6. At the point of induction, cells were placed on ice for 20 min to slow growth, and then shaken at 180 rpm overnight at 16 ºC. Induced *E. coli* cells were then pelleted at 5,000*g* for 20 min at 4 ºC and flash frozen with liquid nitrogen before storing at -20 ºC.

*For co-expression of TgLaforin with chaperone proteins*: BL21 *E. coli* containing TgLaforin in pET28b+ expression vector were subsequently transfected with pG-KJE8 (**Table 2.3**, TaKaRa). dnaJ and grPE were expressed under an arabinose-inducible promotor, and groES and groEL were expressed a tetracycline-inducible promotor. Chaperone expression was induced with 0.5 mg/mL arabinose and 5 ng/mL tetracycline.

*For refolding experiments*: 6xHis-TgLaforin in pET28b+ was expressed in BL21 *E. coli* and purified from inclusion bodies as described in section 2.1.4.

*For expression in Sf9 insect cells*: The bacmid and baculovirus used in TgLaforin expression were created using the manufacturer's product specifications (Invitrogen, MAN0000414) with several modifications. Briefly, the TgLaforin bacmid was created by transforming pFastBac-HTA (**Table 2.3**) containing TgLaforin into DH10Bac cells (Invitrogen) where transposition of TgLaforin into a bacmid occurred over the course of 48 h on LB-agar (50 μg/mL kanamycin, 7 μg/mL gentamycin, 10 μg/mL tetracycline). Successful transposition was selected for by using blue/white colony screening, and only white colonies were chosen for bacmid purification. The bacmid was then purified from a transformed colony after overnight growth in SOC media using alkaline lysis followed by isopropanol precipitation.

The baculovirus was subsequently produced by transfecting 2 μg of purified bacmid into $10^6$ adherent Sf9 insect cells (Invitrogen) in a 6-well plate using Cellfectin II reagent (Invitrogen), and the supernatant containing the initial baculovirus was harvested 72 h later. Serial passage of the baculovirus through insect cells in suspension was used to increase viral titer. This was done by

repeatedly infecting Sf9 cells in log phase of growth (1.5-2.5x$10^6$ cells/mL) at a ratio of 1:10 (viral stock to insect cell volume) and harvesting supernatant containing baculovirus 72 h later. Final viral stock infection volume was optimized by infecting insect cells in log phase at various concentrations (1:100-1:2000) and measuring cell viability and morphology after 72 h using Trypan blue staining. Ideal viral concentrations resulted in >80% living cells, the majority of which were enlarged as determined on a hemacytometer. An effective infection ratio was determined to be 1:1000 (v/v) of the P3 TgLaforin baculovirus into log-phase insect cells. Protein production was then initiated using the optimized volume ratio of viral stock to infect log-phase insect cells. After 72 h, insect cells were pelleted at 500*g* for 10 min at 4 $^oC$, washed once with PBS to remove media, and then flash frozen and stored at -20 $^oC$ until purification. Throughout study, insect cells were cultured in ESF 921 protein-free media (Expression Systems) at 27 $^oC$ rotating at 135 rpm without antibiotics and maintained between $10^6$ and $10^7$ cells/mL.

### 2.1.4 Purification of TgLaforin and TgGWD protein constructs

To generate highly pure and active protein, several purification schemes were tested throughout this study. Regardless of protein construct or expression system, all protein constructs were first purified using immobilized metal affinity chromatography (IMAC). To purify, cells (*E. coli* or Sf9) were resuspended in lysis buffer (50 mM HEPES, 100 mM NaCl, 15 mM imidazole, 2 mM DTT, 0.1% TritonX-100, pH 8.0). Cells were lysed by sonication, lysate was clarified by centrifugation at 14,000*g* for 30 mins at 4 $^oC$, and supernatant containing protein was harvested. Protein was purified from the lysate using IMAC with Ni-agarose beads (Sigma). Protein bound to beads was washed three times with purification buffer (lysis buffer without TritonX-100) and eluted in elution buffer [purification buffer containing 300 mM imidazole (Sigma)].

For the further purification of $His_6$-SUMO-TgLaforin construct from *E. coli*, contamination with other *E. coli* protein following IMAC purification was a significant issue. Moreover, the protein contaminants were of a similar molecular weight (MW) to TgLaforin, so anion-exchange (AEX) chromatography was used instead of size-exclusion chromatography (SEC). Briefly, protein was first bound in purification buffer to a 5 mL HiTrap Q HP exchange column (Cytivia) fitted to an ÄKTA pure fast protein liquid chromatography (FPLC) system and then washed with two column-volumes of purification buffer. Protein was then eluted from the AEX column by increasing ionic strength with a gradient of 100 to 500 mM NaCl and then collected in 2 mL fractions. TgLaforin eluted at a concentration of 320 mM NaCl.

For the purification of TgLaforin-FL (WT and C452S) from insect cells, TgGWD-FL (WT and H1241A) from insect cells, and all TgLaforin CBM constructs from *E. coli*, protein was purified to >95% homogeneity via SEC using an ÄKTA pure FPLC system fitted with a Superdex 200 16/200 column (GE Healthcare). IMAC elution

buffer was exchanged on column with storage buffer (purification buffer containing 10% glycerol), and 2 mL fractions were collected at a rate of 0.5 mL/min.

In all cases, protein was analyzed for purity by SDS-PAGE with 10% Mini-PROTEAN TGX stain-free precast gels (BioRad) imaged on a GelDoc. Only fractions containing pure protein were combined and concentrated to 1-3 mg/mL using Amicon centrifugal filters with an appropriate MW cutoff value (10 kDa for CBM constructs and 30 kDa for TgLaforin-FL and TgGWD). Final protein concentration was calculated using absorbance at 280 nm, the MW of each protein, and the extinction coefficient of each protein ($\varepsilon$; calculated using Expasy ProtParam online tool) on a Nanodrop (ThermoFisher). Protein was flash-frozen in liquid nitrogen and stored at -80 $^{o}$C.

For purification of $His_6$-TgLaforin from inclusion bodies (IBs), cells were resuspended in lysis buffer as described above, lysed by sonication, and IBs were collected by centrifugation at 14,000*g* for 30 mins at 4 $^{o}$C. Supernatant was discarded, and IBs were washed 4x with 2M Urea containing 2% Triton X-100. IBs were extracted in 6M guanidine containing 2% Triton X-100. IB extract was then rapidly diluted by 20-fold resulting in a final concentration of 0.1 mg/mL as described previously (259) in a 96 different buffer conditions contained in 96-well deep well plate (**Figure 2.1**), and then allowed to refold for 36 h at 4 $^{o}$C. Insoluble material was then pelleted in the deep-well plate and supernatant containing soluble protein was analyzed by SDS-PAGE and Coomassie blue staining. Wells containing soluble protein were then further analyzed by differential scanning fluorimetry (section 2.1.5).

### 2.1.5 Differential scanning fluorimetry

Thermal stability of refolded TgLaforin, Sf9-genrated TgLaforin and TgGWD, and TgCBM constructs in the presence of oligosaccharides was determined as previously described (260,261). Briefly, DSF was performed using a CFX96 Real-Time PCR system (BioRad) with the FRET channel excitation and emission wavelength set to 450-470 nm and 560-580 nm, respectively. Melting temperature of each protein (2 $\mu$M final concentration) was measured in 40 $\mu$L volumes in DSF buffer (50 mM HEPES, 100 mM NaCl, 2 mM DTT, pH 7.5) in the presence of 5X SYPRO Orange (final concentration; Invitrogen). Thermal denaturation curves were obtained by measuring fluorescence intensity in the FRET channel as the temperature was increased from 20 to 95 $^{o}$C at a rate of 1 $^{o}$C/min. The melting temperature ($T_m$) of each protein with and without carbohydrate was obtained by calculating the first derivative of the fluorescence melt curve, fitting the derived curve with a Gaussian peak using Prism 9, and determining the mean of the peak which corresponded to the $T_m$ (the inflection point of the original melt curve).

### 2.1.6 Size-exclusion chromatography with multi-angle light scattering

SEC-MALS analysis was performed as previously described (262). Proteins were run on an ÄKTA Pure system using a Superdex 75 Increase 100/300 column (TgCBM) or a Superdex 200 10/300 column (full-length TgLaforin; GE Healthcare Life Sciences), miniDAWN TREOS, and Optilab T-rEX (Wyatt Technologies, Santa Barbara, CA) arranged in sequence with one another. The columns were first equilibrated with the purification buffer used for each protein (described in section 2.1.4). Then, 500 μL of 2 mg/mL protein was loaded and run at 0.5 mL/min, and elution profiles were monitored using UV-Vis absorbance. Light scattering data was analyzed on ASTRA software (Wyatt Technologies). The MW of each protein was determined by analyzing peaks at half height using the refractive index to determine accurate protein concentration. UV and MW data was exported and plotted in Prism 9.

### 2.1.7 Hydrogen Deuterium Exchange Mass Spectrometry

HDX-MS experiments were performed using a Synapt G2-SX HDMS system (Waters). For the partially deuterated samples, 3 μL of TgLaforin (1 mg/mL) was diluted with 57 μL of labeling buffer (20 mM Tris, 100 mM NaCl, $D_2O$, pH 7.4), the deuteration reactions were incubated at 20 °C for 15 s, 150 s, 1500 s and 15000 s in triplicate. To quench, 50 μL of reaction solution was mixed with 50 μL of cold quench buffer (100 mM phosphate, $H_2O$, pH 2.5) and incubated at 0 °C. 95 μL of the quenched sample were then loaded onto an UPLC system for on-line pepsin digestion (Waters Enzymate Beh Pepsin column, 2.1 mm x 30 mm) and MS data acquisition. The nondeuterated samples were incubated with equilibration buffer (20 mM Tris, 100 mM NaCl, H2O, pH 7.4). To measure the maximum hydrogen-deuterium exchange rate, a fully deuterated sample was prepared by incubating TgLaforin in $D_2O$ buffer (1% (v/v) formic acid) for 24 h at room temperature. All the other steps were the same as the partially deuterated samples. HDX-MS was performed using a robotic autosampler (LEAP), thus the experimental variations were minimized. Back exchange was corrected as described previously (263,264). Data were processed using ProteinLynx Global Server and DynamX (Waters).

### 2.1.8 pNPP phosphatase assays

Hydrolysis of pNPP to 4-nitrophenylphosphate (4NP) was performed in 50 μL reactions containing phosphatase buffer (0.1 M sodium acetate, 0.05 M bis-Tris, 0.05 M Tris-HCl, and 2 mM DTT at pH 5.5) at 37 °C. pNPP concentration was equivalent to the $K_m$ value determined for each phosphatase under these reaction conditions containing 50 nM enzyme (unless otherwise indicated). Reactions were terminated by the addition of 200 μL of 0.25 N NaOH at indicated timepoints, and the production of 4NP was determined by measuring the absorbance at 410 nm

using a Synergy HTX Multi-Mode Reader (BioTek). Absorbance was converted to nmol phosphate released (1:1-phosphate:4NP ratio) using a 4NP standard curve.

$V_{max}$ and $K_m$ were calculated by varying pNPP concentrations and measuring absorbance in the linear range of enzyme activity. $K_m$ values are as follows for each enzyme: TgLaforin=0.71 mM, PTP1B=0.990 mM, VHR=2.53 mM, calf intestinal phosphatase=53.75 μM. Parameters were calculated using the Michaelis-Menten nonlinear curve-fitting function in Prism 9 software. The optimal pH (5.5) for TgLaforin was selected by testing reaction pH from 5.0-9.0 and determining the specific activity at each pH.

### 2.1.9 Malachite green phosphatase assays

Release of phosphate from potato amylopectin was determined as done previously (204,247,260,265) with the following modifications. Briefly, phosphate release was monitored using the PiColorLock™ Phosphate Detection Reagent (Novus Biologicals), a malachite green based assay. Recombinant TgLaforin (50 nM) was incubated with 1.125 mg/mL solubilized potato amylopectin (Sigma) in phosphatase buffer (pH 6.5) in a final volume of 80 μL at 37°C. Potato amylopectin was supplied as a powder from the manufacturer and solubilized to make a stock concentration of 5 mg/mL using the alcohol/alkaline method (also referred to as the "Roach method" in Ref. (265)). Reactions were terminated by the addition of 20 μL (0.25 initial reaction volume) Gold Mix (PiColorLock Gold solution mixed with Accelerator in a 100:1 ratio). After 5-min incubation at room temperature, 8 μL stabilizer solution (0.1 initial reaction volume) was added and reaction was allowed to develop for 30 mins at room temperature before the absorbance of each reaction was measured at 635 nm using a Synergy HTX Multi-Mode Reader (BioTek). Absorbance was converted to $P_i$ released using a $P_i$ absorbance standard curve.

### 2.1.10 Radiolabeled Starch Phosphatase Assay

Position-dependent phosphate release from $^{33}$P-labeled starch was performed as previously described (251,252,260,261). The substrate for this assay was generated by phosphorylating phosphate-free *Arabidopsis sex1-3* starch with $\beta^{33}$P labeled ATP (Hartmann Analytic, Braunschweig) at the C6 and C3 positions sequentially. The starch granules were phosphorylated at the C6 position using purified recombinant StGWD enzyme. The granules were next phosphorylated at the C3 position using purified recombinant AtPWD enzyme.

To determine the site-specificity of TgLaforin, 42 nM enzyme was incubated separately with 0.6 mg both C6- and C3-$^{33}$P-labeled starch in phosphatase buffer (pH 6.5) containing 1 mg/mL bovine serum albumin (BSA) in a final volume of 150 μL. Dephosphorylation was allowed to proceed for 15 mins with shaking at room temperature. The reaction was terminated with 50 μL 10% SDS (2.5% final), and starch was pelleted by centrifugation at maximum speed for 5 min. Supernatant

was then transferred to 3 mL scintillation fluid. The amount of phosphate released from each starch suspension was quantified by measuring counts per minute (CPM) of the supernatant on a 1900 TR liquid scintillation counter (Packard). CPM measurements were then converted to % phosphate release by dividing CPM in the supernatant (released phosphate) by initial CPM on starch (bound phosphate).

### 2.1.11 Inhibitor Assays

L319-M21-M49 stock solutions were prepared by resuspending the inhibitor in DMSO at a concentration of 20 mM. Various concentrations of inhibitor were prepared by serial dilution in DMSO such that stock concentrations were 50X the working concentration, and the final concentration of DMSO in each assay was 2% (v/v). The efficacy of L319-M21-M49 against various phosphatases was determined using the assay conditions described above. Enzymes were pre-incubated with L319-M21-M49 for 5 min on ice before initiating the assay with the addition of substrate. All inhibitor assays were performed within the linear time/concentration range of phosphatase activity.

### 2.1.12 *In vitro* radiolabel phosphorylation assay

TgGWD-WT and TgGWD-H/A (5 pmol each) were incubated in freshly prepared 3X phosphorylation buffer [10X phosphorylation buffer (500 mM HEPES-KOH, pH 7.5, 10 mM EDTA, 60 mM MgCl2, and 0.5% TritonX-100), 5 mM ATP, 0.1 M DTT, and 10 mg/mL BSA] with *A. thaliana ⊿sex1-3* phosphate free starch (final concentration of 5 mg/mL), 0.25 mCi $\beta$-$P^{33}$-ATP or $\gamma$-$P^{33}$-ATP (Hartmann Analytic)—in a final volume that adjusted the 3X buffer to 1X. Starch was prepared by first washing it twice in 1 mL 0.05% TritonX-100, once in water, and then resuspending it in water at a concentration of 20 mg/mL before adding it to the reaction. Reactions were agitated slowly by vortexing for the time indicated at room temperature. 10% SDS was added to terminate the reaction, with a final concentration of 2%. Starch was then pelleted at 5000*g* for 5 mins, the supernatant was removed, and starch was washed 5-7x with wash buffer (2% SDS, 2 mM ATP) until radiolabel counts were reduced to a low, unchanging level (60-90 CPM). Radiolabeled starch was then resuspended in a final volume of 100 $\mu$L $H_20$, and 50 $\mu$L was then measured (corresponding to 0.25 mg starch) in 3 mL scintillation fluid. The CPM of the starch was then determined on a Packard 1900 TR scintillation analyzer. Background of the reaction was determined with a no-enzyme control.

### 2.1.13 Water dikinase autophosphorylation assay

TgGWD-WT and TgGWD-H/A were incubated with both $\beta$-$P^{33}$-ATP and $\gamma$-$P^{33}$-ATP as has been described previously (266) with the following modifications. In

this reaction, 5 μg enzyme was incubated with 2.2 μCi radiolabeled ATP (either β- or γ-$P^{33}$) in 2X autophosphorylation buffer (50 mM HEPES-KOH, pH 7.5, 1 mM EDTA, 6 mM $MgCl_2$, 10% glycerol) at a final concentration of 1X. Reaction was terminated after 30 min at room temperature with 4X Laemmli sample buffer and incubated for 20 mins at 30 ºC. Samples were then separated from radioactive ATP by SDS-PAGE on 10% Mini-PROTEAN TGX stain-free precast gels (BioRad) and total protein was imaged on a GelDoc (BioRad). Radioactive (autophosphorylated) protein was then visualized by exposing gel to a phosphor screen (GE Healthcare) for 4 h before imaging it on a Typhoon FLA 9500 Imager. For all imaging steps, radioactive gel was wrapped in Saran wrap so as not to contaminate lab equipment with radioactive material.

2.1.14 Glucan, water dikinase site specificity assay

TgGWD-WT and TgGWD-H/A (5 pmol) were separately incubated in freshly prepared 3X phosphorylation buffer (section 2.1.12) with *A. thaliana ∆sex1-3* phosphate free starch (final concentration of 5 mg/mL) and β-$P^{33}$-ATP (final concentration of 5 μCi/μL) for 6 h and then spiked with an additional 5 pmol protein before incubating overnight. The sequential addition of protein and long incubation time ensured a high level of radiolabel incorporation into starch for downstream analysis. To terminate the reaction, 10% SDS was added to a final concentration of 2%. Radiolabeled starch was pelleted by centrifugation at 5000*g*, supernatant removed, and starch was washed with wash buffer (2% SDS, 2mM ATP) until radioactivity of supernatant dropped below 100 CPM (5-7 washes). This extensive washing ensures a low background. Total CPM on starch was then determined by adding 0.2 mg of labeled starch to 3 mL scintillation fluid and determining total CPM/mg starch.

TgGWD-labeled starch (WT or H/A) was then treated with glucan phosphatases with known site specificities to determine the position on which TgGWD phosphorylated the glucose within the phosphate free starch (**Figure 4.3b**). The glucan phosphatases used in this experiment were either AtSEX4 (C6:C3 specificity=2:1), LSF2 (entirely C3 specific), or their catalytically inactive counterparts as controls (SEX4- and LSF2-C/S). Because SEX4 has the capability of removing phosphate from both C6 and C3 positions, each aliquot of radiolabeled starch was treated with both glucan phosphatases in sequence to ensure specificity was accurately determined (e.g., starch was treated with LSF and then SEX4, and *vice versa*). Catalytically inactive C/S controls were used to determine background radioactivity levels. Labeled starch (0.6 mg/reaction; 4 mg/mL final concentration) was incubated in 5X phosphatase buffer (0.5 M sodium acetate, 0.25 M bis-Tris, 0.25 M Tris HCl, pH 6.5), 2mM DTT, 1 mg/mL BSA, and 0.0025% TritonX-100 (v/v) with a glucan phosphatase (7.5 ng/mL final) at a final concentration that diluted the 5X buffer to 1X. Reactions were constantly and slowly agitated by vortexing for 15 mins at room temperature, reactions were

terminated with 10% SDS (2.5% final concentration), and centrifuged at maximum speed for 5 mins. Three-quarters (150 μL) of supernatant was removed and added to 3 mL scintillation fluid before CPM was determined on a Packard 1900 TR scintillation analyzer. Specificity was determined by calculating % phosphate removed by comparing CPM in supernatant to total CPM on starch.

### 2.1.15 CE-based AMP release assay

CE-based detection of AMP is pictured in **Figure 4.5a**, and based on a previously developed protocol for whole capillary stacking (267). Briefly, starch was phosphorylated in the presence of TgGWD as described in section 2.1.14. for the times indicated and terminated by the addition of 10% SDS to a final concentration of 2%. Starch was pelleted at 14000*g* for 5 mins at room temperature, and supernatant containing reaction mixture, including AMP, was a used for further analysis. Protein was then filtered from reaction mixture using centrifugal filtration with unit containing a filter with a 30 kDa molecular-weight-cut-off (Amicon Ultra, Millipore). Filtrate was then analyzed on an Agilent 7100 CE system equipped with a UV detector fitted with a fused silica capillary. Capillary was first preconditioned with 50 mM carbonate (pH 9.6) before sample injection. Sample was injected via vacuum for 10 mins at 1 Pa to completely fill capillary. Sample stacking then proceeded by applying a voltage of -18 kV for 15 mins. The nucleotides in the sample were then separated at a voltage of +18 kV for 22 mins and absorbance at 256 nm was monitored with a UV-Vis detector. Capillary was extensively washed with carbonate buffer between runs. Data was exported, plotted, and analyzed in Prism 9.

### 2.1.16 TgLaforin yeast two-hybrid screen

Yeast two-hybrid screening for putative *in vitro* TgLaforin interacting partners was conducted by Hybrigenics Services (www.hybrigenics-services.com; Paris, France) using their patented ULTImate-Y2H Screen. Briefly, codon-optimized TgLaforin cDNA used in insect-cell expression (section 2.1.3) was fused to an N-terminal LexA or N-terminal Gal4 DNA binding domains to generate the TgLaforin-bait construct. TgLaforin bait was screened against a library of *T. gondii* (TGRH) prey encoded by 800-1000 bp inserts (average size of a protein domain) fused to activator domains. Prey fragments from positive interactions were amplified by PCR and sequenced to identify the proteins in the GenBank database. Confidence, a protein biological score (PBS) ranging from A to E, was assigned to each interaction and presented in **Table 6.1**.

## 2.2 Generation of *T. gondii* mutants and *in vitro* characterization of ΔTgLaf parasites

### 2.2.1 Fibroblast and parasite culture and maintenance

All parasite lines were maintained in human foreskin fibroblasts (HFFs; ATCC) in Minimal Essential Media-α (MEM-α; Gibco) supplemented with 7% heat-inactivated fetal bovine serum (Gemini Bio), 100 U/mL penicillin, 100-μg/mL streptomycin, and an additional 2 mM L-glutamine (Gibco; 4 mM total L-glutamine in media). Cells and parasites were incubated at 37 $^{o}$C and 5% $CO_2$ in a humidified incubator. Genetically modified parasites were maintained in MEM-α containing 7% dialyzed FBS (Gemini Bio) and either pyrimethamine (1 μM), mycophenolic acid/xanthine (MPA: 25 μg/mL, xanthine: 50 μg/mL), or 6-thioxanthine (80 μg/mL).

Assays analyzing the effects of glutamine deprivation used DMEM. Both glutamine replete (Gibco, 11966025) and depleted (Gibco, 11054020) DMEM were supplemented with 7% dialyzed FBS. Glutamine replete media from the supplier also lacked other key nutrients and was further modified to contain 5 mM glucose, 1 mM sodium pyruvate, and 4 mM L-glutamine.

### 2.2.2 Generation of *T. gondii* mutant lines

*Type II ME49ΔHXGPRT* ("WT"—the parental line utilized to generate all other lines in this study, depicted in **Figure 5.1**): To disrupt the hypoxanthine-xanthine-guanine phosphoribosyl transferase (HXGPRT) gene in *T. gondii* Type II ME49 parasites, a shotgun CRISPR-Cas9 strategy was employed in which multiple sgRNA constructs were transfected into *T. gondii* to disrupt the gene with several Cas9 cut sites (known as protospacer-adjacent motifs; PAMs). A single plasmid containing both Cas9-GFP and an interchangeable sgRNA scaffold was used for this purpose (pSAG1::CAS9-U6::sgUPRT; **Table 2.3**) (268). Three previously identified sgRNAs (10) targeting three separate exons (2,3, and 5) in the HXGPRT gene were chosen, and used to replace the sgRNA sequence in the CRISPR-plasmid to make three separate plasmids (**Table 2.4**) using a Q5 site-directed mutagenesis kit (New England BioLabs). Mutagenesis primers were designed using NEBaseChanger (**Table 2.5**). The three modified sgRNA/Cas9-GPF plasmids (8 μg each) were transfected into $1.4x10^7$ *T. gondii* parasites by electroporation with a time constant between 0.16 and 0.20 msec (BioRad Gene Pulser II). HFFs were then infected with electroporated parasites to allow the parasites to recover. After 24 h, surviving parasites were syringe-passaged from infected HFFs with a 27G needle to lyse host cells, and gravity filtered through a 10 μm filter to remove host-cell debris. Successful transformants were then enriched by use of fluorescence activated cell-sorting (FACS; Sony SY3200, installed in a biosafety level II cabinet) to select parasites expressing Cas9-GFP from the transfected plasmid by isolating GFP+ parasites only. HFFs were infected

with GFP+ parasites, and then placed in 6-thioxanthine media 24 h later to select for ΔHXGPRT mutants. After 10 days of culturing parasites in 6-thioxanthine (about 3 passages), the parasites were cloned by limiting dilution into a 96-well plate containing confluent HFFs. Wells containing single plaques were picked 7 days later and further expanded. Genomic DNA was extracted using a Proteinase K treatment detailed elsewhere (9), and the HXGPRT locus was sequenced to verify a successful knockout.

*TgLaforin-3xHA-HXGPRT* (depicted in **Figure 5.3**): TgLaforin was epitope tagged at the C-terminus utilizing a CRISPR-Cas9 strategy by disrupting the TgLaforin 3'UTR immediately downstream of the endogenous stop codon. This approach promoted homologous recombination (HR) with a co-transfected TgLaforin-HA construct as has been done previously (269). Briefly, the sgRNA adjacent to a PAM sequence immediately downstream of the TgLaforin stop codon was designed using the EuPaGDT design tool (http://grna.ctegd.uga.edu). The top hit for this region was selected and used to replace the sgRNA scaffold in pSAG1::CAS9-U6::sgUPRT as was done above (**Tables 2.4** and **2.5**). The TgLaforin-HA tagging construct was generated by amplifying the 3' end of the TgLaforin-HA construct generated for complementation (see generation of COMP line below and **Table 2.3**) along with the connected HXGPRT selectable marker. Both the PCR-amplicon and the CRISPR-Cas-GFP plasmid containing the sgRNA toward TgLaforin were transfected into $1.4x10^7$ *T. gondii* ME49ΔHXGPRT parasites (2:1 insert:plasmid molar ratio; 30 μg DNA total) as was done above. After 24-hours, parasites were then isolated, sorted by FACs, and GFP+ parasites were again allowed to infect HFFs and grow for 24 h before drug selection with media containing MPA/xanthine. After 10 days of culturing parasites in MPA/xanthine (about 3 passages), the parasites were cloned by limiting dilution into a 96-well plate. Wells containing single plaques were picked 7 days later and expanded. Successful tagging of TgLaforin was verified using sequencing, immunoblot, and immunofluorescence.

*ME49ΔHXΔTgLaforin* ("ΔTgLaf"; depicted in **Figure 5.5**): The TgLaforin ORF was disrupted using a CRISPR-Cas9 mediated strategy as detailed above, with several differences. Briefly, a single sgRNA was designed to target the first exon of TgLaforin with the top hit from EuPaGDT (**Table 2.4**). To disrupt TgLaforin with a selectable drug marker, a pyrimethamine-resistant mutant of the dihydrofolate reductase (DHFR*) gene containing a 5'-NcGra7 promotor and DHFR 3'UTR was amplified from pJET-NcGra7_DHFR (**Table 2.3**). Amplification utilized primers containing 40 nt extensions homologous to the 5'- and 3'-UTR of TgLaforin to encourage HR-mediated whole-gene replacement with the drug cassette (**Table 2.5**). Both the PCR-amplified DHFR* homology cassette and the CRISPR-Cas-GFP plasmid were transfected and FACS-sorted as described above. GFP+ parasites underwent drug selection in pyrimethamine. Parasites were then cloned and expanded as detailed above. Successful integration of the DHFR* cassette

into the TgLaforin locus was verified using PCR with inside/out primer pairs to the chimeric, interrupted gene (**Table 2.5**).

*ME49ΔHXΔTgLaforin+ChrVI-TgLaforin* ("COMP", depicted in **Figure 5.8**): Complementation of TgLaforin was also executed using a CRISPR-mediated strategy. A sgRNA to a neutral locus on Chromosome VI identified previously (270) was generated using the same mutagenesis strategy as above. A full length TgLaforin cDNA containing its endogenous 5'UTR (2000 bp upstream from gDNA) was synthesized by GenScript and inserted into the pHA3x-LIC vector (**Table 2.3**) containing a C-terminal HA tag and a DHFR 3'UTR, linked to the HXGPRT selectable marker (named "TgLaforin-HA3x-LIC"; also used above for endogenous tagging to create TgLaforin-HA line). The entire construct (5'UTR:TgLaforin-cDNA:DHFR-3'UTR:HXGPRT) was amplified from the vector and co-transfected into ΔTgLaf parasites with the CRISPR-Cas9 plasmid as done above. Successful transformants that received the HXGPRT marker were selected with MPA/xanthine. Successful insertion of TgLaforin along with its promoter was verified using PCR, by immunoblot analysis, and immunofluorescence with an anti-HA antibody (Abcam).

### 2.2.3 Western blotting

Parasites were syringe lysed from host cells, pelleted, and $2x10^6$ parasites were resuspended in SDS-PAGE sample buffer and boiled before being run on a single lane of a 10% polyacrylamide gel for 30 mins at 225 V. Lysate was then transferred from gel to 0.2 μm PVDF membrane (BioRad) using a Turbotransfer System (BioRad) for 7 min at 25 V. The PVDF membrane was then blocked in either 5% (w/v) non-fat milk (for HRP-conjugated secondary antibodies) or 3% (w/v) BSA (for fluorophore conjugated antibodies) in PBS for 20 mins before being probed with a primary antibody in either non-fat milk or BSA overnight at 4 $^oC$ (Cell Signaling C29F4). Blot was then washed 3x with TBST (0.1% Tween-20, 5 min/wash) before probing with one of the following secondary antibodies for 45 min at room temperature: HRP-conjugated α-rabbit/mouse-IgG (Jackson Laboratories), DyLight488 (α-mouse) or DyLight680 (α-rabbit). Blot was washed 3x in TBST once more, and then developed for 5 min using SuperSignal™ West Pico PLUS (Thermo Scientific) for HRP-conjugated antibodies and visualized on a GelDoc station (BioRad).

### 2.2.4 Immunofluorescence (IF)/histology staining

HFFs were grown on coverslips in a 24-well plate until confluent and subsequently infected with $10^4$ parasites/well. At the indicated time post-infection, the infected HFFs were fixed with either methanol (MeOH) (100%, -20$^oC$) or methanol-free paraformaldehyde (PFA) (4% in PBS; Electron Microscopy Sciences) as indicated for each antibody. Infected HFFs fixed with PFA were

permeabilized in 0.1% TritonX-100 in PBS++ (PBS containing 0.5 mM $CaCl_2$ and 0.5 mM $MgCl_2$) for 10 mins at RT. Primary and secondary antibodies were diluted in 3% (w/v) bovine serum albumin (BSA; Fisher) in PBS++. Samples were first incubated with the primary antibody at RT for 45 mins, washed 3x with PBS++, and then incubated with fluorescent secondary antibodies (1:2,000) and DAPI (300 nM final) for 45 mins. Secondary antibodies (Invitrogen) were conjugated to either Oregon Green or Texas Red fluorophores and specific to the species and class of primary antibody used. Samples were then washed 3x with PBS++ before mounting the coverslip on a glass slide using MOWIOL mounting media.

IF staining was visualized using a Zeiss AxioVision upright microscope with a 100X 1.4 numerical-aperture oil immersion objective, and images were acquired using a grayscale Zeiss AxioCam MRM digital camera. Grayscale images were pseudo-colored in ImageJ using magenta (red fluorophore), yellow (green fluorophore), and cyan (DAPI), and further alterations to brightness and contrast were also made in ImageJ when deemed appropriate. For all assays in which staining intensity was compared across treatments and parasite lines, concentrations of antibodies, exposure times, and alterations to brightness/contrast were standardized.

Colocalization of fluorescent antibodies/reagents was quantified using Pearson's coefficient calculated with the JACoP plugin on ImageJ (271).

### 2.2.5 Periodic acid-Schiff staining

Periodic acid-Schiff (PAS) staining was done on coverslips with infected HFFs fixed in 4% PFA. After removing PFA, samples were permeabilized as above. Coverslips were then washed 3x in tap water before the addition of 1% periodic acid (Sigma-Aldrich) for 5 mins. Coverslips were then washed 3x in tap water, and Schiff's reagent (diluted 1:4 in tap water) was added for 15 mins. Coverslips were subsequently washed 10x with tap water to develop stain before being incubated with DAPI in tap water for 10 mins. Stained coverslips were then mounted as above. All reagents were utilized at room temperature during PAS staining. PAS stained samples were visualized using fluorescent microscopy (excitation: 545 nm, emission: 605 nm). When PAS was costained with antibodies, primary antibodies were incubated with PAS stained slides overnight in BSA at 4 $^{o}$C before standard secondary staining. Specificity of IF staining in the presence of PAS was verified using secondary-only controls.

Samples treated with amyloglucosidase (GAA) (from *Aspergillus niger*, >260 U/mL, Sigma) were incubated with GAA after permeabilization. GAA was diluted 1:50 in 50 mM sodium phthalate buffer, pH 5.5 and samples were treated for 24 h at room temperature. Untreated controls were incubated in phthalate buffer without GAA. Samples were then stained with PAS or mAb IV58B6 as described above or in section 2.2.4.

### 2.2.6 *In vitro* bradyzoite conversion assay

Tachyzoites were converted to bradyzoites *in vitro* using alkaline stress as has been done previously with several modifications (**Figure 2.2a**) (272). HFFs grown on coverslips were infected with tachyzoites in standard cell culture media. 4 h later, media was replaced with RPMI 1640 (Gibco 31800022) supplemented with 50 mM HEPES, no sodium bicarbonate, and adjusted to pH 8.2 with NaOH. Parasites were then cultured for 2-6 days at 37 $^{o}$C, ambient $CO_2$, and wrapped in Parafilm. Media was replaced every other day to maintain the basic pH. Parasites were fixed in PFA and stained with either fluorescein conjugated *Dolichos biflorus* agglutinin (DBA; 1:1000, Vector Laboratories) and PAS. Images were obtained in grayscale on a Zeiss AxioVision upright microscope as described above using identical exposure times across sample sets.

To determine the degree of labeling with DBA or PAS, the Fiji distribution of ImageJ (273) was used to create a binary mask outlining cysts that was applied to the original DBA/PAS-stained image to measure the greyscale intensity of each ROI (i.e. each individual cyst) (**Figure 2.2b**). The mask was created with DBA staining by adjusting the threshold of each image to include all cysts, creating a binary image that outlined each cyst, and then applying the watershed algorithm to separate cysts in contact with one another.

### 2.2.7 Transmission electron microscopy of *in vitro* tachyzoites and bradyzoites

Transmission-electron microscopy (TEM) was performed as done previously (26). Briefly, HFFs in 10-cm cell culture dishes were infected and harvested at the timepoint indicated or converted to bradyzoites for 6 days as described above. To harvest, media was removed, and cells were washed with PBS twice and then fixed in the 10 cm dish with 3% glutaraldehyde (GA) (Electron Microscopy Sciences) in 100 mM sodium cacodylate, pH 7.4, for 1 h at room temperature. After 1 h, fixative was removed and replaced with 1 mL 1% BSA in 100 mM sodium cacodylate. Cells were then scraped from surface of plate, collected into the BSA, transferred to 1.5-mL Eppendorf tubes, and then centrifuged at 1000*g* to pellet. Supernatant was carefully removed, and the pellet was transferred to a 10 cm Petri dish using a wooden spoon. A razor blade was used to chop the pellet into blocks that were each <1mm$^3$, and blocks were transferred into GA/cacodylate fixative overnight at 4 $^{o}$C.

The remaining steps were executed in the University of Kentucky's Imaging Center in the College of Arts and Sciences. Blocks were washed with 100 mM sodium cacodylate buffer 3x before post-fixation in 2% osmium tetroxide for 1 h on ice. Blocks were then washed in water 3x before being washed 3x in 50 mM sodium maleate (pH 5.2). Next, blocks were stained in 1% uranyl acetate in maleate buffer for 1 h at RT, washed again in water 3x, and then dehydrated in a series of washes with increasing ethanol concentrations (70%, 95%, 100%). Pellet

was next washed twice with propylene oxide, left in propylene oxide for 20 mins, then incubated in a 1:1 mixture of Epon and propylene oxide overnight. Tubes were left open for 2 h before Epon was removed, replaced with fresh Epon, and rotated 4 h on mixing wheel. Finally, blocks were transferred to fresh Epon in molds and left at 60 $^{o}$C overnight before trimming and thin sectioning on an ultramicrotome with a diamond knife. Sections were placed on copper grids and then contrast stained with lead citrate. Micrographs were collected at the University of Kentucky's Electron Microscopy Center on a Talos F200X TEM (Thermo) operated at 200 kV accelerating voltage with a 50 μm objective aperture inserted to enhance contrast using a 16M pixel 4k x 4k CMOS camera (Ceta, Thermo Scientific).

### 2.2.8 Plaque assays

HFFs were grown in 12-well plates until confluent. HFFs were subsequently infected with 200 parasites/well in the media indicated. Any indicated media changes were done 4 h post-infection to allow for invasion, and residual invasion media was washed away with two changes of PBS. Plates remained undisturbed for 7-10 days before the infected HFFs were fixed with 100% MeOH for 20 mins, stained with 1% crystal violet solution for 20 mins, and then the plaques were de-stained with repeated washes with tap water. Thus, zones of lysis (white clearings) could be visualized against intact cells (purple). Images of plaques were obtained by scanning plates on an Epson Perfection V600 photo scanner at a resolution of 600 dpi. The plaques were measured by pixel area using ImageJ and presented in arbitrary units.

### 2.2.9 Ionophore and zaprinast-mediated egress assays

HFFs were grown to confluency in 35 mm glass bottom dishes (MatTek, P35G-0-14-C). Two days before infecting HFFs on glass bottom dishes, both HFFs and parasites were independently pre-treated in either glutamine-replete or -depleted media (see above for media formulations). After 48 h pre-treatment, $10^5$ parasites of each line (WT, ΔTgLaf, and COMP) in each condition (gln+/-) were added to 3 dishes each and allowed to grow for 48 h so that most vacuoles contained >32 parasites each. Several hours before egress, media in each infected plate was adjusted to 1.5 mL and allowed to equilibrate at 37 $^{o}$C in 5% $CO_2$. The calcium ionophore A23187 (Cayman Chemical Company) was prepared as a 2 mM stock in DMSO and diluted in (+/-) gln media to make a 4X concentration of 12 μM and maintained at 37 $^{o}$C throughout the assay. Zaprinast was likewise prepared as a 100 mM stock in DMSO, and diluted into media at a 4X concentration of 2 mM. Egress was triggered by the addition of 0.5 mL 4X A23187 to infected HFFs (3.0 μM final concentration) or 0.5 mL 4X-zaprinast (500 μM final concentration). Egress was monitored on a Nikon Eclipse Ti2 inverted microscope with a 40X phase air objective modified with a 1.5X optivar. Five fields containing vacuoles

were selected from each plate, and an image was obtained 10 s after triggering egress from each field once every 5 s for 5 mins (61 images/field) on a Nikon DS-Ri2 color camera. Videos of each field were assembled on NIS Elements software. Egress was monitored using standard deviation of pixel intensity (**Figure 2.3a**) and determined by inflection point of change in standard deviation of pixel intensity (**Figure 2.3b-c**). Inflection point was calculated by fitting a gaussian curve to the first derivative of the standard deviation in pixel intensity and calculating the mean of the curve. Technical replicates (fields on each plate) were averaged for each biological replicate (average of fields from each plate). Data analysis, preparation, and statistics were performed using GraphPad Prism 9.

### 2.2.10 Replication assay

HFFs were grown on untreated glass coverslips in a 24-well plate until confluent. Two days before infecting HFFs on coverslips, both HFFs and parasites were independently pre-treated in either glutamine-replete or -depleted media. After pre-treatment, $10^4$ parasites of each line (WT, ΔTgLaf, and COMP) in each condition (gln+/-) were added to 3 coverslips each. 24 hours later, infected HFFs were fixed in MeOH and stained with Rb-α-SAG1 (1:10,000) and DAPI for ease of visualization as detailed in section 2.2.4. Counting of parasites/vacuole was performed blindly for each line/condition such that identifying information was removed before counting was not revealed until the completion of counting.

### 2.2.11 Metabolomics

Confluent HFFs were infected with parasites at an MOI of 2 to achieve a high density of parasites after 48-hours of growth (>80% cells containing >32 parasites each). Plates containing infected HFFs were placed on ice, media removed, and monolayer was wash 2X with ice-cold PBS. Cells were scraped from plate surface, resuspended in PBS (8 plates cell-equivalents per 50 mL PBS), and centrifuged at 1000*g* for 10 mins at 4 °C. PBS was removed, cell pellet was resuspended in 2 mL PBS, and syringe passaged successively in 23 G and 27 G needles and then host cell lysate was removed by centrifuging filtering by centrifugation. The pellet was resuspended in 5 mL PBS and host-cell debris was removed by syringe-filtering suspension through a 5 μm filter (Whatman). Filtered parasites were then pelleted, resuspended in 1 mL PBS, and counted on a hemacytometer. Parasites were pelleted a final time at 14,000*g* for 30 s at 4 °C, supernatant was removed, and pelleted parasites were flash frozen in liquid nitrogen and stored at -80 °C until metabolite extraction.

*Polar metabolite extraction:* Polar metabolites were extracted in 0.5 mL -20 °C 50% methanol (MeOH) containing 20 μM L-norvaline (procedural control) for 30 mins on ice. During the 30 min incubation, samples were regularly vortexed. Samples were then centrifuged at 14000*g* for 10 mins to pellet insoluble material

(protein, DNA, RNA, and glycans). Supernatant containing polar metabolites and pellet were dried separately on a SpeedVac (Thermo) at $10^{-3}$ mBar until MeOH was completely sublimated and only dried pellet remained.

*Pellet hydrolysis and extraction:* Dried fraction containing protein was hydrolyzed by resuspending the pellet in 2 N HCl (final concentration) at 95 $^{o}$C for 2 h. Hydrolysis was quenched, and hydrolyzed amino acids were extracted by the addition of an equal volume of 100% MeOH with 40 μM L-norvaline such that the final concentration was 50% and 20 μM, respectively. Extraction and drying then proceeded as described above.

*Sample derivatization*: Dried samples (both polar and hydrolyzed protein) were derivatized in 70 μL 20 mg/mL methoxyamine hydrochloride in pyridine for 90 mins at 30 $^{o}$C. Samples were then centrifuged at 14000*g* for 10 mins to remove any particulate, and 50 μL of the methoxyamine superantent was mixed with 80 μL *N*-methyl-*N*-trimethylsilyl trifluoroacetamide (MSTFA) and incubated for 30 mins at 37 $^{o}$C. Samples were then transferred to amber glass chromatography vials and analyzed by GCMS.

*GCMS analysis*: Metabolites were analyzed on an Agilent 7800B GC coupled to a 5977B MS detector. GCMS protocol was identical to one described previously (274). Automated Mass Spectral Deconvolution and Identification System (AMDIS) was used to analyze metabolites by matching metabolites to the FiehnLib metabolomics library via retention time and fragmentation pattern. Quantification of metabolite levels was performed in Mnova. Sample abundance was normalized to L-norvaline (procedural control) and protein from protein pellet (experimental control).

## 2.3 Establishing the role of TgLaforin in the acute and chronic infection of mice

### 2.3.1 Mouse infection with *T. gondii*

4 to 6 week old male and female CBA/J mice from Jackson Laboratories (Bar Harbor, ME) were injected intraperitoneally (IP) with either 100 ME49 tachyzoites (parasite lines generated in section 2.2) or 20 tissue-cysts from brain homogenate from previously infected mice. In either case, parasites were suspended in 0.2 mL serum-free, Opti-MEM media (Gibco). Mice were then monitored and assigned a body index score once or twice a day throughout the course of infection (**Table 2.6**). When symptomatic, mice were administered gel diet and wet chow on the cage floor and given 0.25-0.5 mL saline solution subcutaneously if dehydrated. Moribund mice were immediately euthanized. Euthanasia of both moribund mice and mice sacrificed at the time of tissue cyst harvest was performed by $CO_2$ asphyxiation, followed by cervical dislocation. All protocols were carried out under the approval of the University of Kentucky's Institutional Animal Care and Use Committee (IACUC).

### 2.3.2 Tissue cyst purification

Tissue cysts were purified as done previously (55,275). Briefly, mice were dissected immediately following euthanasia and brains were harvested. Brains were then homogenized in pairs in ice-cold PBS containing 0.3% Tween-80 (final concentration) using a mortar and pestle, and then homogenate was sequentially passaged through needles ranging from 16 G to 23 G. Homogenate was layered onto a discontinuous Percoll gradient (Sigma) (90%:9-mL / 40%:4.5mL / 20%:4.5mL) in a 50 mL conical tube. Homogenate was then centrifuged at 2200 rpm for 18 min at 4 $^{o}$C on a Beckman Allegra tabletop centrifuge with a swinging bucket rotor using the high brake setting. Cysts were collected in 1 mL fractions from the bottom of the centrifuged Percoll gradient using a peristaltic pump adjusted to a flow rate of 2 mL/min. To count cysts, 10-20 μL of each fraction was placed into 100 μL PBS in the well of a 96-well plate. The 96-well plate was centrifuged at 1000*g* for 5 min at 4 $^{o}$C. Cysts were then counted in each well using an inverted microscope at 20x magnification (Nikon), and the number of cysts in each well was used to determine the total number of cysts in each fraction. Total cysts per mouse were calculated by summing the total number of cysts in each fraction and dividing the total by two to adjust for brain homogenization in pairs. Each pair of mice was presented as a single averaged data point.

To fix tissue cysts onto microscope slides for further analysis, fractions containing tissue cysts were combined and diluted between five- and ten-fold using PBS. Diluted cysts were then centrifuged at 1000*g* for 15 mins at 4 $^{o}$C. Diluted Percoll was carefully removed, leaving ~0.1 mL at the bottom of the tube. Pelleted cysts were then resuspended in PBS at 300-600 cysts/mL. 0.5 mL cyst suspension was spun onto glass slides using a Cytospin (Shandon Cytospin 4) at 750 rpm for 5 mins with medium acceleration and brake. Slides were then immediately submerged in ice-cold 100% MeOH and stored in an explosion-proof freezer until time of staining.

### 2.3.3 Staining and analysis of tissue cysts

Tissue cysts were stained as described previously (55). Briefly, cysts fixed on glass slides were washed 3x in PBS++ in a Coplin jar to remove MeOH. Slides were then briefly air-dried before drawing a wax circle around the area containing the tissue cysts. This wax circle created a hydrophobic barrier that could then contain antibody solutions. PAS or IF staining otherwise proceeded as described in section 2.2.4 by adding staining solutions into the area contained by the wax circle. If washing damaged the wax circle, it was redrawn before secondary antibodies were added. After labeling, coverslips were then mounted onto slide by the addition of MOWIOL and a coverslip directly over the cysts.

### 2.3.4 Preparation of tissue cysts for TEM imaging

To prepare *T. gondii* tissue cysts generated *in vivo* for TEM, cysts were isolated from the brains of infected mice as detailed in section 2.3.2 through the counting step. Fraction containing mouse red blood cells (RBCs) was saved for further use in this protocol. After combining Percoll fractions containing tissue cysts and diluting with PBS to a volume of 15 mL (maximum of 2 mL combined fractions before dilution), cysts were pelleted for 15 mins at 1000*g* at 4 $^{o}$C. To maximize cyst recovery, 10 mL supernatant was removed, and then the bottom 5 mL was divided into 1 mL fractions for the top 4 mL, and the final 1 mL directly above the cysts was sub-fractionated into 100 μL volumes. Typically, the majority of cysts were localized to within 300 μL of the pellet. Sub-fractions containing cysts were once again combined and diluted (typically 200-300 μL diluted with 1-mL PBS) in a 1.5 mL Eppendorf tube, and then pelleted in a swinging-bucket rotor for 10 min at 1000*g* and 4 $^{o}$C. Leaving the pellet undisturbed, all but 50 μL of the supernatant was removed. A small volume (~5-10 μL) of RBC fraction was added to the remaining volume for ease of visualizing the pellet throughout the remaining steps.

To ensure the detection of the relatively rare cyst population, a previously described protocol (276,277) was adapted to concentrate the cysts into a small agarose block. A 1.33X solution of GA in cacodylate buffer was prepared containing 4% GA and 133 mM sodium cacodylate. 150 μL fixative solution was then added to sample, bringing the total volume to 200 μL such that the final concentration of GA was 3% and sodium cacodylate was 100 mM. Cysts were then incubated at room temperature for 1 h in fixative. While cysts were in fixative, 4% low-melt agarose (BioRad) was prepared in 100 mM sodium cacodylate buffer and kept liquid at 70 $^{o}$C until needed. After fixation, cysts were pelleted again at 1000*g* for 10 mins at room temperature in a table-top centrifuge. All but 50 μL supernatant was once again removed, and 200 μL warm low-melt agarose was slowly added on top of fixed, pelleted cysts (3.2% agarose, final concentration). Suspension was then centrifuged again at 1000*g* for 10 mins at 30 $^{o}$C to keep the agarose semi-liquid, and then placed on ice for 20 mins to solidify agarose. After solidification, entire agarose plug was removed from tube with a small a wooden dowel that had been whittled into a thin scoop. Agarose plug was placed in a Petri dish, and the pellet was carefully cut out of the plug with a razor blade to create a 1 $mm^3$ block. The agarose block was then stored in 3% GA/cacodylate buffer overnight at 4$^{o}$C. Processing of the block from post-stain onward was then identical to TEM processing described in section 2.2.7. During sectioning, thick sections were examined on a light microscope to verify the presence of tissue cysts before proceeding with ultra-thin sectioning.

### 2.3.5 Determination of cyst diameter and packing density

Tissue cysts fixed on slides (described in section 2.3.2.) were co-stained with DAPI and DBA to obtain nuclear profiles for bradyzoites and an outline of the cyst for diameter measurement. The diameter was determined in Fiji (ImageJ) by drawing a circle around the cyst and computing the diameter. Packing density was determined as described previously (55). Briefly, DAPI images of cysts were opened in BradyCount1.0, and threshold levels were adjusted as needed to capture all nuclear profiles. After BradyCount1.0 provided the number of bradyzoite nuclei, the packing density was determined by dividing the number of bradyzoites by the volume of the section. The formula describing this calculation is: $\mathbf{PD = N / (\pi r^2 \, x \, h)}$ where PD=packing density, N = # of bradyzoites, r = radius calculated from cyst diameter, and h = height of section (0.22 μm throughout this study).

**Table 2.1 Glucan phosphatases used in this study.**
The accession number of each glucan phosphatase used in CBM/DSP alignments is listed here, along with its UniProt accession number, and the domain boundaries that were assigned to the CBM and DSP within each (if applicable).

| Name | Accession No. (UniProt) | CBM | DSP |
|---|---|---|---|
| *H. sapiens* laforin | O95278 | 1-136 | 137-331 |
| *A. carolinensis* laforin | G1KGK2 | 1-140 | 141-304 |
| *G. gallus* laforin | Q5ZL46 | 1-136 | 137-319 |
| *D. rerio* laforin | E9QCC5 | 2-131 | 132-294 |
| *X. laevis* laforin | Q6GPD8 | 1-124 | 125-313 |
| *A. thaliana* SEX4 | Q9SRK5 | 253-340 | 84-252 |
| *A. thaliana* LSF2 | Q9FEB5 | N/A | 75-232 |

**Table 2.2 Glucan, water dikinase sequences used in this study.**
The accession number of each glucan, water dikinase used in this study is listed here, along with its UniProt accession number. The domain boundaries that were assigned to the CBM and His-domain are also indicated.

| | | Including transit peptide | |
|---|---|---|---|
| **Name** | **Accession No. (UniProt)** | **CBM45** | **His-catalytic site** |
| *Solanum tuberosum* GWD (StGWD) | I0DFJ7 | 1: 127-203<br>2: 458-538 | 1059-1080 |
| *Arabidopsis thaliana GWD (AtGWD)* | Q0SAC6 | 1: 120-196<br>2: 394-473 | 994-1015 |

**Table 2.3 Plasmids used in this study.**

| Name | Use | Source |
|---|---|---|
| pET28b+ | Expression of TgLaforin CBM truncations | Novagen |
| ppSUMO | Expression of 6xHis-SUMO-TgLaforin in *E. coli* | Jack Dixon, UCSD |
| pG-KJE8 | Co-expression of TgLaforin with chaperone proteins | TaKaRa |
| pFastBac-HTA | Generation of bacmid for expression of TgLaforin and TgGWD in Sf9 insect cells | Invitrogen |
| pSAG1::CAS9-U6::sgUPRT | Genetic modifications in *T. gondii* | David Sibley, Washington University |
| pJET-NcGra7_DHFR | TgLaforin knockout via DHFR-TS* knock in | Peter Bradley, UCLA |
| pHA3x-LIC | Tagging and complementation of TgLaforin | Peter Bradley, UCLA |
| TgLaforin-HA3x-LIC | Tagging and complementation, derived from pHA3x-LIC | GenScript |

**Table 2.4 sgRNA sequences used in this study.**

| Target | Use | Sequence | Strand |
|---|---|---|---|
| HXGPRT (exon 2) | HXGPRT knockout | ATGGTCTCCACCAGTGCTCC | + |
| HXGPRT (exon 3) | | GACAAAATCCTCCTCCCTGG | - |
| HXGPRT (exon 5) | | CTTCTTCGAGCACTATGTCC | + |
| TgLaforin 3'UTR | TgLaforin epitope tag | GCTTAGCGTGTGAACAGCAG | + |
| TgLaforin (exon 1) | TgLaforin KO | GAAGTCCCGATAACCTACGC | + |
| Chromosome VI | TgLaforin complementation | GCCGTTCTGTCTCACGATGC | + |

**Table 2.5 Primers used in this study.**
Mutagenesis primers are presented in uppercase where the primer binds directly to the template, and in lowercase-bold where new sequence is being introduced.

| Name | Use | Sequence (5' to 3') |
|---|---|---|
| HXGPRT_sgRNA_E2_F | sgRNA mutagenesis for each construct used in HXGPRT knockout | **ctcgaagaag**GTTTTAGAGCTAGAAATAGC |
| HXGPRT_sgRNA_E2_R | | **cactatgtcc**AACTTGACATCCCCATTTAC |
| HXGPRT_sgRNA_E3_F | | **tcctccctgg**GTTTTAGAGCTAGAAATAGC |
| HXGPRT_sgRNA_E3_R | | **ggattttgtc**AACTTGACATCCCCATTTAC |
| HXGPRT_sgRNA_E5_F | | **tggagaccat**GTTTTAGAGCTAGAAATAGC |
| HXGPRT_sgRNA_E5_R | | **ccagtgctcc**AACTTGACATCCCCATTTAC |
| TgLaf_3'UTR_sgRNA_F | sgRNA mutagenesis for TgLaf-HA epitope tagging | **tgaacagcag**GTTTTAGAGCTAGAAATAGC |
| TgLaf_3'UTR_sgRNA_R | | **cacgctaagc**AACTTGACATCCCCATTTAC |
| TgLaf_exon5_homology_F | Generation of TgLaf-HA tagging construct | AGAGGAGGCGGAGGAGAG |
| TgLaf_3'UTR_HX+homology_R | | TCCGTATCGCCCCCTCTCGTCTGACACGCCCTC TTTCCTCCAGCACGAAACCTTGCATTC |
| TgLaforin_sgRNA_E1_F | sgRNA for TgLaf-KO | **taacctacgc**GTTTTAGAGCTAGAAATAGC |
| TgLaforin_sgRNA_E1_R | | **tcgggacttc**AACTTGACATCCCCATTTAC |
| TgME49_ChrVI_sgRNA_F | sgRNA for ChrVI used in TgLaf complementation | ctcacgatgcGTTTTAGAGCTAGAAATAGC |
| TgME49_ChrVI_sgRNA_R | | acagaacggcAACTTGACATCCCCATTTAC |
| TgLAF_WT_F | Amplification of the first exon of TgLaforin, uninterrupted | TCCTACATTCTGGAGCGAAG |
| TgLAF_WT_R | | AAAGCCACTTTCTCCAGGAG |
| DHFR*_R | Binds to drug cassette from pJET-NcGra7_DHFR | GCATTATGAGGAAAGCCCsAC |
| TgChrVI_WT_F | Amplification of WT Chr VI locus | CAGGAAATATGCTGCGAGGA |
| TgChrVI_WT_R | | TGTGTCTGCTCTTGAAGGTG |
| TgLaf_COMP_F | Binds to HXGPRT cassette within complementation construct (derived from pHA3x_LICs | TGCAAGCCCTACATTGACAA |

**Table 2.6 *T. gondii*-infected mouse body index scoring guide.**

| | | Ruffled Fur | Slight decrease in activity | Bilateral eye squinting | Shallow breathing | Hunched | Dehydrated | Marked decrease in activity | Inactive/no movement when prompted | Agonal breathing | Found deceased |
|---|---|---|---|---|---|---|---|---|---|---|---|
| Healthy | Stage 0 | | | | | | | | | | |
| Progression of acute illness | Stage 1 | X | X | | | | | | | | |
| | Stage 2 | X | X | X | X | | | | | | |
| | Stage 3 | X | X | X | X | X | X | X | | | |
| Moribund/ deceased | Stage 4 | X | X | X | X | X | X | X | X | X | X |

| | 1 | 2 | 3 | 4 | 5 | 6 | 7 | 8 | 9 | 10 | 11 | 12 | | |
|---|---|---|---|---|---|---|---|---|---|---|---|---|---|---|
| **A** | NDSB256 | Buffer alone | PEG3300 | NaCl | ZWITT 3-14 | Sucrose | ARG w/o GSH/GSSG | ARG | ARG + PEG 3300 | ARG + NaCl | ARG + ZWITT 3-14 | ARG + Sucrose | +DTT | Citrate, 0.5M, pH 6.5 |
| **B** | Buffer w/o GSH/GSSG | Buffer alone | PEG3300 | NaCl | ZWITT 3-14 | Sucrose | NDSB256 | ARG | ARG + PEG 3300 | ARG + NaCl | ARG + ZWITT 3-14 | ARG + Sucrose | -DTT | |
| **C** | NDSB256 | Buffer alone | PEG3300 | NaCl | ZWITT 3-14 | Sucrose | ARG w/o GSH/GSSG | ARG | ARG + PEG 3300 | ARG + NaCl | ARG + ZWITT 3-14 | ARG + Sucrose | +DTT | Tris, 0.5M pH 7.5 |
| **D** | Buffer w/o GSH/GSSG | Buffer alone | PEG3300 | NaCl | ZWITT 3-14 | Sucrose | NDSB256 | ARG | ARG + PEG 3300 | ARG + NaCl | ARG + ZWITT 3-14 | ARG + Sucrose | -DTT | |
| **E** | NDSB256 | Buffer alone | PEG3300 | NaCl | ZWITT 3-14 | Sucrose | ARG w/o GSH/GSSG | ARG | ARG + PEG 3300 | ARG + NaCl | ARG + ZWITT 3-14 | ARG + Sucrose | +DTT | Tris, 0.5M pH 8.5 |
| **F** | Buffer w/o GSH/GSSG | Buffer alone | PEG3300 | NaCl | ZWITT 3-14 | Sucrose | NDSB256 | ARG | ARG + PEG 3300 | ARG + NaCl | ARG + ZWITT 3-14 | ARG + Sucrose | -DTT | |
| **G** | NDSB256 | Buffer alone | PEG3300 | NaCl | ZWITT 3-14 | Sucrose | ARG w/o GSH/GSSG | ARG | ARG + PEG 3300 | ARG + NaCl | ARG + ZWITT 3-14 | ARG + Sucrose | +DTT | EtOHHN2, 0.5M pH 9.5 |
| **H** | Buffer w/o GSH/GSSG | Buffer alone | PEG3300 | NaCl | ZWITT 3-14 | Sucrose | NDSB256 | ARG | ARG + PEG 3300 | ARG + NaCl | ARG + ZWITT 3-14 | ARG + Sucrose | -DTT | |

**Figure 2.1 Refolding conditions for TgLaforin.**
Refolding screen with minor modifications was adapted from (259). *Abbreivations:* ARG = arginine; DTT = dithiothreitol; EtOHHN2 = ethanoloamine; GSH/GSSG = reduced/oxidized glutathione; NaCl = sodium chloride; NDSB = non-detergent sulfobetaines; PEG = polyethylene glycol; ZWITT = zwitterionic detergent.

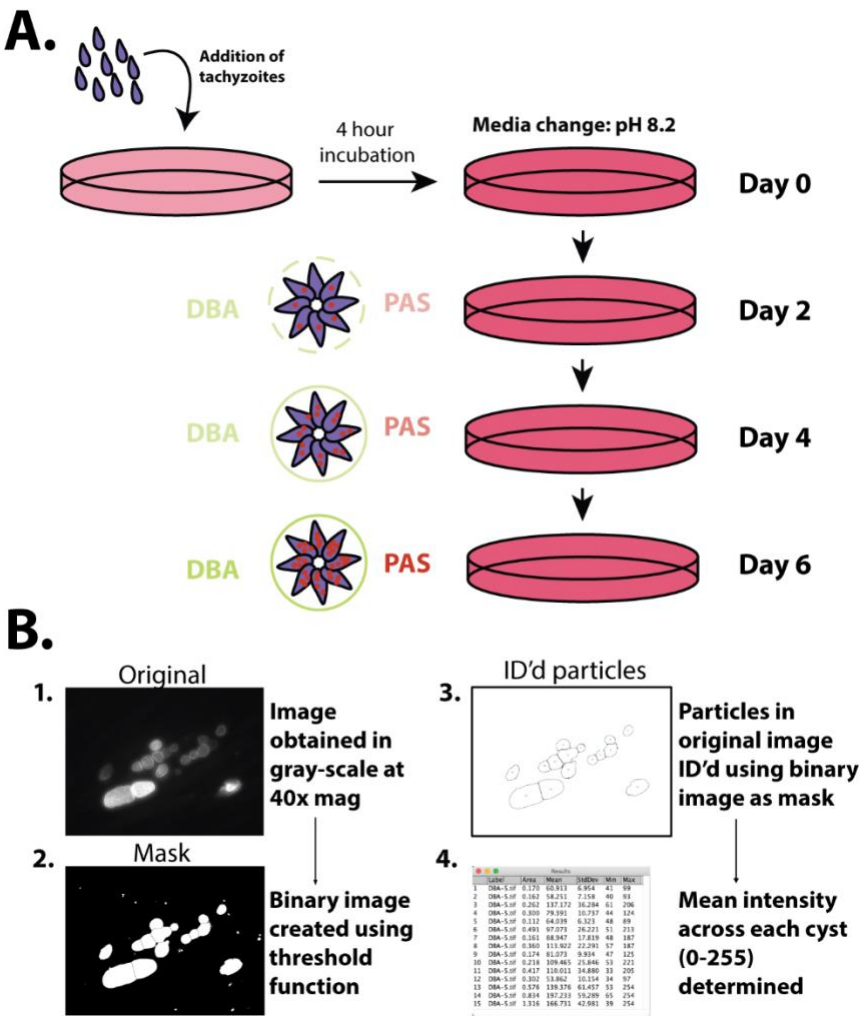


**Figure 2.2 ImageJ analysis of *in vitro* bradyzoite conversion.**
**A,** Tachyzoites were converted to bradyzoites *in vitro* using alkaline stress for 2-6 days. During this time, classic bradyzoite markers detected with DBA and PAS are upregulated. **B,** Determination of DBA and PAS intensity using a four-step ImageJ workflow.

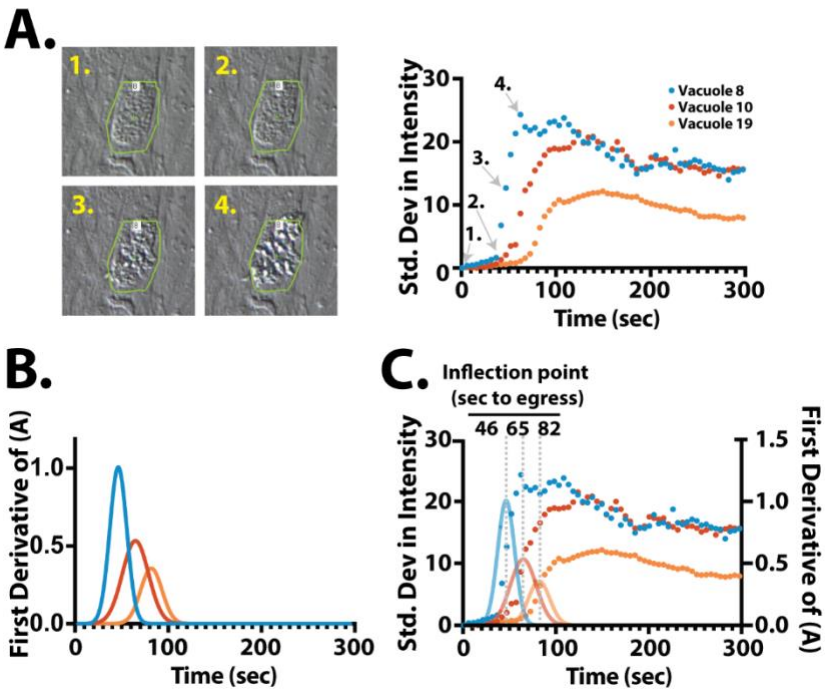


**Figure 2.3 Video monitoring and automated analysis of *T. gondii* induced egress.**

**A,** Vacuoles in each field are identified (left panels) as ROIs in which the standard deviation in intensity is monitored (right panel). Representative states of vacuoles are pictured, and each state (1-4) is labeled on the tracking graph. State 3 is the point of egress, as parasites begin to emerge from vacuole, and this corresponds to the inflection point on the standard deviation in intensity tracking graph. **B,** Gaussian fit of the first derivative of the curves from (A). **C,** Overlay of (A) and (B) as validation that analysis generating data in (B) reflects the inflection point from (A).

# CHAPTER 3. THE TOXOPLASMA GLUCAN PHOSPHATASE, TGLAFORIN, UTILIZES A DISTINCT FUNCTIONAL MECHANISM ENABLING INHIBITOR IDENTIFICATION

## 3.1 Introduction

*Toxoplasma gondii* is an obligate, intracellular, protozoan parasite that can infect any warm blooded animal and chronically infects one-third of humans worldwide (3). Infection with the parasite occurs through several routes, including ingestion of environmental oocysts shed through cat feces, consumption of tissue cysts in raw or undercooked meat, or through vertical transmission from an acutely infected individual to their fetus (77,85). Upon consumption, the cyst-forms (oocysts and tissue cysts) of the parasite eventually convert into the rapidly dividing tachyzoite that disseminates throughout the body of the host, defining the acute stage of infection (278). Under host immune pressure, a small number of tachyzoites evade host defenses by converting into bradyzoites that populate tissue cysts located in the central nervous system or muscle tissue of the host (83,120). If the host becomes immunocompromised during the course of the life-long chronic infection, spontaneous reactivation of bradyzoites into tachyzoites can result in symptomatic toxoplasmosis that primarily manifests as the life-threatening toxoplasmic encephalitis (114). The current first-line treatment is a combination of pyrimethamine and sulfadiazine that targets folate synthesis in tachyzoites during the acute phase of infection or after reactivation. However, this treatment regime only targets tachyzoites, results in serious side effects, must be taken for long periods of time, and cannot be administered to pregnant individuals (123). Notably this drug combination does not reduce the overall cyst burden. Other drugs, targeting the parasite mitochondrion result in a partial clearance of tissue cysts, without achievement of a sterile cure. The potential for AG metabolism as a target for drug intervention provides a unique molecular target for *T. gondii* therapeutics that has not been explored.

A distinguishing feature of *T. gondii* bradyzoites is their accumulation of large glucose-based polymers known as amylopectin granules (AGs) (101,196,279). AGs are believed to function as an insoluble form of glucose storage for use in bradyzoite persistence, replication, transmission, and reactivation, analogous to starch utilization during the night in plants (55,101,144). Purified AGs were found to be similar to plant amylopectin, the major glucose component of starch, with respect to glucose chain-length and branching frequency, demonstrating that the structure of AGs is more similar to plant starch than to animal and fungal glycogen (40,196,197). Unexpectedly, it was demonstrated that AGs are synthesized from UDP-glucose, similar to the sugar nucleotide used in fungal and animal glycogen synthesis, rather than ADP-glucose, which is used by plants (40). Additionally, *T. gondii* AGs reside in the cytoplasm, which is also characteristic of fungal and animal glycogen, and are visible by transmission electron microscopy (TEM) in

encysted bradyzoites but not the rapidly dividing tachyzoites (**Figure 1.1b and 1.1f**). The presence of AGs in the cytoplasm is noteworthy given that *Toxoplasma* retains a plastid remnant organelle termed the apicoplast that has its origins in red alga.

These seemingly disparate findings regarding AGs are consistent with the fact that the *T. gondii* proteome contains a hybrid molecular machinery exhibiting characteristics of plants, fungi, and animals (280,281). This hybrid machinery is exemplified in T. gondii's putative cycle of reversible glucan phosphorylation (**Figure 1.4** and **1.6**). In plants, the cycle begins with the actions of glucan, water dikinase (GWD) and phosphoglucan, water dikinase (PWD) that use ATP to phosphorylate glucose at the C6- and C3-hydroxyl positions within the glucan, respectively (167,168). The presence of covalently attached phosphate disrupts the crystalline organization of starch, thus solubilizing the surface glucose chains and enhancing access of multiple amylases that release glucose, maltose, or other oligosaccharides (169,170,172). To allow processive hydrolysis, the activity of a glucan phosphatase is required to remove the residual phosphate groups and reset the cycle (173,174,247). The *T. gondii* genome contains sequences that encode putative enzymes with these activities: a glucan, water-dikinase (TgGWD (TgME49_214260); plant-like), multiple amylases and debranching enzymes, and the glucan phosphatase *T. gondii* laforin (TgLaforin (TgME49_205290); animal-like), along with all of the enzymes needed in glucan synthesis (**Figure 1.4, Table 1.1**) (40,204,205,212).

The mechanism regulating the utilization of AGs in the *T. gondii* lifecycle is only beginning to be defined. The critical regulatory role of reversible phosphorylation of both starch and glycogen has been increasingly recognized, leading to potentially unique insights and molecular targets in the *T. gondii* system (154,282). Notably, glucan phosphatases are a family of carbohydrate-specific enzymes that play a critical role in controlling polyglucan utilization in both plants and animals. Glucan phosphatases are required for efficient starch catabolism as loss of starch excess4 (SEX4), the prototypical glucan phosphatase found in plants, leads to aberrant starch accumulation and morphology (174,239). Strikingly, mutations in human laforin (HsLaforin), the glucan phosphatase in humans, results in hyperphosphorylated and aberrantly branched glycogen that is the driver of Lafora disease (LD), a fatal epilepsy and childhood dementia (184,187,283).

Glucan phosphatases are an enzyme family that dephosphorylate glucans via a dual specificity phosphatase (DSP) domain coupled with either a carbohydrate binding module (CBM) domain or carbohydrate surface binding sites (204,247). Glucan phosphatases are members of the protein tyrosine phosphatase (PTP) superfamily within the DSP clade (284-286). Previous work has demonstrated that glucan phosphatases employ a wide variety of platforms that allow them to bind and dephosphorylate carbohydrates (261,287-289). In land plants, SEX4 binds and dephosphorylates carbohydrates by utilizing an integrated binding pocket formed by the CBM/DSP interface (250,252,260). Like Sex Four-2, LSF2, another

plant glucan phosphatase, lacks a traditional CBM and instead binds carbohydrates through surface binding sites within its DSP domain (251). Human laforin is an antiparallel dimer with a spatially separated CBM and DSP that are each capable of binding to carbohydrates independently (253). While they are not orthologs, SEX4 and laforin are functional equivalents as complementation of laforin into Δ*sex4 A. thaliana* plants rescues the starch excess phenotype (204).

In this study, we build on our understanding of glucan phosphatases and reversible phosphorylation in *T. gondii* by defining the biophysical and biochemical properties of TgLaforin. We identified an atypical CBM in TgLaforin, defined TgLaforin's oligomerization status, and determined its activity. Moreover, we developed and characterized the first reported TgLaforin inhibitor. These findings demonstrate the value of a detailed examination of the enzymology related to glucan metabolism in *T. gondii* and open new doors for anti-*Toxoplasma* therapeutics.

## 3.2 Results

### 3.2.1 Expression of recombinant, full-length TgLaforin

To express recombinant TgLaforin in BL21-DE3 *E. coli*, an *E. coli* codon-optimized cDNA was fused with an N-terminal, 6x-His-tagged small ubiquitin-like modifier (SUMO) protein. SUMO protein is believed to act as a protein folding initiator that increases protein solubility (290). While a significant portion of the protein remained insoluble, a fraction of soluble SUMO-TgLaforin was successfully expressed in *E. coli* and purified using immobilized metal affinity chromatography (IMAC) (**Figure 3.1a; panel 1, "E"**). Moreover, the SUMO-tag was readily removed with ubiquitin-like-protease (ULP) treatment. However, recombinant TgLaforin was not pure as several other proteins were also co-purified alongside it. Because many of these proteins were in a similar molecular weight (MW) range, size-exclusion chromatography (SEC) was not utilized for further purification. Instead, anion exchange chromatography (AEX) was chosen due to the predicted pI of TgLaforin (6.47). To elute TgLaforin, a salt gradient of 100 mM→500 mM NaCl was used, and TgLaforin eluted at ~320 mM NaCl (**Figure 3.1a; panel 2**). While some bands of lower MW were successfully eliminated from the purified protein, several contaminants still remained. Regardless, protein purified from *E. coli* demonstrated activity against the artificial substrate para-nitrophenylphosphate (pNPP) (**Figure 3.2c**), but further purification strategies were pursued to generate highly pure protein for use in downstream studies in which biophysical properties and conformational dynamics could be determined.

Because a significant amount of TgLaforin remains insoluble upon expression (**Figure 3.1b, panel 1, "+IPTG"**), it was reasoned that co-expression of TgLaforin with several chaperones might aid in its proper folding without the attachment of a large fusion protein such as SUMO. Therefore, TgLaforin was co-expressed in

BL21 *E. coli* with 4 chaperones: DnaK, GroEL, DnaJ, and GrpE (**Figure 3.1b**). Each chaperone or set of chaperones was under the control of differentially inducible promoters, so the induction of each chaperone with either arabinose or tetracycline, or all three in combination was first verified (**Figure 3.1b, panel 1, "+arab/+tet"**). The solubility of 6xHis-TgLaforin (a 61.5 kDa protein) alongside these chaperones was obscured by the expression of GroEL (a 60 kDa protein). Further purification with IMAC revealed almost no soluble protein (**Figure 3.1b, panel 2, "E"**). To determine if any of the protein in the IMAC eluate was soluble, protein fractions analyzed were western blot analysis with an $\alpha$-His antibody (**Figure 3.1b, panel 3**). Alongside these four chaperones, TgLaforin remained insoluble, and no soluble protein was detected by western blot.

To take advantage of the high levels of insoluble protein, refolding of TgLaforin in *E. coli* inclusion bodies (IBs) was attempted as IBs have been demonstrated to be a relatively pure source of protein (291). IBs were first washed of soluble protein with 2M Urea and 2% Triton X-100 before being solubilized in 6M guanidine, resulting in relatively pure, soluble protein (**Figure 3.1c, "Ex"**). Protein was then rapidly diluted in a range of buffers at various pHs with or without multiple additives and reducing agents. This screen was designed around 96 total conditions previously identified by *Dechavanne, et al. 2010* (259); (detailed in section 2.1.4) (**Figure 3.1d** and **Figure 2.1**). Rapid dilution of protein has been demonstrated to be effective in protein refolding (292) as opposed to slower refolding by dialysis, and was thus selected for the purposes of a large-scale screen. Indeed, several conditions resulted in soluble protein (**Figure 3.1d**). To determine if the soluble protein was properly folded, differential scanning fluorimetry (DSF) was used. DSF is a technique that monitors protein unfolding in the presence of SYPRO orange. Hydrophobic, interior residues of protein bind SYPRO during the unfolding process, and a melt-curve with an inflection point, from which the melting temperature ($T_m$) is derived, indicates the presence of folded protein. In general, the presence and relative value of the melting temperature can be used as a surrogate for protein stability. DSF analysis of soluble TgLaforin revealed that none of the soluble protein identified by the refolding screen possessed a fluorescence inflection point that allowed for the identification of a $T_m$ (**Figure 3.1e**; **c.f. Figure 3.3a**), indicating that the protein may not have been folded despite its solubility.

It was then reasoned that a eukaryotic expression system with more extensive protein post-translational modifications might benefit the solubility and purity of TgLaforin. Therefore, baculovirus-induced expression in Sf9 insect cells was selected to express 6xHis-TgLaforin. After increasing viral titer through three passages, various baculovirus:Sf9-cells (v/v) were tested, and an optimal ratio of 1:1000 was selected (**Figure 3.2a**). Western blot analysis with an $\alpha$-His antibody confirmed the identity of the expressed protein (**Figure 3.2b**). Isolation of protein from Sf9 cells and subsequent IMAC purification yielded pure protein. Moreover, SEC or AEX polishing steps resulted in equally pure protein (**Figure 3.2a**), so SEC was selected for its convenience and increased control over final buffer

composition, yielding >95% pure protein. When compared to protein produced in *E. coli* (purified by AEX, **Figure 3.1a**), the specific activity of TgLaforin remained the same when adjusted for total TgLaforin across expression systems (**Figure 3.2c**), but the purity was greatly increased. The enzymatic activity of TgLaforin will be further dissected in section 3.2.6.

### 3.2.2 Recombinant Sf9-expressed TgLaforin is stably folded

To determine if the baculovirus-expressed TgLaforin was indeed stably folded in solution, DSF was once again utilized (**Figure 3.3**). DSF analysis of TgLaforin expressed in Sf9 insect cells yielded a standard melting curve (**Figure 3.3a**). By taking the first derivative of the melt curve and fitting the first derivative with a gaussian curve, a $T_m$ could be determined at maximum of the fitted curve (**Figure 3.3b**). Without any ligand, the $T_m$ of full-length TgLaforin was 47.6 $^oC$ (**Figure 3.3c**). To define TgLaforin carbohydrate binding, TgLaforin was incubated with various carbohydrates and analyzed with DSF. An increase in $T_m$ is associated with increased protein stability due to protein-ligand interaction (185,293). When incubated with DP4 (four linear glucose units) or DP7 (seven linear glucose units), TgLaforin was robustly stabilized (**Figure 3.3b-c**). Moreover, TgLaforin was also stabilized in the presence of complex carbohydrates such as amylopectin and glycogen (**Figure 3.3b-c**). The stabilization of TgLaforin with these carbohydrates was demonstrated to be dose dependent (**Figure 3.3d-e**), demonstrating that Sf9-expression of TgLaforin yielded both pure and folded protein.

### 3.2.3 Bioinformatic evidence for a split-CBM20 in TgLaforin

*T. gondii* AG metabolism employs reversible glucan phosphorylation where the plant-like TgGWD dikinase and animal-like TgLaforin phosphatase are utilized (**Figure 1.4** and **1.6**). In addition to this plant-like versus animal like axis, TgLaforin is also unique in its domain organization. We previously predicted that the *T. gondii* genome encodes for a glucan phosphatase that is more similar to human laforin than other glucan phosphatases based on its domain orientation with an N-terminal CBM family 20 (CBM20) followed by a DSP domain (204,205). However, TgLaforin contains 523 amino acids, and the combined length of a typical CBM (90-120 amino acids) and DSP (150 amino acids) is only 240-270 amino acids, leaving approximately half of the protein uncharacterized. Bioinformatic analyses suggested that TgLaforin contains two unusual inserts within its CBM20 domain (**Figure 3.4a**) (294).

Rather than pursuing protein crystallography with the Sf9-generated protein, the architecture of TgLaforin and its CBM were predicted utilizing AlphaFold2 (258) to generate a putative three-dimensional model of TgLaforin. The model generated by AlphaFold2 predicted that TgLaforin contains a single CBM20 over the span of 325 amino acids. With high confidence (predicted Local Distance Difference Test

(pLDDT) score >70%), AlphaFold2 modeled a core CBM that consists of β-strands from the three distally located sub-domains of the CBM region. The model predicts that the unusual inserts form large unstructured linker regions connecting the core structured CBM regions (**Figure 3.4b**). The unstructured portions of the CBM20 modeled with low confidence (pLDDT<50%) (**Figure 3.4b**). A canonical DSP domain (reviewed in (284)) was also modeled in TgLaforin containing the characteristic DSP α+β structure with a central β-sheet consisting of five twisted β-strands (**Figure 3.5a**). TgLaforin contains the canonical $CX_5R$ motif with C452 serving as the catalytic cysteine (**Figure 3.5a-b**), and R458 that coordinates the three non-bridging oxygens of the incoming phosphoryl substrate. This catalytic motif is located between a β-strand and α-helix as expected. DSP domains also contain a critical, upstream aspartate (D421 in TgLaforin) that defines the D-loop and functions as an acid-base catalyst, modeled in TgLaforin as participating in the active site (**Figure 3.5**). The presence and location of these residues places TgLaforin in the PTP superfamily (295).

To validate the AlphaFold2 model of TgLaforin, we utilized full-length TgLaforin expressed in Sf9 insect cells and purified by SEC (**Figure 3.2a**) in hydrogen-deuterium exchange (HDX) mass-spectrometry (MS) experiments. This technique has previously been used to illuminate conformational dynamics of proteins by demonstrating areas of high and low solvent accessibility (253,296). We first determined deuterium uptake across the entire protein from 15-15,000 s (**Figure 3.6**) and mapped the results onto the AlphaFold2 model (**Figure 3.4c**). Critically, the core CBM20 β-sandwich exhibited low uptake of deuterium while the CBM insert regions that were modeled with low confidence displayed much higher rates of deuterium uptake (**Figure 3.4c-d**). These regions with high deuterium exchange are thus more mobile and less structured. Conversely, β-sheets within the core CBM were among the structural elements with the lowest deuterium uptake. Within the DSP domain, core structural elements had low uptake while elements of the DSP active site, known to undergo conformational changes required for substrate interaction (253,297), displayed higher uptake. These active site regions included the recognition domain, variable loop, D-loop, PTP-loop, and R-motif (**Figure 3.4d** and **Figure 3.6**) that have previously been reported as exhibiting higher solvent accessibility in SEX4 and laforin (253,264).

### 3.2.4 Integrated CBM is required for carbohydrate binding

To further define the nature of the unique split-CBM domain found in TgLaforin, we aligned the TgLaforin CBM with other glucan phosphatases containing a CBM20 (**Figure 3.7a**). The three regions of the TgLaforin CBM20-domain, split over 325 amino acids and interrupted by linker regions, each contain a part of the key consensus amino acids predicted to be critical to glucan binding. However, none of the individual regions contain a complete array of consensus amino acids that would allow it to be an individual CBM domain. Moreover, these three

subdomains contain the predicted number of β-strands that are typically identified in a CBM that are predicted to come together to form two anti-parallel β-sheets, comprising the canonical β-sandwich fold that is characteristic of CBM20 domains (**Figure 3.7b**). Each sub-domain contains one of the three conserved amino acids involved in either aromatic glucose stacking interactions (W29 and W278) or hydrogen bonding with glucose rings (K206) that are each critical to glucan binding (298). Conversely, the linker regions do not contain the key conserved glucan-binding residues. Importantly, the three critical carbohydrate binding residues (W29, K206, and W278) are organized into a single three-dimensional binding site similar to other CBM20s (**Figure 3.7c** and **Figure 3.8a**).

To further test if TgLaforin contains a single integrated CBM, we expressed each of the three sub-domains (CBM20-1, -2, and -3) separately and in different combinatorial arrangements (**Figure 3.8b**). Each of the constructs encoding individual portions of this region were either not expressed, not folded, or aggregated (**Figure 3.8c-e**). However, we were able to express and purify the predicted full TgCBM comprising all three subdomains with the two linkers, TgCBM123 (referred to simply as "TgCBM") (**Figure 3.8d**).

We next analyzed TgCBM using size exclusion chromatography coupled with multi-angle light scattering (SEC-MALS) to define its oligomerization state. SEC-MALS analysis demonstrated that TgCBM has a MW of 36.6 ± 6.8 kDa, compared to the predicted monomeric mass of 35.6 kDa, indicating that the TgCBM is a stable monomer in solution (**Figure 3.9a**). To define TgCBM carbohydrate binding, DSF was utilized as described in section 3.2.1 (185,293). We incubated TgCBM with the linear oligosaccharide maltohexaose and observed a robust dose-dependent stabilization of TgCBM with an $K_{d,app}$=20 ± 4 mM (**Figure 3.9b**).

To further probe the glucan binding of TgCBM, we designed alanine mutants of the three predicted critical carbohydrate-binding residues. K206A and W278A were produced and purified to near homogeneity, while W29A was deleterious to protein folding. We then tested the effect of the K206A and W278A mutations on carbohydrate binding. Strikingly, neither mutant was able to bind to maltohexaose, demonstrating their key function in carbohydrate binding (**Figure 3.9b**). If TgLaforin contained two distinct CBMs, then carbohydrate binding should have been only partially reduced by each independent mutant. Taken together, these data demonstrate the structure, dynamics, and carbohydrate binding of the split CBM20 of TgLaforin.

### 3.2.5 TgLaforin is an antiparallel dimer

Previous work demonstrated that glucan phosphatases utilize unique platforms to bind and dephosphorylate carbohydrates (287). While the plant glucan phosphatases SEX4 and LSF2 are monomeric, dimerization is a critical feature of human laforin activity and stability, and dimerization is mediated through the DSP domain resulting in an antiparallel dimer (253). To determine the glucan binding

platform employed by TgLaforin, we analyzed the oligomerization status of full-length TgLaforin and found that TgLaforin eluted as a single species from SEC (**Figure 3.10a**). However, like other glucan phosphatases, it was significantly shifted in elution volume due to interactions with the carbohydrate-based SEC matrix and eluted at a higher volume than would be expected when compared to SEC standards (262). We therefore utilized SEC-MALS to determine the oligomeric state of TgLaforin. SEC-MALS demonstrated that TgLaforin has a MW of 136.6 ± 0.6 kDa, twice the predicted size of the 61.5 kDa monomeric protein, signifying it exists in solution as a stable dimer (**Figure 3.10a**). When considered alongside the fact that TgLaforin-CBM is a monomer in solution (**Figure 3.9a**), this is highly suggestive that dimerization of TgLaforin is mediated through the DSP domain. To test this, we utilized the multimer modeling functionality of AlphaFold2 (257). We predicted the structure of a homodimer of TgLaforin, which produced an anti-parallel dimer model which was exclusively DSP-driven (**Figure 3.10b**). The core CBM and DSP domains were modeled with high confidence (pLDDT>70%), and adopted an orientation very similar to that observed in human laforin (253).

### 3.2.6 TgLaforin is an active glucan phosphatase

Phospho-tyrosine specificity is conferred to PTPs through the ~40 amino acid recognition domain that forms a deep catalytic pocket. In DSPs, however, the recognition region is much shorter, which results in a shallower active site that allows DSPs to dephosphorylate phospho-serine/threonine residues as well (284). As with other DSP containing proteins, the TgLaforin recognition region is much shorter than a typical PTP, confirming its placement in the DSP family. When compared with other glucan phosphatases, the TgLaforin DSP domain also shares many of the same glucan binding residues with human laforin, but not with plant glucan phosphatases [(**Figure 3.5b**); residues highlighted in blue)].

These carbohydrate-binding residues identified in the DSP play a role in both specific and selective activity against glucan substrates. To determine optimal TgLaforin activity, we first tested its phosphatase activity against pNPP over a pH range from 5.0-9.0 (**Figure 3.11a**). Over the range tested, TgLaforin displayed the highest activity at pH 5.0. To determine if TgLaforin activity remains stable under these acidic conditions, TgLaforin was pre-incubated in phosphatase buffer at various pHs from 5.0-6.5 before the addition of substrate (**Figure 3.11b**). Strikingly, TgLaforin lost activity over time if incubated at a pH of 5.0, but retained most of its maximum activity level at higher pH values. Therefore, all the following pNPP activity assays were conducted at pH 5.5. At pH 5.5, TgLaforin demonstrated robust activity against pNPP that was both dose- and time-dependent (**Figure 3.12a**). Moreover, when the catalytic cysteine (C452) was mutated to a serine (C452S), the activity was completely ablated, consistent with its role as the catalytic nucleophile (**Figure 3.11a** and **3.12a**).

To test its activity against a biologically relevant substrate, we used a malachite green-based assay to detect phosphate release from solubilized potato amylopectin. We once again tested the optimal pH of TgLaforin activity against amylopectin (**Figure 3.11c**). Generally, the activity of TgLaforin was higher at acidic pH values, and activity at pH 6.5 was significantly higher than several other basic pH values. Because malachite-green based glucan phosphatase assays are typically conducted at pH 6.5, and TgLaforin activity was optimal at this pH, all following amylopectin assays were conducted at pH 6.5. TgLaforin readily dephosphorylated amylopectin in a time-dependent manner, whereas the catalytically inactive C452S control did not (**Figure 3.12b**). Importantly, VHR, a member of the DSP family lacking a CBM, was unable to release phosphate from amylopectin (**Figure 3.12b**). Therefore, in addition to providing evidence for its glucan phosphatase activity, these data also demonstrate the ability of TgLaforin to bind carbohydrates and confirm the function of its split CBM.

Glucose within both starch and glycogen is phosphorylated at both the C3- and C6-hydroxyl groups, and glucan phosphatases display varying specificities with regards to the site that they dephosphorylate (289). SEX4 displays a preference for dephosphorylating the C6-position while human laforin displays a preference for the C3-position (252,261). LSF2, however, exclusively dephosphorylates the C3-position (251). We tested TgLaforin for C3- or C6-selectivity by incubating it with starch differentially radio-labeled at the C3- or C6-position. TgLaforin displayed a strong preference for dephosphorylating the C3-position with 78% of its activity directed against C3, and only 22% against C6 (**Figure 3.12c**). Together, these data demonstrate that TgLaforin is a glucan phosphatase with a preference for C3-phosphate.

### 3.2.7 Design, synthesis, and testing of a TgLaforin inhibitor

Because TgLaforin represents a possible therapeutic target as a critical regulator of AG metabolism in *T. gondii*, we sought to exploit its observed unique features to identify a specific inhibitor. We utilized the SulfoPhenyl Acetic Amide (SPAA) platform for inhibitor development, which is a novel pTyr-mimetic derived from the FDA-approved drug cefsulodin (299,300). Based on SPAA, potent and specific inhibitors to several PTP enzymes have been developed, including SHP2, mPTPA, mPTPB, and LMW-PTP (299-302). These inhibitors were discovered by fragment-based combinatorial chemistry approach where a library of compounds was prepared by reacting SPAA containing cores with a set of carboxylic acids or amines. To increase the potency and selectivity of an inhibitor for TgLaforin, molecular diversity was installed in order to capture additional and less conserved interactions outside the pTyr binding cleft (i.e., active site), generating inhibitor L319-21-M49 (**Figure 3.13a**). Screening and selection of this compound was conducted at Purdue Institute for Drug Discovery under the direction of Dr. Zhong-Yin Zhang.

To test the specificity and potency of L319-21-M49, we used the pNPP assay with TgLaforin and a variety of other phosphatases (**Figure 3.13b**). To determine a linear range of activity with respect to time, 50 nM TgLaforin was incubated with pNPP and demonstrated to possess linear activity over the course of 10 min (**Figure 3.14a**). To determine the optimal pNPP concentration for inhibitor analysis, TgLaforin was incubated with a wide range of pNPP concentrations (**Figure 3.14b**) to determine its $K_m$ (**Figure 3.14c**). Additionally, the linear time range of all other phosphatases used in this study for inhibitor comparison (PTP1B, VHR, and CIP) was verified (**Figure 3.15a**), and the $K_m$ for each phosphatase was determined (**Figure 3.15b)**. For inhibitor assays, each phosphatase was incubated with a concentration of pNPP equivalent to the $K_m$ value for each respective enzyme alongside a range of inhibitor concentrations.

Under these conditions, L319-21-M49 possessed an $IC_{50}$ of 1.49 μM against TgLaforin (**Figure 13.16a**). Moreover, when tested against other phosphatases, the inhibitor was remarkably specific to TgLaforin. L319-21-M49 was at least 100-fold selective towards TgLaforin compared to another DSP (VHR), a general PTP (PTP1B), and an alkaline phosphatase (CIP) (**Figure 13.16a**).

Next, L319-21-M49 was tested against the glucan phosphatase activity of TgLaforin in the malachite green based assay at its linear activity range (**Figure 3.15b**). To do this, we incubated TgLaforin with amylopectin in the presence of the inhibitor and detected phosphate release with malachite green. Importantly, the inhibitor was also effective at preventing TgLaforin activity against soluble amylopectin with an $IC_{50}$ of 5.10 μM (**Figure 3.16b**). Finally, we tested the inhibitor's ability to inhibit phosphate release using the radiolabel assay within TgLaforin's linear activity range (**Figure 3.15c**). L319-21-M49 was also effective in preventing phosphate release from both the C3 and C6 positions with similar $IC_{50}$s of 6.68 μM and 6.47 μM, respectively (**Figure 3.16c**). Thus, in L319-21-M49, we have identified a first-in-class lead compound for the inhibition TgLaforin.

## 3.3 Discussion

In animals, glycogen breakdown provides substrates for epigenetic modifications, central carbon metabolism, and protein post-translational modifications (154,303,304). In plants, starch characteristically acts as both a transient and long-term storage form of glucose, dictating the level of free sugars and allowing for energy maintenance through dark periods (144). Interestingly, *T. gondii* appears to utilize both plant-like and animal-like systems of glucan storage and degradation making this system an appealing candidate for therapeutic development. Glucan phosphatases are critical regulators of polyglucan metabolism in both plants and animals. Here, we characterized the structure, dynamics, and activity of the unique *T. gondii* glucan phosphatase TgLaforin, demonstrating it possesses a single CBM20 N-terminal to its DSP, a dimerization interface via the DSP domain, and preference for dephosphorylating the C3-

hydroxyl position on glucose. Finally, we identified a first-in-class lead compound that inhibits TgLaforin.

To elucidate the split nature of this novel CBM20, we employed the recently developed AlphaFold2 neural network for an initial structural prediction. In agreement with our sequence predictions and site-directed mutagenesis experiments, the computational prediction of AlphaFold2 suggested that TgLaforin's CBM20 folds into a central core β-sandwich with large unstructured loops outside of this core. This orientation connects the β-sheets so that they form the canonical immunoglobulin-like fold. The linker regions were modeled with a very low level of confidence by AlphaFold2, so we utilized HDX to define both core and linker regions of the TgCBM20. Strikingly, HDX demonstrated that regions we predicted to form the CBM20 core exhibited much lower solvent exchange. Conversely, regions displaying the highest solvent uptake were also the low-confidence regions of the AlphaFold2 model, potentially revealing intrinsically disordered protein-like character of these inserts (305,306). Indeed, low complexity inserts have been previously noted as being unusually abundant in the proteome of *T. gondii* and other related parasitic protozoa, often confounding protein identification (307-309).

We further demonstrated that each homologous region and the aromatic residues within them are critical to the ability of TgLaforin to bind carbohydrates, consistent with the fact that it indeed contains a single CBM20. This combination of protein modeling, mutagenesis, and HDX-MS allowed us to define the first reported split-CBM. We attempted to identify other proteomes containing a split-CBM20 using BLASTp and TgCBM as a query, but we were only able to identify putative split-CBM20 orthologues in highly related *T. gondii* genera that are also cyst forming members of the Phylum Apicomplexa such as *Neospora*, *Besnoitia*, and *Eimeria*.

Therefore, despite its similarities to vertebrate glucan phosphatases, TgLaforin employs a unique starch binding domain (SBD) in the form of a split-CBM20. Currently, there are 88 CBM families identified in the CAZy database, fifteen of which are SBDs (298). The accepted definition of a SBD requires that it must bind to complex polysaccharides, and that it be a continuous and discreet domain of about 100 amino acids. However, the discovery and characterization of a *Microbacterium aurum* GH13 α-amylase (MyAmyA) revealed the first *bona fide* SBD containing 300 amino acid residues (CBM74), demonstrating that SBDs can be much longer than the previously expected length (310). In characterizing the CBM74, structural and mutagenesis studies were not performed, and 3D modeling with the Phyre2 server, a previous modeling software, was unable to generate a confident tertiary structure prediction for the domain. Phyre2 predicted 12 β-strands throughout the CBM74 domain, but no continuous sequence between strands approached the length of the linkers in the TgCBM. Here, we describe a CBM20 that is similar in length to CBM74, but distinct in that its carbohydrate binding residues and secondary structures are split over approximately 325 amino

acids. This split-CBM20 contains discreet regions of homology to other CBM20s, separated by long linker regions with high solvent accessibility.

Recent work has demonstrated that glucan metabolism is not restricted to bradyzoites in *T. gondii*, but is critical throughout the asexual lifecycle, playing a role in parasite growth, morphology, and infection (203,206,228,235,311). Tachyzoites have been recognized as containing a much smaller cytoplasmic polyglucan that is not typically visible by electron microscopy but is detectable using a carbohydrate-specific stain such as periodic-acid Schiff (PAS) (203,228,234,312). This tachyzoite polyglucan is rapidly turned over as observed in other protozoan glucans during their trophozoite stages (228,312,313). Of note, $Ca^{2+}$ dependent protein kinase 2, CDPK2, was identified as a regulator of AG metabolism in tachyzoites and bradyzoites. The ability of CDPK2 to regulate glucan metabolism in tachyzoites was mediated through its CBM20 domain. As such, loss of CDPK2 results in parasites with aberrant cell morphology, excess AG accumulation, and the inability to form tissue cysts in mice (228). Importantly, multiple CDPK2 substrates are involved in glucan turnover including glycogen phosphorylase, $\alpha$-amylase, debranching enzyme, and TgGWD. These data highlight the critical role reversible phosphorylation might play in *T. gondii* beyond its role in bradyzoites. Additionally, they suggest that enzymes involved in glucan metabolism are potential drug targets throughout the parasite's asexual lifecycle.

Historically, phosphatases have been difficult to specifically target (314). However, recent breakthroughs have resulted in a number of successful compounds being developed (315-321). For TgLaforin, we exploited differences in phosphatase tertiary structure outside of the well-conserved PTP-loop to develop an inhibitor. L319-21-M49 was selective for TgLaforin with >100-fold specificity compared to VHR, another member of the DSP family. L319-21-M49 not only inhibited the generic pNPP activity of TgLaforin, but it also inhibited the ability of TgLaforin to dephosphorylate complex carbohydrates. Future studies will define specificity and potency within the more closely related glucan phosphatase family.

Glucose metabolism plays a critical role in central carbon metabolism and cellular signaling from bacteria to humans. Glucose storage and utilization in AGs is beginning to be elucidated in *T. gondii*. Given that a glucose aggregate has now been established in both life cycles that replicate in humans (55), the enzymes that control AG metabolism are potential therapeutic targets, especially the enzymes involved in AG reversible phosphorylation. Importantly, AG metabolism is intricately linked to bradyzoite development (54), making AG reversible phosphorylation in AGs an intriguing target. Our studies demonstrate the key enzymatic features of TgLaforin as a glucan phosphatase and lay the groundwork for targeting TgLaforin as a means to prevent *T. gondii* bradyzoite reactivation and transmission.

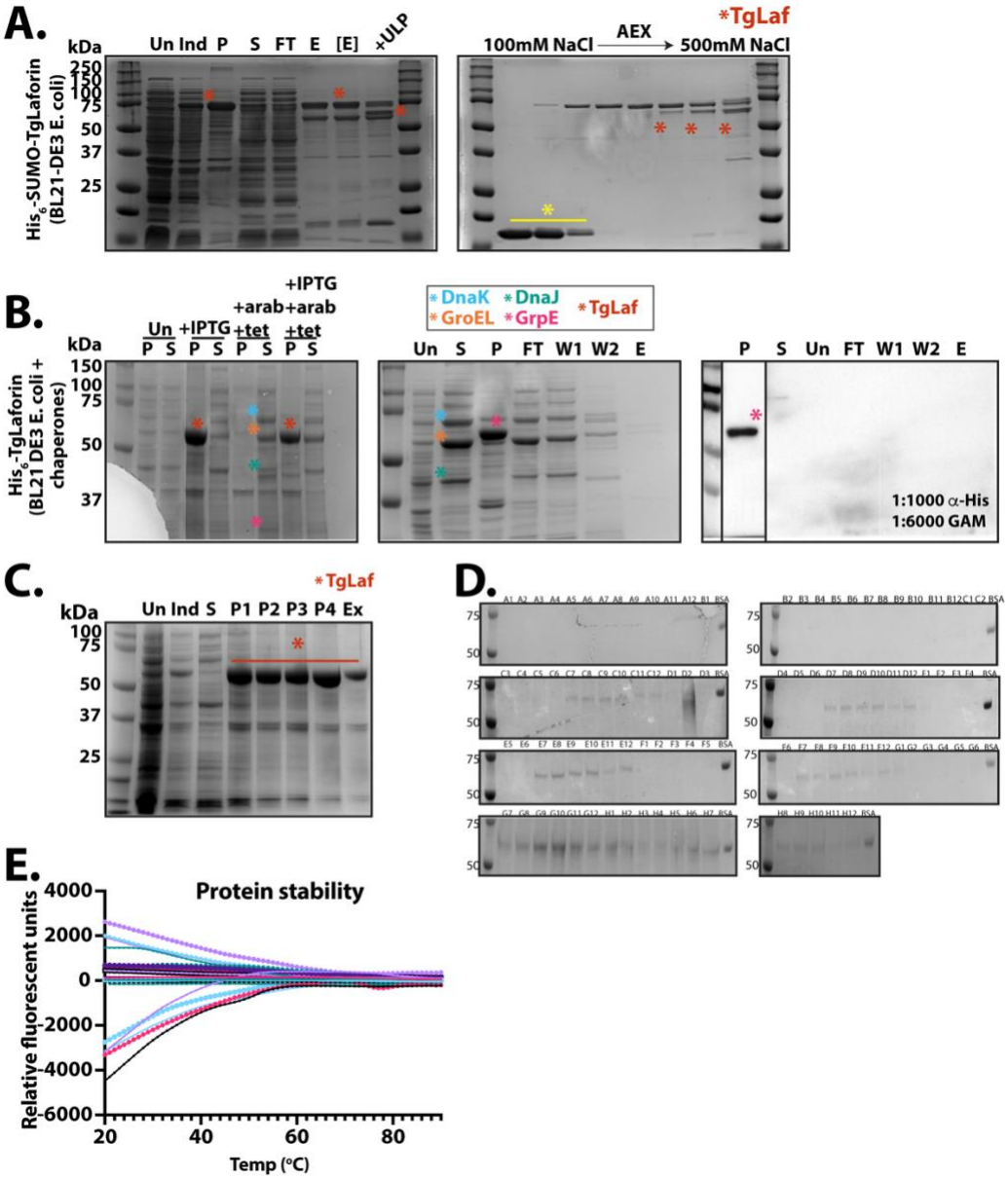


**Figure 3.1 TgLaforin expression in BL21 *E. coli* and SDS-PAGE tracking of protein throughout purification process.**

**A,** 6xHis-SUMO-TgLaforin was expressed and SUMO-tag was removed with ULP (left panel). Protein was purified using AEX (right panel). Yellow asterisk placed above ULP removed by AEX, red asterisk placed adjacent to TgLaforin. **B,** 6xHis-TgLaforin was co-expressed with chaperones (left and middle panel). Solubility of TgLaforin was interrogated by western blot. Pellet (P) was probed separately due to its intense signal (right panel). **C,** Purification of TgLaforin from inclusion bodies. P1-P4 represent pellet washed with 2M Urea, Ex (extract) are inclusion bodies solubilized with 6M guanidine. **D,** Soluble protein from refolding screen (conditions correspond to **Figure 2.1**). **E,** DSF analysis of soluble protein from refolding screen. *Abbreviations*: E = eluate; FT = flow through; GAM = goat-anti-mouse; In = induced; P = pellet; S = supernatant; Un = uninduced; W = wash.

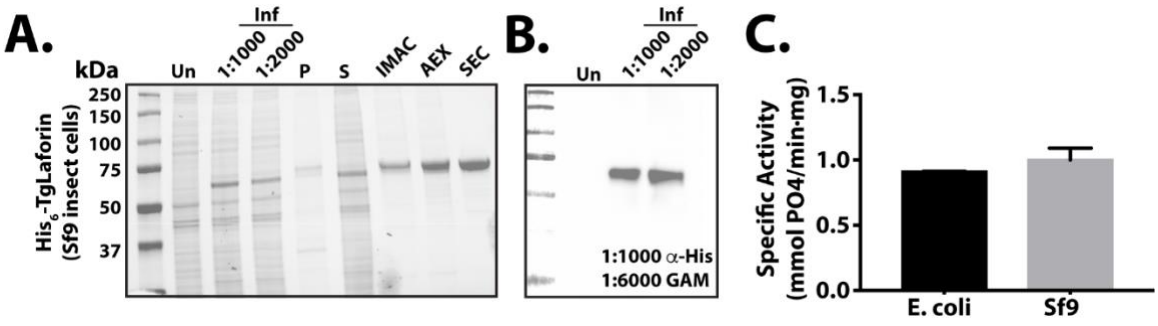


**Figure 3.2 Expression of TgLaforin in Sf9 insect cells.**
**A,** Coomassie-stained SDS-PAGE of protein through purification process. **B,** Western blot of expressed protein. **C,** Comparison of specific phosphatase activity of *E. coli* expressed protein versus Sf9-expressed protein. *Abbreviations*: AEX = anion-exchange; IMAC = immobilized metal affinity chromatography; Inf = infected; P = pellet; SEC = size exclusions chromatography; S = supernatant; Un = uninfected.

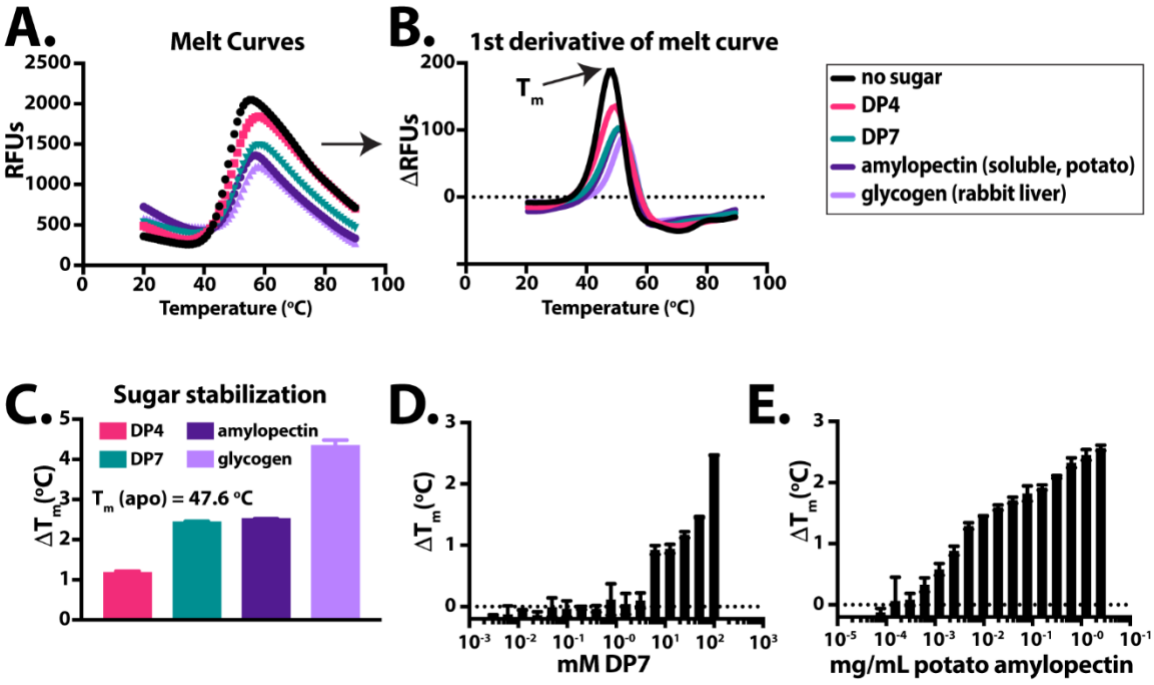


**Figure 3.3 DSF analysis of Sf9-expressed TgLaforin.**
**A,** Raw fluorescence melt curves of TgLaforin with or without carbohydrate ligands. **B,** First derivative of melt curves from **3.3a**. **C,** Effect of various carbohydrates on TgLaforin $T_m$. **D,** Dose-dependent stabilization of TgLaforin with DP7 (maltoheptaose; linear chain of 7 glucosyl units). **E,** Dose-dependent stabilization of TgLaforin with solubilized potato amylopectin.

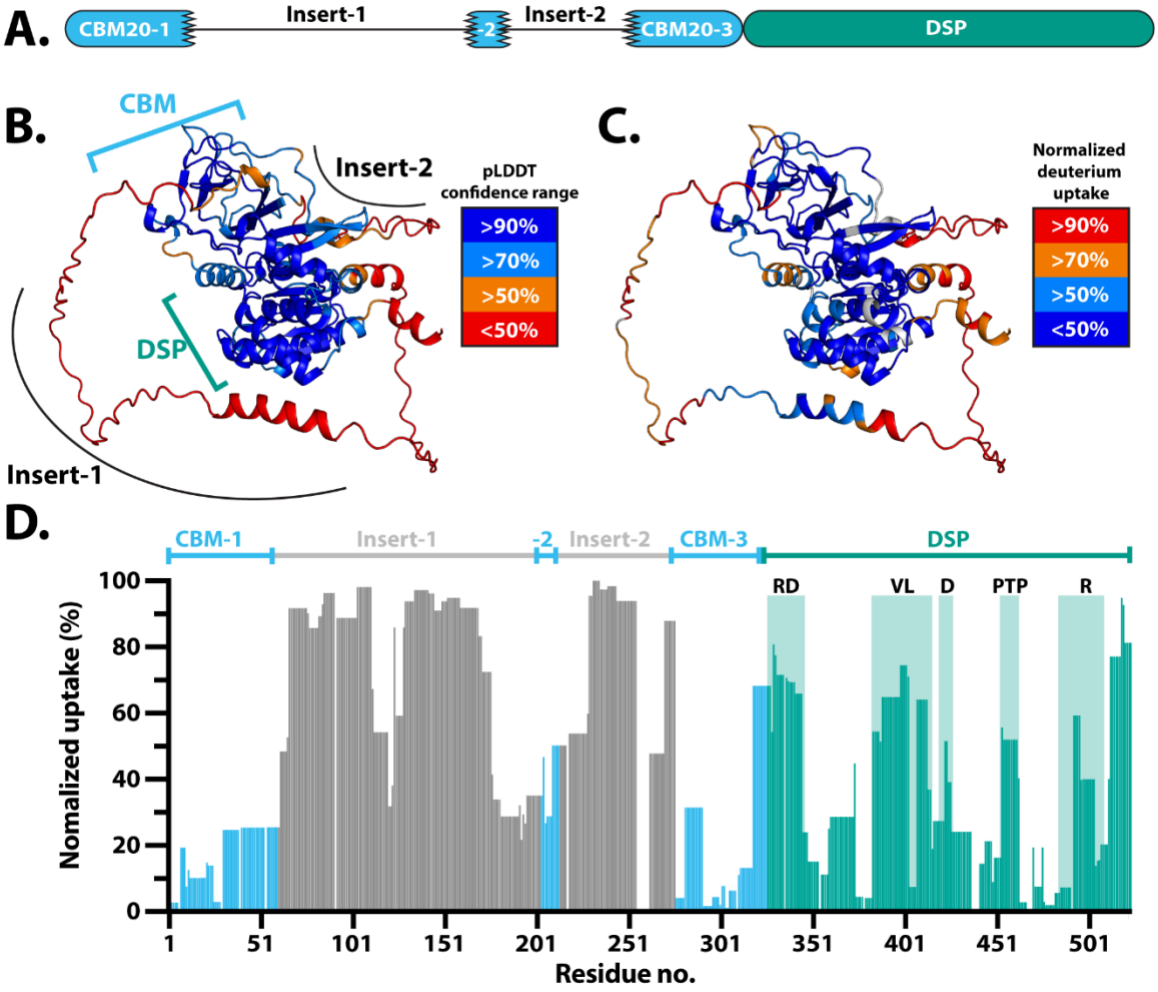


**Figure 3.4 Modeling and HDX data indicate that TgLaforin contains a split-CBM20.**

**A,** Schematic of a previously proposed domain arrangement of TgLaforin (294). **B,** TgLaforin modeled by AlphaFold2 with confidence levels mapped onto the structure. CBM, DSP, and inserts are indicated. **C,** Deuterium uptake of TgLaforin after 15 s as determined by HDX-MS mapped onto the AlphaFold2 model. **D,** Normalized deuterium uptake by TgLaforin after 15 s deuteration represented in 2D, highlighting uptake in each domain of the protein. Other time-points from 15 s to 15000 s displayed in Figure 3.6. *Abbreviations:* RD = recognition domain; VL = variable loop; D = D-loop; PTP = protein tyrosine phosphatase loop; R = R-motif.

AlphaFold2 models generated, and confidence/HDX data superimposed by Tiantian Chen.

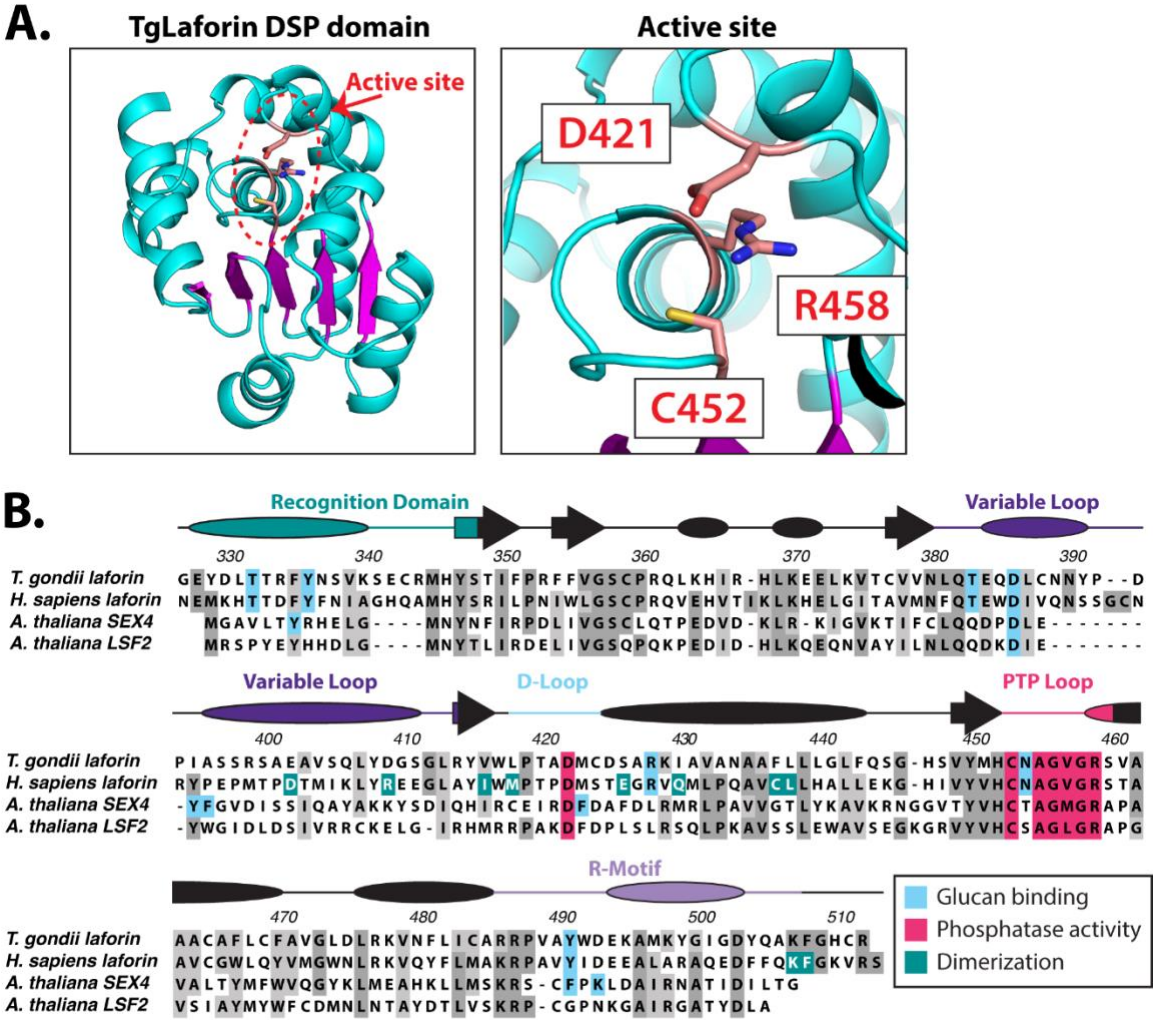


**Figure 3.5 TgLaforin's DSP domain.**

**A,** AlphaFold2 models a typical DSP domain in TgLaforin containing a central β-sheet (magenta) surrounded by α-helices (cyan). The critical catalytic residues are brought into the active site. Side chain colors are as follows: carbon=salmon, nitrogen=blue, oxygen=red, sulfur=yellow. **B,** Alignment of TgLaforin's DSP domain with DSP domains from other glucan phosphatases. Residues critical to glucan binding, phosphate removal, and dimerization (for human laforin) are compared alongside the motifs that define DSP domains with residue colors defined in legend. Dark gray boxes indicate identical residues and light grey boxes indicate similar residues. Arrows indicate β-sheets and ovals indicate α-helices. Numbering corresponds to TgLaforin's amino acid sequence.

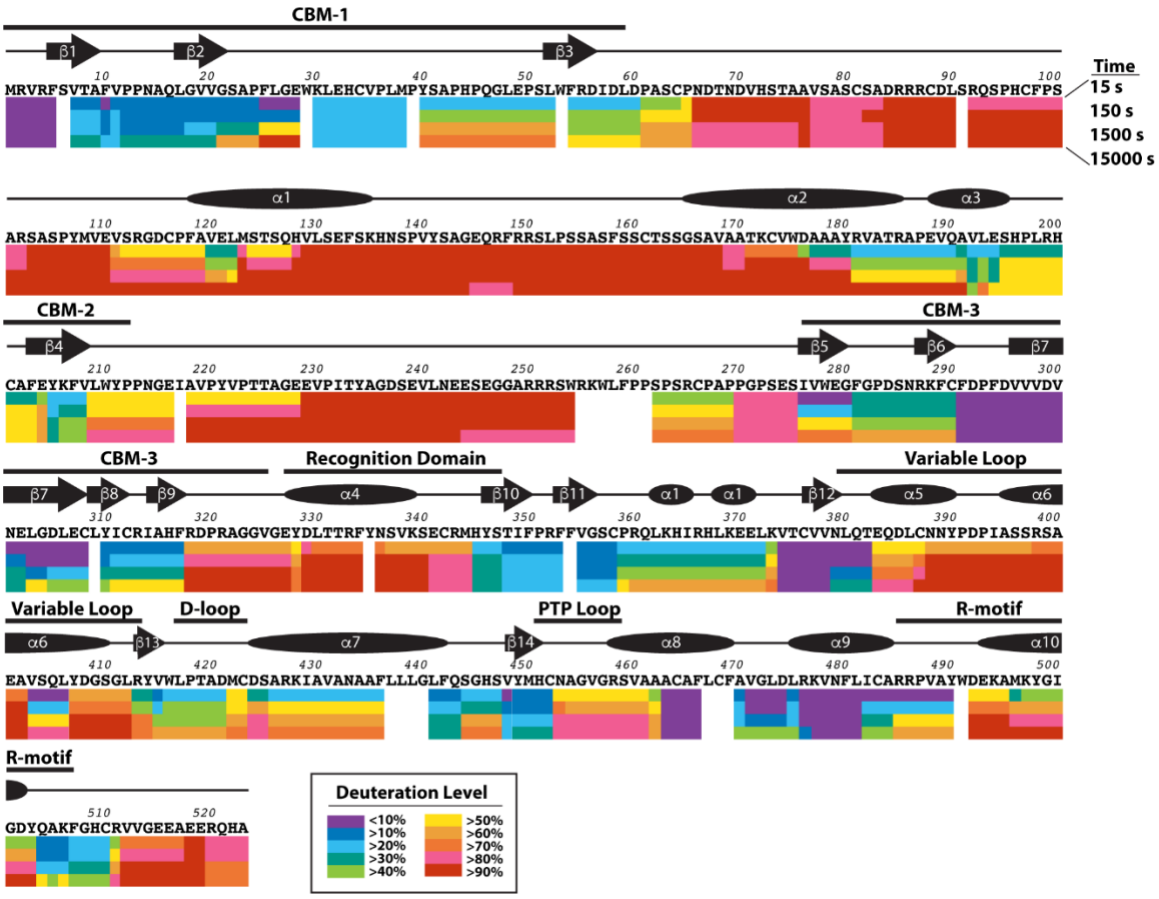


**Figure 3.6 Deuteration level of TgLaforin peptides as a function of time.** The TgLaforin primary sequence is displayed above colored bars that represent individual peptides from pepsin proteolysis. Bar color indicates the percent deuteration of a peptide at a given time point, ranging from lowest deuteration (purple) to highest deuteration (deep red) as indicated in the inset. Secondary structure is displayed above primary sequence with arrows symbolizing β-sheets and ovals symbolizing α-helices. CBM sub-domains and DSP motifs are labeled using thick bars to indicate their predicted location, and numbers correspond to amino acid positions.

HDX data analysis by Caden R. Pearson.

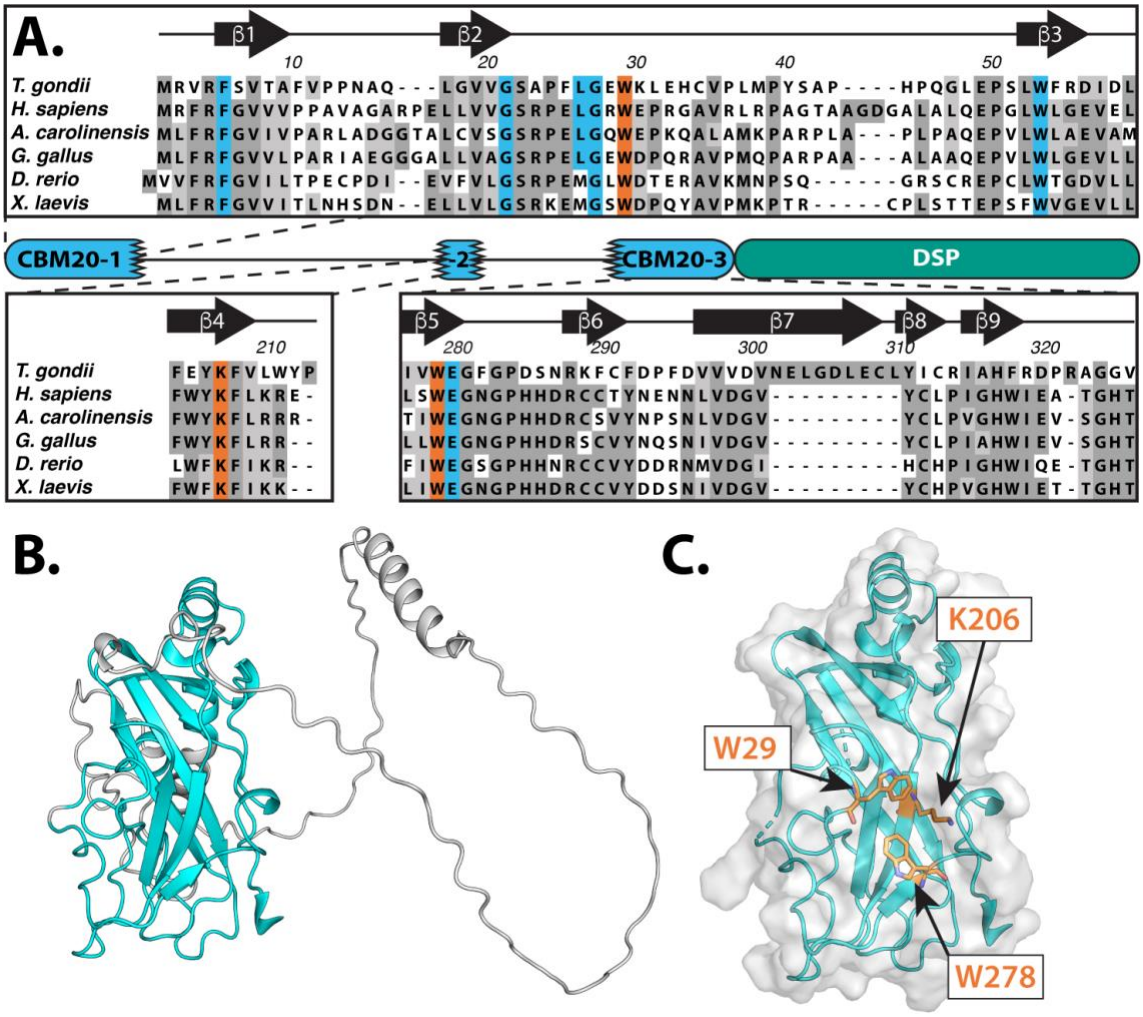


**Figure 3.7 TgLaforin's CBM domain.**
**A**, Multiple sequence alignment of laforin orthologue CBMs found across multiple vertebrate species, overlaid with the predicted domain structure of TgLaforin. Black lines connecting CBM20 fragments are predicted to be largely unstructured loops. Residues highlighted in blue are involved in carbohydrate binding specificity, and residues in orange are consensus residues needed to engage carbohydrates. Arrows symbolize β-strands, and numbering corresponds to the TgLaforin sequence. **B**, AlphaFold2 model of TgLaforin's split CBM20 highlighting the core CBM predicted with high confidence in cyan and the low confidence insert regions in grey. **C**, TgLaforin's CBM core structure is predicted to bring together 3 putative, canonical residues used in carbohydrate interactions: W29, K206, and W278.

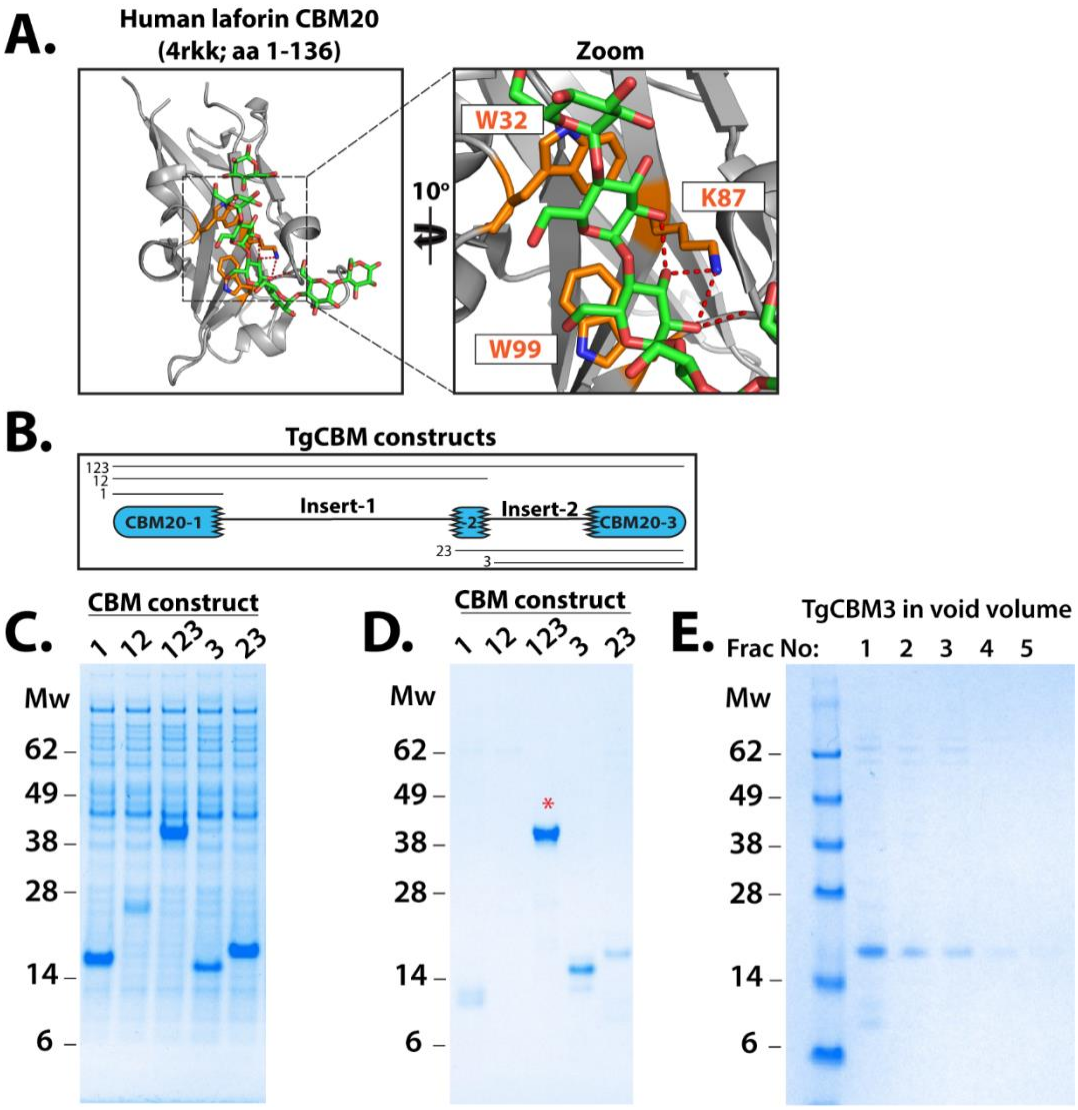


**Figure 3.8. Expression of protein constructs used in this study.**
**A,** 3D crystal structure of human laforin (4rkk) crystalized with maltohexaose highlighting the concerted carbohydrate binding interactions of CBM20 domain. Binding residues are highlighted in orange with N colored in blue, and maltohexaose chain colored by element (C=green, O=red). Zoom displays stacking interactions between glucose and W32/W99 (W29/W287 in TgLaforin), and red dashed lines indicate hydrogen bonding between glucose hydroxyls and K87 (K206 in TgLaforin). **B,** Schematic of constructs generated in this study. TgCBM123, the full-length CBM, is referred to as "TgCBM." **C,** Expression levels of constructs in BL21 whole cell lysate demonstrates success or failure to express each construct. **D,** TgCBM constructs after Ni-IMAC purification demonstrates recovery of soluble protein. **E,** TgCBM3's presence in the void volume as indicated by its presence in early fractions from SEC demonstrates that it aggregates.

TgCBM constructs purified by: Carl D. Vander Kooi, MD.

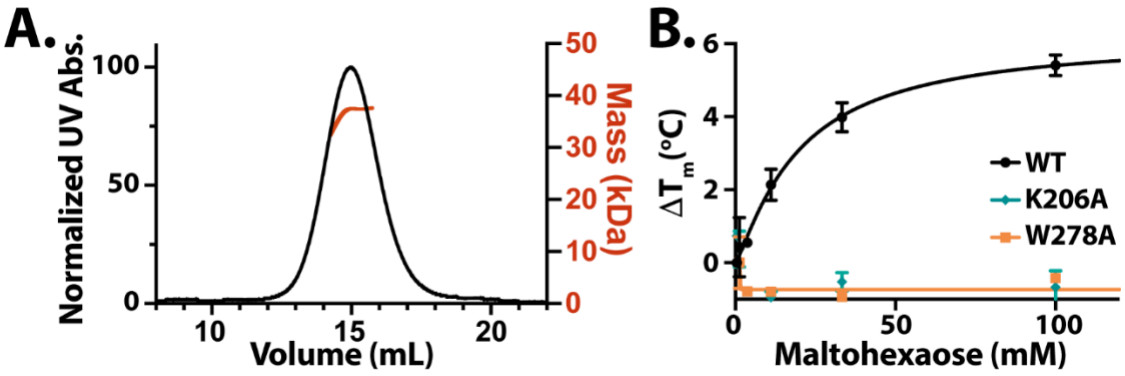


**Figure 3.9 TgCBM characterization.**
**A**, TgCBM SEC profile with MW prediction overlay determines that TgCBM MW is 36.6 ± 6.8 kDa. **B**, TgCBM is stabilized in the presence of increasing concentrations of maltohexaose, while mutagenesis of carbohydrate binding residues no longer exhibit carbohydrate binding.

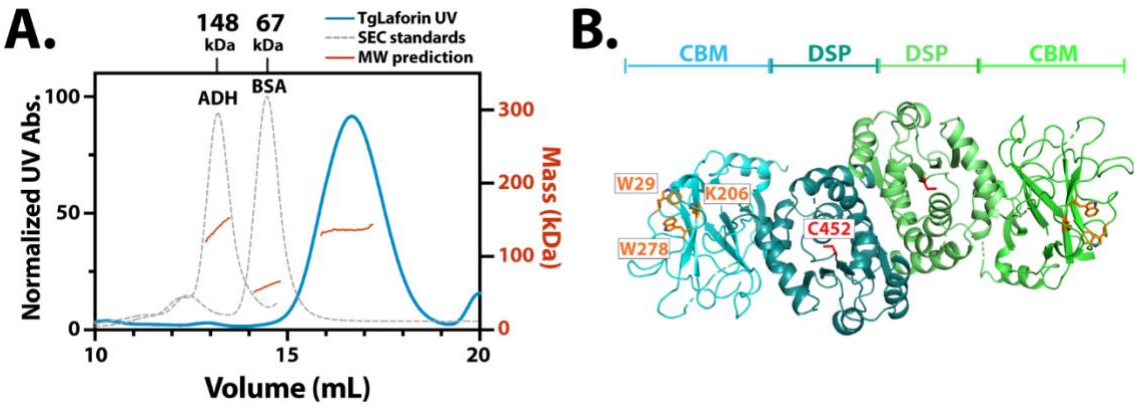


**Figure 3.10 TgLaforin is an antiparallel dimer.**
**A**, SEC elution profile overlayed with MALS-measured mass (red) for two SEC standards (grey; MW of standards indicated at elution volume on top) and TgLaforin (blue). MALS predicts that TgLaforin is 136.6 ± 0.6 kDa in solution. **B**, AlphaFold2 model of TgLaforin as a dimer, showing high confidence regions (pLDDT>70%). Subunits are shown in shades of blue and green. Residues critical to glucan phosphatase function are shown highlighted with core CBM residues depicted in orange, and the catalytic cysteine shown in red.

AlphaFold2 dimer model generated by Tiantian Chen.

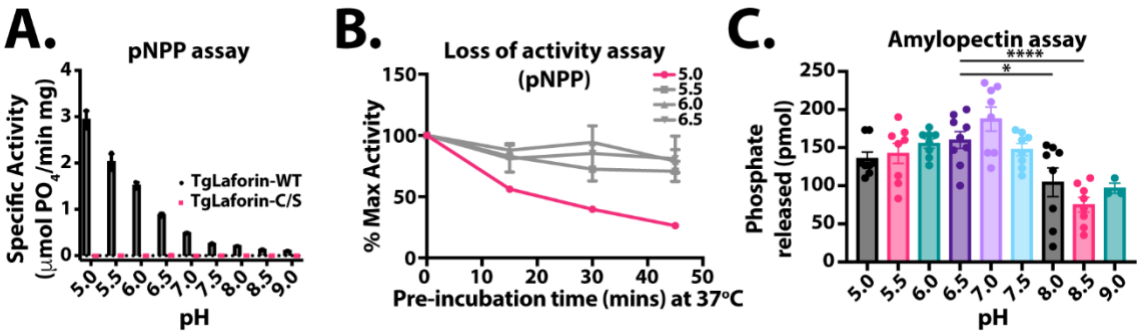


**Figure 3.11 Initial characterization of TgLaforin phosphatase activity.**
**A,** pH dependence of TgLaforin activity against pNPP. **B,** The effect of pH on TgLaforin activity against pNPP over time. **C,** pH dependence of TgLaforin activity against potato amylopectin.

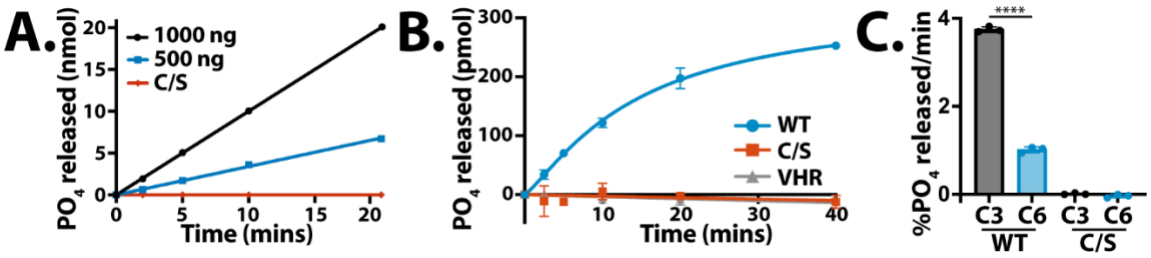


**Figure 3.12 Full-length TgLaforin is an active glucan phosphatase that preferentially dephosphorylates starch at the C3 position.**

**A**, TgLaforin activity against pNPP is both dose and time-dependent and abrogated when the catalytic cysteine (C452) is mutated to serine (C/S). **B,** TgLaforin releases phosphate from solubilized potato amylopectin, whereas the C/S mutant and VHR cannot. **C**, TgLaforin preferentially dephosphorylates glucose from insoluble, $^{33}$P-radiolabeld *A. thaliana* starch at the C3 position. Statistical comparison of site specificity was done using an unpaired two-tailed t-test; statistical significance: ****p<0.0001.

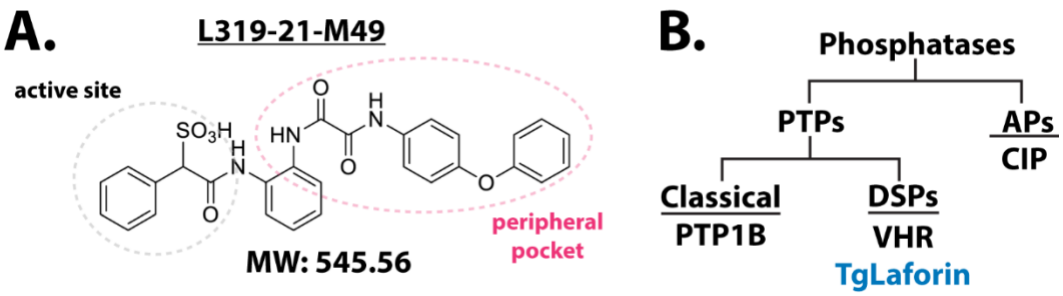


**Figure 3.13 Development of a novel glucan phosphatase inhibitor.**
**A**, The structure the TgLaforin inhibitor L319-21-M49. **B,** Classification tree of the phosphatases used in this study. *Abbreviations: AP = alkaline phosphatase; CIP = calf intestinal phosphatase; DSP = dual-specificity phosphatase; PTP = protein tyrosine phosphatase; VHR = Vaccinia H1-related phosphatase*

L319-21-M49 design, screen, and synthesis by Rongjun He, Ph.D., Jianping Lin, Ph.D., and Li Wu under the direction of Zhong-Yin Zhang, Ph.D.

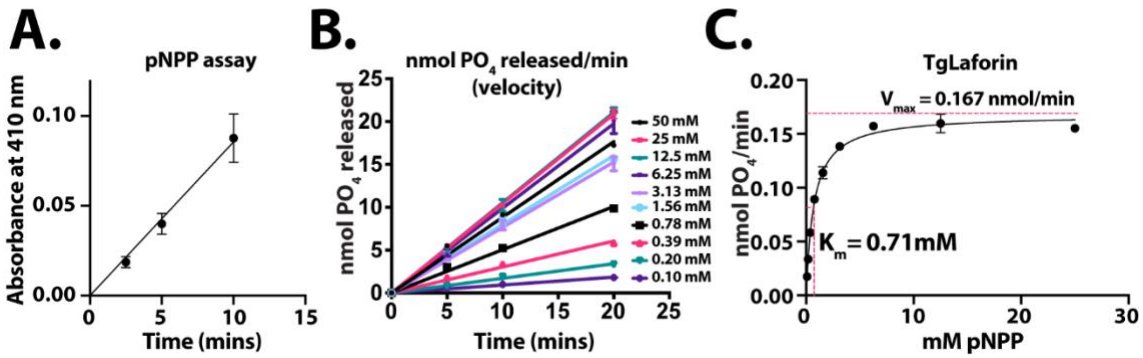


**Figure 3.14 Determination of TgLaforin kinetic parameters.**
**A,** TgLaforin (50 nM) activity over the course of 10 min. **B,** TgLaforin activity over time with varying substrate concentration. **C,** Determination of $K_m$ and $V_{max}$ of TgLaforin by plotting initial velocities from **3.14b** against substrate concentration.

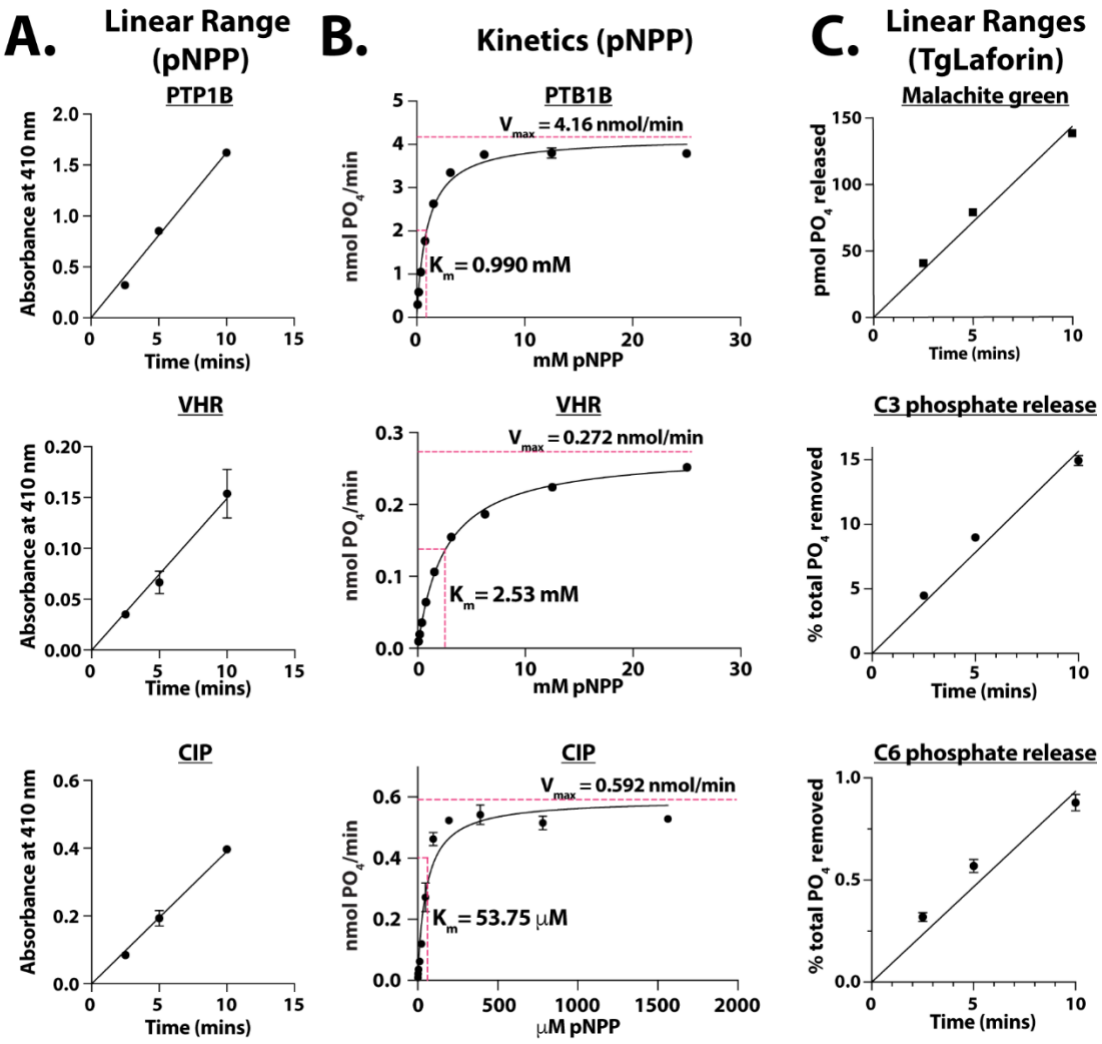


**Figure 3.15 Linear range determination of phosphatases used in inhibitor screening.**

**A,** Phosphatase activity over the course of 10 min. **B,** Determination of $K_m$ and $V_{max}$ of phosphatases by plotting initial velocities from against substrate concentration. **C,** TgLaforin activity over the course of 10 min in amylopectin assay (top panel) and site-specificity assays (bottom two panels).

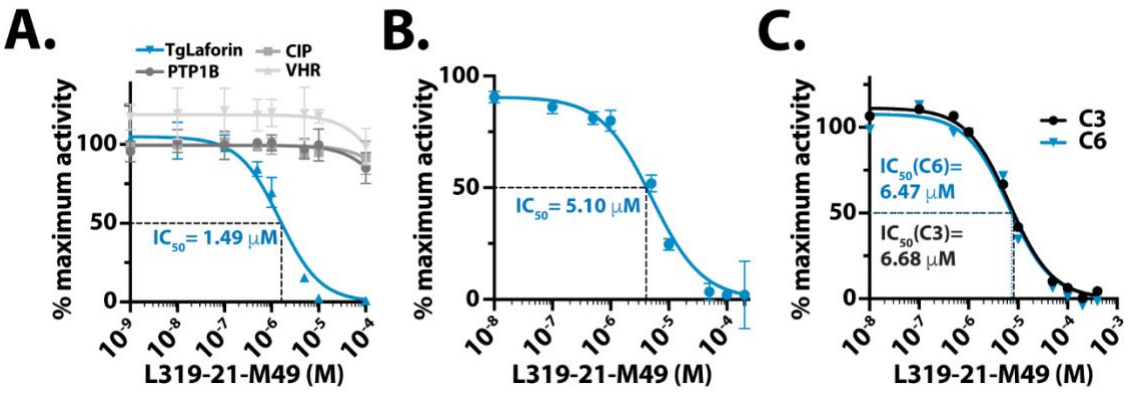


**Figure 3.16 Testing of a novel glucan phosphatase inhibitor.**
**A,** L319-M21-M49 inhibits TgLaforin activity against the model phosphatase substrate pNPP with >100-fold specificity over other phosphatases. **B,** L319-M21-M49 inhibits TgLaforin activity against soluble amylopectin, and **C,** activity against insoluble starch with similar efficiency. *Abbreviations: AP = alkaline phosphatase; CIP = calf intestinal phosphatase; DSP = dual-specificity phosphatase; PTP = protein tyrosine phosphatase; VHR = Vaccinia H1-related phosphatase.*

# CHAPTER 4. BIOCHEMICAL AND BIOPHYSICAL CHARACTERIZATION OF THE T. GONDII GLUCAN, WATER DIKINASE USING BOTH CONVENTIONAL AND NOVEL METHODS

## 4.1 Introduction

The presence of covalently bound phosphate in starch has been recognized since the 1970s (322,323), and its importance in facilitating starch breakdown via a cycle of reversible glucan phosphorylation is discussed in sections 1.5.3 and 1.7.1. The introduction here will primarily serve to convey the general mechanistic basis by which the glucan, water dikinase (GWD) both phosphorylates carbohydrates (section 4.1.2) and binds to them (section 4.1.3).

### 4.1.1 The discovery of the role of GWD in starch phosphorylation and degradation

The role of GWD in plant starch degradation was first documented in 1991 before any knowledge of its enzymology. Plants mutagenized by irradiation were placed in the dark for 3 days, and those displaying starch-excess (*sex*) phenotypes at the end of the dark stress were subsequently selected and studied (324). Of particular interest in this initial study was the line designated "*sex1*," in which enlarged starch morphology was visualized both by iodine staining (324) and electron microscopy (325), but the mechanistic basis underlying this phenotype was not then ascribed to a glucan dikinase. The first indication that a glucan dikinase played a role in starch phosphorylation and turnover was suggested in a 1998 study that knocked down a starch-associated kinase that was then named "R1" (238). After knockdown of R1, mature leaves stained heavily with iodine (indicative of a starch excess, i.e. *sex*, phenotype), starch granules from these leaves had much lower phosphate levels, and degradation of starch during the night was demonstrated to be diminished without R1.

Several years later, another group determined the DNA sequence of the *sex1* locus and discovered that *sex1* encoded an amino acid sequence with significant homology to the R1 protein, suggesting that they may be the same protein (326). It was also demonstrated that this protein contained a dikinase domain, multiple "starch granule association domains," and a chloroplast transit peptide (326). Production of recombinant *Solanum tuberosum* (potato) GWD (StGWD) confirmed these domain predictions in a subsequent study (167). Incubation of the protein with various substrates then lead to the conclusion that GWD utilizes a dikinase mechanism that transfers the $\beta$-phosphate from ATP to starch, and simultaneously releases orthophosphate and AMP. As such, this reaction was determined to have 3 substrates: ATP, $H_2O$, and an $\alpha$-glucan, and to release 3 products: AMP, orthophosphate, and a phospho-$\alpha$-glucan.

### 4.1.2 The dikinase mechanism of GWD

The mechanism by which GWD/R1/SEX1 phosphorylates starch was determined in a series of studies following its identification (167,266,327), depicted in **Figure 4.1**. First, multiple groups determined that the β-phosphate from ATP is transferred directly to GWD in an autophosphorylation reaction that results in the formation of a phospho-histidine enzyme intermediate. The phosphate is then transferred from the catalytic histidine directly to the hydroxyl group of a glucosyl reside in starch to form a phosphate-ester at the C6 position. This is accompanied by the release of AMP, the γ-phosphate from ATP (orthophosphate), and the newly phosphorylated glucan (167). The contribution of each GWD domain to this catalytic activity was directly demonstrated using limited proteolysis and domain truncations of StGWD, revealing that autophosphorylation depends on a phosphohistidine (His) domain, and that ATP binding depended on a nucleotide binding domain (NBD) (327). Importantly, the His+NBD domains constitute a phosphoenolpyruvate-dikinase-like (PPDK-like) region of the protein (**Figure 4.1a**).

Protein dynamics were also determined by use of circular dichroism (CD) that demonstrated a significant conformational change in StGWD upon autophosphorylation, and this change was shown to be independent of ATP binding. This data was consistent with previous studies that proposed a swivel mechanism by which a His-domain could interact with both the NBD and its other substrate binding domain after autophosphorylation through insights provided by the crystal structure of the *Cenarchaeum symbiosum* PPDK (328,329).

With these mechanistic and structural data, the entire catalytic cycle by which GWD phosphorylates glucans was proposed (327), and is presented in **Figure 4.1a.** *Step 1*: Apo-GWD binds ATP via $Mg^{2+}$-dependent electrostatic interactions within the NBD. *Step 2*: The catalytic histidine residue within the His-domain forms a phospho-histidine intermediate with the β-phosphate from ATP, with simultaneous release of AMP and transfer of the γ-phosphate to $H_2O$, releasing orthophosphate. The His-domain also undergoes a long-range movement from the NBD toward the CBM domains. *Step 3*: GWD binds to a glucan substrate via its N-terminal CBM domains, and the β-phosphate is then transferred to the C6 position of the glucan substrate. *Step 4:* The phospho-glucan is released, and the His-domain moves back toward the NBD.

The dynamics of the His-domain movement between the two substrate binding domains is not well understood, but the His-domain has been noted to be flanked by two flexible polypeptides that display both helical and disorganized characteristics (328). Therefore, these linkers may allow for significant displacement from either 1) autophosphorylation resulting in repulsion of the His-domain from the NBD domain, or 2) constant movement of the His-domain between its substrate-binding domains.

### 4.1.3 GWD orthologues possess a CBM45 for starch binding

The N-terminus of GWD was determined to be critical in carbohydrate binding as its domains were initially being classified (327), and the novelty of its N-terminal CBMs was subsequently recognized in both primary amino acid sequence and substrate preference (254). The N-terminal CBMs were shown to confer specificity to amylopectin, as truncation constructs lacking the CBMs were able to phosphorylate a wider variety of linear glucans such as amylose. No GWD constructs, however, were able to efficiently phosphorylate glycogen, demonstrating the specificity of this new CBM for crystalline, branched substrates. Moreover, several tryptophans were classified as critical to carbohydrate binding, as is often the case in CBMs (298). This unique CBM has since been classified as a CBM45 (CAZy.org).

Thus far, CBM45s have been restricted to GWD orthologues and to plastidial $\alpha$-amylase3 enzymes (AMY3) (330). No CBM45 structure has been published, but it has been modeled using Phyre2 and is predicted to adopt the immunoglobulin-like fold that is common in starch binding domains (SBDs) (331). Interestingly, CBM45s appear to be restricted to organisms that produce semi-crystalline glucans such as starch (330). CBM45s are often present in tandem within the same protein and possess a low affinity for starch that is believed to allow for their dynamic association with starch granules.

### 4.1.4 A GWD orthologue in *T. gondii*

The presence of a GWD orthologue in *T. gondii* (TgGWD) has been well documented (40,203,206,212,228), and TgGWD has been suggested to be a target of CDPK2, a *T. gondii* plant-like kinase that orchestrates starch turnover in *T. gondii* (228). To further elucidate the biochemical and biophysical underpinnings of reversible phosphorylation in *T. gondii* we expressed recombinant TgGWD and demonstrate that it employs the standard glucan, water dikinase mechanism utilized by other GWD orthologues. Moreover, we define its site specificity, demonstrate that it exists as a monomer in solution, and develop a novel assay by which to monitor AMP release by TgGWD. The monitoring of AMP release will be of use in dikinase inhibitor screening or as a means by which to more fully understand the GWD mechanism.

## 4.2 Results

### 4.2.1 *T. gondii* encodes a putative glucan, water dikinase orthologue

The amino acid sequence of TgGWD was retrieved from ToxoDB.org (TGME49_214260) and was analyzed using the conserved domain database

(CDD). The CDD recognized only the PPDK region at its C-terminus, but the remainder of the protein was undefined. To determine if TgGWD contains one or more CBM45s as other GWD orthologues do (254), the undefined N-terminus was aligned with CBM45 domains from StGWD and *A. thaliana* GWD (AtGWD) (**Figure 4.1b**). This alignment revealed that TgGWD indeed contains at least two CBM45s at its N-terminus, each containing the consensus carbohydrate-binding tryptophan residues characteristic of CBM45s. Moreover, TgGWD contains the required catalytic histidine within its His-domain, demonstrating that TgGWD is composed of the three domain types that are characteristic of GWD orthologues: two CBM45s, a His domain, and an NBD (**Figure 4.1b**). Despite containing all the required domains, TgGWD displays low sequence similarity and identify with other GWD orthologues (**Figure 4.1b**). TgGWD is only ~36% similar and ~21% identical to St- and AtGWD, respectively. These values are quite low in comparison to StGWD and AtGWD sharing 77.8% and 66.1% similarity and identity, respectively.

Interestingly, it appears possible that transcription of TgGWD is upregulated in bradyzoites by RT-PCR (40). The upregulation of TgGWD with the simultaneous appearance of an insoluble glucan in *T. gondii* creates temptation to speculate about the role of TgGWD in AG formation given its restriction to organisms that possess an insoluble polyglucan. However, transcriptomic data made available on ToxoDB.org does not support the RT-PCR data, and instead suggests that TgGWD transcription remains constant across the asexual life stages (332) (**Figure 4.1c**).

### 4.2.2 TgGWD utilizes a standard glucan dikinase mechanism

To determine if TgGWD is an active glucan, dikinase, we expressed full-length recombinant 6xHis-TgGWD in Sf9 insect cells and purified it to >95% homogeneity using size-exclusion chromatography (**Figure 4.2a**). To determine if TgGWD autophosphorylates itself with the β-phosphate from ATP, TgGWD was incubated with both $^{33}$β-ATP and $^{33}$γ-ATP for 30 mins before purified protein was separated by SDS-PAGE to remove all excess radio-labeled ATP. The gel containing TgGWD then was exposed to a phosphor screen, and then radioactive bands corresponding to autophosphorylated protein were imaged. Detection of radio-labeled protein revealed that TgGWD-WT, like StGWD, autophosphorylates with the β-phosphate from ATP, and not the γ-phosphate (**Figure 4.2b**). Moreover, mutation of the catalytic histidine to an alanine, H1241A (H/A), demonstrated that TgGWD also utilizes the histidine residue identified via sequence alignment to form a phospho-histidine intermediate with the β-phosphate (**Figure 4.2b**). Curiously, it was noted that the H/A mutant appeared to incorporate the γ-phosphate from ATP whereas the H/A mutant of StGWD did not. A study noted the incorporation of γ-phosphate into both St- and AtGWD previously (333), although it was not seen here. GWD orthologues display a wide variety of specific activities (333), and it is

possible that TgGWD incorporates γ-phosphate at a higher rate than StGWD. This phenomenon was repeatable, but not explored further in this study.

After autophosphorylation, GWD then transfers phosphate from the phospho-histidine to its glucan substrate. To determine if TgGWD retains this ability, TgGWD was incubated with both $^{33}$β-ATP and $^{33}$γ-ATP in the presence of *At-Δsex1-3* starch (phosphate-free starch) for 4 hours. Radioactive phosphate incorporation into starch was then determined using a scintillation counter after extensive washing to remove all other reaction components. As expected, TgGWD utilizes the β-phosphate from ATP to phosphorylate starch as evidenced by its incorporation into starch, and not the γ-phosphate to any appreciable extent (**Figure 4.2c**), demonstrating that TgGWD employs the same dikinase mechanism seen in other GWD orthologues.

The incorporation of β-phosphate into insoluble starch by TgGWD was then monitored over the course of 12 hours by incubating TgGWD with phosphate-free starch and $^{33}$β-ATP (**Figure 4.3a**). TgGWD displayed time-dependent kinetics in starch phosphorylation, and the catalytically inactive mutant, TgGWD-H/A, was unable to transfer any phosphate to starch (**Figure 4.3a**). Plant starch is phosphorylated at both the C6 and C3 positions. To determine if TgGWD phosphorylates the C6 or C3 position of glucosyl units within starch, a previously developed glucan dikinase site specificity assay was used (**Figure 4.3b**). Briefly, TgGWD was incubated with phosphate-free starch and $^{33}$β-ATP for 16 hours. To determine where TgGWD places phosphate on glucosyl-residues, TgGWD-treated starch was then incubated with a C3-specific phosphatase (LSF2), and the supernatant from this reaction was monitored on a scintillation counter. LSF2 removed no phosphate from the TgGWD starch (**Figure 4.3c**), indicating that TgGWD does not phosphorylate the C3-position. Starch was then dephosphorylated with SEX4, a glucan phosphatase that removes both C6 and C3 phosphate (with a preference for C6), and the supernatant was measured. SEX4 released almost 20% of the TgGWD-added phosphate within 15 minutes, indicating that TgGWD phosphorylates starch at exclusively the C6 position (**Figure 4.3c**). Interestingly, this is the opposite site-specificity of TgLaforin (**Figure 3.12c**). It should be noted, however, that this does not result in the incompatibility of these two enzymes, as TgLaforin does not exclusively dephosphorylate the C3 position and can also remove C6 phosphate.

### 4.2.3 Biophysical properties of TgGWD

To determine if TgGWD is stabilized in the presence of its various substrates, dual scanning fluorimetry (DSF) was utilized to monitor the melting temperature ($T_m$) of TgGWD with or without carbohydrates and ATP as done previously (185). An increase in melting temperature in the presence of various substrates suggests protein-ligand interaction. In the presence of linear oligosaccharides, TgGWD displayed very little or no increase in stabilization (**Figure 4.4a**). This is not

altogether surprising as linear glucans such as amylose have been demonstrated to be a much poorer substrate for StGWD than a branched glucan, such as amylopectin (266). However, in the presence of ATP, TgGWD was stabilized by almost 4 $^{o}$C in comparison to the apo-protein (**Figure 4.4a**).

It has been previously reported that StGWD forms a stable homodimer in solution that is not dependent on autophosphorylation or substrate binding (266), with dimerization most likely mediated through the PPDK domain (254). To determine the quaternary structure of TgGWD, size-exclusion chromatography coupled to multi-angle light scattering (SEC-MALS) was utilized to determine the molecular weight of TgGWD in solution, as has been done previously with other glucan binding recombinant proteins (262). As expected, TgGWD eluted as a single peak at an earlier volume than the elution standards (**Figure 4.4b**). The elution volume is consistent with its predicted molecular weight of 197.8 kDa that exceeds those of the standards used in this study. Interestingly, TgGWD was not retained on the column due to its CBM domains, a phenomenon that has been previously reported in CBM20-containing laforin orthologues (262) and demonstrated in **Figure 3.10**. Moreover, MALS analysis predicted that TgGWD has a MW of 191.4 $\pm$ .5 kDa (**Figure 4.4b**). Compared with the calculated MW for recombinant TgGWD of 197.8 kDa, the MALS prediction indicates that TgGWD is a monomer in solution, unlike StGWD.

### 4.2.4 Development of a CE-based assay to monitor glucan dikinase activity

The standard for monitoring glucan dikinase activity relies on radioactive ATP that is both a costly reagent with many associated laboratory regulations, and one that requires extensive washing to remove background. Such issues are prohibitive to high throughput inhibitor screens of glucan dikinases for downstream use as potential therapeutics against parasitic organisms such as *T. gondii.*

The labeling of starch with the $\beta$-phosphate from ATP is accompanied the release of AMP and the $\gamma$-phosphate. Therefore, it was reasoned that monitoring the release of AMP during the course of the dikinase reaction could provide an alternative to monitoring $^{33}$P incorporation into starch and eliminate the need for washing out the reaction. Capillary-electrophoresis (CE) is a technique that has been used to analyze nucleotides previously (334). CE takes advantage of UV-absorbance by nucleotides for detection, and the ability of electrophoretic techniques to separate nucleotides based on their migration through a charged field (335). An important consideration in dikinase assays are the relatively low amounts of AMP released in a reaction, resulting in mid-nM to low-$\mu$M final concentrations. Because the path length of light analyzed by CE is short, low sample concentrations present a problem for this technique.

To circumvent the problem presented by low AMP concentrations, a method known as whole capillary stacking has been developed for CE (267) (illustrated in **Figure 4.5a**). Briefly, *Step 1*: a capillary is filled with a sample mixture containing

a compound of interest using a vacuum to draw sample in. *Step 2*: a highly negative charge is applied to the capillary to move compounds back toward the buffer at the negative electrode, both removing positive compounds and simultaneously stacking negative compounds at the buffer/capillary interface. This step effectively concentrates low-abundance molecules into a small volume. *Step 3*: the voltage is reversed to a highly positive charge, and negative components are separated over the volume of the capillary, and an absorbance detector is utilized to monitor compounds at wavelengths of interest. In the case of monitoring nucleotides, the UV-Vis detector is set to 256 nm.

To determine if AMP/ATP could be separated with buffer, injection, and voltage conditions specified in section 2.1.15, 10 μM AMP was mixed with 50 μM ATP (the amount used in *in vitro* labeling reactions) and run using the whole stacking methodology. Peaks corresponding to AMP and ATP could be resolved from one another (**Figure 4.5b**), as these retention times were confirmed with each nucleotide alone. AMP always eluted at about 14 mins under the specified conditions. To determine the linear range in which AMP could be detected, a range of concentrations of AMP were run on the CE (**Figure 4.5c**), and the area under each peak was determined and plotted against AMP concentration (**Figure 4.5d**). Using this technique, the linear range of AMP detection was determined to be 100 nM up to 10 μM, although concentrations outside of this range were not tested.

To determine if AMP release from a glucan dikinase reaction could be monitored using this CE-based assay, 50 nM TgGWD was incubated with phosphate-free starch and ATP, and the reaction was terminated at various time points from 1-12 hours. After terminating reactions, starch was pelleted, and the supernatant was saved for AMP analysis. Before analyzing the supernatant on the CE, protein was filtered out using centrifugal filtration to provide cleaner UV-Vis spectra. The flowthrough from the filtration containing the AMP was then analyzed by whole capillary stacking on the CE. AMP release by TgGWD-WT could be monitored using this technique in a time dependent manner, whereas TgGWD-H/A released no AMP over the course of the reaction, validating that the assay was specific to the dikinase mechanism (**Figure 4.5e**). Interestingly, AMP release remained linear over the course of the 12 hour reaction, which contrasted with the results obtained from direct incorporation of phosphate into starch that clearly level off by 8 hours (**Figure 4.3a**). This prompted the direct comparison of the two methods. Strikingly, release of AMP appears to occur at a much more rapid rate than phosphate addition onto starch, even at early timepoints (**Figure 4.5e**). This observation suggests the possibility that AMP production by TgGWD is stoichiometrically uncoupled from its transfer of phosphate to starch.

## 4.3 Discussion

Herein, we demonstrate that *T. gondii* encodes an active glucan, water-dikinase that employs a standard GWD mechanism. TgGWD first utilizes the β-

phosphate from ATP to autophosphorylate itself on a conserved histidine residue within its PPDK domain. Next, TgGWD transfers the β-phosphate from the phospho-histidine intermediate to the C6 position of a glucan substrate while simultaneously releasing orthophosphate and AMP. Moreover, we developed a CE-based assay for the detection of AMP released as a result of this reaction that is specific to the catalytically active protein.

Importantly, demonstration of the activity of TgGWD *in vitro* paves the way for the therapeutic targeting of this plant-like protein in the human parasite, *T. gondii*. Such targeting could begin with widely available kinase inhibitor screens coupled with the relatively high throughput CE-based assay that requires no radioactive ATP, minimal centrifugation, and largely unmonitored analysis of AMP release. While this assay cannot monitor the transfer of phosphate to a glucan substrate, it monitors the hydrolysis of ATP to AMP+$P_i$ during the autophosphorylation step. Thus, identified kinase inhibitors would be specific to the ATP hydrolysis that occurs in Steps 1 and 2 depicted in **Figure 4.1a**.

Previous studies have demonstrated that the GWD mechanism is likely more complicated than the one that is typically presented (176,333). One study demonstrated that levels of autophosphorylated GWD decreases over time after separation from $^{33}$β-ATP in the absence of any glucan, implying that phosphate transfer from the catalytic histidine does not necessitate the presence of a glucan (176). In fact, a follow up study demonstrated that 20% of ATP utilized by GWD does not result in phosphate transfer to a glucan substrate (333), calling into question the 1:1:1 stoichiometry that has been proposed for the products of the reaction (167). Moreover, it was demonstrated that GWD can continuously hydrolyze ATP in the absence of any glucan acceptor (333).

The data presented here support the observations that ATP hydrolysis is uncoupled from the formation of glucosyl phosphate esters, as release of AMP far exceeds the placement of phosphate on starch (**Figure 4.5e**). Moreover, the linear reaction kinetics of AMP release versus the plateau effect seen during phosphate transfer implies a potential saturation of the starch surface granule with phosphate. Utilization of assays such as CE that monitor reaction products like AMP in comparison with the generation of a phosphorylated glucan could help reveal the limits of starch granule surface phosphorylation.

In addition to demonstrating GWD hydrolyzes ATP faster than it transfers phosphate to starch, it was also previously demonstrated that both WT and H/A mutants of GWD could autophosphorylate with the γ-phosphate from ATP (333). This observation implies the presence of a histidine outside of the canonical active site that can bind this terminal phosphate, possibly as the first step in generating orthophosphate. Such a histidine, however, awaits identification. Once again, the data presented here support the possibility of a second phospho-histidine intermediate as significant labeling of TgGWD-H/A was also seen with $^{33}$γ-ATP.

Overall, these observations confirm the presence of a canonical GWD orthologue in *T. gondii*, possessing multiple CBM45 domains and a PPDK domain.

We demonstrated that TgGWD behaves as a standard glucan, dikinase, in both the well characterized aspects of GWD enzymology and the newly suggested peculiarities inherent to the mechanism. These observations also lay the groundwork for dissecting the general GWD mechanism further through the use of a novel method for the detection of AMP release, and thus provides another perspective on GWD activity. Future work in identifying compounds to inhibit TgGWD for testing as therapeutics can use the reagents and methods developed here.

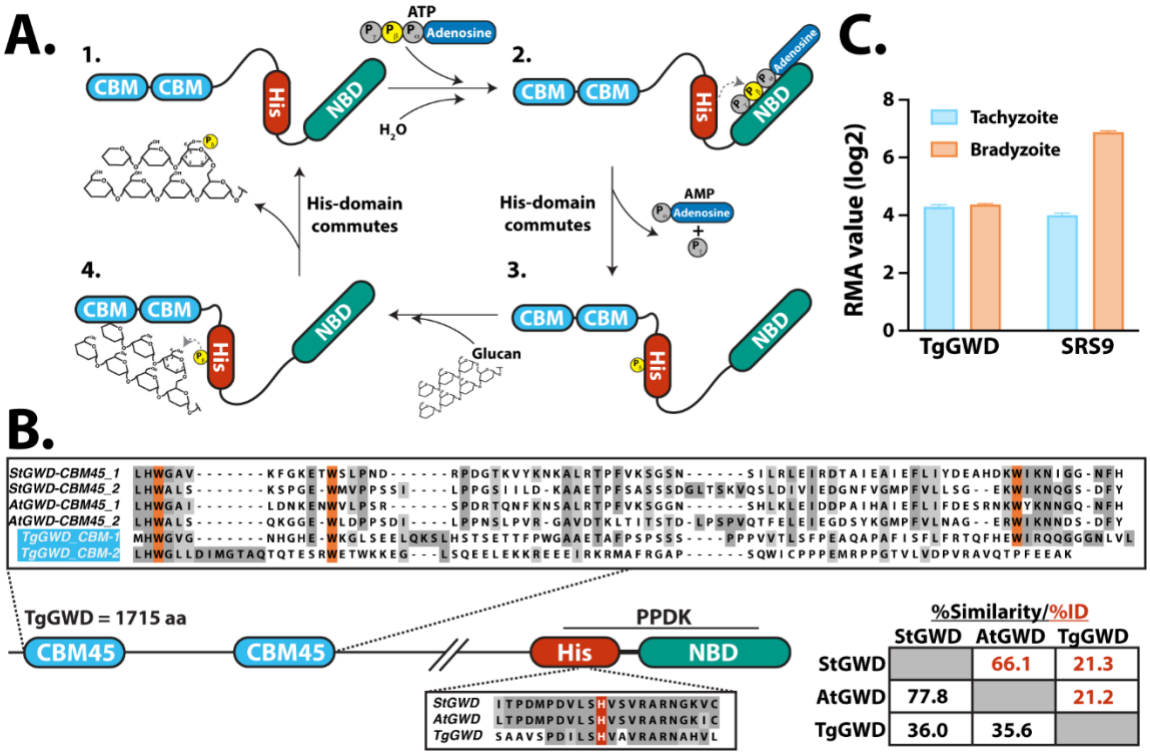


**Figure 4.1 TgGWD bioinformatics and expression.**
**A,** Glucan, water-dikinase swivel mechanism. Steps 1-4 discussed in Section 4.1.2, figure adapted from *Mikkelsen, et al. (2005)* (327). **B,** Alignment of TgGWD N-terminus and His-domain with AtGWD and StGWD. Orange residues are conserved tryptophans found in CBM45s. % Similarity and % ID presented for full-length proteins. **C**, Comparative levels of TgGWD mRNA in tachyzoites and bradyzoites alongside levels of the bradyzoite marker, SRS9 for comparison. Transcriptomic data was plotted from ToxoDB.org derived that is based on data from Fritz, *et al* (332). *Abbreviations:* CBM = carbohydrate binding module; His = phosphohistidine domain; NBD = nucleotide binding domain; PPDK = phosphoenolpyruvate dikinase.

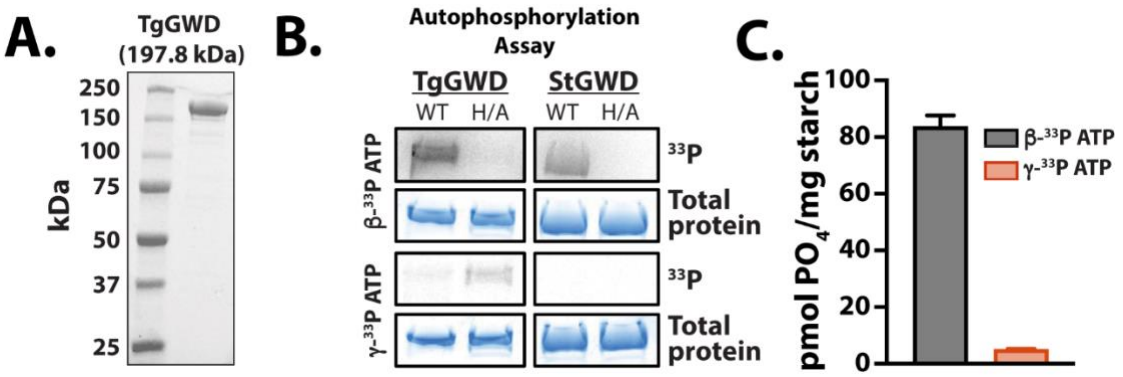


**Figure 4.2 TgGWD employs a standard dikinase mechanism.**
**A,** TgGWD was expressed in Sf9 insect cells and purified by IMAC/SEC. Purity was evaluated using Coomassie. **B,** Autophosphorylation assay with both WT TgGWD and H1241A (H/A) mutant with StGWD used as a control. All four proteins were incubated with both $\beta^{33}$P-ATP and $\gamma^{33}$P-ATP and then separated by SDS-PAGE. Autophosphorylated protein is presented above total protein loaded as determined by Coomassie staining. **C,** Total radio-labeled phosphate transferred to starch after 4 h from either the $\beta$ or $\gamma$-phosphate in ATP.

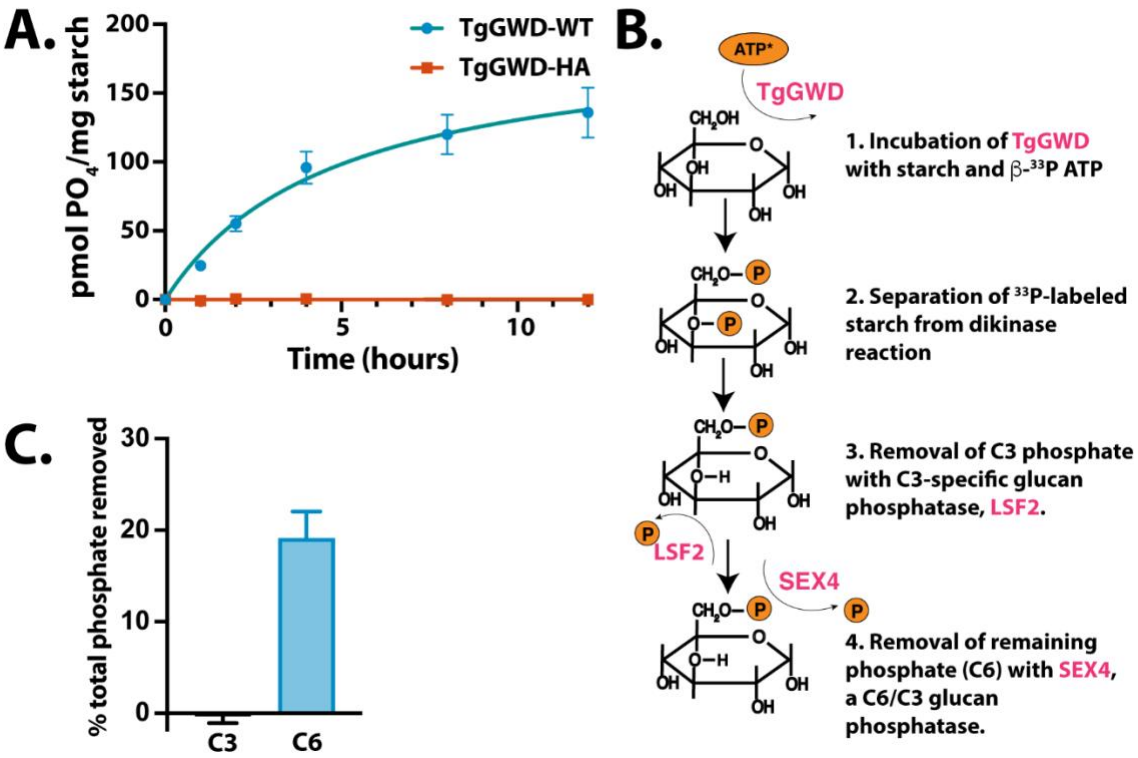


**Figure 4.3 TgGWD phosphorylates glucose at the C6 position in a time dependent manner.**

**A,** Time course assay monitoring β-$^{33}$P incorporation by TgGWD-WT and -H/A into starch. **B,** Schematic of glucan dikinase site specificity assay as described in section 4.2.2. **C**, C3-bound phosphate was determined by treatment of TgGWD-labeled starch by LSF2 (C3-specific phosphatase), and C6-bound phosphate was determined with follow-up treatment of TgGWD/LSF2-treated starch with SEX4 (C6/C3 specific).

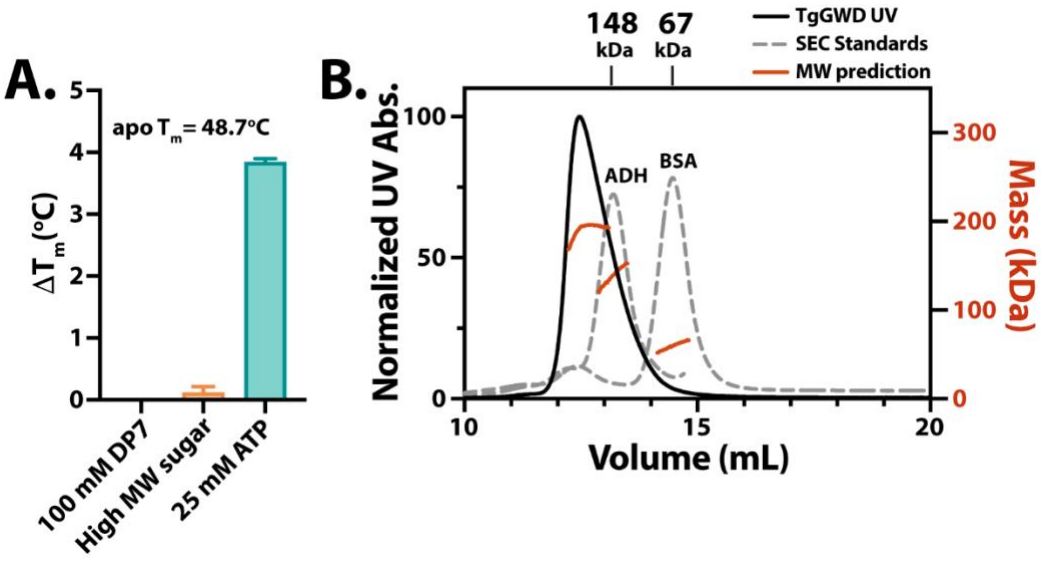


**Figure 4.4 Biophysical properties of TgGWD.**
**A,** DSF analysis of TgGWD stabilization in the presence of DP7 (maltoheptaose; 7 linear glucosyl units), a mixture of high-MW sugars, and ATP. **B,** SEC-MALS analysis of TgGWD compared elution profiles and predictions for ADH and BSA. TgGWD was predicted to have a MW of 191.4 ± .5 kDa.

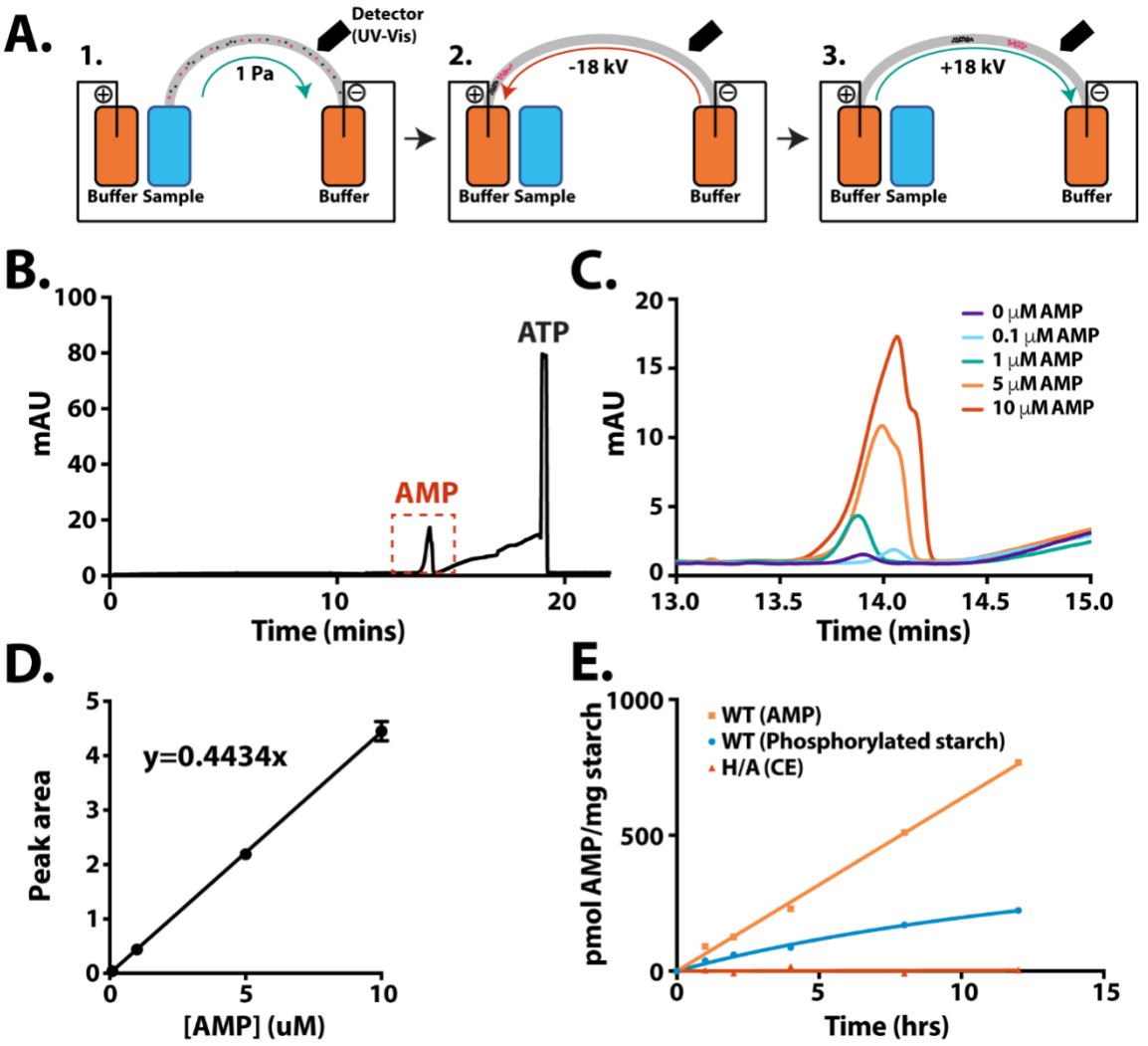


**Figure 4.5 Development of a CE-based assay for monitoring dikinase activity.**

**A,** Schematic of whole capillary stacking utilized for AMP detection, adapted from *Brown, et al. (1998)* (267). Steps 1-3 are explained in section 4.2.4. **B,** Retention times of AMP and ATP after whole capillary stacking, monitored using absorbance at 256 nm. **C,** Representative curves of AMP at various concentrations. **D,** AMP standard curve generated from (C). **E,** AMP release from TgGWD over the course of 12 hours as determined by CE, compared with phosphate incorporation into starch by radio-labeled ATP assay.

# CHAPTER 5. LOSS OF THE GLUCAN PHOSPHATASE, TGLAFORIN, IN *T. GONDII* REVEALS A ROLE FOR AMYLOPECTIN GRANULES ACROSS THE ASEXUAL LIFE CYCLE

## 5.1 Introduction

*Toxoplasma gondii* as an opportunistic protozoan parasite of humans, and all warm-blooded animals, that infects one-third of humans worldwide (336). Humans are primarily infected through the consumption of an encysted form of the parasite: either the oocysts shed in cat feces or tissue cysts found in undercooked meat from a chronically infected animal (85). The acute phase of infection then begins when encysted parasites convert into tachyzoites that rapidly divide and disseminate throughout the body of the host (278). The chronic infection begins under host immune pressure resulting in the conversion of tachyzoites into slow-growing bradyzoites that populate tissue cysts and are found predominantly in the CNS and muscle tissue (97). Tissue cysts are believed to persist for the lifetime of the host and facilitate transmission via carnivory or reactivation into tachyzoites within their current host. In the context of immunosuppression, reactivation can result in the life-threatening conditions posed by systemic toxoplasmosis with toxoplasmic encephalitis being the primary condition (114). Current therapeutic options are poorly tolerated with prolonged use and only effective against tachyzoites (120,123). Thus, there is a need for the development of new anti-*Toxoplasma* treatments that can clear tissue cysts or prevent their reactivation.

The current lack of insights into bradyzoite physiology *in vivo*, however, precludes the basic understanding needed for the development of drugs that can clear them (96). This is highlighted by the fact that until recently, this form of the parasite was viewed as being entirely dormant and largely devoid of metabolic activity. Moreover, tissue cysts have been treated as homogenous entities with little consideration for the heterogeneity of the bradyzoites within them (101). Contrary to these prevailing notions, we demonstrated that individual bradyzoites can indeed replicate within a tissue cyst (55), and that bradyzoites are diverse regarding their physiological status as viewed through the lens of mitochondrial activity, replication status, and amylopectin granule (AG) accumulation (337). Such heterogeneity has been speculated to provide bradyzoites the plasticity needed to navigate the cell-cycle mediated decisions underpinning their choices to persist as bradyzoites, reactivate into tachyzoites, or convert into sexual cycle merozoite forms in felids (54).

At the core of all bradyzoite developmental choices, and thus their ability to remain plastic, must be stored energy and biosynthetic building blocks needed to execute such transitions. Although their function has not been confirmed, an understanding of the roles of polysaccharides elsewhere (144) has resulted in the assumption that amylopectin granules (AG) are such a source of energy and biosynthetic potential needed for persistence, replication, reactivation, and

transmission. However, these assumptions remain to be tested, and thus much like bradyzoites themselves, AGs are poorly understood. What is known, however, is that AGs are large glucans found in the cytoplasm of bradyzoites that have classically served as a morphological feature distinguishing them from tachyzoites (196,338). Early studies characterized AGs as pure amylopectin (40), so AGs are much like plant starch in that they are insoluble storage polysaccharides composed of branched chains of glucose. Unlike plant starch, however, AGs contain no detectable amylose (unbranched chains of glucose) (40,197). More recently, it has been demonstrated that tachyzoites also contain a small, punctate glucan in their cytoplasm only visible by periodic-acid Schiff (PAS) staining (228,234), and its presence is dependent TgStarchSynthase (TgSS) (203). Like animal glycogen, this tachyzoite storage polysaccharide is rapidly turned over (228), as has been observed in other protozoa (209,312,313), and has been previously demonstrated to provide glucose for glycolysis (203). These recent discoveries highlight how little has historically been understood about glucan metabolism in *T. gondii*.

Glucose release from starch in plants utilizes a suite of degradation enzymes including amylases, debranching enzymes, and a phosphorylase that collectively release glucose in multiple forms: glucose monomers, linear and branched oligosaccharides, and glucose phosphates (339). In other systems containing insoluble glucans such as plants, access of starch degrading enzymes is dependent on solubilization of the starch surface by a cycle of direct, reversible glucan phosphorylation (340,341) (**Table 1.1** and **Figure 1.4**). The cycle begins with the addition of phosphate directly to glucose by the glucan, water-dikinase (GWD) and phospho-glucan, water dikinase (PWD) that results in the unwinding of glucose chains within starch, solubilizing the surface (167,168). Glucose-releasing enzymes (amylases) then degrade starch until the added phosphate becomes a steric hindrance, at which point a glucan phosphatase is needed to remove the phosphate and reset the cycle (169,170,172,173). *T. gondii* encodes all the activities needed for glucan degradation and reversible glucan phosphorylation (212) including the glucan phosphatase, TgLaforin, and *T. gondii* GWD (TgGWD).

Glucan access through reversible phosphorylation is critical in plants and animals. In *Arabidopsis thaliana*, loss of a glucan phosphatase, starch-excess 4 (SEX4), results in excess starch accumulation and aberrant starch morphology (174,239). Additionally, loss of the glucan phosphatase in humans (laforin) results in hyperphosphorylated glycogen that precipitates in neurons and causes a fatal, neurodegenerative childhood dementia and epilepsy (184,187,283,342). In *T. gondii* perturbations of several genes related to glucan metabolism also resulted in aberrant glucan accumulation ($Ca^{2+}$ dependent protein kinase 2 [CDPK2], glycogen phosphorylase [TgGP], and $\alpha$-amylase [$\alpha$-AMY]), a rewiring of central carbon metabolism (CDPK2 and starch synthase [TgSS]), and decreased cyst formation in mice (CDPK2, TgGP, $\alpha$-AMY, and amylo-$\alpha$-1,6-glucosidase [debranching enzyme; Aa16GL]), highlighting the central metabolic role glucan

metabolism might play in *T. gondii* (highlighted in section 1.6.3) (203,206,228,234,311).

CDPK2 was shown to have several targets related to glucan metabolism (228). Importantly, TgGWD was suggested as a potential CDPK2 target, indirectly suggesting a role for reversible phosphorylation in the parasite's glucan metabolism. More recently, it has been extensively demonstrated that glucose plays critical, diverse roles in *T. gondii* metabolism through its incorporation into central carbon reactions, amino acids, and RNA (210,211,226). Taken together with the findings that loss of the tachyzoite glucan has profound effects in the parasite, an understanding of how AGs are accessed in *T. gondii* is needed.

In this study, we build on our understanding of reversible glucan phosphorylation and its relevance to parasite metabolism in *T. gondii*. We have recently demonstrated that the glucan phosphatase in *T. gondii*, TgLaforin, is an active, unique, and druggable glucan phosphatase *in vitro* (Chapter 3) (204,205). Here, we investigated TgLaforin's role throughout the asexual stages by knocking out TgLaforin in Type II ME49 parasites. In tachyzoites, we demonstrate that dysregulation of glucan breakdown via TgLaforin knockout results in a profound impact on central carbon metabolism that renders the parasites completely dependent on glutamine. This defect most likely results in their highly attenuated virulence and cyst forming ability in CBA/J mice. Moreover, loss of TgLaforin resulted in bradyzoites, both *in vitro* and *in vivo*, with altered AG morphology, packing density in tissue cysts, and tissue cyst diameter. These findings build upon previous studies that are increasingly demonstrating a central role for glucan metabolism throughout the parasite's asexual life cycle.

## 5.2 Results

### 5.2.1 Background and generation of the *T. gondii* parental strain used in this study

Considerable effort has been made to characterize the molecular and epidemiological structure of *T. gondii* around the globe. Early studies using PCR/RFLP analysis characterized strains primarily obtained from North America and Europe into three clonal lineages/haplotypes: Type I, II, and III (343). Several years prior to this study, parasites in the Type I lineage were recognized as being the most virulent in mice with an $LD_{100}$=1 tachyzoite (IP injection) (344), but Type I parasites are unable to efficiently form tissue cysts in mice. Type II and III parasites are also much less virulent in mice, but are much more prevalent in humans in the Western Hemisphere. Importantly, Type II parasites are more often associated with cyst formation and reactivation in the context of HIV-AIDS (3). While it remains true that these three lineages dominate North America and Europe, more recent studies analyzing much a wider geographical sampling have defined at least 16 haplotypes of *T. gondii* organized into 6 different clades using

a mixture of low-resolution molecular techniques and whole-genome-sequencing (345,346). These haplogroups represent a spectrum of virulence characteristics that range from avirulent to those predominantly from South America that can cause symptomatic disease in immune competent individuals.

In the present study, we sought to select a strain of *T. gondii* that was relevant to human infection and that would allow for studies across the asexual phase of infection. We chose to use the ME49 strain from the Type II haplogroup, first isolated from sheep muscle in the 1960s (347,348). This strain, obtained from the HIV-AIDS resource center, is also used as a reference strain for genome annotation. Importantly for this study, ME49 parasites are only mildly virulent (although anecdotal evidence indicates selection for increased virulence with serial passage in tissue culture), and readily form tissue cysts in mice (349). ME49 parasites are extensively characterized with genomic, proteomic, and transcriptomic data readily available on ToxoDB.org.

We modified the wildtype ME49 line to eliminate the hypoxanthine-xanthine-guanine phosphoribosyltransferase (HXGPRT) gene as has been done in a commonly used and widely available Type I line of parasites (RHΔku80Δ**HXGPRT**). The HXGPRT gene provides a powerful tool for positive and negative selection through its participation in the purine salvage pathway in *T. gondii* (350), and we desired such a tool for downstream genetic manipulations, including the selection of complementation lines for gene knock-outs using DHFR as the selection. The mechanism underlying this tool stems from *T. gondii*'s purine auxotrophy that renders the parasite reliant on purine interconversion using its purine salvage pathway (351). HXGPRT plays an critical role in purine interconversions (detailed in **Figure 5.1a**), and its enzymatic activity can be taken advantage of using subversive purine analogues such as 6-thioxanthine (6-TX) (350). HXGPRT converts 6-TX to the IMP dehydrogenase (IMPDH) inhibitor, 6-thioXMP, which results in a guanine nucleotide deficiency (**Figure 5.1a, bottom**) (352). Because loss of HXGPRT can be circumvented by other enzymes in the salvage pathway, ΔHXGPRT parasites can be selected for using 6-TX with no growth penalty imposed on the mutant parasites (6,353). Restoration of HXGPRT can be selected for using mycophenolic acid (MPA) with Xanthine supplementation. MPA is also an inhibitor of IMPDH (an enzyme also critical in circumventing loss of HXGPRT), which when supplemented with xanthine provides HXGPRT+ parasites the substrate needed for XMP synthesis (an HXGPRT activity) in the absence of functioning IMPDH (**Figure 5.1a, top**) (350). Deletion of HXPGRT thus allows for genetic manipulations linked to its restoration, including gene complementation and epitope tagging (354).

To knockout HXGPRT using a CrispR-CAS9 based strategy, three synthetic guide RNAs (sgRNA) were selected from a previous study to target three separate exons and transfected alongside CAS9 to introduce double stranded breaks throughout the gene (**Figure 5.1b**) (10). As has been shown previously in *T. gondii*, this is an efficient way to allow nonhomologous end-joining (NHEJ) machinery to

create insertions or deletions that ultimately disrupt the gene in the parasite (268). As loss of HXGPRT provides its own drug selectable marker, only the CRISPR/Cas9 system utilizing the three sgRNAs was transfected in the absence of any additional drug resistance genes. ΔHXGPRT parasites were selected with 6-TX, and disruption of the HXGPRT gene was confirmed using sequencing (**Figure 5.1c**). In the clonal line of ΔHXGPRT parasites that were selected, NHEJ joined the double strand breaks introduced in exon 2 and exon 5 resulting in a 1214 nucleotide deletion in the HXGPRT gene and a fusion of these two exons. Moreover, exon fusion resulted in a downstream frameshift that introduced a stop codon in exon 5 (**Figure 5.1c**). For the remainder of this study, ME49ΔHXGPRT parasites are used as the parental line and will be designated as wild type "WT."

### 5.2.2 *T. gondii* tachyzoites contain, punctate, cytoplasmic glucan granules

Previous studies have presented biochemical evidence for rapid glucan turnover in *T. gondii* Type I RH tachyzoites (228). Moreover, small PAS+ granules have also been noted in the cytoplasm of tachyzoites as well (203,228). Under acid-stress conditions, these tachyzoite glucans have been biochemically characterized as pure amylopectin, and resemble AGs seen in bradyzoites (197). To further characterize the nature of this glucan found tachyzoites, we utilized multiple methods to visualize them under normal media conditions (**Figure 5.2a, top**). Type II ME49 tachyzoites contain small punctate glucan granules distributed throughout the cytoplasm with 5-10 granules being noted per parasite. To determine if these PAS+ granules were more glycogen- or starch-like in unstressed tachyzoites, they were next stained with IV58B6, an anti-glycogen IgM monoclonal antibody that has previously been demonstrated to be specific to glycogen (355,356) and is has been shown to recognize glycogen branch-points (357). Moreover, IV58B6 does not detect other glucans such as amylopectin or amylose (the primary constituents of plant starch) (358). Tachyzoites stained with a similar pattern to PAS-stained parasites, containing 5-10 small punctate granules distributed throughout the cytoplasm (**Figure 5.2a, top**), suggesting that the glucan found in tachyzoites is more glycogen-like than starch like. Finally, as is well-known, *T. gondii* tachyzoites contain almost no visible glucan within their cytoplasm by TEM (**Figure 5.2a, top**), suggesting that the glucan detected by both PAS staining and IV58B6 is either soluble or too small to be resolved by TEM, another suggestion that this glucan may be like glycogen (the distinguishing properties of starch and glycogen are presented in section 1.5.1 and **Figure 1.3**).

Bradyzoites have been extensively characterized as containing a starch-like glucan known as amylopectin granules (AGs) (40,135,196,197). Upon *in vitro* conversion to bradyzoites, much of the cytoplasm becomes PAS+, precluding the ability to count individual AGs (**Figure 5.2a, bottom**). Interestingly, IV58B6 staining intensity appeared to correlate negatively with *Dolichos lectin* (DBA) staining intensity that defines the cyst wall, suggesting that IV58B6 does not stain

the PAS+ glucan in mature bradyzoites, further reinforcing that structurally distinct polysaccharides exist in tachyzoites and bradyzoites (**Figure 5.2a, bottom**). Finally, AGs are easily identified as electron-lucent structures throughout the bradyzoite cytoplasm by TEM. Notably, these structures do not appear to stain with IV58B6.

To verify the specificity of PAS and IV58B6 for glucose polymers, tachyzoites and bradyzoites were treated with acid-α-amyloglucosidase (GAA) before staining. GAA cleaves both α-1,4- and α-1,6-glycosidic bonds and can therefore completely digest any glucan. Indeed, GAA treatment resulted in the disappearance of both stains (**Figure 5.2b**), demonstrating their specificity for glucose polymers.

### 5.2.3 TgLaforin colocalizes with the tachyzoite glucan

Because *T. gondii* contains a glucan phosphatase, TgLaforin, that is more animal-like than plant-like (204,205), we epitope-tagged TgLaforin to determine if it co-localizes with the potentially glycogen/animal-like glucan in tachyzoites. TgLaforin was epitope-tagged using a CRISPR/Cas9 mediated strategy as has been done previously (269); a sgRNA was transfected into *T. gondii* Type II ME49ΔHXGPRT targeting a PAM immediately downstream of TgLaforin's stop codon, and this construct was introduced alongside a donor patch containing the 3'-end of TgLaforin fused to a 3xHA tag (**Figure 5.3a**). The HA-tagged gene was linked to the HXGPRT gene, allowing for selection of TgLaforin-HA-tagged parasites with MPA/xanthine. Successful HA-tagging was confirmed by the presence of an ~60-kDa HA-tagged protein by western-blot (**Figure 5.3b**). Immunofluorescence (IF) analysis of *T. gondii* tachyzoites indicated that TgLaforin is present in small puncta throughout the cytoplasm, similar to the distribution of the tachyzoite glucan (**Figure 5.3c**). Surprisingly, we saw TgLaforin was seemingly absent in *in vitro* bradyzoites by IF analysis.

To verify that TgLaforin levels decrease during the tachyzoite to bradyzoite transition, we converted *T. gondii* tachyzoites to bradyzoites using alkaline stress for 6 days and compared equal numbers of parasites by western blot. As seen by IF staining, TgLaforin-HA expression decreases dramatically over the course of bradyzoite differentiation (**Figure 5.4a**), even though transcriptomic data obtained from a previous study (332) indicates that transcript levels of TgLaforin do not change (**Figure 5.4b**). This indicates the possibility that post-translational regulation of TgLaforin is responsible for its decline in bradyzoites, and that the down regulation of TgLaforin may be related to the growth and appearance of crystalline AGs by TEM.

To determine if TgLaforin colocalizes with the glucan present in tachyzoites or with AGs in bradyzoites, we co-stained TgLaforin-HA-tagged tachyzoites and bradyzoites with either PAS or IV58B6 along with an anti-HA antibody. In tachyzoites, TgLaforin almost completely colocalized with both PAS (**Figure 5.3d**)

and with IV58B6 (**Figure 5.3e**), suggesting its involvement in the metabolism of the tachyzoite glucan.

### 5.2.4 Loss of TgLaforin and its impact on *T. gondii* tachyzoites and bradyzoites

To further dissect TgLaforin's role in relation to glucan metabolism in *T. gondii*, TgLaforin was knocked out using a CRISPR/Cas9-GFP approach (268). Cas9 was targeted to the first exon of TgLaforin and was transfected alongside a pyrimethamine-resistant form of DHFR (DHFR-TS*) under an NcGRA7 (*Neospora caninum GRA7* promotor) (359) with the goal of gene replacement using the DHFR marker (**Figure 5.5a**). To achieve this, the linear DFHR-TS* construct was flanked by 40nt homologous sequence to TgLaforin in Exon 1 and 3'UTR on the 5' and 3' end, respectively, using PCR (**Figure 5.5b**). Transfected parasites were allowed to recover for 24 hours post-transfection, and then GFP+ parasites expressing Cas9 were selected to enrich the pool of successful transformants (**Figure 5.5c**). In agreement with previous reports (10), TgLaforin is a non-essential gene under standard cell culture conditions, as a TgLaforin-KO clone was successfully recovered (ΔTgLaf). Integration of the DHFR construct into the TgLaforin locus was verified using inside/out PCR at the chimeric locus (**Figure 5.5d**) along with verifying the loss of TgLaforin transcription (**Figure 5.5e**).

To evaluate the effects of loss of TgLaforin on *T. gondii*, we first compared glucan levels in WT and ΔTgLaf tachyzoites using our suite of glucan detection techniques (**Figure 5.6a**). Surprisingly, the size and number of PAS+ granules were unchanged in ΔTgLaf tachyzoites relative to WT parasites. Levels of IV58B6 also remained unaltered after the loss of TgLaforin, and no aberrant glucan accumulation was observed by TEM as has been observed previously when genes related to AG or central carbon metabolism were knocked out (206,228,234,235). To determine if loss of TgLaforin resulted in bradyzoite conversion defects or aberrant AG accumulation, parasites were converted to bradyzoites *in vitro* under alkaline stress and monitored for defects related to the loss of TgLaforin (**Figure 5.6b-c**). During differentiation, the parasitophorous vacuole (PV), the replicative niche established by tachyzoites within host cells, converts into the cyst wall that surrounds bradyzoites within their host cell (100,360). In general, the cyst wall is heavily glycosylated and contains N-acetylgalactosamine (Gal-NAc) that is detectible by the lectin *Dolichos biflorus* agglutinin (DBA) (361). Using DBA intensity as a marker for the progress of differentiation, we again saw no penalty imposed by the loss of TgLaforin on cyst wall formation over the course of six days, indicating that ΔTgLaf parasites are not defective in the initial stages of bradyzoite differentiation (**Figure 5.6b**). Moreover, when we stained bradyzoites with PAS over the course of six days, we again saw no difference in accumulated AG levels (**Figure 5.6c**).

Because PAS is not specific to glucans and can stain other glucose-containing molecules such as glycosylated protein, and provides no resolution on glucan

morphology, we utilized TEM to gain higher resolution on bradyzoite differentiation. After 6 days of conversion, it was noted that a ΔTgLaf parasites contained irregular AGs that were not commonly found in WT parasites (**Figure 5.7a**). In WT parasites, the AGs were largely white in appearance and organized in ovoid or circular shapes. However, the ΔTgLaf parasites contained AGs that were often gray, with the appearance of being flattened and irregular in shape that seemed to occupy more of the cytoplasm than the WT granules occupied. To quantify this, the area of AGs was calculated relative to the parasite area in both WT and ΔTgLaf strains (**Figure 5.7b**). Strikingly, AGs occupied approximately 4x more area in KO parasites when compared to WT. Additionally, when analyzed on an 8-bit gray scale, AGs in ΔTgLaf parasites were significantly grayer than those found in WT parasites (**Figure 5.7b**).

To demonstrate aberrant AG accumulation in *in vitro* bradyzoites was specific to the loss of TgLaforin, the ΔTgLaf line was complemented with an HA-tagged TgLaforin cDNA under its native promoter containing the HXGPRT selectable drug marker (**Figure 5.8a**). The complementation construct was inserted into a locus previously identified in Chromosome VI as having no coding sequences or regulatory elements (270). Therefore, true complementation was achieved by leaving the ΔTgLaf/DHFR-TS* knockout scar intact. A complemented line was successfully identified (COMP) by PCR (**Figure 5.8b**), and TgLaforin expression was verified using Western Blot (**Figure 5.8c**), and the cytoplasmic, punctate staining was restored by IF analysis (**Figure 5.8d**). Importantly, western blot analysis demonstrated that endogenous levels of expression were restored (**Figure 5.8c**).

After examination and quantification of AGs in the COMP line, it was noted that the COMP line did accumulate a low level of aberrant AGs, but COMP parasites did not demonstrate a statistically significant difference in AG levels as was found in ΔTgLaf parasites (**Figure 5.7a-b**), suggesting complementation was successful. Moreover, complementation restored AGs that were more similar to those found in WT parasites as they were also whiter in appearance.

### 5.2.5 Loss of TgLaforin results in upregulation of glutaminolysis in tachyzoites

Despite the fact that loss of TgLaforin had no gross morphological effect on the tachyzoite glucan, the observation that its loss did indeed impact AGs in bradyzoites implies that TgLaforin does have a role in glucan metabolism in *T. gondii*. Because glucan catabolism is significantly affected by the presence of covalently bound phosphate, we speculated that loss of TgLaforin resulted in the inability of *T. gondii* bradyzoites to breakdown their AGs efficiently. To first determine if this was having any metabolic effects in tachyzoites, a more tractable stage for such studies where TgLaforin expression is higher, we employed GC/MS steady-state metabolic analysis of intracellular tachyzoites (**Figure 5.9**).

While metabolite levels remained unaltered across much of the TCA cycle, metabolites immediately downstream of glutamine were much more abundant in ΔTgLaf parasites than in their WT counterparts. Previously, it was demonstrated that *T. gondii* tachyzoites primarily utilize glucose and glutamine for synthesis of macromolecules and normal progression through the lytic cycle (226). Glucose is utilized primarily to fuel glycolysis, and glutamine undergoes glutaminolysis to fuel the TCA cycle. In the absence of glucose, *T. gondii* can upregulate both glutaminolysis and gluconeogenesis to make up for the loss of glucose (211,226), suggesting that ΔTgLaf parasites are deficient in glucose metabolism. This finding further suggests that the turnover of the tachyzoite glucan serves as a potential intermediate in overall glucose metabolism.

### 5.2.6 Loss of TgLaforin renders T. gondii tachyzoites dependent on glutamine

Without both glucose and glutamine, parasites are significantly hampered in their ability to invade and establish plaques (226). To determine if the loss of TgLaforin resulted in impaired access to glucan stores in tachyzoites, and thus a dependence on glutaminolysis, we performed plaque assays in the presence and absence of glutamine (**Figure 5.10**). In the presence of glutamine, ΔTgLaf parasites formed plaques that were slightly larger than both the WT and COMP lines. Upon removal of glutamine after the parasites had invaded the HFF monolayer, however, ΔTgLaf parasites were completely unable to form plaques, whereas the WT and COMP lines were able to form plaques with normal efficiency. Importantly, the growth of the COMP line under glutamine depleted conditions indicated that glutamine dependence was specific to the loss of TgLaforin, suggesting that loss of TgLaforin results in loss of normal glucose metabolism.

### 5.2.7 Analysis of lytic cycle

Plaque formation is the result of the cumulative effects of invasion replication and egress extended over multiple cycles. To determine how glutamine deprivation was impacting the lytic cycle in the ΔTgLaf parasites, we analyzed replication and egress (**Figure 5.11**). In each assay, parasites were pre-starved of glutamine for 48 hours before the assay. In the replication assay, replication was analyzed 24 hours after invasion (72 hours of glutamine starvation total). Among the three lines, we saw no significant difference in replication under glutamine replete or depleted conditions (**Figure 5.11a**). Thus, glutamine depletion appeared to have no overall effect on replication without TgLaforin. The fact that the glutamine starved parasites were able to establish the infection argued against a major defect in invasion, and invasion efficiency was not explored further here.

Finally, we analyzed egress efficiency among the three lines with two different small molecules (**Figure 5.11b-c**). First, we used the calcium ionophore, A23187 (**Figure 5.11b**), that results in rapid increases of cytoplasmic calcium, microneme

discharge, and subsequent egress. Secondly, we tested zaprinast (**Figure 5.11c**), a phosphodiesterase inhibitor that results in rapid increase of cGMP levels that then trigger the signaling pathway that ultimately leads to egress. Surprisingly, no induced egress defect was seen when parasites were treated with either 3 μM A23187 or 500 μM zaprinast.

We hypothesized that WT parasites were able to survive in the absence of glutamine partially due to their ability to access internal glucan stores to which the ΔTgLaf parasites may not have efficient access. To determine if glutamine starvation resulted in differential utilization of the tachyzoite glucan, parasites were starved of glutamine for 72 hours and then evaluated for glucan content using IV58B6. Interestingly, it appears that IV58B6 staining is lower in mutant parasites after glutamine starvation than their WT counterparts, but more rigorous quantification of this phenomenon will need to be performed (**Figure 5.12**). Regardless, we did see a slight decrease in IV58B6 staining in both lines with glutamine starvation, implying that the absence of glutamine might result in the utilization of AGs.

### 5.2.8 Loss of TgLaforin results in attenuated virulence and cyst formation *in vivo*

While ΔTgLaf parasites grew normally in nutrient replete media, they were unable to grow without glutamine. We therefore hypothesized that while loss of TgLaforin might not impose a penalty under the ideal conditions of cell culture, it may impose a steeper penalty under the stresses and potential nutrient scarcities encountered *in vivo*. To test the importance of TgLaforin in the acute phase of infection in mice, we infected equal numbers of male and female CBA/J mice with 100 tachyzoites IP and monitored the mice daily using previously developed a five-stage body index score (**Table 2.6**) to track the severity of symptoms associated with a tachyzoite infection over the course of 28 days (**Figure 5.13a**).

The acute phase of infection was highly attenuated by the loss of TgLaforin. Mice infected with WT parasites began demonstrating symptoms of infection 10 days after infection with tachyzoites (**Figure 5.13a**). However, mice infected with ΔTgLaf parasites did not begin to experience symptoms until 15 days after infection. Moreover, mice that became symptomatic from WT parasite infections often proceeded through all stages of symptomology, and only a minor proportion of mice that became sick were able to recover from infection (>50% of mice proceeded to stage 4 (moribund)). Infection from TgLAF-KO parasites, however, resulted in a majority of mice that only developed mild symptoms (Stage 2 or less) with many of these mice recovering (**Figure 5.13a**). The inability of the ΔTgLaf parasites to cause symptoms in mice was reflected in the mortality rates of the infected mice: infection with WT parasites resulted in 73% mortality rate after 28 days whereas ΔTgLaf parasites only caused 17% mortality (**Figure 5.13b**). Complementation of TgLaforin rescued this defect in virulence as COMP parasites

resulted in an earlier onset of symptomatic infection at Day 11, and the majority (53%) of mice dying after 28 days (**Figure 5.13a-b**).

Because the acute phase of infection was significantly attenuated by the loss of TgLaforin, we hypothesized that cyst numbers would be significantly lowered. To determine the number of cysts formed after 28 days of acute infection, we used a previously established protocol for harvesting and counting tissue cysts from infected mice (55,275). Briefly, brain homogenate from infected mice was layered on a discontinuous Percoll gradient and centrifuged to separate brain material and red blood cells from cysts. Fractions were then collected from the bottom of the Percoll gradient proceeding from most dense (bottom of Percoll gradient) to least dense (top of Percoll gradient). In all cases, red blood cells (RBCs) traveled the furthest through the Percoll gradient and defined the fraction with the highest density in which cysts could be found, with brain homogenate on the top defining the fraction of least density. Cysts were thus harvested from the fractions between the RBCs and brain homogenate.

Indeed, after isolating tissue cysts and counting them, it was determined that mice infected with ΔTgLaf parasites contained significantly fewer tissue cysts than those infected with WT (**Figure 5.13c**). Most likely, the lower cyst number in the ΔTgLaf parasites was a result of failure to establish WT levels of virulence during the acute phase of infection, and not in actual bradyzoite conversion, as *in vitro* conversion assays demonstrated no defect in cyst formation (**Figure 5.6b**). Due to the low survival rate of the mice infected with the COMP parasites, only two data points could be generated for this parasite line as each data point is the average of cyst-counts from 2 mouse brains. Therefore, this low statistical power precluded statistical analysis. However, the two data points that were obtained for the COMP line almost identically represented the range of cyst burden detected in WT-infected mice. One of the data points was far outside of the range that the ΔTgLaf parasites were able to generate. Therefore, it appears that complementation of TgLaforin at least partially restored the defect in cyst formation.

### 5.2.9 ΔTgLaf tissue cysts can re-establish infections in naïve mice

To determine if the physiological defects we observed of *in vitro* cysts translated into a lower level of infectivity, brain homogenate containing 20 cysts from each line of parasites was injected IP into CBA/J mice, and symptomology and death were once again monitored for 28 days. The symptoms related to infection resulting from cysts was much milder than that from tachyzoites (**Figure 5.14a**), and this held true across all three lines of parasites. Moreover, the death rate related to cyst infection was much lower than seen in tachyzoites across all three lines. After 28 days, cyst burdens were established from each line. Interestingly, the death/illness rate was slightly higher in the WT and COMP lines. Again, ΔTgLaf parasites were much less competent at forming cysts *in vivo*. However, the COMP line was unable to rescue this defect in cyst formation (**Figure**

**5.14b**), suggesting that physiological and metabolic changes associated with the loss of TgLaforin manifest differently based in the life cycle stage impacting their capacity to be complemented.

### 5.2.10 Proper AG formation relies on the presence of TgLaforin

To understand if a loss in cyst infectivity was related to the formation of aberrant AGs in ΔTgLaf bradyzoites as seen after 6 days of *in vitro* conversion, we devised an efficient way to utilize TEM to investigate AG morphology in purified *in vivo derived tissue cysts*. Our protocol was developed based on a previously developed method for imaging rare cell populations that we coupled with our previously developed cyst harvesting protocol (276,277). After isolating tissue cysts from CBA/J mice as described above, Percoll was washed out and cysts were fixed and then suspended in low-melt agarose before gelling, post-staining, and embedding in Epon (see Materials and Methods). TEM imaging revealed that while WT parasites formed largely normal/canonical AGs *in vivo* as seen *in vitro* [**Figure 5.15** (compare with **Figure 5.7a**)], ΔTgLaf parasites contained almost exclusively aberrant AGs that mirrored the same morphological defects seen *in vitro* (**Figure 5.15** and **Figure 5.16**). Namely, AGs were irregularly sharpened with a flat, multi-lobed appearance. Importantly, COMP parasites did not over-accumulate or form aberrant AGs, demonstrating that this defect is specific to loss of TgLaforin.

In addition to containing aberrant AGs, the internal morphology of ΔTgLaf parasites appeared to be altered by the presence of the AGs. Significant organelle displacement was noted. Moreover, many of the ΔTgLaf parasites appeared hollow or “ghost-like” in appearance as a result of their unstained cytoplasm. We interpreted this to mean that a significant number of the ΔTgLaf bradyzoites were dead within the cyst (additional images of ghost-like parasites depicted in **Figure 5.16b**).

Because ΔTgLaf contained high levels of AGs, we hypothesized that this would result in an altered density of mutant cysts in Percoll gradients relative to the WT . To determine if the ΔTgLaf cysts exhibited a different density profile, we analyzed the distribution of cysts across Percoll fractions. To account for potential differences in gradients preparations across experiments, we standardized the distribution based on the location of the RBC layer the Percoll prep (fraction 0; highest density-typically corresponding to fraction 8-10 in individual gradients) proceeding up to the brain homogenate layer (fraction 12; lowest density). Surprisingly, we noted that the overall distribution of cysts remained relatively constant among the 3 lines. This indicated that despite the increase in AGs in the ΔTgLaf bradyzoites, their ability to travel through Percoll remained unchanged (**Figure 5.17a**).

To understand how other factors might contribute to this outcome, we analyzed the packing density of bradyzoites in each line. This previously defined metric establishes a relationship between the number of bradyzoites within a cyst and the

overall volume of the cyst. This is achieved through counting the number of bradyzoite nuclei within an optical section of a cyst using BradyCount 1.0 (55) and dividing that number by the volume of the optical section. When we analyzed the packing density of each line of parasites, we noted that ΔTgLaf parasites had significantly lower packing density than that of the WT or COMP parasites (**Figure 5.17b)**, indicating that loss of TgLaforin indeed resulted in significant parasite death. Moreover, when analyzing cyst diameter, we also saw a significant decrease in overall cyst size (**Figure 5.17c**). We interpreted these data as indicating that although ΔTgLaf bradyzoites contain many more AGs than either WT or COMP bradyzoites, their overall lower packing density and cyst size counterbalance their potential increase in overall density. Therefore, their overall distribution through the Percoll gradients remained unchanged.

## 5.3 Discussion

We investigated the role of TgLaforin, and by extension polysaccharide storage, throughout the asexual cycle in *T. gondii*. Through comparative microscopy, we first characterized a potentially glycogen-like glucan in the cytoplasm of ME49 tachyzoites. To determine the role of reversible phosphorylation on this glucan, we knocked out the parasite's glucan phosphatase, TgLaforin. We showed that tachyzoites become dependent on glutamine in the absence of TgLaforin, and this nutrient defect appeared to result in highly attenuated parasite virulence *in vivo* and defective cyst formation as measured by multiple metrics. Moreover, while perturbation of TgLaforin did not result in any obvious defects related to the tachyzoite glucan, it did result in bradyzoites containing AGs with significant morphological defects.

Therefore, our studies demonstrate a fundamental role for reversible glucan phosphorylation in *T. gondii*. As predicted, loss of proper AG turnover in bradyzoites resulted in aberrant AG morphology, as seen previously in other protozoa, plants, and vertebrates. These defects appeared to result in smaller cysts with a lower packing density—upending the trend previously reported in ME49-WT bradyzoites that smaller cysts typically demonstrate higher packing density (55). Most interestingly, however, these studies add to the growing literature pointing to the importance of glucan metabolism in tachyzoites. This study suggests that tachyzoites utilize glucans for glucose allocation as suggested in a study examining the role of the *T. gondii* starch synthase (TgSS) (203), as loss of glucan access via TgLaforin results in complete glutamine dependence. As *T. gondii* tachyzoites primarily utilize exogenous glucose and glutamine to support their rapid growth, this dependence on glutamine implies upregulation of glutaminolysis to fuel gluconeogenesis, highlighting the possibility that loss of TgLaforin resulted in deficient glucan degradation and glucose allocation in tachyzoites.

These results are consistent with previous studies that disrupt glucose and/or glucan metabolism, but also contrast them in significant ways (**Figure 1.7**). Disruption of TgGT1, the only plasma-membrane glucose transporter in *T. gondii* (225,226), or TgHK, *T. gondii*-hexokinase, resulted in upregulation of glutaminolysis and gluconeogenesis, and thus parasite growth was highly attenuated with glutamine depletion (211). However, neither of these mutants became *entirely* dependent on glutamine as in the present study. Most strikingly, ΔTgSS parasites displayed no dependence on glutamine and, in fact, grew faster than WT parasites when both glucose and glutamine were removed from the culture media (203). Perturbations of other glycolytic enzymes also demonstrated varied effects related to the presence of glutamine: loss of the essential GAPDH1 could be rescued with high levels of glutamine (362), but glutamine could not rescue pyruvate kinase (TgPYK1) knockdown parasites (235). Therefore, while many other studies have demonstrated that perturbations in glucan metabolism result in an increased importance of glutamine through gluconeogenic flux, only loss of TgLaforin and GAPDH1 demonstrate a complete dependence of tachyzoites on glutamine to our knowledge at the time of writing this manuscript.

Regardless, loss of TgLaforin renders the parasites much more sensitive to the nutrient composition of their environment. This was most clearly seen in their attenuated virulence and cyst burden in mice. Like other studies of glucan perturbations, the number of cysts formed by ΔTgLaf parasites was much lower than its WT counterparts (206,228,234,311). The cysts that were formed also appeared to be highly defective. Interestingly, there was a large increase in the number of parasites containing high levels of aberrant AGs in when comparing ΔTgLaf bradyzoites converted *in vitro* (6 days) vs *in vivo* (>6 days). This suggests that either the *in vitro* conversion conditions are not adequate to produce this phenotype, or that the accumulation of these aberrant AGs is time dependent. If true, one could assume that an increase in the duration of the chronic infection for these mutants may lower the infectivity of their cysts, a possibility that is supported by a large number of parasites that appeared to no longer be viable by TEM. Our *in vivo* work highlights that targeting the parasites on the level of reversible phosphorylation, especially in the context of its interaction with CDPK2, may inhibit the parasite's ability to reactivate. This process utilizes several plant-like enzymes that represent ideal drug targets in humans (TgGWD and CDPK2), and we recently developed an inhibitor to TgLaforin (Chapter 3).

The present study has many strengths that allow for the detailed dissection of *in vivo* bradyzoites. This includes the utilization of our previously developed cyst purification protocol and automated computer-based methods that allowed us to accurately count, measure, and determine packing density on all cysts in this study. Moreover, we developed a method to concentrate purified cysts into agarose blocks which allowed for the relative ease of cyst visualization by TEM that would otherwise have been much more difficult if searching through brain homogenate as is done traditionally. The limitations of this study were primarily

related to our inability to purify the tachyzoite glucan from ME49 parasites and inability to pinpoint the exact reason for arrest of parasite growth. With these data, a more precise mechanism could be described. While the exact mechanism related to the parasite's inability to grow without glutamine is unknown at present, the rescue of this defect by complementation ensures the effects we observed were indeed specific to TgLaforin. Moreover, the limitations posed here did not prevent a detailed, thorough characterization of many aspects of glucan phosphatase biology.

Therefore, future work should seek to characterize the nature of the glucan in tachyzoites with respect to chain length and phosphate content. Such a characterization would determine the overall architecture of the glucan and allow for classification as more glycogen-like or amylopectin-like, as well as reveal what is stored within. Curiously, loss of TgLaforin resulted in the selective disruption of AG morphology in bradyzoites while seemingly having no effect on tachyzoites as it did in other knockouts such as such as $\alpha$-amylase, CDPK2, and glycogen phosphorylase (in which bradyzoites also accumulated excess AGs). Understanding if/how the tachyzoite glucan is broken down in the absence of a glucan phosphatase would yield insights into the requirements of glucan degradation in *T. gondii*. Overall, this work necessitates such a characterization as it advances what is known about the role of storage polysaccharides in both tachyzoites and bradyzoites, what results from the fact that they are present and inaccessible and opens up reversible glucan phosphorylation as both a window into understanding AGs and into developing therapeutics.

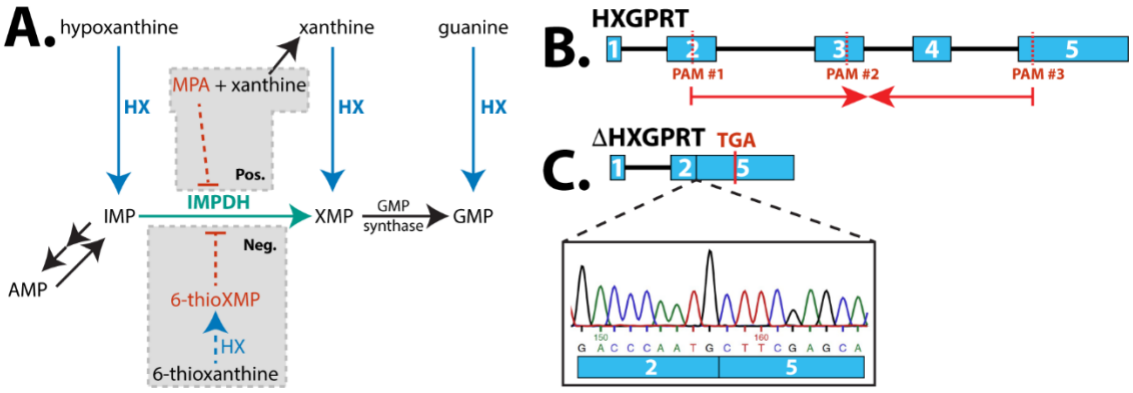


**Figure 5.1 Generation of a parental ME49 line by knocking out HXGPRT.** **A,** Purine interconversion pathways in *T. gondii* and the drugs used in HXGPRT+/- selection; adapted from (352). **B,** Schematic of HXGPRT locus and PAM sites used in this study. Numbered exons depicted as blue boxes and introns as black lines. CRISPR/Cas9 nuclease sites are 3-bp upstream of PAM sites. **C,** Depiction of modified HXGPRT locus after 1214-bp deletion resulted in the fusion of partial exons 2 and 5, creating a TGA codon in exon 5. Sequencing of the fusion site is depicted below. *Abbreviations*: 6-thioXMP = 6-thioxanthosine monophosphate; AMP = adenosine monophosphate; GMP = guanosine monophosphate; HXGPRT/HX = hypoxanthine-xanthine-guanine phosphoribosyl transferase; IMP = inosine monophosphate; IMPDH = IMP dehydrogenase; MPA = mycophenolic acid; PAM = protospacer adjacent motif; XMP = xanthine monophosphate.

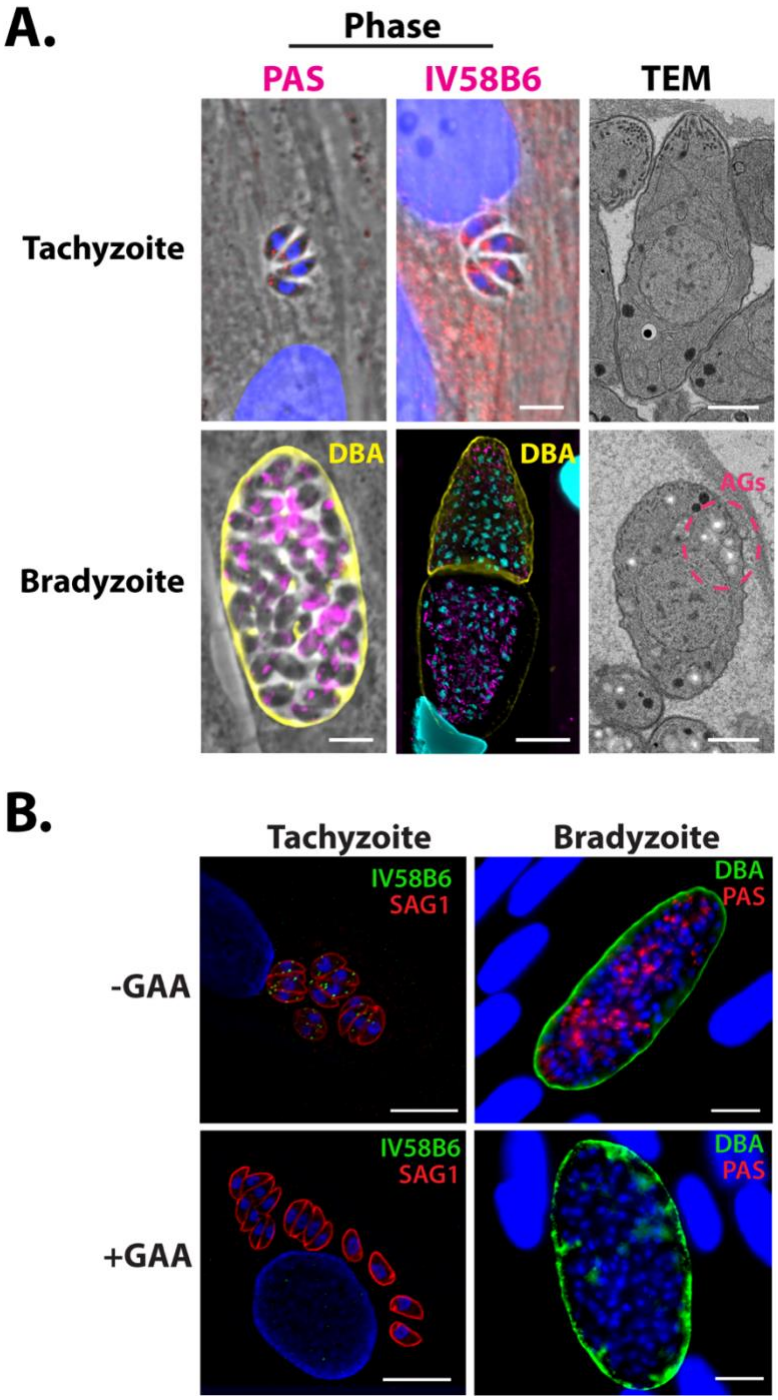


**Figure 5.2 Glucan dynamics in *T. gondii* ME49 parasites.**
**A,** Microscopy-based glucan evaluation of *T. gondii* tachyzoites and bradyzoites using PAS, IV58B6 (α-glycogen IgM mAb), and TEM. **B,** GAA digest of AGs in tachyzoites and bradyzoites results in disappearance of IV58B6 and PAS signal by IF analysis. *Abbreviations:* AG = amylopectin granule; DBA = *Dolichos* biflorus agglutinin; GAA = acid α-glucosidase; PAS = periodic acid-Schiff; TEM = transmission electron microscopy.

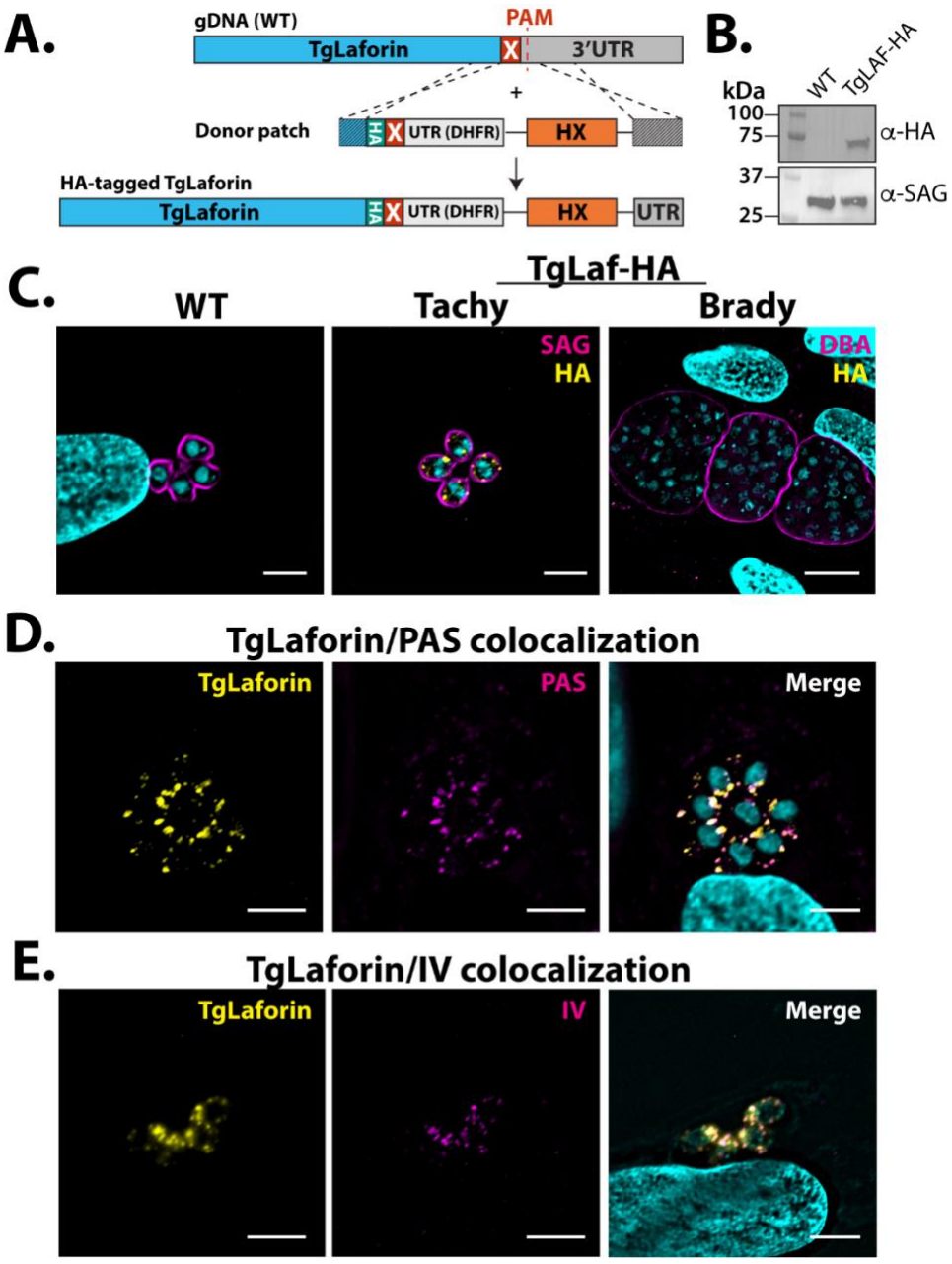


**Figure 5.3 Endogenous tagging and localization of TgLaforin.**
**A,** Schematic depicting the TgLaforin 3xHA-epitope tagging strategy. **B,** Successful tagging of TgLaforin (62 kDa) was verified using immunoblot analysis with an α-HA antibody with SAG1 used as a loading control. **C,** IF analysis in WT/tagged parasites with α-HA antibody. **D**, IF analysis of TgLaforin colocalization with PAS. Pearson's coefficient: 0.765. **E**, IF analysis of TgLaforin colocalization with IV58B6. Pearson's coefficient: 0.737. All scale bars = 5 μm. *Abbreviations*: HX = hypoxanthine-xanthine-guanine phosphoribosyl transferase; PAS = periodic acid-Schiff.

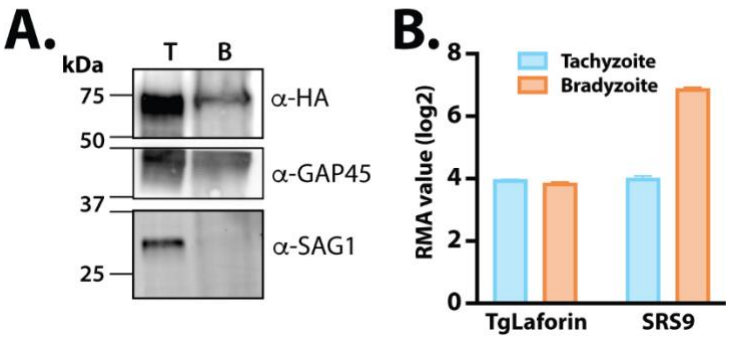


**Figure 5.4 Downregulation of TgLaforin in *T. gondii* bradyzoites.**
**A,** Western blot analysis of TgLaforin expression levels in tachyzoites and bradyzoites. GAP45 is the loading control, and loss of SAG1 serves as confirmation of tachyzoite to bradyzoite conversion. **B,** Comparative levels of TgLaforin mRNA in tachyzoites and bradyzoites alongside levels of the bradyzoite marker, SRS9 for comparison. Transcriptomic data was plotted from ToxoDB.org derived that is based on data from Fritz, *et al.* (332). In this study, *in vitro* bradyzoites were harvested at 4 days after induction.

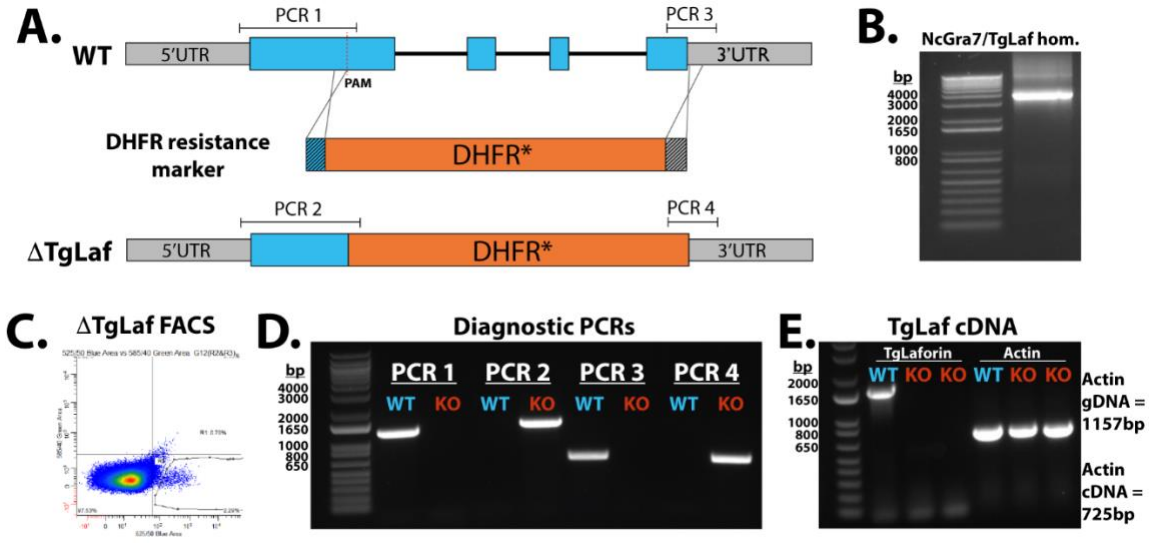


**Figure 5.5 Schematic of TgLaforin knockout strategy, and PCR confirmation of DHFR disruption of TgLaforin.**

**A,** Schematic of TgLaforin KO strategy: the pyrimethamine-resistant DHFR* gene containing 40-nt homologous arms (hashed boxes) was inserted into the TgLaforin locus by eliminating most of the gene by homologous recombination. A double stranded break was induced using CRISPR/Cas9-GFP with a PAM site in the first exon. **B,** PCR amplification of NcGra7-DHFR cassette with 40-nt homologous arms. **C,** Representative image of FACS plot used to select GFP+ parasites. Area circled indicates gating used to select GFP+ parasites that were chosen for further drug selection. **D,** Inside/out PCR verification of DHFR integration into TgLaforin locus. Amplicons (PCR1-4) illustrated in (A). **E,** Loss of TgLaforin mRNA was confirmed by generating cDNA from both WT and ΔTgLaf knockout strains. Actin cDNA amplification serves both as a loading control and as a control to verify the absence of gDNA. *Abbreviations:* DHFR = dihydrofolate reductase; FACS = fluorescence-activated cell sorting; PAM = protospacer adjacent motif.

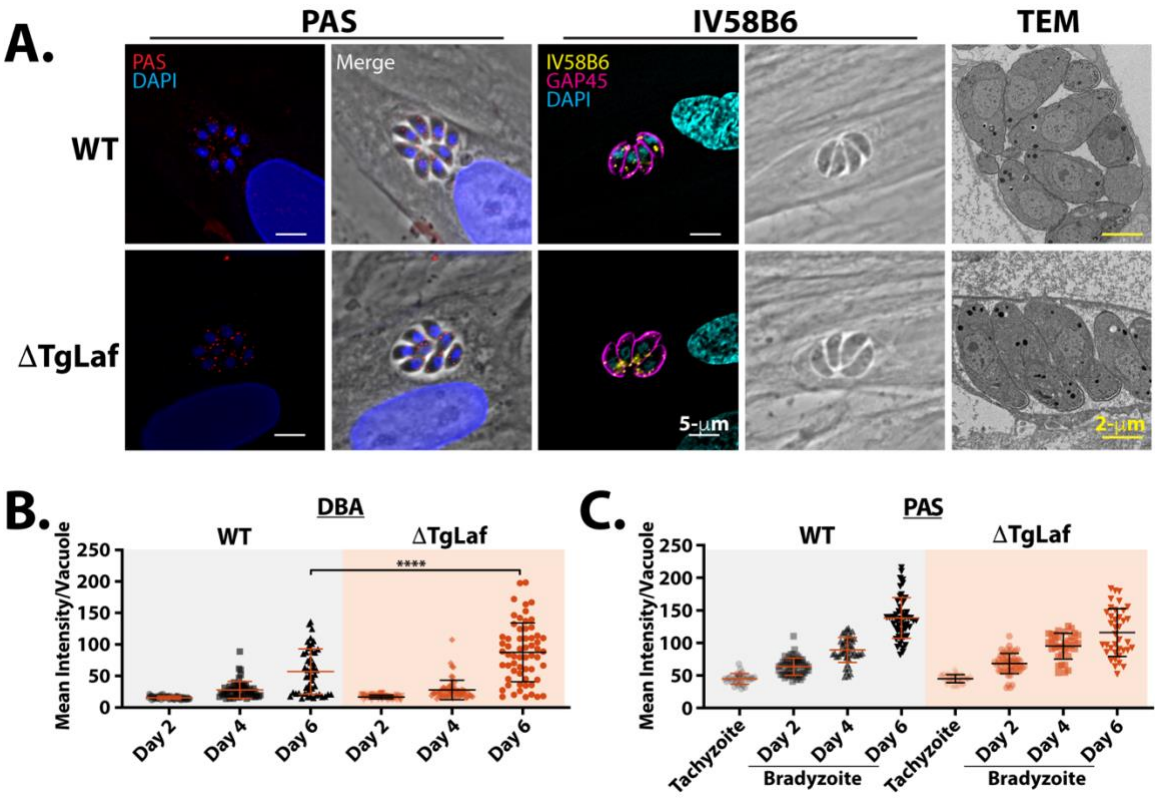


**Figure 5.6 Loss of TgLaforin selectively alters glucan morphology in bradyzoites with no AG defects in tachyzoites.**

**A,** Analysis of glucan levels in ΔTgLaf tachyzoites using three different approaches: PAS and IV58B6 immunofluorescence, and TEM. **B,** *in vitro* tachyzoite to bradyzoite conversion efficiency of ΔTgLaf vs WT parasites as measured by DBA. **C**, Change in PAS levels during bradyzoite conversion by PAS levels. *Abbreviations*: AG = amylopectin granule; DBA = *Dolichos biflorus* agglutinin; PAS = periodic acid-Schiff. Statistical comparisons were done with an ordinary one-way ANOVA using Tukey's post-hoc test to correct for multiple comparisons. Statistical significance is indicated as follows: ****p<0.0001.

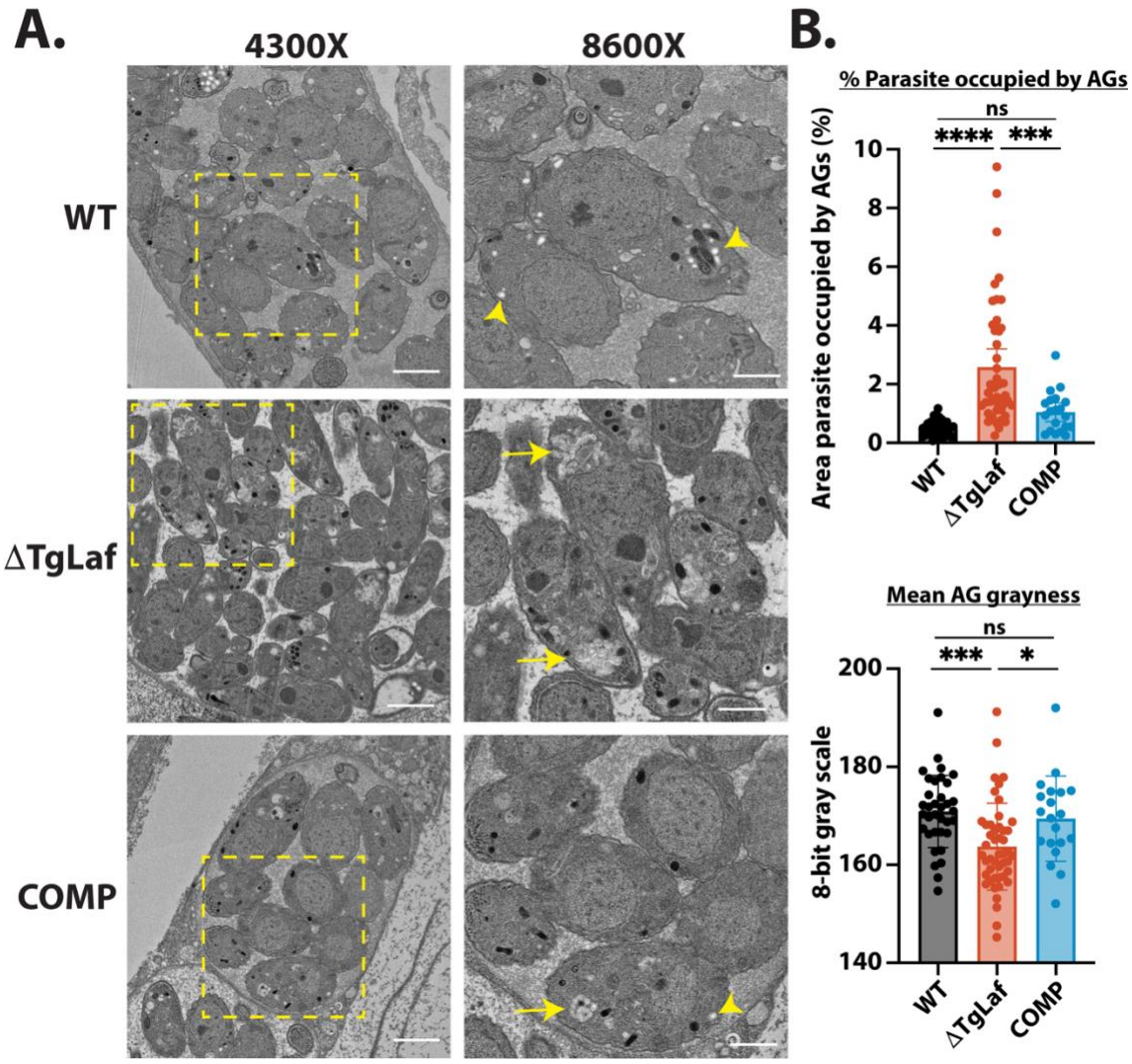


**Figure 5.7 TEM images of *in vitro* bradyzoites.**
**A,** Representative images of bradyzoites from each parasite line. At 4300x magnification, scale bar = 2 μm; at 8600x magnification, scale bar = 1μm. COMP = complemented parasites generated by complementing ΔTgLaf parasites with TgLaforin cDNA. Arrowhead = canonical AG (white, round/ovoid); Arrow = aberrant AG (grey, flattened, multi-lobed). **B,** Quantification of relative parasite AG content and grayness across lines used in this study. Statistical comparisons were done using an ordinary one-way ANOVA with Tukey's post-hoc test to correct for multiple comparisons. Statistical significance is indicated as follows: *p<0.05, ***p<0.01, ****p<0.001, ns=p>0.05.

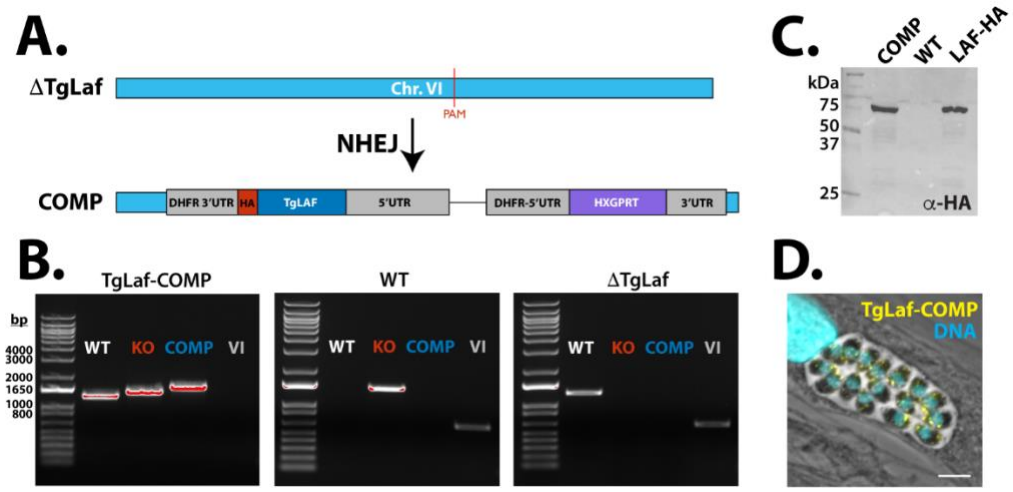


**Figure 5.8 Schematic of TgLaforin complementation strategy and confirmation of successful expression of TgLaforin.**

**A,** Schematic of TgLaforin complementation into ΔTgLaf parasites in which a PAM site was chosen at a neutral locus previously identified in Chr. VI (270) to insert TgLaforin cDNA containing its endogenous promoter. The TgLaforin construct was connected to the HXGPRT selectable drug marker and inserted using NHEJ. **B,** PCR confirmation of integration of TgLaforin construct into Chr. VI. Primer sets are indicated above amplicons. WT amplicon demonstrates restoration of TgLaforin, and KO amplicon confirms that KO locus is still intact. WT/ΔTgLaf gels serve as controls for these PCR reactions. **C,** Western blot confirmation of expression of TgLaforin in complemented parasites. Tagged LAF-HA parasites confirm the correct MW (~60 kDa) and expression level. **D,** IF analysis demonstrates restoration of cytoplasmic, punctate localization of TgLaforin. Scale bar = 5 μm. *Abbreviations:* NHEJ = non-homologous end joining; PAM = protospacer-adjacent motif.

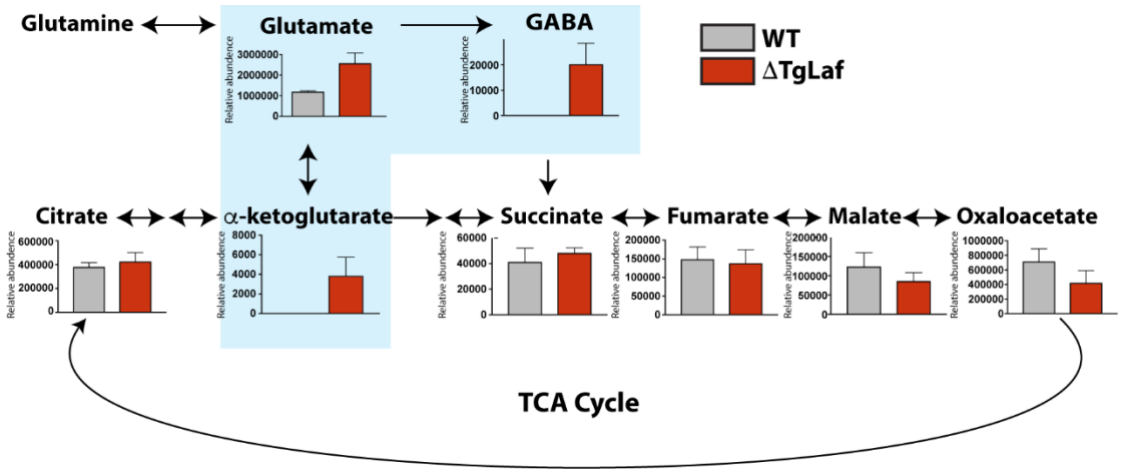


**Figure 5.9 Steady-state metabolomics reveals upregulation of glutaminolysis in ΔTgLaf parasites.**
Metabolite levels of intracellular tachyzoites were analyzed after 48 hours of growth in HFFs by GC/MS analysis.

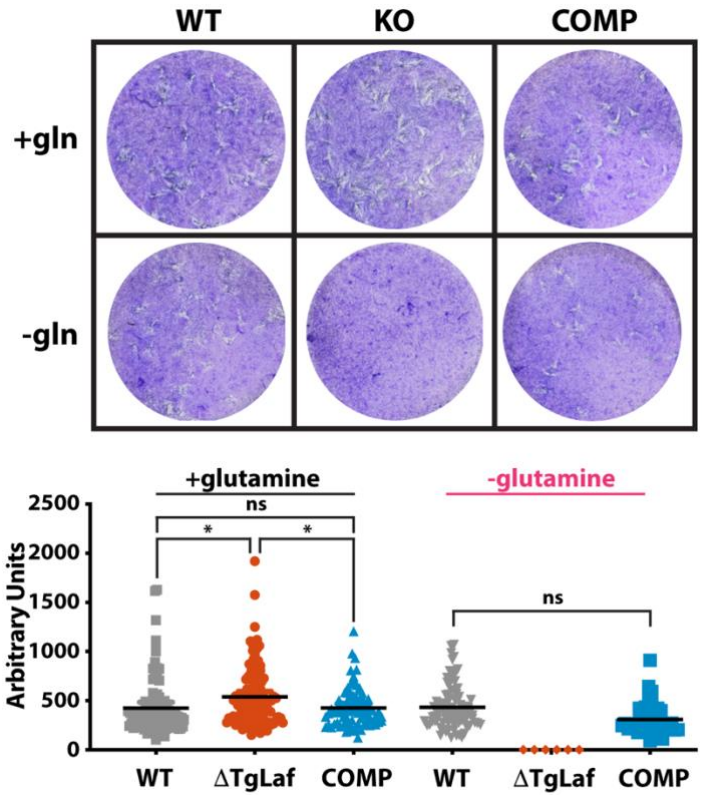


**Figure 5.10 Loss of TgLaforin renders *T. gondii* tachyzoites dependent on glutamine.**

Representative plaque assay pictures are presented for each line and condition. Total plaque area was measured in ImageJ and plotted in arbitrary units. Statistical comparisons were done using an ordinary one-way ANOVA using Tukey's post-hoc test to correct for multiple comparisons. Statistical significance is indicated as follows: *p<0.05, ns=p>0.05.

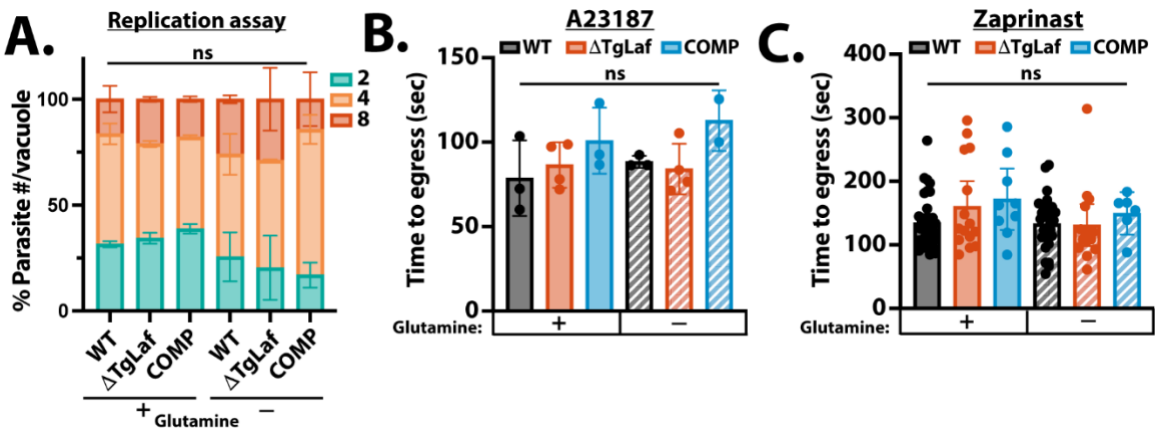


**Figure 5.11 The effects of glutamine deprivation on the tachyzoite lytic cycle.**

**A,** Replication assay in which parasites were pre-starved of glutamine for 48 hours, seeded into HFFs, and counted after 24-hours of growth. Data is the average of 3 biological replicates with at least 70 vacuoles counted per replicate. **B,** Calcium ionophore stimulated egress assay in which parasites were pre-starved of glutamine for 48 hours, seeded onto HFFs and allowed to grow for 48 hours to produce vacuoles containing >16 parasites, and stimulated with 3-μM A23187. Egress was monitored by video microscopy and time to egress was monitored as described in Materials and Methods. Data is the average of 3 biological replicates. **C,** Zaprinast stimulated egress assay performed as described for ionophore, however 500-μM zaprinast was used to stimulate egress. Error bars depict SD from the mean. Statistical comparisons were done using an ordinary one-way ANOVA using Tukey's post-hoc test to correct for multiple comparisons. Statistical significance is indicated as follows: ns=p>0.05.

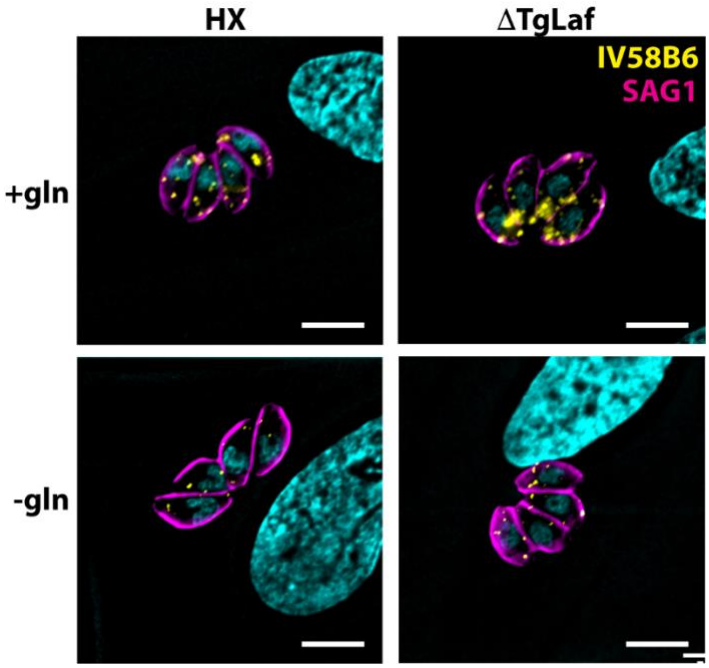


**Figure 5.12 The effects of glutamine starvation on IV58B6 staining.**
Parasites were starved of glutamine for 72-hours total before monitoring the effect of glutamine starvation on tachyzoite AG levels. Scale bar = 5 μm.

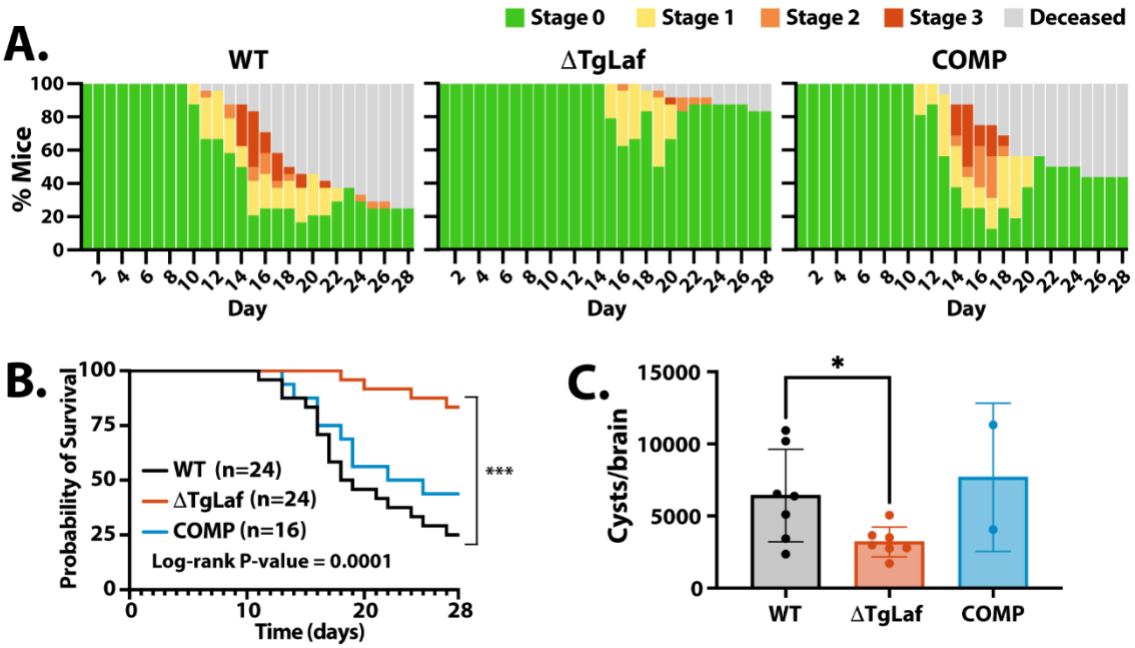


**Figure 5.13 Loss of TgLaforin attenuates virulence and cyst burden in mice.** Equal numbers of male and female CBA/J mice were infected IP with 100 tachyzoites from each group for symptoms and death: **A,** Symptomology throughout acute phase of infection. Mice were monitored 1-2x/day and assigned a body score index ranging from asymptomatic (Stage 0) to moribund/deceased (**Table 2.6**). WT and ΔTgLaf groups contain 24 mice each, and COMP group contains 16. **B,** Kaplan-Meier curve of mouse survival during acute tachyzoite infection. **C,** Mice that survived 4-weeks were euthanized, and brains were homogenized in pairs, layered over Percoll for purification of cysts, and cysts were counted as done previously (55,275). Error bars depict SD from the mean. Statistical comparison for Kaplan Meier curve is indicated on plot, and statistical comparison of cyst burden resulting from WT/ΔTgLaf infection was done using an unpaired t-test. Statistical significance: *p<0.05, ***p<0.0002.

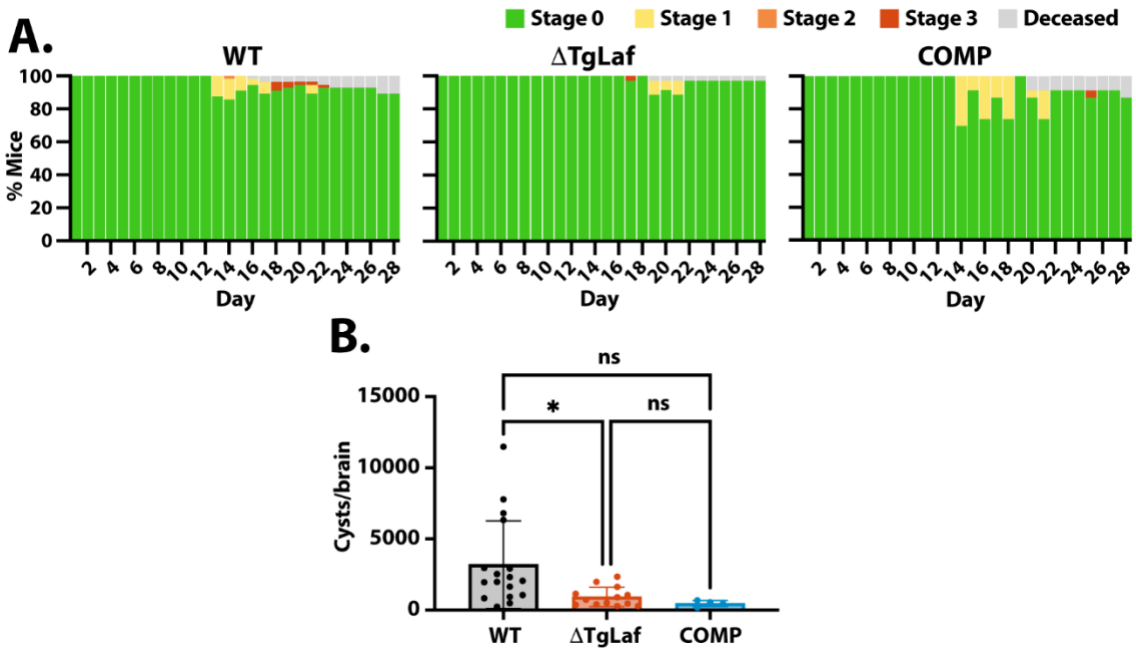


**Figure 5.14 Mouse infection with ΔTgLaf tissue cysts results in less symptomology, death, and lower cyst burden.**
CBA/J mice were infected IP with 20 cysts taken from previously infected mouse brains and monitored for symptomology and death. **A,** Symptomology throughout acute phase of infection as described in Figure 6B. **B,** Cysts/brain after 4-week bradyzoite infection. Cyst numbers were determined as described in Figure 6C. Statistical comparisons were done using an ordinary one-way ANOVA using Tukey's post-hoc test to correct for multiple comparisons. Statistical significance is indicated as follows: *p<0.05, ns=p>0.05.

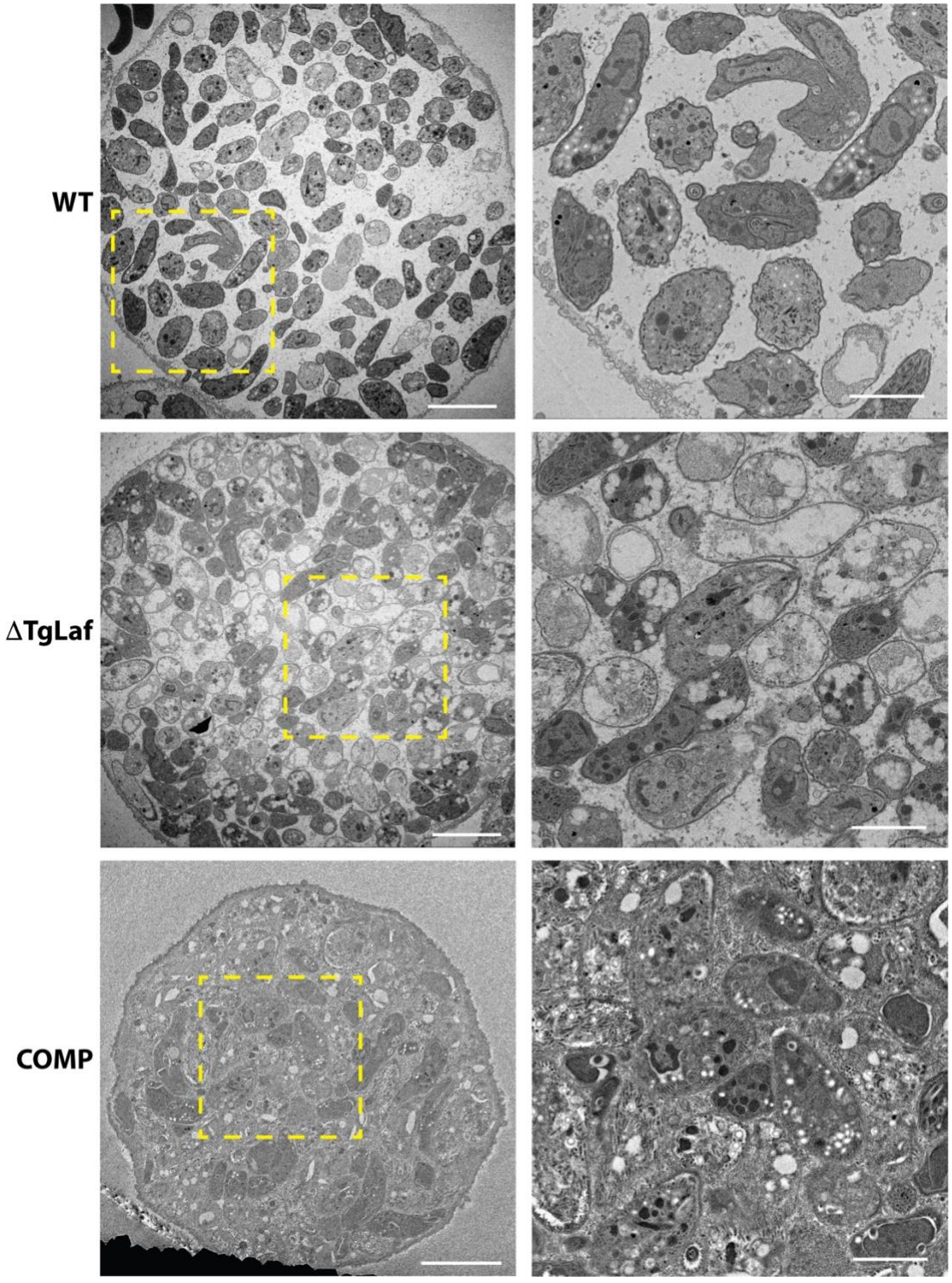


**Figure 5.15 *T. gondii* bradyzoites accumulate excess AGs in the absence of TgLaforin.**
Left panels: scale bar = 5 μm; right panels (zoom of boxed region from left panel): scale bar = 2 μm.

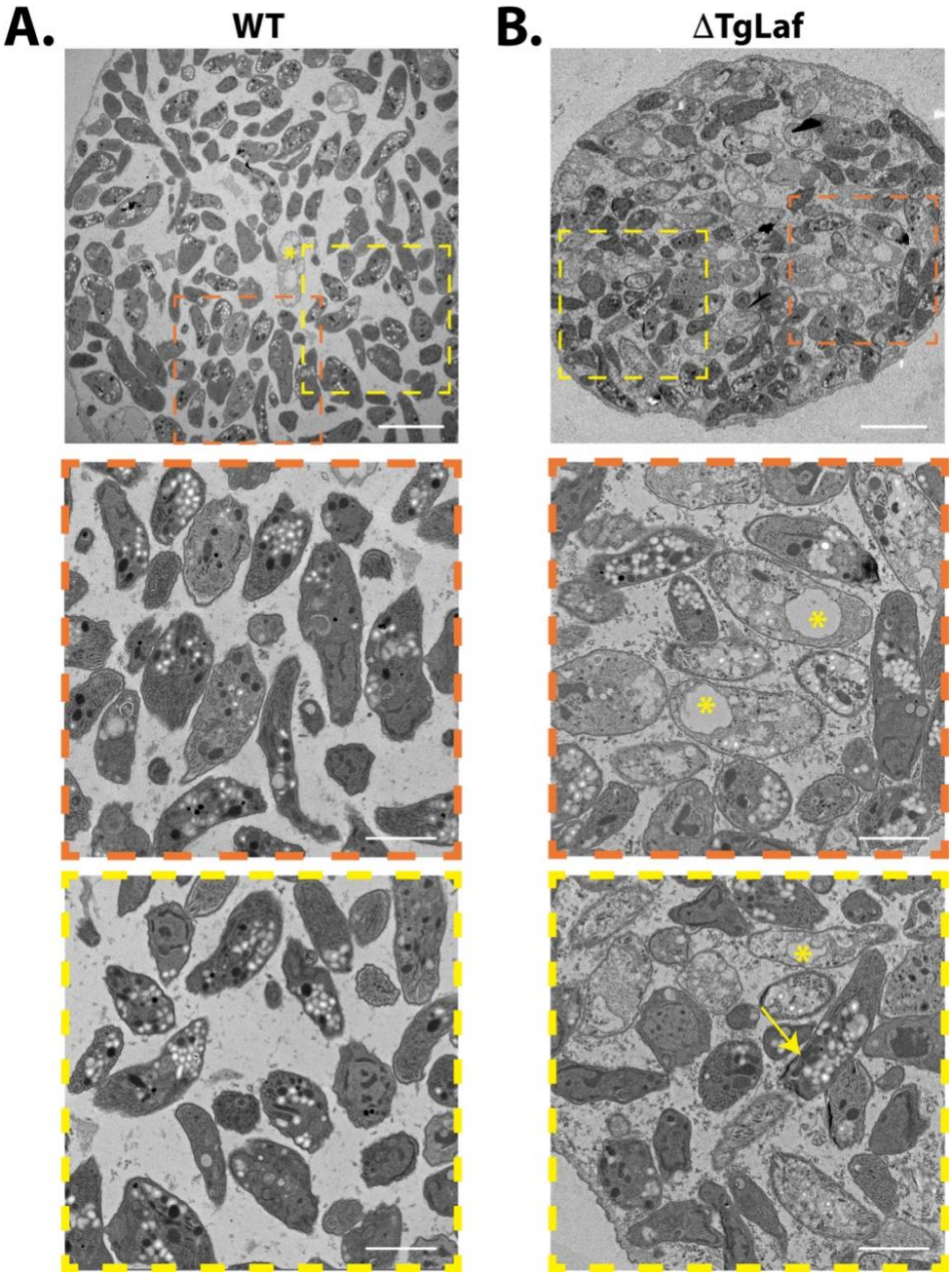


**Figure 5.16 Additional images of *in vivo* tissue cysts.**
**A,** WT tissue cyst (too large to fit in camera view) with two zooms depicted below. **B,** ΔTgLaf tissue cyst also with two zooms depicted below. Asterisks highlight empty nuclei and arrow shows example of rhoptry displacement by AGs.
Top row scale bar = 5 μm; Zoom scale bars = 2 μm.

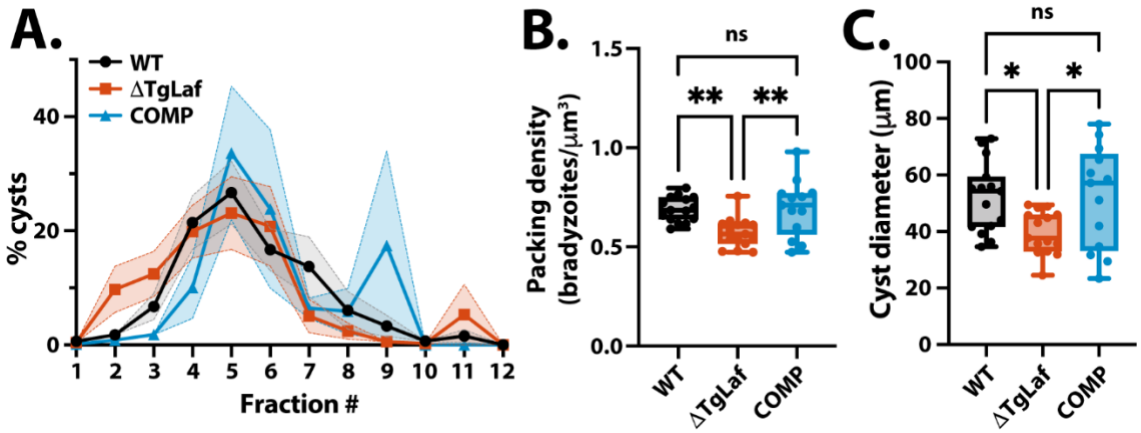


**Figure 5.17 Cysts formed by ΔTgLaf parasites are smaller and contain a lower bradyzoite packing density.**

**A,** Distribution of cysts in Percoll gradient after centrifugation. Fraction 1 is defined as the furthest traveling fraction adjacent to the RBC layer (most dense), and fraction 12 is the least mobile fraction adjacent to brain homogenate (least dense). Shaded area corresponds to SEM for each fraction. **B,** Packing density comparison among WT, ΔTgLaf, and COMP lines, a metric that describes cyst occupancy that has been described previously (55). Calculations were made using BradyCount1.0 to identify and quantify nuclear profiles from DAPI-stained tissue cysts. **C,** Cyst diameter comparison among WT, ΔTgLaf, and COMP lines as measured in ImageJ. Statistical comparisons were done using an ordinary one-way ANOVA using Tukey's post-hoc test to correct for multiple comparisons. Error bars in (B) and (C) depict SD from the mean. Statistical significance is indicated as follows: *p<0.05, **p<0.01, ns=p>0.05.

# CHAPTER 6. CONCLUDING REMARKS

## 6.1 Summary

After the discovery of reversible glucan phosphorylation in both plants (167,174,239) and animals (184,186,191,247), it was suggested that this cycle might also play a role in red alga and starch accumulating protists of red algal descent such as *T. gondii* (204,205). Herein, we demonstrated the functionality of the cycle of reversible glucan phosphorylation in *T. gondii*. We demonstrated that both the glucan phosphatase (TgLaforin, TGME49_205290) and glucan, water dikinase (TgGWD, TGME49_214260) are active against glucan substrates *in vitro*. We also defined the unique biophysical and biochemical properties of these enzymes using a wide range of techniques. In characterizing TgLaforin, we provided the first biophysical evidence for a split CBM domain, we demonstrated that TgLaforin is an anti-parallel DSP-mediated dimer, and we found that TgLaforin is an active glucan phosphatase that prefers to dephosphorylate the C3-position of glucosyl residues (**Chapter 3**). Moreover, we exploited the unique active site topology of glucan phosphatases to identify an inhibitor of TgLaforin that is selective against other DSPs and PTPs. In characterizing TgGWD, we showed that TgGWD is a monomer, we discovered that it phosphorylates exclusively the C6-position of glucosyl units, and we created a CE-based AMP detection assay for use in studying the general GWD catalytic mechanism (**Chapter 4**).

To explore the relevance of reversible glucan phosphorylation in *T. gondii* across its asexual life cycle, we first investigated the nature of the tachyzoite glucan that has been recently recognized by PAS staining and $^{14}$C-glucose pulse-chase experiments (203,212,228,363,364). Through comparative microscopy techniques, we demonstrated that the PAS+ tachyzoite glucan is not visible by TEM, but that it is recognized by an anti-glycogen antibody, IV58B6. We then verified that this tachyzoite glucan co-localizes with TgLaforin. Loss of TgLaforin did not appear to result in aberrant glucan morphology in tachyzoites as was expected, but it did result in tachyzoite dependence on glutamine. Further, loss of TgLaforin resulted in parasites with decreased virulence in mice and defective cyst formation with regard to glucan content, size, and bradyzoite packing density (**Chapter 5**).

In summary, this work builds upon recent work that recognizes the importance of glucan turnover in tachyzoites through the contribution of glucan turnover to central carbon metabolism, and its influence in acute virulence and cyst formation in mice. Together with the identification of an inhibitor to TgLaforin, the entirety of this work has characterized a valuable therapeutic target in the process of reversible glucan phosphorylation in *T. gondii*. Such a target is unique in that it has the potential to reduce the efficiency of reactivation, as *T. gondii* cysts lacking TgLaforin appear to be less virulent than their wildtype counterparts.

## 6.2 Discussion

### 6.2.1 The role of reversible glucan phosphorylation in tachyzoites

Our study supports the hypothesis that the glucan in *T. gondii* tachyzoites plays a crucial role in providing glucose for central carbon metabolism, as loss of TgLaforin, and thus loss of functioning reversible glucan phosphorylation and turnover, in tachyzoites appears to necessitate glutaminolysis and gluconeogenesis to make up for a glucose defect.

The mechanism potentially underlying this hypothesis is explained by recent discoveries in *T. gondii* and other systems. In *T. gondii*, the metabolic alterations seen in the starch synthase (TgSS) knockout are highly suggestive that AGs play a role in glucose allocation, as loss of TgSS resulted in a decreased flux of glucose through glycolysis (203). In other systems, such a function has been attributed to mammalian glycogen as it has been demonstrated that the majority of glycolytic intermediates in mammals are provided by glycogen, and not directly by circulating glucose (365). This suggests that glucose storage precedes utilization and thus implies a degree of metabolic compartmentalization and buffering against fluctuating glucose levels (365). Such a model is consistent with a recent study performed in *Leishmania* parasites that demonstrated mannogen, the *Leishmania* carbohydrate reserve, is constantly cycled in the amastigote life stage, acting as a proposed “metabolic rheostat” to buffer metabolic flux (313). A similar function of AGs is supported by continuous incorporation of glucose into and breakdown of AGs in WT parasites (228,312). In fact, the term “futile metabolic cycling” was applied to *T. gondii* metabolism in light of the discovery that both glycolytic and gluconeogenic enzymes are co-expressed and constitutively active in tachyzoites (**Figure 1.7**). This is hypothesized to allow maximum metabolic flexibility and steady levels of hexose phosphates at all times (209). Continuous storage and liberation of glucose into and out of AGs may serve a similar function.

Loss of TgLaforin might be enough to disrupt the efficiency of this cycle in providing needed glucose without completely halting it, explaining the lack of glucan overaccumulation. Such a model would involve continuous storage and degradation of glucose into and out of AGs under normal conditions, akin to the charging and discharging of a battery (**Figure 6.1a**). Glucose liberated from AGs would then be utilized for glycolysis, the TCA cycle, the pentose phosphate pathway, and in providing substrates for glycosylation. In the absence of reversible glucan phosphorylation, the liberation of glucose from AGs might be significantly slowed such that glutaminolysis and gluconeogenesis are needed to provide carbon to fuel central carbon reactions, and possibly carbon for the creation of glucose needed to make AGs, as this possibility has also been previously demonstrated (**Figure 6.1b**) (235). Without glutamine, however, the glucose liberated from AGs in the context of a TgLaforin knockout might not be enough to

sustain the rapidly dividing tachyzoite, explaining why glutamine imposes such a strong penalty in the absence of TgLaforin (**Figure 6.1c**).

This mechanism does not explain why other disruptions of glucan/glucose metabolism do not also result in a complete glutamine dependence. Recently, our understanding of glycogen's role in metabolism has changed to include functions beyond energy storage, as there is now evidence that glycogen may provide substrates for epigenetic modifications in the nucleus (282) and for protein glycosylation (154). An impairment in glucan access might also extend beyond glucose deprivation, as very recent studies demonstrated glycogen in humans is not entirely composed of glucose (154). Glycogen is comprised of 25% glucosamine in neurons. Loss of laforin in humans was shown to result in N-linked protein glycosylation defects, and this was due to sequestration of glucosamine into glycogen that could not be liberated efficiently without HsLaforin. Therefore, the distinct mechanism underlying the ΔTgLaf parasite's inability to survive in the absence of glutamine may indeed be a result of hindered access to glucose, but potentially glucosamine as well. Under such a mechanism, glutamine would play two roles in ΔTgLaf parasites that it would not necessarily be playing in the ΔGT1 or ΔHK parasites: 1) providing a carbon skeleton to operate the TCA cycle and gluconeogenesis in the absence of efficient glucan turnover, *and* 2) providing an amino group for the formation of glucosamine that may be sequestered away.

Alternatively, it was recently demonstrated that glutamine deprivation resulted in the downregulation of the arginine transporter TgApiAT1 (366), indicating that a lack of glutamine may initiate a generalized starvation response in *T. gondii*. Under such conditions, ΔTgLaf parasites would not have easy access to internal energy stores as their WT counterparts might, providing another possible mechanism that explains this phenotype.

### 6.2.2 The role of reversible glucan phosphorylation in stage conversion

Strikingly, and somewhat unexpectedly, we discovered that TgLaforin expression decreases during the tachyzoite to bradyzoite conversion *in vitro* even though its transcript levels do not change (**Figure 5.4a-b**). Moreover, a previous study indicates the possibility that transcript levels of TgGWD increase during the course of differentiation (40). During differentiation, both *in vitro* and *in vivo*, the appearance of crystalline AGs is also observed, raising the possibility that expression levels of these two enzymes relative to one another may contribute to the crystallinity of the *T. gondii* glucan. Loss of glucan phosphatases, and thus increased glucan phosphate content, results in enlarged granule morphology in plants (137), and the precipitation of glycogen into amylopectin-like Lafora bodies in animals (186). The programmed downregulation of TgLaforin and upregulation of TgGWD in *T. gondii* might result in the fine-tuned precipitation of the tachyzoite glucan into the bradyzoite AG. As such, *T. gondii* might provide a system in which to explore the interplay of these two enzymes and their contributions to crystallinity

through their controlled expression, and the controlled phosphorylation of glucans. Moreover, expression levels of branching and debranching enzymes, the two enzymes that have the biggest impact on glycogen and starch crystallinity in other systems (166), have not been explored during stage conversion in *T. gondii*. Because the enzymology related *T. gondii* starch synthesis and degradation is relatively simple compared to plants and green algae (199), the interplay of these limited number of enzymes could be more easily untangled and provide models for more complex systems in plants.

### 6.2.3 The role of reversible glucan phosphorylation in bradyzoites

In bradyzoites, the proposed roles of AGs traditionally been rooted in inferred, albeit reasonable, observations. AGs are believed to serve bradyzoites in persistence, reactivation, and transmission; essentially, they function as glucose-storage molecules to be used in situations of uncertainty such as the digestive system of a new host or in weathering nutrient fluctuations in the brain. These roles are attributed to AGs for a number of reasons, one being that such storage molecules are used in plants and algae for survival when photosynthesis is not possible (144). Further support of their role comes from the observations that the only life stages of *T. gondii* that accumulate large, visible AGs are those that are responsible for transmission, and that encounter the most challenging environments: the bradyzoite and the sporozoite (134,367). Indeed, in *Eimeria*, it was shown that the levels of amylopectin in sporozoites was directly correlated with their ability to invade chicken cells in cell culture (368), lending further legitimacy to this assumption in *T. gondii*. Some direct evidence has been provided for these assumptions as well—a study from Stanislas Tomavo's lab provided an undocumented observation that bradyzoites in cell culture lose their AGs upon conversion to tachyzoites (196), and the recent knockout of TgSS demonstrated that bradyzoite conversion to tachyzoites was significantly reduced compared to its WT counterpart (203). In light of the discovery that bradyzoites undergo cyclical bursts of replication (55), it has been suggested that AGs serve as a marker for replication potential and fuel these events as well (101,369). Toward an understanding of this relationship, software for the analysis of AGs, replication, and mitochondrial activity has recently been developed to untangle the relationships among these three physiological parameters (337).

The role of TgLaforin in the context AG metabolism in bradyzoites is, therefore, possibly more straightforward than its role in tachyzoites. Loss of TgLaforin results in bradyzoites with a "starch-excess" phenotype as has now been observed in plants, animals, and red algae (174,187,207). Moreover, this phenotype is progressive, as *in vitro* ΔTgLaf bradyzoites (day 6) display a milder defect in overaccumulation of AGs than *in vivo* bradyzoites (>day 6). However, by the time mature tissue cysts have formed in mice, many ΔTgLaf bradyzoites appear dead. Interestingly, ΔTgLaf bradyzoites are capable of reinfecting new mice when

injected IP. It should noted, however, IP injection allows for the bypassing of the stomach where cysts usually initiate infections in new hosts, and thus does not provide any insight into whether or not these parasites would be able to survive an oral route of infection, or if they could reactivate in the context of the immune system.

### 6.2.4 Limitations and future directions of these studies

While AG turnover in *T. gondii* was partially characterized through the lens of reversible phosphorylation in these studies, several limitations prevented a full mechanistic understanding of TgLaforin's role in *T. gondii*. Primarily, purification of the *T. gondii* glucan from tachyzoites or bradyzoites was unsuccessful, most likely due to attempted purifications from an insufficient quantity of parasites. Because *T. gondii* is an obligate, intracellular pathogen, extensive washing and filtration of parasites is required to rid them of host material, such as host glycogen that could easily confound parasite glucan analysis. Extensive washing and filtering results in the loss of at up to 95% of parasites over the course of purification (370). Therefore, we were unable to directly characterize relevant properties of the glucan such as phosphorylation status, chain length, and crystallinity in both WT and ΔTgLaf parasites. With regard to metabolomics, we were unable to visualize glycolysis using GCMS analysis, and we have not yet performed stable isotope tracing of glucose or glutamine. Therefore, while we speculate that glutaminolysis is being upregulated in ΔTgLaf parasites due to the inaccessibility of a hyperphosphorylated glucan, we have yet to complete the studies that would prove this.

Toward understanding TgLaforin's role in tachyzoites, we have also not yet identified what precisely results in the inability of ΔTgLaf tachyzoites to form plaques in the absence of glutamine. While we have explored replication and egress, neither of these components of the lytic cycle seem to be affected in the simultaneous absence of both TgLaforin and glutamine. The fact that ΔTgLaf parasites were identified and counted in replication assays with the same ease as WT parasites argues against a significant invasion defect. In replication assays performed in this study, parasites were pre-starved of glutamine and then subsequently forced to reinvade host cell monolayers and divide for 24 hours before counting. Therefore, the defect in ΔTgLaf growth under glutamine depleted conditions likely lies in either a natural egress defect, as opposed to the stimulated egress assays we utilized, or in a progressive decline in overall parasite fitness during the course of glutamine starvation that is not specific to any portion of the lytic cycle.

Finally, restoration of TgLaforin into ΔTgLaf parasites did not result in a perfect complementation, despite its having been restored under its native promoter to near identical expression levels found in WT parasites (**Figure 5.8e**). Importantly, complementation did restore the ability of the parasite to grow in the absence of

glutamine, tachyzoite virulence in mice, and its ability to form normal cysts from tachyzoite infection. However, in cyst re-infection studies, complementation did not rescue the number cysts formed in the ΔTgLaf line. This suggests that the lower cyst burden from reinfection is either unrelated to TgLaforin and possibly the result of an off-target effect of CRISPR/Cas9, or that loss of TgLaforin resulted in metabolically re-programmed parasites that could not be completely returned to WT levels. To further explore these possibilities, conditional knockdown of TgLaforin could address if the lower cyst burden during re-infection with cysts is specific to ΔTgLaf parasites or the result of some other mechanism. Recently, an auxin-inducible degron (AID) system has been adapted to *T. gondii*. AID knockdown of AID-tagged proteins relies on indole-3-acetic acid (IAA) treatment that can be safely administered to mice to maintain the knockdown (9).

These studies also present the opportunity for future directions in understanding basic glucan metabolism in *T. gondii*. So far, the glucan within tachyzoites has not been biochemically characterized under unstressed conditions. Moreover, it has not been characterized throughout the tachyzoite lytic cycle. Future studies could address whether the glucan is utilized during energy intensive processes such as invasion, replication, egress, or motility. Correlations between glucan levels and the parasite's progress through each of these events could be easily monitored in conjunction with well-established assays used in evaluating each of the components of the lytic cycle. We demonstrated the disappearance of IV58B6 staining during bradyzoite differentiation (**Figure 5.2**) as a mature cyst wall develops. Future studies can also examine the reasons for this disappearance. For example, does IV58B6 staining disappear because the fundamental properties of the tachyzoite glucan shift toward amylopectin-like crystallinity? Or does IV58B6 staining disappear because the tachyzoite glucan is completely degraded while the bradyzoite AGs are synthesized *de novo*? Experiments exploring the staining patterns over the course of differentiation in conjunction with determining the biochemical characteristics of the parasite's glucan over the course of differentiation could begin answering these questions.

HsLaforin and the role of phosphate in glycogen have often been the subject of debate as it has been difficult to separate the importance of its catalytic phosphatase activity from its scaffolding roles in bringing other degradation machinery to glycogen (189). Thus, future work could include investigating the nuanced functions of TgLaforin through a dissection of the relevance of its catalytic activity versus its scaffolding activity by mutating TgLaforin's catalytic cysteine *in vivo*, or attempting complementation of the ΔTgLaf parasites with catalytically inactive versions of the protein. Notably, TgLaforin's CBM domain contains large unstructured inserts (**Chapter 3**). While the role of these inserts is unclear, it is possible that these intrinsically disordered regions (IDRs) in TgLaforin might play a role in protein-protein interactions. IDRs are unusually abundant in parasitic protozoa (308) and have been speculated to be crucial in protein-protein interactions in *Plasmodium* (307). Therefore, further work could characterize

TgLaforin's interacting partners. Toward this end, we collaborated with Hybrigenics Services (Paris, France) to conduct a yeast-two-hybrid screen utilizing TgLaforin fused to both an N-terminal LexA and Gal4 DNA-binding domain as bait against a fragment-based library of the *T. gondii* proteome (**Table 6.1**) and discovered several putative interacting partners related to glucan metabolism including debranching enzyme, CDPK2, and TgGWD. Of note, the LexA fusion screen indicated the possibility that TgLaforin interacts with BFD1, a transcription factor recently identified as being both necessary and sufficient for bradyzoite differentiation (107). However, the confidence in this interaction was low. Further immunoprecipitation experiments with the TgLaforin-HA epitope-tagged line that we generated could determine which of these interactions are relevant *in vivo*.

## 6.3 Conclusion

From its initial discovery (1,2), *T. gondii* was initially mis-identified as *Leishmania* in both labs that first found it (371). Since then, *T. gondii* has not ceased in its ability to surprise and confuse scientists. Such attributes are especially evident in its glucan biology, which itself has provided surprising insights into the evolutionary history of *T. gondii*.

Herein, we build on the recent surprise that glucan biology is relevant in *T. gondii* tachyzoites and provide evidence that the tachyzoite glucan may have glycogen-like properties that distinguish it from AGs in bradyzoites. We then demonstrated that TgLaforin colocalizes with this glucan in tachyzoites but is likely downregulated in bradyzoites coinciding with the appearance of crystalline AGs. We also characterized the enzymology TgLaforin alongside TgGWD. We demonstrated that TgLaforin contains an incredibly unique CBM20 domain that is split by flexible linkers that possibly allow for protein-protein interactions and provide evidence that the enzymatic activity of TgLaforin can be selectively inhibited. Analysis of a TgLaforin knockout *in vivo* suggested the value in such an inhibitor as we further built on recent discoveries suggesting that the tachyzoite glucan might also behave like animal glycogen in its potential metabolic buffering capacity. Critically, through loss of TgLaforin, we saw that reversible glucan phosphorylation, and thus glucan degradation, play a critical role in *T. gondii*'s ability to survive nutrient scarcity, establishment of virulence in mice, formation of proper AGs in bradyzoites.

In summary, this work has contributed not only to our knowledge of *T. gondii* biology, but to more general themes of glucan solubility versus crystallinity, the diversity of CBM organizations, and diversity of DSP domain active sites. Future work should seek to exploit these unique traits in TgLaforin to further home in on more effective *T. gondii* therapeutics.

**Table 6.1 Yeast-two hybrid screen to identify TgLaforin interacting proteins.** Yeast two hybrid screen using TgLaforin as bait. Table lists prey interacting domains, indicating the amino acid residues of prey and which domain prey falls into, along with the name and accession number of the protein. PBS = protein biological score, an indicator of confidence in the interaction, proceeding from highest (A) to lowest (E).

| Fusion construct | ToxoDB Accession # | Protein name | Interaction domain [AA# (Pfam ID)] | PBS |
|---|---|---|---|---|
| Gal4 | TGME49_226910 | Debranching enzyme | 857-1039 (CBM48) | B |
| | TGME49_225490 | CDPK2 | 1-118 (CBM20) | B |
| | TGME49_206640 | Hypothetical protein | 630-993 | B |
| | TGME49_223985 | Serine/threonine protein phosphatase | 1538-1785 (CBM48) | B |
| | TGME49_254140 | RNA polymerase II | 20-52 (subunit CX) | C |
| | TGME49_268960 | AMPK β-subunit | 80-192 (CBM48) | D |
| | TGME49_214260 | TgGWD | 1-324 (CBM45) | D |
| | TGME49_229260 | Hypothetical protein | 1668-2268 | D |
| | TGME49_215520 | Hypothetical protein | 145-315 | E |
| LexA | TGME49_200385 | BFD1 | 2562-4092 | E |

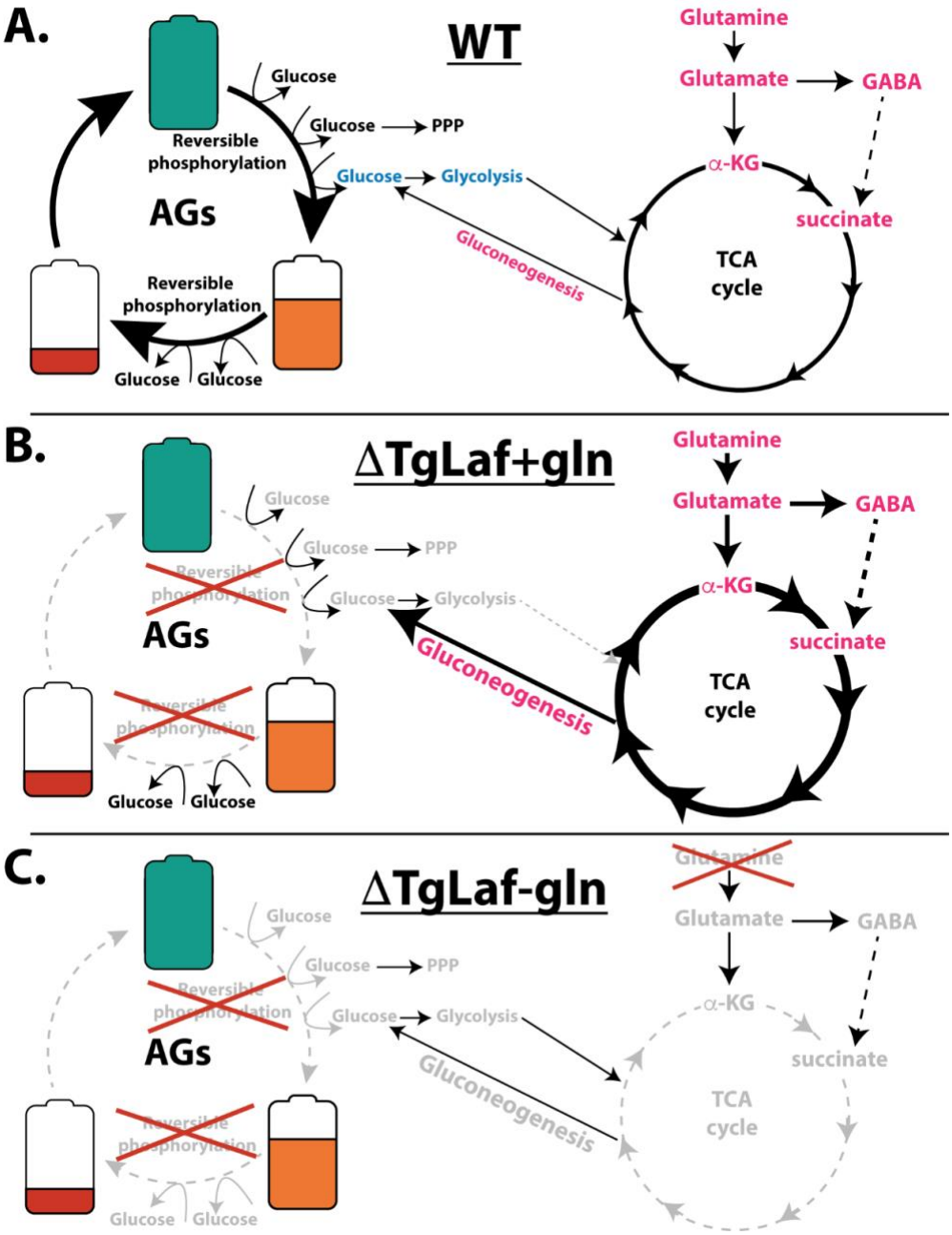


**Figure 6.1 Proposed mechanism underlying ΔTgLaf tachyzoite dependence on glutamine.**

**A,** Unperturbed conditions in which reversible glucan phosphorylation allows for efficient glucan degradation in tachyzoites. Glucose and glutamine usage is balanced as seen in **Figure 1.7**. **B,** Loss of TgLaforin results in upregulation of glutaminolysis due to loss of glucan breakdown efficiency. Glutamine-derived carbon fuels the entire TCA cycle and provides glycolytic intermediates through gluconeogenesis. **C,** Removal of glutamine from ΔTgLaf parasites removes the only carbon source, resulting in the complete loss of central carbon metabolism.

## REFERENCES


1. Nicolle, C. (1908) Sur une infection a corps de Leishman (on organismes voisons) du gondi. *CR Acad Sci* **147**, 736
2. Splendore, A. (1908) Un nuovo protozoa parassita de'conigli. incontrato nelle lesioni anatomiche d'une malattia che ricorda in molti punti il Kala-azar dell'uomo. Nota preliminare pel. *Rev Soc Sci Sao Paulo* **3**, 109-112
3. Robert-Gangneux, F., and Dardé, M. L. (2012) Epidemiology of and diagnostic strategies for toxoplasmosis. *Clin Microbiol Rev* **25**, 264-296
4. Kim, K., and Weiss, L. M. (2004) Toxoplasma gondii: the model apicomplexan. *International Journal for Parasitology* **34**, 423-432
5. Roos, D. S., Donald, R. G., Morrissette, N. S., and Moulton, A. L. (1994) Molecular tools for genetic dissection of the protozoan parasite Toxoplasma gondii. *Methods Cell Biol* **45**, 27-63
6. Donald, R. G., Carter, D., Ullman, B., and Roos, D. S. (1996) Insertional tagging, cloning, and expression of the Toxoplasma gondii hypoxanthine-xanthine-guanine phosphoribosyltransferase gene. Use as a selectable marker for stable transformation. *J Biol Chem* **271**, 14010-14019
7. Donald, R., and Roos, D. S. (1993) Stable molecular transformation of Toxoplasma gondii: a selectable dihydrofolate reductase-thymidylate synthase marker based on drug-resistance mutations in malaria. *Proceedings of the National Academy of Sciences* **90**, 11703-11707
8. Jiménez-Ruiz, E., Wong, E. H., Pall, G. S., and Meissner, M. (2014) Advantages and disadvantages of conditional systems for characterization of essential genes in Toxoplasma gondii. *Parasitology* **141**, 1390-1398
9. Brown, K. M., Long, S., and Sibley, L. D. (2018) Conditional Knockdown of Proteins Using Auxin-inducible Degron (AID) Fusions in Toxoplasma gondii. *Bio Protoc* **8**
10. Sidik, S. M., Huet, D., Ganesan, S. M., Huynh, M. H., Wang, T., Nasamu, A. S., Thiru, P., Saeij, J. P. J., Carruthers, V. B., Niles, J. C., and Lourido, S. (2016) A Genome-wide CRISPR Screen in Toxoplasma Identifies Essential Apicomplexan Genes. *Cell* **166**, 1423-1435.e1412
11. Waller, R., Barylyuk, K., Koreny, L., Ke, H., Butterworth, S., Crook, O., Lassadi, I., Gupta, V., Tromer, E., and Stevens, T. (2020) A comprehensive subcellular atlas of Toxoplasma proteome via hyperLOPIT provides spatial context for protein functions.
12. Xue, Y., Theisen, T. C., Rastogi, S., Ferrel, A., Quake, S. R., and Boothroyd, J. C. (2020) A single-parasite transcriptional atlas of Toxoplasma gondii reveals novel control of antigen expression. *Elife* **9**, e54129
13. (2020) *Toxoplasma gondi: the model apicomplexan—perspectives and methods*, 3 ed., Academic Press
14. (2020) *Toxoplasma gondii*, Humana, New York, NY
15. Dubey, J. P., Lindsay, D. S., and Speer, C. A. (1998) Structures of Toxoplasma gondii tachyzoites, bradyzoites, and sporozoites and biology and development of tissue cysts. *Clin Microbiol Rev* **11**, 267-299
16. Gustafson, P. V., Agar, H. D., and Cramer, D. I. (1954) An electron microscope study of Toxoplasma. *Am J Trop Med Hyg* **3**, 1008-1022

17. Goldman, M., Carver, R. K., and Sulzer, A. J. (1957) Similar internal morphology of Toxoplasma gondii and Besnoitia jellisoni stained with silver protein. *J Parasitol* **43**, 490-491
18. Sheffield, H. G., and Melton, M. L. (1968) The fine structure and reproduction of Toxoplasma gondii. *J Parasitol* **54**, 209-226
19. Zhang, Y., Lai, B. S., Juhas, M., and Zhang, Y. (2019) Toxoplasma gondii secretory proteins and their role in invasion and pathogenesis. *Microbiological Research* **227**, 126293
20. Dubois, D. J., and Soldati-Favre, D. (2019) Biogenesis and secretion of micronemes in Toxoplasma gondii. *Cellular microbiology* **21**, e13018
21. Boothroyd, J. C., and Hakimi, M.-A. (2020) Effectors produced by rhoptries and dense granules: an intense conversation between parasite and host in many languages. in *Toxoplasma gondii*, Elsevier. pp 789-806
22. Ben Chaabene, R., Lentini, G., and Soldati-Favre, D. (2020) Biogenesis and discharge of the rhoptries: key organelles for entry and hijack of host cells by the Apicomplexa. *Mol Microbiol*
23. Molestina, R. E., El-Guendy, N., and Sinai, A. P. (2008) Infection with Toxoplasma gondii results in dysregulation of the host cell cycle. *Cellular microbiology* **10**, 1153-1165
24. Panas, M. W., and Boothroyd, J. C. (2021) Seizing control: How dense granule effector proteins enable Toxoplasma to take charge. *Molecular Microbiology* **115**, 466-477
25. Blank, M. L., Parker, M. L., Ramaswamy, R., Powell, C. J., English, E. D., Adomako-Ankomah, Y., Pernas, L. F., Workman, S. D., Boothroyd, J. C., Boulanger, M. J., and Boyle, J. P. (2018) A Toxoplasma gondii locus required for the direct manipulation of host mitochondria has maintained multiple ancestral functions. *Molecular Microbiology* **108**, 519-535
26. Sinai, A. P., Webster, P., and Joiner, K. A. (1997) Association of host cell endoplasmic reticulum and mitochondria with the Toxoplasma gondii parasitophorous vacuole membrane: a high affinity interaction. *J Cell Sci* **110 ( Pt 17)**, 2117-2128
27. Sinai, A. P., and Joiner, K. A. (2001) The Toxoplasma gondii protein ROP2 mediates host organelle association with the parasitophorous vacuole membrane. *The Journal of cell biology* **154**, 95-108
28. Chen, A. L., Moon, A. S., Bell, H. N., Huang, A. S., Vashisht, A. A., Toh, J. Y., Lin, A. H., Nadipuram, S. M., Kim, E. W., and Choi, C. P. (2017) Novel insights into the composition and function of the Toxoplasma IMC sutures. *Cellular microbiology* **19**, e12678
29. Sun, S. Y., Segev-Zarko, L. A., Chen, M., Pintilie, G. D., Schmid, M. F., Ludtke, S. J., Boothroyd, J. C., and Chiu, W. (2022) Cryo-ET of Toxoplasma parasites gives subnanometer insight into tubulin-based structures. *Proc Natl Acad Sci U S A* **119**
30. Katris, N. J., van Dooren, G. G., McMillan, P. J., Hanssen, E., Tilley, L., and Waller, R. F. (2014) The Apical Complex Provides a Regulated Gateway for Secretion of Invasion Factors in Toxoplasma. *PLOS Pathogens* **10**, e1004074

31. Miranda, K., Pace, D. A., Cintron, R., Rodrigues, J. C., Fang, J., Smith, A., Rohloff, P., Coelho, E., De Haas, F., and De Souza, W. (2010) Characterization of a novel organelle in Toxoplasma gondii with similar composition and function to the plant vacuole. *Molecular microbiology* **76**, 1358-1375
32. Moreno, S. N., and Zhong, L. (1996) Acidocalcisomes in Toxoplasma gondii tachyzoites. *Biochemical Journal* **313**, 655-659
33. McFadden, G. I., Reith, M. E., Munholland, J., and Lang-Unnasch, N. (1996) Plastid in human parasites. *Nature* **381**, 482-482
34. Scholtyseck, E., and Piekarski, G. (1965) [Electron microscopic studies on merozoites of Eimeria (Eimeria perforans and E. stidae) and Toxoplasma gondii. On the systematic position of T. gondii]. *Z Parasitenkd* **26**, 91-115
35. Siddall, M. E. (1992) Hohlzylinders. *Parasitol Today* **8**, 90-91
36. Feagin, J. E. (1994) The extrachromosomal DNAs of apicomplexan parasites. *Annu Rev Microbiol* **48**, 81-104
37. Wilson, R. J., Williamson, D. H., and Preiser, P. (1994) Malaria and other Apicomplexans: the "plant" connection. *Infect Agents Dis* **3**, 29-37
38. Köhler, S., Delwiche, C. F., Denny, P. W., Tilney, L. G., Webster, P., Wilson, R., Palmer, J. D., and Roos, D. S. (1997) A plastid of probable green algal origin in Apicomplexan parasites. *Science* **275**, 1485-1489
39. Roos, D. S., Crawford, M. J., Donald, R. G., Kissinger, J. C., Klimczak, L. J., and Striepen, B. (1999) Origin, targeting, and function of the apicomplexan plastid. *Curr Opin Microbiol* **2**, 426-432
40. Coppin, A., Varre, J.-S., Lienard, L., Dauvillee, D., Guerardel, Y., Soyer-Gobillard, M.-O., Buleon, A., Ball, S., and Tomavo, S. (2005) Evolution of plant-like crystalline storage polysaccharide in the protozoan parasite Toxoplasma gondii argues for a red alga ancestry. *Journal of Molecular Evolution* **60**, 257-267
41. Seeber, F., Feagin, J. E., and Parsons, M. (2014) The apicoplast and mitochondrion of Toxoplasma gondii. in *Toxoplasma gondii*, Elsevier. pp 297-350
42. McFadden, G. I., and Yeh, E. (2017) The apicoplast: now you see it, now you don't. *International journal for parasitology* **47**, 137-144
43. Lim, L., and McFadden, G. I. (2010) The evolution, metabolism and functions of the apicoplast. *Philosophical Transactions of the Royal Society B: Biological Sciences* **365**, 749-763
44. Ramakrishnan, S., Docampo, M. D., Macrae, J. I., Pujol, F. M., Brooks, C. F., van Dooren, G. G., Hiltunen, J. K., Kastaniotis, A. J., McConville, M. J., and Striepen, B. (2012) Apicoplast and endoplasmic reticulum cooperate in fatty acid biosynthesis in apicomplexan parasite Toxoplasma gondii. *J Biol Chem* **287**, 4957-4971
45. He, C. Y., Shaw, M. K., Pletcher, C. H., Striepen, B., Tilney, L. G., and Roos, D. S. (2001) A plastid segregation defect in the protozoan parasite Toxoplasma gondii. *The EMBO journal* **20**, 330-339
46. Fichera, M. E., and Roos, D. S. (1997) A plastid organelle as a drug target in apicomplexan parasites. *Nature* **390**, 407-409

47. Camps, M., Arrizabalaga, G., and Boothroyd, J. (2002) An rRNA mutation identifies the apicoplast as the target for clindamycin in Toxoplasma gondii. *Molecular microbiology* **43**, 1309-1318
48. Blader, I. J., Coleman, B. I., Chen, C. T., and Gubbels, M. J. (2015) Lytic Cycle of Toxoplasma gondii: 15 Years Later. *Annu Rev Microbiol* **69**, 463-485
49. Martin, A. M., Liu, T., Lynn, B. C., and Sinai, A. P. (2007) The Toxoplasma gondii Parasitophorous Vacuole Membrane: Transactions Across the Border 1. *Journal of Eukaryotic Microbiology* **54**, 25-28
50. Radke, J. R., Striepen, B., Guerini, M. N., Jerome, M. E., Roos, D. S., and White, M. W. (2001) Defining the cell cycle for the tachyzoite stage of Toxoplasma gondii. *Mol Biochem Parasitol* **115**, 165-175
51. Brown, K. M., Tonkin, C. J., Billker, O., and Sibley, L. D. (2020) Calcium and cyclic nucleotide signaling networks in Toxoplasma gondii. in *Toxoplasma gondii*, Elsevier. pp 577-605
52. Eyles, D. E., Coleman, N., and Cavanaugh, D. J. (1956) Preservation of Toxoplasma gondii by freezing. *J Parasitol* **42**, 408-413
53. Bohne, W., Heesemann, J., and Gross, U. (1994) Reduced replication of Toxoplasma gondii is necessary for induction of bradyzoite-specific antigens: a possible role for nitric oxide in triggering stage conversion. *Infect Immun* **62**, 1761-1767
54. Sinai, A. P., and Suvorova, E. S. (2020) The RESTRICTION checkpoint: a window of opportunity governing developmental transitions in Toxoplasma gondii. *Curr Opin Microbiol* **58**, 99-105
55. Watts, E., Zhao, Y., Dhara, A., Eller, B., Patwardhan, A., and Sinai, A. P. (2015) Novel approaches reveal that Toxoplasma gondii bradyzoites within tissue cysts are dynamic and replicating entities in vivo. *MBio* **6**, e01155-01115
56. Freppel, W., Ferguson, D. J. P., Shapiro, K., Dubey, J. P., Puech, P.-H., and Dumètre, A. (2019) Structure, composition, and roles of the Toxoplasma gondii oocyst and sporocyst walls. *The Cell Surface* **5**, 100016
57. Torrey, E. F., and Yolken, R. H. (2013) Toxoplasma oocysts as a public health problem. *Trends Parasitol* **29**, 380-384
58. Frenkel, J. K. (1973) Toxoplasma in and around Us. *BioScience* **23**, 343-352
59. Frenkel, J. K. (1949) Pathogenesis, diagnosis and treatment of human toxoplasmosis. *J Am Med Assoc* **140**, 369-377
60. Dubey, J. P., Lago, E. G., Gennari, S. M., Su, C., and Jones, J. L. (2012) Toxoplasmosis in humans and animals in Brazil: high prevalence, high burden of disease, and epidemiology. *Parasitology* **139**, 1375-1424
61. Grigg, M. E., Dubey, J. P., and Nussenblatt, R. B. (2015) Ocular toxoplasmosis: lessons from Brazil. *Am J Ophthalmol* **159**, 999-1001
62. Levaditi, C., Schoen, R., Sanchis Bayarri, V. (1928) L'encéphalo-myélite toxoplasmique chronique du lapin et de la souris. *CR Soc. Biol* **99**, 37-40
63. Wolf, A., Cowen, D., and Paige, B. H. (1939) Toxoplasmic encephalomyelitis: III. A new case of granulomatous encephalomyelitis due to a protozoon. *Am J Pathol* **15**, 657-694.611

64. Torgerson, P. R., and Mastroiacovo, P. (2013) The global burden of congenital toxoplasmosis: a systematic review. *Bull World Health Organ* **91**, 501-508
65. Plaut, A. (1946) The Problem of Human Toxoplasma Carriers. *Am J Pathol* **22**, 427-431
66. Mantz, F. A., Jr., Dailey, H. R., and Grocott, R. G. (1949) Toxoplasmosis in Panama; report of two additional cases. *Am J Trop Med Hyg* **29**, 895-908, illust
67. Ruchman, I., and Fowler, J. C. (1951) Localization and persistence of toxoplasma in tissues of experimentally infected white rats. *Proc Soc Exp Biol Med* **76**, 793-796
68. Sabin, A. B., and Feldman, H. A. (1948) Dyes as Microchemical Indicators of a New Immunity Phenomenon Affecting a Protozoon Parasite (Toxoplasma). *Science* **108**, 660-663
69. Feldman, H. A., and Miller, L. T. (1956) Serological study of toxoplasmosis prevalence. *Am J Hyg* **64**, 320-335
70. Jacobs, L., Remington, J. S., and Melton, M. L. (1960) A survey of meat samples from swine, cattle, and sheep for the presence of encysted Toxoplasma. *J Parasitol* **46**, 23-28
71. Weinman, D., and Chandler, A. H. (1954) Toxoplasmosis in swine and rodents; reciprocal oral infection and potential human hazard. *Proc Soc Exp Biol Med* **87**, 211-216
72. Weinman, D., and Chandler, A. H. (1956) Toxoplasmosis in man and swine; an investigation of the possible relationship. *J Am Med Assoc* **161**, 229-232
73. Jacobs, L., Remington, J. S., and Melton, M. L. (1960) The resistance of the encysted form of Toxoplasma gondii. *J Parasitol* **46**, 11-21
74. Kotula, A., Dubey, J., Sharar, A., Andrews, C., Shen, S., and Lindsay, D. (1991) Effect of freezing on infectivity of Toxoplasma gondii tissue cysts in pork. *Journal of food protection* **54**, 687-690
75. Hutchison, W. M. (1965) Experimental transmission of Toxoplasma gondii. *Nature* **206**, 961-962
76. Frenkel, J. K., Dubey, J. P., and Miller, N. L. (1969) Toxoplasma gondii: fecal forms separated from eggs of the nematode Toxocara cati. *Science* **164**, 432-433
77. Frenkel, J. K., Dubey, J. P., and Miller, N. L. (1970) Toxoplasma gondii in cats: fecal stages identified as coccidian oocysts. *Science* **167**, 893-896
78. Dubey, J. P., Miller, N. L., and Frenkel, J. K. (1970) The Toxoplasma gondii oocyst from cat feces. *J Exp Med* **132**, 636-662
79. Dubey, J. P., and Frenkel, J. K. (1972) Cyst-induced toxoplasmosis in cats. *J Protozool* **19**, 155-177
80. Speer, C. A., and Dubey, J. P. (2005) Ultrastructural differentiation of Toxoplasma gondii schizonts (types B to E) and gamonts in the intestines of cats fed bradyzoites. *Int J Parasitol* **35**, 193-206

81. Martorelli Di Genova, B., Wilson, S. K., Dubey, J., and Knoll, L. J. (2019) Intestinal delta-6-desaturase activity determines host range for Toxoplasma sexual reproduction. *PLoS biology* **17**, e3000364
82. RYNING, F. W., McLEOD, R., MADDOX, J. C., HUNT, S., and REMINGTON, J. S. (1979) Probable transmission of Toxoplasma gondii by organ transplantation. *Annals of internal medicine* **90**, 47-49
83. Montoya, J. G., and Liesenfeld, O. (2004) Toxoplasmosis. *Lancet* **363**, 1965-1976
84. Pappas, G., Roussos, N., and Falagas, M. E. (2009) Toxoplasmosis snapshots: global status of Toxoplasma gondii seroprevalence and implications for pregnancy and congenital toxoplasmosis. *Int J Parasitol* **39**, 1385-1394
85. Jones, J. L., and Dubey, J. P. (2012) Foodborne toxoplasmosis. *Clin Infect Dis* **55**, 845-851
86. Sacks, J. J., Roberto, R. R., and Brooks, N. F. (1982) Toxoplasmosis infection associated with raw goat's milk. *Jama* **248**, 1728-1732
87. Goldman, M., Carver, R. K., and Sulzer, A. J. (1958) Reproduction of Toxoplasma gondii by internal budding. *J Parasitol* **44**, 161-171
88. Dubey, J., Speer, C., Shen, S., Kwok, O., and Blixt, J. (1997) Oocyst-induced murine toxoplasmosis: life cycle, pathogenicity, and stage conversion in mice fed Toxoplasma gondii oocysts. *The Journal of parasitology* **83**, 870-882
89. Speer, C. A., and Dubey, J. P. (1998) Ultrastructure of early stages of infections in mice fed Toxoplasma gondii oocysts. *Parasitology* **116 ( Pt 1)**, 35-42
90. Snyder, L. M., and Denkers, E. Y. (2020) From Initiators to Effectors: Roadmap Through the Intestine During Encounter of Toxoplasma gondii With the Mucosal Immune System. *Front Cell Infect Microbiol* **10**, 614701
91. Ólafsson, E. B., and Barragan, A. (2020) The unicellular eukaryotic parasite Toxoplasma gondii hijacks the migration machinery of mononuclear phagocytes to promote its dissemination. *Biol Cell* **112**, 239-250
92. Unno, A., Suzuki, K., Xuan, X., Nishikawa, Y., Kitoh, K., and Takashima, Y. (2008) Dissemination of extracellular and intracellular Toxoplasma gondii tachyzoites in the blood flow. *Parasitol Int* **57**, 515-518
93. Lambert, H., Hitziger, N., Dellacasa, I., Svensson, M., and Barragan, A. (2006) Induction of dendritic cell migration upon Toxoplasma gondii infection potentiates parasite dissemination. *Cell Microbiol* **8**, 1611-1623
94. Lachenmaier, S. M., Deli, M. A., Meissner, M., and Liesenfeld, O. (2011) Intracellular transport of Toxoplasma gondii through the blood–brain barrier. *Journal of neuroimmunology* **232**, 119-130
95. Attias, M., Teixeira, D. E., Benchimol, M., Vommaro, R. C., Crepaldi, P. H., and De Souza, W. (2020) The life-cycle of Toxoplasma gondii reviewed using animations. *Parasit Vectors* **13**, 588
96. Cerutti, A., Blanchard, N., and Besteiro, S. (2020) The Bradyzoite: A Key Developmental Stage for the Persistence and Pathogenesis of Toxoplasmosis. *Pathogens* **9**, 234

97. Jeffers, V., Tampaki, Z., Kim, K., and Sullivan, W. J., Jr. (2018) A latent ability to persist: differentiation in Toxoplasma gondii. *Cell Mol Life Sci* **75**, 2355-2373
98. Lüder, C. G. K., and Rahman, T. (2017) Impact of the host on Toxoplasma stage differentiation. *Microb Cell* **4**, 203-211
99. Swierzy, I. J., and Lüder, C. G. (2015) Withdrawal of skeletal muscle cells from cell cycle progression triggers differentiation of Toxoplasma gondii towards the bradyzoite stage. *Cell Microbiol* **17**, 2-17
100. Ferguson, D. J. (2004) Use of molecular and ultrastructural markers to evaluate stage conversion of Toxoplasma gondii in both the intermediate and definitive host. *Int J Parasitol* **34**, 347-360
101. Sinai, A. P., Watts, E. A., Dhara, A., Murphy, R. D., Gentry, M. S., and Patwardhan, A. (2016) Reexamining Chronic Toxoplasma gondii Infection: Surprising Activity for a "Dormant" Parasite. *Curr Clin Microbiol Rep* **3**, 175-185
102. Hay, J., Graham, D. I., Dutton, G. N., and Logan, S. (1986) The immunocytochemical demonstration of Toxoplasma antigen in the brains of congenitally infected mice. *Z Parasitenkd* **72**, 609-615
103. Tu, V., Yakubu, R., and Weiss, L. M. (2018) Observations on bradyzoite biology. *Microbes Infect* **20**, 466-476
104. Kim, S. K., and Boothroyd, J. C. (2005) Stage-specific expression of surface antigens by Toxoplasma gondii as a mechanism to facilitate parasite persistence. *J Immunol* **174**, 8038-8048
105. Tomavo, S. (2001) The differential expression of multiple isoenzyme forms during stage conversion of Toxoplasma gondii: an adaptive developmental strategy. *International journal for parasitology* **31**, 1023-1031
106. White, M. W., Radke, J. R., and Radke, J. B. (2014) Toxoplasma development - turn the switch on or off? *Cell Microbiol* **16**, 466-472
107. Waldman, B. S., Schwarz, D., Wadsworth II, M. H., Saeij, J. P., Shalek, A. K., and Lourido, S. (2020) Identification of a master regulator of differentiation in Toxoplasma. *Cell* **180**, 359-372. e316
108. Kochanowsky, J. A., and Koshy, A. A. (2020) A Single Transcription Factor Drives Toxoplasma gondii Differentiation. *Cell* **180**, 216-218
109. Flament-Durand, J., Coërs, C., Waelbroeck, C., Van Geertruyden, J., and Tousaint, C. (1967) [Toxoplasmic encephalitis and myositis during treatment with immunodepressive drugs]. *Acta Clin Belg* **22**, 44-54
110. Vietzke, W. M., Gelderman, A. H., Grimley, P. M., and Valsamis, M. P. (1968) Toxoplasmosis complicating malignancy. Experience at the National Cancer Institute. *Cancer* **21**, 816-827
111. Rostami, A., Karanis, P., and Fallahi, S. (2018) Advances in serological, imaging techniques and molecular diagnosis of Toxoplasma gondii infection. *Infection* **46**, 303-315
112. Richardson, E. P., Jr. (1961) Progressive multifocal leukoencephalopathy. *N Engl J Med* **265**, 815-823

113. Vidal, J. E. (2019) HIV-Related Cerebral Toxoplasmosis Revisited: Current Concepts and Controversies of an Old Disease. *J Int Assoc Provid AIDS Care* **18**, 2325958219867315
114. Luft, B. J., and Remington, J. S. (1992) Toxoplasmic Encephalitis in AIDS. *Clinical Infectious Diseases* **15**, 211-222
115. Wang, Z. D., Wang, S. C., Liu, H. H., Ma, H. Y., Li, Z. Y., Wei, F., Zhu, X. Q., and Liu, Q. (2017) Prevalence and burden of Toxoplasma gondii infection in HIV-infected people: a systematic review and meta-analysis. *Lancet HIV* **4**, e177-e188
116. Dunay, I. R., Gajurel, K., Dhakal, R., Liesenfeld, O., and Montoya, J. G. (2018) Treatment of Toxoplasmosis: Historical Perspective, Animal Models, and Current Clinical Practice. *Clin Microbiol Rev* **31**
117. Eyles, D. E., and Coleman, N. (1953) Synergistic effect of sulfadiazine and daraprim against experimental toxoplasmosis in the mouse. *Antibiot Chemother (Northfield)* **3**, 483-490
118. Konstantinovic, N., Guegan, H., Stäjner, T., Belaz, S., and Robert-Gangneux, F. (2019) Treatment of toxoplasmosis: Current options and future perspectives. *Food Waterborne Parasitol* **15**, e00036
119. Rajapakse, S., Chrishan Shivanthan, M., Samaranayake, N., Rodrigo, C., and Deepika Fernando, S. (2013) Antibiotics for human toxoplasmosis: a systematic review of randomized trials. *Pathog Glob Health* **107**, 162-169
120. Smith, N. C., Goulart, C., Hayward, J. A., Kupz, A., Miller, C. M., and van Dooren, G. G. (2021) Control of human toxoplasmosis. *Int J Parasitol* **51**, 95-121
121. Villena, I., Aubert, D., Leroux, B., Dupouy, D., Talmud, M., Chemla, C., Trenque, T., Schmit, G., Quereux, C., and Guenounou, M. (1998) Pyrimethamine-sulfadoxine treatment of congenital toxoplasmosis: follow-up of 78 cases between 1980 and 1997. *Scandinavian journal of infectious diseases* **30**, 295-300
122. Barrett, M. P., Kyle, D. E., Sibley, L. D., Radke, J. B., and Tarleton, R. L. (2019) Protozoan persister-like cells and drug treatment failure. *Nature reviews. Microbiology* **17**, 607-620
123. Silva, M. d., Teixeira, C., Gomes, P., and Borges, M. (2021) Promising Drug Targets and Compounds with Anti-Toxoplasma gondii Activity. *Microorganisms* **9**, 1960
124. Cross, J. B. (1947) A cytologic study of Toxoplasma with special reference to its effect on the host's cell. *J Infect Dis* **80**, 278-296
125. Frenkel, J. K. (1956) PATHOGENESIS OF TOXOPLASMOSIS AND OF INFECTIONS WITH ORGANISMS RESEMBLING TOXOPLASMA. *Annals of the New York Academy of Sciences* **64**, 215-251
126. Jacobs, L. (1956) PROPAGATION, MORPHOLOGY, AND BIOLOGY OF TOXOPLASMA. *Annals of the New York Academy of Sciences* **64**, 154-179
127. Lainson, R. (1958) Observations on the development and nature of pseudocysts and cysts of Toxoplasma gondii. *Trans R Soc Trop Med Hyg* **52**, 396-407

128. Wanko, T., Jacobs, L., and Gavin, M. A. (1962) Electron microscope study of Toxoplasma cysts in mouse brain. *J Protozool* **9**, 235-242
129. Matsubayashi, H., and Akao, S. (1963) MORPHOLOGICAL STUDIES ON THE DEVELOPMENT OF THE TOXOPLASMA CYST. *Am J Trop Med Hyg* **12**, 321-333
130. Edgar, S. A., Herrick, C. A., and Fraser, L. A. (1944) Glycogen in the Life Cycle of the Coccidium, Eimeria tenella. *Transactions of the American Microscopical Society* **63**, 199-202
131. Ryley, J. F., Bentley, M., Manners, D. J., and Stark, J. R. (1969) Amylopectin, the storage polysaccharide of the Coccidia Eimeria brunetti and E. tenella. *J Parasitol* **55**, 839-845
132. Ferguson, D. J., Birch-Andersen, A., Siim, J. C., and Hutchison, W. M. (1979) Ultrastructural studies on the sporulation of oocysts of Toxoplasma gondii. I. Development of the zygote and formation of the sporoblasts. *Acta Pathol Microbiol Scand B* **87b**, 171-181
133. Ferguson, D. J., Hutchison, W. M., Dunachie, J. F., and Siim, J. C. (1974) Ultrastructural study of early stages of asexual multiplication and microgametogony of Toxoplasma gondii in the small intestine of the cat. *Acta Pathol Microbiol Scand B Microbiol Immunol* **82**, 167-181
134. Ferguson, D. J., and Hutchison, W. M. (1987) An ultrastructural study of the early development and tissue cyst formation of Toxoplasma gondii in the brains of mice. *Parasitol Res* **73**, 483-491
135. Guimarães, E. V., de Carvalho, L., and Barbosa, H. S. (2003) An alternative technique to reveal polysaccharides in Toxoplasma gondii tissue cysts. *Mem Inst Oswaldo Cruz* **98**, 915-917
136. (2015) *Starch: Metabolism and Structure*, Springer Japan
137. Zeeman, S. C., Tiessen, A., Pilling, E., Kato, K. L., Donald, A. M., and Smith, A. M. (2002) Starch synthesis in Arabidopsis. Granule synthesis, composition, and structure. *Plant Physiol* **129**, 516-529
138. Crumpton-Taylor, M., Grandison, S., Png, K. M., Bushby, A. J., and Smith, A. M. (2012) Control of starch granule numbers in Arabidopsis chloroplasts. *Plant Physiol* **158**, 905-916
139. Badenhuizen, N. (1963) Formation and distribution of amylose and amylopectin in the starch granule. *Nature* **197**, 464-467
140. Manners, D. J. (1989) Recent developments in our understanding of amylopectin structure. *Carbohydrate Polymers* **11**, 87-112
141. Bertoft, E. (2013) On the Building Block and Backbone Concepts of Amylopectin Structure. *Cereal Chemistry* **90**, 294-311
142. Pérez, S., and Bertoft, E. (2010) The molecular structures of starch components and their contribution to the architecture of starch granules: A comprehensive review. *Starch - Stärke* **62**, 389-420
143. Imberty, A., and Perez, S. (1988) A revisit to the three-dimensional structure of B-type starch. *Biopolymers: Original Research on Biomolecules* **27**, 1205-1221
144. MacNeill, G. J., Mehrpouyan, S., Minow, M. A., Patterson, J. A., Tetlow, I. J., Emes, M. J., and Raines, C. (2017) Starch as a source, starch as a

sink: the bifunctional role of starch in carbon allocation. *Journal of Experimental Botany* **68**, 4433-4453
145. Prats, C., Graham, T. E., and Shearer, J. (2018) The dynamic life of the glycogen granule. *J Biol Chem* **293**, 7089-7098
146. Roach, P. J., Depaoli-Roach, A. A., Hurley, T. D., and Tagliabracci, V. S. (2012) Glycogen and its metabolism: some new developments and old themes. *Biochemical Journal* **441**, 763-787
147. Brust, H., Orzechowski, S., and Fettke, J. (2020) Starch and Glycogen Analyses: Methods and Techniques. *Biomolecules* **10**
148. Goldsmith, E., Sprang, S., and Fletterick, R. (1982) Structure of maltoheptaose by difference Fourier methods and a model for glycogen. *J Mol Biol* **156**, 411-427
149. Calder, P. C. (1991) Glycogen structure and biogenesis. *Int J Biochem* **23**, 1335-1352
150. Meléndez, R., Meléndez-Hevia, E., and Cascante, M. (1997) How did glycogen structure evolve to satisfy the requirement for rapid mobilization of glucose? A problem of physical constraints in structure building. *J Mol Evol* **45**, 446-455
151. Shearer, J., and Graham, T. E. (2004) Novel aspects of skeletal muscle glycogen and its regulation during rest and exercise. *Exerc Sport Sci Rev* **32**, 120-126
152. Rybicka, K. K. (1996) Glycosomes--the organelles of glycogen metabolism. *Tissue Cell* **28**, 253-265
153. Chandramouli, C., Varma, U., Stevens, E. M., Xiao, R. P., Stapleton, D. I., Mellor, K. M., and Delbridge, L. M. (2015) Myocardial glycogen dynamics: new perspectives on disease mechanisms. *Clin Exp Pharmacol Physiol* **42**, 415-425
154. Sun, R. C., Young, L. E. A., Bruntz, R. C., Markussen, K. H., Zhou, Z., Conroy, L. R., Hawkinson, T. R., Clarke, H. A., Stanback, A. E., Macedo, J. K. A., Emanuelle, S., Brewer, M. K., Rondon, A. L., Mestas, A., Sanders, W. C., Mahalingan, K. K., Tang, B., Chikwana, V. M., Segvich, D. M., Contreras, C. J., Allenger, E. J., Brainson, C. F., Johnson, L. A., Taylor, R. E., Armstrong, D. D., Shaffer, R., Waechter, C. J., Vander Kooi, C. W., DePaoli-Roach, A. A., Roach, P. J., Hurley, T. D., Drake, R. R., and Gentry, M. S. (2021) Brain glycogen serves as a critical glucosamine cache required for protein glycosylation. *Cell Metab* **33**, 1404-1417.e1409
155. Preiss, J., Ball, K., Smith-White, B., Iglesias, A., Kakefuda, G., and Li, L. (1991) Starch biosynthesis and its regulation. *Biochemical Society Transactions* **19**, 539-547
156. Zeeman, S. C., Smith, S. M., and Smith, A. M. (2007) The diurnal metabolism of leaf starch. *Biochemical Journal* **401**, 13-28
157. Pfister, B., and Zeeman, S. C. (2016) Formation of starch in plant cells. *Cell Mol Life Sci* **73**, 2781-2807
158. Tetlow, I. J., and Emes, M. J. (2014) A review of starch-branching enzymes and their role in amylopectin biosynthesis. *IUBMB Life* **66**, 546-558

159. Delatte, T., Trevisan, M., Parker, M. L., and Zeeman, S. C. (2005) Arabidopsis mutants Atisa1 and Atisa2 have identical phenotypes and lack the same multimeric isoamylase, which influences the branch point distribution of amylopectin during starch synthesis. *The Plant Journal* **41**, 815-830
160. Denyer, K., Waite, D., Motawia, S., Møller, B. L., and Smith, A. M. (1999) Granule-bound starch synthase I in isolated starch granules elongates malto-oligosaccharides processively. *Biochem J* **340 ( Pt 1)**, 183-191
161. Lomako, J., Lomako, W. M., and Whelan, W. J. (1988) A self-glucosylating protein is the primer for rabbit muscle glycogen biosynthesis. *Faseb j* **2**, 3097-3103
162. Gibbons, B. J., Roach, P. J., and Hurley, T. D. (2002) Crystal structure of the autocatalytic initiator of glycogen biosynthesis, glycogenin. *J Mol Biol* **319**, 463-477
163. Lomako, J., Lomako, W. M., and Whelan, W. J. (2004) Glycogenin: the primer for mammalian and yeast glycogen synthesis. *Biochim Biophys Acta* **1673**, 45-55
164. Roach, P. J. (1990) Control of glycogen synthase by hierarchal protein phosphorylation. *The FASEB journal* **4**, 2961-2968
165. Verhue, W., and Hers, H. G. (1966) A study of the reaction catalysed by the liver branching enzyme. *Biochem J* **99**, 222-227
166. Tolmasky, D. S., and Krisman, C. R. (1987) The degree of branching in (alpha 1,4)-(alpha 1,6)-linked glucopolysaccharides is dependent on intrinsic properties of the branching enzymes. *Eur J Biochem* **168**, 393-397
167. Ritte, G., Lloyd, J. R., Eckermann, N., Rottmann, A., Kossmann, J., and Steup, M. (2002) The starch-related R1 protein is an alpha -glucan, water dikinase. *Proc Natl Acad Sci U S A* **99**, 7166-7171
168. Kötting, O., Pusch, K., Tiessen, A., Geigenberger, P., Steup, M., and Ritte, G. (2005) Identification of a novel enzyme required for starch metabolism in Arabidopsis leaves. The phosphoglucan, water dikinase. *Plant Physiol* **137**, 242-252
169. Hejazi, M., Fettke, J., Haebel, S., Edner, C., Paris, O., Frohberg, C., Steup, M., and Ritte, G. (2008) Glucan, water dikinase phosphorylates crystalline maltodextrins and thereby initiates solubilization. *Plant J* **55**, 323-334
170. Hansen, P. I., Spraul, M., Dvortsak, P., Larsen, F. H., Blennow, A., Motawia, M. S., and Engelsen, S. B. (2009) Starch phosphorylation--maltosidic restrains upon 3'- and 6'-phosphorylation investigated by chemical synthesis, molecular dynamics and NMR spectroscopy. *Biopolymers* **91**, 179-193
171. Mahlow, S., Orzechowski, S., and Fettke, J. (2016) Starch phosphorylation: insights and perspectives. *Cellular and molecular life sciences* **73**, 2753-2764
172. Edner, C., Li, J., Albrecht, T., Mahlow, S., Hejazi, M., Hussain, H., Kaplan, F., Guy, C., Smith, S. M., Steup, M., and Ritte, G. (2007) Glucan, water

dikinase activity stimulates breakdown of starch granules by plastidial beta-amylases. *Plant Physiol* **145**, 17-28
173. Takeda, Y., and Hizukuri, S. (1981) Re-examination of the action of sweet-potato beta-amylase on phosphorylated (1→4)-χ-d-glucan. *Carbohydrate Research* **89**, 174-178
174. Kötting, O., Santelia, D., Edner, C., Eicke, S., Marthaler, T., Gentry, M. S., Comparot-Moss, S., Chen, J., Smith, A. M., Steup, M., Ritte, G., and Zeeman, S. C. (2009) STARCH-EXCESS4 is a laforin-like Phosphoglucan phosphatase required for starch degradation in Arabidopsis thaliana. *Plant Cell* **21**, 334-346
175. Santelia, D., and Zeeman, S. C. (2011) Progress in Arabidopsis starch research and potential biotechnological applications. *Curr Opin Biotechnol* **22**, 271-280
176. Hejazi, M., Fettke, J., Kötting, O., Zeeman, S. C., and Steup, M. (2010) The Laforin-like dual-specificity phosphatase SEX4 from Arabidopsis hydrolyzes both C6- and C3-phosphate esters introduced by starch-related dikinases and thereby affects phase transition of alpha-glucans. *Plant Physiol* **152**, 711-722
177. Santelia, D., Kötting, O., Seung, D., Schubert, M., Thalmann, M., Bischof, S., Meekins, D. A., Lutz, A., Patron, N., Gentry, M. S., Allain, F. H., and Zeeman, S. C. (2011) The phosphoglucan phosphatase like sex Four2 dephosphorylates starch at the C3-position in Arabidopsis. *Plant Cell* **23**, 4096-4111
178. Critchley, J. H., Zeeman, S. C., Takaha, T., Smith, A. M., and Smith, S. M. (2001) A critical role for disproportionating enzyme in starch breakdown is revealed by a knock-out mutation in Arabidopsis. *Plant J* **26**, 89-100
179. Roach, P. J. (2002) Glycogen and its metabolism. *Curr Mol Med* **2**, 101-120
180. Cori, G. T., and Cori, C. F. (1943) Crystalline muscle phosphorylase: iv. formation of glycogen. *Journal of Biological Chemistry* **151**, 57-63
181. Alonso-Casajús, N., Dauvillée, D., Viale, A. M., Muñoz, F. J., Baroja-Fernández, E., Morán-Zorzano, M. T., Eydallin, G., Ball, S., and Pozueta-Romero, J. (2006) Glycogen phosphorylase, the product of the glgP Gene, catalyzes glycogen breakdown by removing glucose units from the nonreducing ends in Escherichia coli. *Journal of bacteriology* **188**, 5266-5272
182. Nakayama, A., Yamamoto, K., and Tabata, S. (2001) Identification of the catalytic residues of bifunctional glycogen debranching enzyme. *Journal of Biological Chemistry* **276**, 28824-28828
183. Contreras, C. J., Segvich, D. M., Mahalingan, K., Chikwana, V. M., Kirley, T. L., Hurley, T. D., DePaoli-Roach, A. A., and Roach, P. J. (2016) Incorporation of phosphate into glycogen by glycogen synthase. *Arch Biochem Biophys* **597**, 21-29
184. Minassian, B. A., Lee, J. R., Herbrick, J. A., Huizenga, J., Soder, S., Mungall, A. J., Dunham, I., Gardner, R., Fong, C. Y., Carpenter, S., Jardim, L., Satishchandra, P., Andermann, E., Snead, O. C., 3rd, Lopes-

Cendes, I., Tsui, L. C., Delgado-Escueta, A. V., Rouleau, G. A., and Scherer, S. W. (1998) Mutations in a gene encoding a novel protein tyrosine phosphatase cause progressive myoclonus epilepsy. *Nat Genet* **20**, 171-174
185. Brewer, M. K., Machio-Castello, M., Viana, R., Wayne, J. L., Kuchtová, A., Simmons, Z. R., Sternbach, S., Li, S., García-Gimeno, M. A., Serratosa, J. M., Sanz, P., Vander Kooi, C. W., and Gentry, M. S. (2021) An empirical pipeline for personalized diagnosis of Lafora disease mutations. *iScience* **24**, 103276
186. Tagliabracci, V. S., Turnbull, J., Wang, W., Girard, J. M., Zhao, X., Skurat, A. V., Delgado-Escueta, A. V., Minassian, B. A., Depaoli-Roach, A. A., and Roach, P. J. (2007) Laforin is a glycogen phosphatase, deficiency of which leads to elevated phosphorylation of glycogen in vivo. *Proc Natl Acad Sci U S A* **104**, 19262-19266
187. Gentry, M. S., Guinovart, J. J., Minassian, B. A., Roach, P. J., and Serratosa, J. M. (2018) Lafora disease offers a unique window into neuronal glycogen metabolism. *Journal of Biological Chemistry* **293**, 7117-7125
188. Chan, E. M., Young, E. J., Ianzano, L., Munteanu, I., Zhao, X., Christopoulos, C. C., Avanzini, G., Elia, M., Ackerley, C. A., Jovic, N. J., Bohlega, S., Andermann, E., Rouleau, G. A., Delgado-Escueta, A. V., Minassian, B. A., and Scherer, S. W. (2003) Mutations in NHLRC1 cause progressive myoclonus epilepsy. *Nat Genet* **35**, 125-127
189. Gentry, M. S., Romá-Mateo, C., and Sanz, P. (2013) Laforin, a protein with many faces: glucan phosphatase, adapter protein, et alii. *Febs j* **280**, 525-537
190. Gentry, M. S., Worby, C. A., and Dixon, J. E. (2005) Insights into Lafora disease: malin is an E3 ubiquitin ligase that ubiquitinates and promotes the degradation of laforin. *Proc Natl Acad Sci U S A* **102**, 8501-8506
191. Tagliabracci, Vincent S., Heiss, C., Karthik, C., Contreras, Christopher J., Glushka, J., Ishihara, M., Azadi, P., Hurley, Thomas D., DePaoli-Roach, Anna A., and Roach, Peter J. (2011) Phosphate Incorporation during Glycogen Synthesis and Lafora Disease. *Cell Metabolism* **13**, 274-282
192. Nitschke, F., Wang, P., Schmieder, P., Girard, J. M., Awrey, D. E., Wang, T., Israelian, J., Zhao, X., Turnbull, J., Heydenreich, M., Kleinpeter, E., Steup, M., and Minassian, B. A. (2013) Hyperphosphorylation of glucosyl C6 carbons and altered structure of glycogen in the neurodegenerative epilepsy Lafora disease. *Cell Metab* **17**, 756-767
193. Lomako, J., Lomako, W., Kirkman, B., and Whelan, W. (1994) The role of phosphate in muscle glycogen. *BioFactors (Oxford, England)* **4**, 167-171
194. Brewer, M. K., and Gentry, M. S. (2019) Brain glycogen structure and its associated proteins: past, present and future. *Brain Glycogen Metabolism*, 17-81
195. van der Ploeg, A. T., and Reuser, A. J. (2008) Pompe's disease. *Lancet* **372**, 1342-1353

196. Coppin, A., Dzierszinski, F., Legrand, S., Mortuaire, M., Ferguson, D., and Tomavo, S. (2003) Developmentally regulated biosynthesis of carbohydrate and storage polysaccharide during differentiation and tissue cyst formation in Toxoplasma gondii. *Biochimie* **85**, 353-361
197. Guérardel, Y., Leleu, D., Coppin, A., Liénard, L., Slomianny, C., Strecker, G., Ball, S., and Tomavo, S. (2005) Amylopectin biogenesis and characterization in the protozoan parasite Toxoplasma gondii, the intracellular development of which is restricted in the HepG2 cell line. *Microbes and infection* **7**, 41-48
198. Shimonaga, T., Fujiwara, S., Kaneko, M., Izumo, A., Nihei, S., Francisco, P. B., Satoh, A., Fujita, N., Nakamura, Y., and Tsuzuki, M. (2007) Variation in storage α-polyglucans of red algae: amylose and semi-amylopectin types in Porphyridium and glycogen type in Cyanidium. *Marine biotechnology* **9**, 192-202
199. Ball, S., Colleoni, C., and Arias, M. C. (2015) The transition from glycogen to starch metabolism in cyanobacteria and eukaryotes. in *Starch*, Springer. pp 93-158
200. Saha, S., Coleman, B. I., Dubey, R., Blader, I. J., and Gubbels, M.-J. (2017) Two phosphoglucomutase paralogs facilitate ionophore-triggered secretion of the Toxoplasma micronemes. *Msphere* **2**
201. Mandalasi, M., Kim, H. W., Thieker, D., Sheikh, M. O., Gas-Pascual, E., Rahman, K., Zhao, P., Daniel, N. G., van der Wel, H., Ichikawa, H. T., Glushka, J. N., Wells, L., Woods, R. J., Wood, Z. A., and West, C. M. (2020) A terminal α3-galactose modification regulates an E3 ubiquitin ligase subunit in Toxoplasma gondii. *J Biol Chem* **295**, 9223-9243
202. Mandalasi, M., Kim, H. W., Thieker, D., Sheikh, M. O., Gas-Pascual, E., Rahman, K., Zhao, P., Daniel, N. G., van der Wel, H., and Ichikawa, H. T. (2020) A glycogenin homolog controls Toxoplasma gondii growth via glycosylation of an E3 ubiquitin ligase. *bioRxiv*, 764241
203. Lyu, C., Yang, X., Yang, J., Hou, L., Zhou, Y., Zhao, J., and Shen, B. (2021) Role of amylopectin synthesis in Toxoplasma gondii and its implication in vaccine development against toxoplasmosis. *Open Biol* **11**, 200384
204. Gentry, M. S., Dowen, R. H., Worby, C. A., Mattoo, S., Ecker, J. R., and Dixon, J. E. (2007) The phosphatase laforin crosses evolutionary boundaries and links carbohydrate metabolism to neuronal disease. *The Journal of cell biology* **178**, 477-488
205. Gentry, M. S., and Pace, R. M. (2009) Conservation of the glucan phosphatase laforin is linked to rates of molecular evolution and the glucan metabolism of the organism. *BMC evolutionary biology* **9**, 138
206. Sugi, T., Tu, V., Ma, Y., Tomita, T., and Weiss, L. M. (2017) Toxoplasma gondii requires glycogen phosphorylase for balancing amylopectin storage and for efficient production of brain cysts. *MBio* **8**, e01289-01217
207. Brizzee, C. O. (2021) Reversible Glucan Phosphorylation in the Red Alga, Cyanidioschyzon merolae.

208. Pomel, S., Luk, F. C., and Beckers, C. J. (2008) Host cell egress and invasion induce marked relocations of glycolytic enzymes in Toxoplasma gondii tachyzoites. *PLoS pathogens* **4**
209. Blume, M., Nitzsche, R., Sternberg, U., Gerlic, M., Masters, S. L., Gupta, N., and McConville, M. J. (2015) A Toxoplasma gondii gluconeogenic enzyme contributes to robust central carbon metabolism and is essential for replication and virulence. *Cell host & microbe* **18**, 210-220
210. Nitzsche, R., Günay-Esiyok, Ö., Tischer, M., Zagoriy, V., and Gupta, N. (2017) A plant/fungal-type phosphoenolpyruvate carboxykinase located in the parasite mitochondrion ensures glucose-independent survival of Toxoplasma gondii. *Journal of Biological Chemistry* **292**, 15225-15239
211. Shukla, A., Olszewski, K. L., Llinás, M., Rommereim, L. M., Fox, B. A., Bzik, D. J., Xia, D., Wastling, J., Beiting, D., and Roos, D. S. (2018) Glycolysis is important for optimal asexual growth and formation of mature tissue cysts by Toxoplasma gondii. *International journal for parasitology* **48**, 955-968
212. Kloehn, J., Krishnan, A., Tonkin, C. J., McConville, M. J., and Soldati-Favre, D. (2020) Chapter 10 - Metabolic networks and metabolomics. in *Toxoplasma gondii (Third Edition)* (Weiss, L. M., and Kim, K. eds.), Academic Press. pp 451-497
213. Vercesi, A. E., Rodrigues, C. O., Uyemura, S. A., Zhong, L., and Moreno, S. N. (1998) Respiration and oxidative phosphorylation in the apicomplexan parasite Toxoplasma gondii. *J Biol Chem* **273**, 31040-31047
214. Darde, M., Bouteille, B., and Pestre-Alexandre, M. (1990) Comparison of isoenzyme profiles ofToxoplasma gondii tachyzoites produced under different culture conditions. *Parasitology research* **76**, 367-371
215. Yang, S., and Parmley, S. F. (1995) A bradyzoite stage-specifically expressed gene of Toxoplasma gondii encodes a polypeptide homologous to lactate dehydrogenase. *Molecular and biochemical parasitology* **73**, 291-294
216. Yang, S., and Parmley, S. F. (1997) Toxoplasma gondii expresses two distinct lactate dehydrogenase homologous genes during its life cycle in intermediate hosts. *Gene* **184**, 1-12
217. Dzierszinski, F., Popescu, O., Toursel, C., Slomianny, C., Yahiaoui, B., and Tomavo, S. (1999) The protozoan parasite Toxoplasma gondii expresses two functional plant-like glycolytic enzymes Implications for evolutionary origin of apicomplexans. *Journal of Biological Chemistry* **274**, 24888-24895
218. Ferguson, D. J., Parmley, S. F., and Tomavo, S. (2002) Evidence for nuclear localisation of two stage-specific isoenzymes of enolase in Toxoplasma gondii correlates with active parasite replication. *International journal for parasitology* **32**, 1399-1410
219. Denton, H., Roberts, C. W., Alexander, J., Thong, K.-w., and Coombs, G. H. (1996) Enzymes of energy metabolism in the bradyzoites and

tachyzoites of Toxoplasma gondii. *FEMS microbiology letters* **137**, 103-108
220. MacRae, J. I., Sheiner, L., Nahid, A., Tonkin, C., Striepen, B., and McConville, M. J. (2012) Mitochondrial metabolism of glucose and glutamine is required for intracellular growth of Toxoplasma gondii. *Cell host & microbe* **12**, 682-692
221. Oppenheim, R. D., Creek, D. J., Macrae, J. I., Modrzynska, K. K., Pino, P., Limenitakis, J., Polonais, V., Seeber, F., Barrett, M. P., and Billker, O. (2014) BCKDH: the missing link in apicomplexan mitochondrial metabolism is required for full virulence of Toxoplasma gondii and Plasmodium berghei. *PLoS pathogens* **10**
222. Olson, W. J., Martorelli Di Genova, B., Gallego-Lopez, G., Dawson, A. R., Stevenson, D., Amador-Noguez, D., and Knoll, L. J. (2020) Dual metabolomic profiling uncovers Toxoplasma manipulation of the host metabolome and the discovery of a novel parasite metabolic capability. *PLoS pathogens* **16**, e1008432
223. Lin, S. S., Kerscher, S., Saleh, A., Brandt, U., Gross, U., and Bohne, W. (2008) The Toxoplasma gondii type-II NADH dehydrogenase TgNDH2-I is inhibited by 1-hydroxy-2-alkyl-4(1H)quinolones. *Biochim Biophys Acta* **1777**, 1455-1462
224. Lin, S. S., Gross, U., and Bohne, W. (2009) Type II NADH dehydrogenase inhibitor 1-hydroxy-2-dodecyl-4(1H)quinolone leads to collapse of mitochondrial inner-membrane potential and ATP depletion in Toxoplasma gondii. *Eukaryot Cell* **8**, 877-887
225. Blume, M., Rodriguez-Contreras, D., Landfear, S., Fleige, T., Soldati-Favre, D., Lucius, R., and Gupta, N. (2009) Host-derived glucose and its transporter in the obligate intracellular pathogen Toxoplasma gondii are dispensable by glutaminolysis. *Proceedings of the National Academy of Sciences* **106**, 12998-13003
226. Nitzsche, R., Zagoriy, V., Lucius, R., and Gupta, N. (2016) Metabolic cooperation of glucose and glutamine is essential for the lytic cycle of obligate intracellular parasite Toxoplasma gondii. *Journal of Biological Chemistry* **291**, 126-141
227. Krishnan, A., and Soldati-Favre, D. (2021) Amino Acid Metabolism in Apicomplexan Parasites. *Metabolites* **11**
228. Uboldi, A. D., McCoy, J. M., Blume, M., Gerlic, M., Ferguson, D. J., Dagley, L. F., Beahan, C. T., Stapleton, D. I., Gooley, P. R., and Bacic, A. (2015) Regulation of starch stores by a Ca2+-dependent protein kinase is essential for viable cyst development in Toxoplasma gondii. *Cell Host & Microbe* **18**, 670-681
229. Lourido, S., Shuman, J., Zhang, C., Shokat, K. M., Hui, R., and Sibley, L. D. (2010) Calcium-dependent protein kinase 1 is an essential regulator of exocytosis in Toxoplasma. *Nature* **465**, 359-362
230. Garrison, E., Treeck, M., Ehret, E., Butz, H., Garbuz, T., Oswald, B. P., Settles, M., Boothroyd, J., and Arrizabalaga, G. (2012) A forward genetic

screen reveals that calcium-dependent protein kinase 3 regulates egress in Toxoplasma. *PLoS Pathog* **8**, e1003049
231. Lourido, S., Tang, K., and Sibley, L. D. (2012) Distinct signalling pathways control Toxoplasma egress and host-cell invasion. *The EMBO journal* **31**, 4524-4534
232. Morlon-Guyot, J., Berry, L., Chen, C. T., Gubbels, M. J., Lebrun, M., and Daher, W. (2014) The Toxoplasma gondii calcium-dependent protein kinase 7 is involved in early steps of parasite division and is crucial for parasite survival. *Cell Microbiol* **16**, 95-114
233. Billker, O., Lourido, S., and Sibley, L. D. (2009) Calcium-dependent signaling and kinases in apicomplexan parasites. *Cell Host Microbe* **5**, 612-622
234. Yang, J., Yang, C., Qian, J., Li, F., Zhao, J., and Fang, R. (2020) Toxoplasma gondii α-amylase deletion mutant is a promising vaccine against acute and chronic toxoplasmosis. *Microb Biotechnol*
235. Xia, N., Ye, S., Liang, X., Chen, P., Zhou, Y., Fang, R., Zhao, J., Gupta, N., Yang, S., and Yuan, J. (2019) Pyruvate homeostasis as a determinant of parasite growth and metabolic plasticity in Toxoplasma gondii. *MBio* **10**, e00898-00819
236. Gentry, M. S., Dixon, J. E., and Worby, C. A. (2009) Lafora disease: insights into neurodegeneration from plant metabolism. *Trends in Biochemical Sciences* **34**, 628-639
237. Blennow, A., Nielsen, T. H., Baunsgaard, L., Mikkelsen, R., and Engelsen, S. B. (2002) Starch phosphorylation: a new front line in starch research. *Trends Plant Sci* **7**, 445-450
238. Lorberth, R., Ritte, G., Willmitzer, L., and Kossmann, J. (1998) Inhibition of a starch-granule-bound protein leads to modified starch and repression of cold sweetening. *Nat Biotechnol* **16**, 473-477
239. Zeeman, S. C., Northrop, F., Smith, A. M., and Rees, T. (1998) A starch-accumulating mutant of Arabidopsis thaliana deficient in a chloroplastic starch-hydrolysing enzyme. *Plant J* **15**, 357-365
240. Zeeman, S. C., and Rees, T. A. (1999) Changes in carbohydrate metabolism and assimilate export in starch-excess mutants of Arabidopsis. *Plant, Cell & Environment* **22**, 1445-1453
241. Fordham-Skelton, A. P., Chilley, P., Lumbreras, V., Reignoux, S., Fenton, T. R., Dahm, C. C., Pages, M., and Gatehouse, J. A. (2002) A novel higher plant protein tyrosine phosphatase interacts with SNF1-related protein kinases via a KIS (kinase interaction sequence) domain. *Plant J* **29**, 705-715
242. Niittylä, T., Comparot-Moss, S., Lue, W. L., Messerli, G., Trevisan, M., Seymour, M. D., Gatehouse, J. A., Villadsen, D., Smith, S. M., Chen, J., Zeeman, S. C., and Smith, A. M. (2006) Similar protein phosphatases control starch metabolism in plants and glycogen metabolism in mammals. *J Biol Chem* **281**, 11815-11818

243. Lafora, G. R. (1911) Über das Vorkommen amyloider Körperchen im innern der Ganglienzellen. *Virchows Archiv für pathologische Anatomie und Physiologie und für klinische Medizin* **205**, 295-303
244. Sakai, M., Austin, J., and Witmer, F. (1968) Polyglucosans in the systemic deposits of myoclonic epilepsy and in corpora amylacea. *Neurology* **18**, 298
245. Yokoi, S., Austin, J., and Witmer, F. (1967) Isolation and characterization of Lafora bodies in two cases of myoclonus epilepsy. *Journal of neuropathology and experimental neurology* **26**, 125-127
246. Wang, J., Stuckey, J. A., Wishart, M. J., and Dixon, J. E. (2002) A unique carbohydrate binding domain targets the lafora disease phosphatase to glycogen. *J Biol Chem* **277**, 2377-2380
247. Worby, C. A., Gentry, M. S., and Dixon, J. E. (2006) Laforin, a dual specificity phosphatase that dephosphorylates complex carbohydrates. *J Biol Chem* **281**, 30412-30418
248. Brewer, M. K., Uittenbogaard, A., Austin, G. L., Segvich, D. M., DePaoli-Roach, A., Roach, P. J., McCarthy, J. J., Simmons, Z. R., Brandon, J. A., Zhou, Z., Zeller, J., Young, L. E. A., Sun, R. C., Pauly, J. R., Aziz, N. M., Hodges, B. L., McKnight, T. R., Armstrong, D. D., and Gentry, M. S. (2019) Targeting Pathogenic Lafora Bodies in Lafora Disease Using an Antibody-Enzyme Fusion. *Cell Metab* **30**, 689-705.e686
249. Consortium, T. U. (2020) UniProt: the universal protein knowledgebase in 2021. *Nucleic Acids Research* **49**, D480-D489
250. Vander Kooi, C. W., Taylor, A. O., Pace, R. M., Meekins, D. A., Guo, H. F., Kim, Y., and Gentry, M. S. (2010) Structural basis for the glucan phosphatase activity of Starch Excess4. *Proc Natl Acad Sci U S A* **107**, 15379-15384
251. Meekins, D. A., Guo, H. F., Husodo, S., Paasch, B. C., Bridges, T. M., Santelia, D., Kötting, O., Vander Kooi, C. W., and Gentry, M. S. (2013) Structure of the Arabidopsis glucan phosphatase like sex four2 reveals a unique mechanism for starch dephosphorylation. *Plant Cell* **25**, 2302-2314
252. Meekins, D. A., Raththagala, M., Husodo, S., White, C. J., Guo, H. F., Kötting, O., Vander Kooi, C. W., and Gentry, M. S. (2014) Phosphoglucan-bound structure of starch phosphatase Starch Excess4 reveals the mechanism for C6 specificity. *Proc Natl Acad Sci U S A* **111**, 7272-7277
253. Raththagala, M., Brewer, M. K., Parker, M. W., Sherwood, A. R., Wong, B. K., Hsu, S., Bridges, T. M., Paasch, B. C., Hellman, L. M., and Husodo, S. (2015) Structural mechanism of laforin function in glycogen dephosphorylation and lafora disease. *Molecular cell* **57**, 261-272
254. Mikkelsen, R., Suszkiewicz, K., and Blennow, A. (2006) A novel type carbohydrate-binding module identified in alpha-glucan, water dikinases is specific for regulated plastidial starch metabolism. *Biochemistry* **45**, 4674-4682
255. Lu, S., Wang, J., Chitsaz, F., Derbyshire, M. K., Geer, R. C., Gonzales, N. R., Gwadz, M., Hurwitz, D. I., Marchler, G. H., Song, J. S., Thanki, N., Yamashita, R. A., Yang, M., Zhang, D., Zheng, C., Lanczycki, C. J., and

Marchler-Bauer, A. (2020) CDD/SPARCLE: the conserved domain database in 2020. *Nucleic Acids Res* **48**, D265-d268
256. Drozdetskiy, A., Cole, C., Procter, J., and Barton, G. J. (2015) JPred4: a protein secondary structure prediction server. *Nucleic Acids Res* **43**, W389-394
257. Evans, R., O'Neill, M., Pritzel, A., Antropova, N., Senior, A., Green, T., Žídek, A., Bates, R., Blackwell, S., Yim, J., Ronneberger, O., Bodenstein, S., Zielinski, M., Bridgland, A., Potapenko, A., Cowie, A., Tunyasuvunakool, K., Jain, R., Clancy, E., Kohli, P., Jumper, J., and Hassabis, D. (2021) Protein complex prediction with AlphaFold-Multimer. *bioRxiv*, 2021.2010.2004.463034
258. Jumper, J., Evans, R., Pritzel, A., Green, T., Figurnov, M., Ronneberger, O., Tunyasuvunakool, K., Bates, R., Žídek, A., Potapenko, A., Bridgland, A., Meyer, C., Kohl, S. A. A., Ballard, A. J., Cowie, A., Romera-Paredes, B., Nikolov, S., Jain, R., Adler, J., Back, T., Petersen, S., Reiman, D., Clancy, E., Zielinski, M., Steinegger, M., Pacholska, M., Berghammer, T., Bodenstein, S., Silver, D., Vinyals, O., Senior, A. W., Kavukcuoglu, K., Kohli, P., and Hassabis, D. (2021) Highly accurate protein structure prediction with AlphaFold. *Nature* **596**, 583-589
259. Dechavanne, V., Barrillat, N., Borlat, F., Hermant, A., Magnenat, L., Paquet, M., Antonsson, B., and Chevalet, L. (2011) A high-throughput protein refolding screen in 96-well format combined with design of experiments to optimize the refolding conditions. *Protein Expr Purif* **75**, 192-203
260. Mak, C. A., Weis, K., Henao, T., Kuchtova, A., Chen, T., Sharma, S., Meekins, D. A., Thalmann, M., Vander Kooi, C. W., and Raththagala, M. (2021) Cooperative Kinetics of the Glucan Phosphatase Starch Excess4. *Biochemistry* **60**, 2425-2435
261. Meekins, D. A., Raththagala, M., Auger, K. D., Turner, B. D., Santelia, D., Kötting, O., Gentry, M. S., and Vander Kooi, C. W. (2015) Mechanistic Insights into Glucan Phosphatase Activity against Polyglucan Substrates. *J Biol Chem* **290**, 23361-23370
262. Sharma, S., Vander Kooi, C. D., Gentry, M. S., and Vander Kooi, C. W. (2018) Oligomerization and carbohydrate binding of glucan phosphatases. *Anal Biochem* **563**, 51-55
263. Zhang, Z., and Smith, D. L. (1993) Determination of amide hydrogen exchange by mass spectrometry: a new tool for protein structure elucidation. *Protein Sci* **2**, 522-531
264. Hsu, S., Kim, Y., Li, S., Durrant, E. S., Pace, R. M., Woods, V. L., Jr., and Gentry, M. S. (2009) Structural insights into glucan phosphatase dynamics using amide hydrogen-deuterium exchange mass spectrometry. *Biochemistry* **48**, 9891-9902
265. Sherwood, A. R., Paasch, B. C., Worby, C. A., and Gentry, M. S. (2013) A malachite green-based assay to assess glucan phosphatase activity. *Anal Biochem* **435**, 54-56

266. Mikkelsen, R., Baunsgaard, L., and Blennow, A. (2004) Functional characterization of alpha-glucan,water dikinase, the starch phosphorylating enzyme. *Biochem J* **377**, 525-532
267. Brown, P. R., and Geldart, S. E. (1998) Improving the sensitivity of the capillary electrophoresis analysis of carbovir triphosphate and purine deoxyribonucleoside triphosphates with whole capillary stacking. *Journal of Microcolumn Separations* **10**, 65-73
268. Shen, B., Brown, K. M., Lee, T. D., and Sibley, L. D. (2014) Efficient gene disruption in diverse strains of Toxoplasma gondii using CRISPR/CAS9. *mBio* **5**, e01114-01114
269. Sidik, S. M., Hackett, C. G., Tran, F., Westwood, N. J., and Lourido, S. (2014) Efficient genome engineering of Toxoplasma gondii using CRISPR/Cas9. *PLoS One* **9**, e100450
270. Markus, B. M., Bell, G. W., Lorenzi, H. A., and Lourido, S. (2019) Optimizing systems for Cas9 expression in Toxoplasma gondii. *MSphere* **4**, e00386-00319
271. Bolte, S., and Cordelières, F. P. (2006) A guided tour into subcellular colocalization analysis in light microscopy. *J Microsc* **224**, 213-232
272. Mayoral, J., Di Cristina, M., Carruthers, V. B., and Weiss, L. M. (2020) Toxoplasma gondii: Bradyzoite Differentiation In Vitro and In Vivo. *Methods Mol Biol* **2071**, 269-282
273. Schindelin, J., Arganda-Carreras, I., Frise, E., Kaynig, V., Longair, M., Pietzsch, T., Preibisch, S., Rueden, C., Saalfeld, S., Schmid, B., Tinevez, J. Y., White, D. J., Hartenstein, V., Eliceiri, K., Tomancak, P., and Cardona, A. (2012) Fiji: an open-source platform for biological-image analysis. *Nat Methods* **9**, 676-682
274. Andres, D. A., Young, L. E. A., Veeranki, S., Hawkinson, T. R., Levitan, B. M., He, D., Wang, C., Satin, J., and Sun, R. C. (2020) Improved workflow for mass spectrometry–based metabolomics analysis of the heart. *Journal of Biological Chemistry* **295**, 2676-2686
275. Watts, E. A., Dhara, A., and Sinai, A. P. (2017) Purification Toxoplasma gondii Tissue Cysts Using Percoll Gradients. *Curr Protoc Microbiol* **45**, 20c.22.21-20c.22.19
276. Kumar, S., Ciraolo, G., Hinge, A., and Filippi, M. D. (2014) An efficient and reproducible process for transmission electron microscopy (TEM) of rare cell populations. *J Immunol Methods* **404**, 87-90
277. Kumar, S., and Filippi, M. D. (2016) An Alternative Approach for Sample Preparation with Low Cell Number for TEM Analysis. *J Vis Exp*
278. Derouin, F., and Garin, Y. J. F. (1991) Toxoplasma gondii: Blood and tissue kinetics during acute and chronic infections in mice. *Experimental Parasitology* **73**, 460-468
279. Tomavo, S. (2015) Too Much Sugar Puts a Parasite in Jeopardy. *Cell Host Microbe* **18**, 641-643
280. Pawlowski, J., Audic, S., Adl, S., Bass, D., Belbahri, L., Berney, C., Bowser, S. S., Cepicka, I., Decelle, J., Dunthorn, M., Fiore-Donno, A. M., Gile, G. H., Holzmann, M., Jahn, R., Jirků, M., Keeling, P. J., Kostka, M.,

Kudryavtsev, A., Lara, E., Lukeš, J., Mann, D. G., Mitchell, E. A., Nitsche, F., Romeralo, M., Saunders, G. W., Simpson, A. G., Smirnov, A. V., Spouge, J. L., Stern, R. F., Stoeck, T., Zimmermann, J., Schindel, D., and de Vargas, C. (2012) CBOL protist working group: barcoding eukaryotic richness beyond the animal, plant, and fungal kingdoms. *PLoS Biol* **10**, e1001419

281. Behnke, M. S., Dubey, J. P., and Sibley, L. D. (2016) Genetic Mapping of Pathogenesis Determinants in Toxoplasma gondii. *Annu Rev Microbiol* **70**, 63-81
282. Sun, R. C., Dukhande, V. V., Zhou, Z., Young, L. E. A., Emanuelle, S., Brainson, C. F., and Gentry, M. S. (2019) Nuclear Glycogenolysis Modulates Histone Acetylation in Human Non-Small Cell Lung Cancers. *Cell Metab* **30**, 903-916.e907
283. Duran, J., Hervera, A., Markussen, K. H., Varea, O., López-Soldado, I., Sun, R. C., Del Río, J. A., Gentry, M. S., and Guinovart, J. J. (2021) Astrocytic glycogen accumulation drives the pathophysiology of neurodegeneration in Lafora disease. *Brain* **144**, 2349-2360
284. Alonso, A., Rojas, A., Godzik, A., and Mustelin, T. (2004) The dual-specific protein tyrosine phosphatase family. in *Protein phosphatases*, Springer. pp 333-358
285. Patterson, K. I., Brummer, T., O'Brien, P. M., and Daly, R. J. (2009) Dual-specificity phosphatases: critical regulators with diverse cellular targets. *Biochem J* **418**, 475-489
286. Alonso, A., and Pulido, R. (2016) The extended human PTPome: a growing tyrosine phosphatase family. *Febs j* **283**, 1404-1429
287. Gentry, M. S., Brewer, M. K., and Vander Kooi, C. W. (2016) Structural biology of glucan phosphatases from humans to plants. *Curr Opin Struct Biol* **40**, 62-69
288. Emanuelle, S., Brewer, M. K., Meekins, D. A., and Gentry, M. S. (2016) Unique carbohydrate binding platforms employed by the glucan phosphatases. *Cell Mol Life Sci* **73**, 2765-2778
289. Meekins, D. A., Vander Kooi, C. W., and Gentry, M. S. (2016) Structural mechanisms of plant glucan phosphatases in starch metabolism. *Febs j* **283**, 2427-2447
290. Butt, T. R., Edavettal, S. C., Hall, J. P., and Mattern, M. R. (2005) SUMO fusion technology for difficult-to-express proteins. *Protein expression and purification* **43**, 1-9
291. Carrio, M., and Villaverde, A. (2002) Construction and deconstruction of bacterial inclusion bodies. *Journal of biotechnology* **96**, 3-12
292. Cabrita, L. D., Chow, M. K., and Bottomley, S. P. (2004) A practical guide to protein expression and refolding from inclusion bodies. *Biotechnol Annu Rev* **10**, 31-50
293. Niesen, F. H., Berglund, H., and Vedadi, M. (2007) The use of differential scanning fluorimetry to detect ligand interactions that promote protein stability. *Nat Protoc* **2**, 2212-2221

294. Kuchtová, A., Gentry, M. S., and Janeček, Š. (2018) The unique evolution of the carbohydrate-binding module CBM20 in laforin. *FEBS Lett* **592**, 586-598
295. Denu, J. M., Stuckey, J. A., Saper, M. A., and Dixon, J. E. (1996) Form and function in protein dephosphorylation. *Cell* **87**, 361-364
296. Simmons, Z. R., Sharma, S., Wayne, J., Li, S., Vander Kooi, C. W., and Gentry, M. S. (2021) Generation and characterization of a laforin nanobody inhibitor. *Clin Biochem* **93**, 80-89
297. Xiao, J., Engel, J. L., Zhang, J., Chen, M. J., Manning, G., and Dixon, J. E. (2011) Structural and functional analysis of PTPMT1, a phosphatase required for cardiolipin synthesis. *Proc Natl Acad Sci U S A* **108**, 11860-11865
298. Janeček, Š., Mareček, F., MacGregor, E. A., and Svensson, B. (2019) Starch-binding domains as CBM families-history, occurrence, structure, function and evolution. *Biotechnol Adv* **37**, 107451
299. He, R., Yu, Z. H., Zhang, R. Y., Wu, L., Gunawan, A. M., Lane, B. S., Shim, J. S., Zeng, L. F., He, Y., Chen, L., Wells, C. D., Liu, J. O., and Zhang, Z. Y. (2015) Exploring the Existing Drug Space for Novel pTyr Mimetic and SHP2 Inhibitors. *ACS Med Chem Lett* **6**, 782-786
300. He, R., Yu, Z. H., Zhang, R. Y., Wu, L., Gunawan, A. M., and Zhang, Z. Y. (2015) Cefsulodin Inspired Potent and Selective Inhibitors of mPTPB, a Virulent Phosphatase from Mycobacterium tuberculosis. *ACS Med Chem Lett* **6**, 1231-1235
301. Dutta, N. K., He, R., Pinn, M. L., He, Y., Burrows, F., Zhang, Z. Y., and Karakousis, P. C. (2016) Mycobacterial Protein Tyrosine Phosphatases A and B Inhibitors Augment the Bactericidal Activity of the Standard Anti-tuberculosis Regimen. *ACS Infect Dis* **2**, 231-239
302. He, R., Wang, J., Yu, Z. H., Zhang, R. Y., Liu, S., Wu, L., and Zhang, Z. Y. (2016) Inhibition of Low Molecular Weight Protein Tyrosine Phosphatase by an Induced-Fit Mechanism. *J Med Chem* **59**, 9094-9106
303. Sun, R. C., Dukhande, V. V., Zhou, Z., Young, L. E., Emanuelle, S., Brainson, C. F., and Gentry, M. S. (2019) Nuclear glycogenolysis modulates histone acetylation in human non-small cell lung cancers. *Cell metabolism* **30**, 903-916. e907
304. Brewer, M. K., Uittenbogaard, A., Austin, G. L., Segvich, D. M., DePaoli-Roach, A., Roach, P. J., McCarthy, J. J., Simmons, Z. R., Brandon, J. A., and Zhou, Z. (2019) Targeting pathogenic Lafora bodies in Lafora disease using an antibody-enzyme fusion. *Cell metabolism* **30**, 689-705. e686
305. Ruff, K. M., and Pappu, R. V. (2021) AlphaFold and Implications for Intrinsically Disordered Proteins. *J Mol Biol* **433**, 167208
306. Strodel, B. (2021) Energy Landscapes of Protein Aggregation and Conformation Switching in Intrinsically Disordered Proteins. *J Mol Biol* **433**, 167182
307. Feng, Z. P., Zhang, X., Han, P., Arora, N., Anders, R. F., and Norton, R. S. (2006) Abundance of intrinsically unstructured proteins in P. falciparum

and other apicomplexan parasite proteomes. *Mol Biochem Parasitol* **150**, 256-267
308. Mohan, A., Sullivan, W. J., Jr., Radivojac, P., Dunker, A. K., and Uversky, V. N. (2008) Intrinsic disorder in pathogenic and non-pathogenic microbes: discovering and analyzing the unfoldomes of early-branching eukaryotes. *Mol Biosyst* **4**, 328-340
309. Dixon, S. E., Bhatti, M. M., Uversky, V. N., Dunker, A. K., and Sullivan, W. J., Jr. (2011) Regions of intrinsic disorder help identify a novel nuclear localization signal in Toxoplasma gondii histone acetyltransferase TgGCN5-B. *Mol Biochem Parasitol* **175**, 192-195
310. Valk, V., Lammerts van Bueren, A., van der Kaaij, R. M., and Dijkhuizen, L. (2016) Carbohydrate-binding module 74 is a novel starch-binding domain associated with large and multidomain α-amylase enzymes. *The FEBS Journal* **283**, 2354-2368
311. Cao, X. Z., Wang, J. L., Elsheikha, H. M., Li, T. T., Sun, L. X., Liang, Q. L., and Zhang, Z. W. (2019) Characterization of the role of Amylo-alpha-1, 6-glucosidase protein in the infectivity of Toxoplasma gondii. *Frontiers in Cellular and Infection Microbiology* **9**, 418
312. Ralton, J. E., Sernee, M. F., and McConville, M. J. (2021) Evolution and function of carbohydrate reserve biosynthesis in parasitic protists. *Trends Parasitol*
313. Sernee, M. F., Ralton, J. E., Nero, T. L., Sobala, L. F., Kloehn, J., Vieira-Lara, M. A., Cobbold, S. A., Stanton, L., Pires, D. E., and Hanssen, E. (2019) A family of dual-activity glycosyltransferase-phosphorylases mediates mannogen turnover and virulence in Leishmania parasites. *Cell host & microbe* **26**, 385-399. e389
314. Mullard, A. (2018) Phosphatases start shedding their stigma of undruggability. *Nat Rev Drug Discov* **17**, 847-849
315. Krabill, A. D., and Zhang, Z. Y. (2021) Functional interrogation and therapeutic targeting of protein tyrosine phosphatases. *Biochem Soc Trans* **49**, 1723-1734
316. Ruddraraju, K. V., Aggarwal, D., and Zhang, Z. Y. (2020) Therapeutic Targeting of Protein Tyrosine Phosphatases from Mycobacterium tuberculosis. *Microorganisms* **9**
317. Ruddraraju, K. V., Aggarwal, D., Niu, C., Baker, E. A., Zhang, R.-y., Wu, L., and Zhang, Z.-Y. (2020) Highly Potent and Selective N-Aryl Oxamic Acid-Based Inhibitors for Mycobacterium tuberculosis Protein Tyrosine Phosphatase B. *Journal of Medicinal Chemistry* **63**, 9212-9227
318. Bai, Y., Yu, Z.-H., Liu, S., Zhang, L., Zhang, R.-Y., Zeng, L.-F., Zhang, S., and Zhang, Z.-Y. (2016) Novel Anticancer Agents Based on Targeting the Trimer Interface of the PRL Phosphatase. *Cancer Research* **76**, 4805-4815
319. He, R., Wang, J., Yu, Z.-H., Zhang, R.-Y., Liu, S., Wu, L., and Zhang, Z.-Y. (2016) Inhibition of Low Molecular Weight Protein Tyrosine Phosphatase by an Induced-Fit Mechanism. *Journal of Medicinal Chemistry* **59**, 9094-9106

320. Zeng, L.-F., Zhang, R.-Y., Yu, Z.-H., Li, S., Wu, L., Gunawan, A. M., Lane, B. S., Mali, R. S., Li, X., Chan, R. J., Kapur, R., Wells, C. D., and Zhang, Z.-Y. (2014) Therapeutic Potential of Targeting the Oncogenic SHP2 Phosphatase. *Journal of Medicinal Chemistry* **57**, 6594-6609
321. Ho, W. J., Croessmann, S., Lin, J., Phyo, Z. H., Charmsaz, S., Danilova, L., Mohan, A. A., Gross, N. E., Chen, F., Dong, J., Aggarwal, D., Bai, Y., Wang, J., He, J., Leatherman, J. M., Yarchoan, M., Armstrong, T. D., Zaidi, N., Fertig, E. J., Denny, J. C., Park, B. H., Zhang, Z. Y., and Jaffee, E. M. (2021) Systemic inhibition of PTPN22 augments anticancer immunity. *J Clin Invest*
322. Hizukuri, S., Tabata, S., Kagoshima, and Nikuni, Z. (1970) Studies on Starch Phosphate Part 1. Estimation of glucose-6-phosphate residues in starch and the presence of other bound phosphate(s). *Starch - Stärke* **22**, 338-343
323. Tabata, S., and Hizukuri, S. (1971) Studies on Starch Phosphate. Part 2. Isolation of Glucose 3-Phosphate and Maltose Phosphate by Acid Hydrolysis of Potato Starch. *Starch - Stärke* **23**, 267-272
324. Caspar, T., Lin, T. P., Kakefuda, G., Benbow, L., Preiss, J., and Somerville, C. (1991) Mutants of Arabidopsis with altered regulation of starch degradation. *Plant Physiol* **95**, 1181-1188
325. Trethewey, R. N., and ap Rees, T. (1994) The role of the hexose transporter in the chloroplasts of Arabidopsis thaliana L. *Planta* **195**, 168-174
326. Yu, T. S., Kofler, H., Häusler, R. E., Hille, D., Flügge, U. I., Zeeman, S. C., Smith, A. M., Kossmann, J., Lloyd, J., Ritte, G., Steup, M., Lue, W. L., Chen, J., and Weber, A. (2001) The Arabidopsis sex1 mutant is defective in the R1 protein, a general regulator of starch degradation in plants, and not in the chloroplast hexose transporter. *Plant Cell* **13**, 1907-1918
327. Mikkelsen, R., and Blennow, A. (2005) Functional domain organization of the potato alpha-glucan, water dikinase (GWD): evidence for separate site catalysis as revealed by limited proteolysis and deletion mutants. *Biochem J* **385**, 355-361
328. Herzberg, O., Chen, C. C., Kapadia, G., McGuire, M., Carroll, L. J., Noh, S. J., and Dunaway-Mariano, D. (1996) Swiveling-domain mechanism for enzymatic phosphotransfer between remote reaction sites. *Proc Natl Acad Sci U S A* **93**, 2652-2657
329. Herzberg, O., Chen, C. C., Liu, S., Tempczyk, A., Howard, A., Wei, M., Ye, D., and Dunaway-Mariano, D. (2002) Pyruvate site of pyruvate phosphate dikinase: crystal structure of the enzyme-phosphonopyruvate complex, and mutant analysis. *Biochemistry* **41**, 780-787
330. Glaring, M. A., Baumann, M. J., Abou Hachem, M., Nakai, H., Nakai, N., Santelia, D., Sigurskjold, B. W., Zeeman, S. C., Blennow, A., and Svensson, B. (2011) Starch-binding domains in the CBM45 family--low-affinity domains from glucan, water dikinase and α-amylase involved in plastidial starch metabolism. *Febs j* **278**, 1175-1185

331. Chou, W. Y., Chou, W. I., Pai, T. W., Lin, S. C., Jiang, T. Y., Tang, C. Y., and Chang, M. D. (2010) Feature-incorporated alignment based ligand-binding residue prediction for carbohydrate-binding modules. *Bioinformatics* **26**, 1022-1028
332. Fritz, H. M., Buchholz, K. R., Chen, X., Durbin-Johnson, B., Rocke, D. M., Conrad, P. A., and Boothroyd, J. C. (2012) Transcriptomic analysis of toxoplasma development reveals many novel functions and structures specific to sporozoites and oocysts. *PLoS One* **7**, e29998
333. Hejazi, M., Steup, M., and Fettke, J. (2012) The plastidial glucan, water dikinase (GWD) catalyses multiple phosphotransfer reactions. *The FEBS Journal* **279**, 1953-1966
334. O'Neill, K., Shao, X., Zhao, Z., Malik, A., and Lee, M. L. (1994) Capillary electrophoresis of nucleotides on ucon-coated fused silica columns. *Anal Biochem* **222**, 185-189
335. Geldart, S. E., and Brown, P. R. (1997) Optimization for the separation of ribonucleotides by capillary electrophoresis at high pH. *Journal of Chromatography A* **792**, 67-73
336. Flegr, J., Prandota, J., Sovičková, M., and Israili, Z. H. (2014) Toxoplasmosis--a global threat. Correlation of latent toxoplasmosis with specific disease burden in a set of 88 countries. *PLoS One* **9**, e90203
337. Place, B. C., Troublefield, C., Murphy, R. D., Sinai, A. P., and Patwardhan, A. (2021) Computer Aided Image Processing to Facilitate Determination of Congruence in Manual Classification of Mitochondrial Morphologies in Toxoplasma gondii Tissue Cysts. *Annu Int Conf IEEE Eng Med Biol Soc* **2021**, 3509-3513
338. Dubey, J. P., and Frenkel, J. K. (1976) Feline toxoplasmosis from acutely infected mice and the development of Toxoplasma cysts. *J Protozool* **23**, 537-546
339. Stitt, M., and Zeeman, S. C. (2012) Starch turnover: pathways, regulation and role in growth. *Curr Opin Plant Biol* **15**, 282-292
340. Kötting, O., Kossmann, J., Zeeman, S. C., and Lloyd, J. R. (2010) Regulation of starch metabolism: the age of enlightenment? *Curr Opin Plant Biol* **13**, 321-329
341. Silver, D. M., Kötting, O., and Moorhead, G. B. (2014) Phosphoglucan phosphatase function sheds light on starch degradation. *Trends in plant science* **19**, 471-478
342. Lafora, G. R. (2021) Band 205. in *XXI. Über das Vorkommen amyloider Körperchen im Innern der Ganglienzellen; zugleich Ein Beitrag zum Studium der amyloiden Substanz im Nervensystem* (Johannes, O. ed.), De Gruyter. pp 295-303
343. Howe, D. K., and Sibley, L. D. (1995) Toxoplasma gondii comprises three clonal lineages: correlation of parasite genotype with human disease. *J Infect Dis* **172**, 1561-1566
344. Sibley, L. D., and Boothroyd, J. C. (1992) Virulent strains of Toxoplasma gondii comprise a single clonal lineage. *Nature* **359**, 82-85

345. Su, C., Khan, A., Zhou, P., Majumdar, D., Ajzenberg, D., Dardé, M. L., Zhu, X. Q., Ajioka, J. W., Rosenthal, B. M., Dubey, J. P., and Sibley, L. D. (2012) Globally diverse Toxoplasma gondii isolates comprise six major clades originating from a small number of distinct ancestral lineages. *Proc Natl Acad Sci U S A* **109**, 5844-5849
346. Lorenzi, H., Khan, A., Behnke, M. S., Namasivayam, S., Swapna, L. S., Hadjithomas, M., Karamycheva, S., Pinney, D., Brunk, B. P., Ajioka, J. W., Ajzenberg, D., Boothroyd, J. C., Boyle, J. P., Dardé, M. L., Diaz-Miranda, M. A., Dubey, J. P., Fritz, H. M., Gennari, S. M., Gregory, B. D., Kim, K., Saeij, J. P., Su, C., White, M. W., Zhu, X. Q., Howe, D. K., Rosenthal, B. M., Grigg, M. E., Parkinson, J., Liu, L., Kissinger, J. C., Roos, D. S., and Sibley, L. D. (2016) Local admixture of amplified and diversified secreted pathogenesis determinants shapes mosaic Toxoplasma gondii genomes. *Nat Commun* **7**, 10147
347. Lunde, M. N., and Jacobs, L. (1983) Antigenic differences between endozoites and cystozoites of Toxoplasma gondii. *J Parasitol* **69**, 806-808
348. Dubey, J. P. (1995) Duration of immunity to shedding of Toxoplasma gondii oocysts by cats. *J Parasitol* **81**, 410-415
349. McLeod, R., Estes, R. G., Mack, D. G., and Cohen, H. (1984) Immune response of mice to ingested Toxoplasma gondii: a model of toxoplasma infection acquired by ingestion. *J Infect Dis* **149**, 234-244
350. Pfefferkorn, E. R., and Borotz, S. E. (1994) Toxoplasma gondii: characterization of a mutant resistant to 6-thioxanthine. *Exp Parasitol* **79**, 374-382
351. Schwartzman, J. D., and Pfefferkorn, E. R. (1982) Toxoplasma gondii: purine synthesis and salvage in mutant host cells and parasites. *Exp Parasitol* **53**, 77-86
352. Pfefferkorn, E. R., Bzik, D. J., and Honsinger, C. P. (2001) Toxoplasma gondii: mechanism of the parasitostatic action of 6-thioxanthine. *Exp Parasitol* **99**, 235-243
353. Donald, R. G., and Roos, D. S. (1998) Gene knock-outs and allelic replacements in Toxoplasma gondii: HXGPRT as a selectable marker for hit-and-run mutagenesis. *Mol Biochem Parasitol* **91**, 295-305
354. Rommereim, L. M., Hortua Triana, M. A., Falla, A., Sanders, K. L., Guevara, R. B., Bzik, D. J., and Fox, B. A. (2013) Genetic manipulation in Δku80 strains for functional genomic analysis of Toxoplasma gondii. *J Vis Exp*, e50598
355. Baba, O. (1993) Production of monoclonal antibody that recognizes glycogen and its application for immunohistochemistry. *Kokubyo Gakkai zasshi. The Journal of the Stomatological Society, Japan* **60**, 264-287
356. Oe, Y., Baba, O., Ashida, H., Nakamura, K. C., and Hirase, H. (2016) Glycogen distribution in the microwave-fixed mouse brain reveals heterogeneous astrocytic patterns. *Glia* **64**, 1532-1545
357. van de Weerd, R., Berbís, M. A., Sparrius, M., Maaskant, J. J., Boot, M., Paauw, N. J., de Vries, N., Boon, L., Baba, O., and Cañada, F. J. (2015) A Murine Monoclonal Antibody to Glycogen: Characterization of Epitope-

Fine Specificity by Saturation Transfer Difference (STD) NMR Spectroscopy and Its Use in Mycobacterial Capsular α-Glucan Research. *Chembiochem* **16**, 977-989
358. Skurat, A. V., Segvich, D. M., DePaoli-Roach, A. A., and Roach, P. J. (2017) Novel method for detection of glycogen in cells. *Glycobiology* **27**, 416-424
359. Choi, C. P., Moon, A. S., Back, P. S., Jami-Alahmadi, Y., Vashisht, A. A., Wohlschlegel, J. A., and Bradley, P. J. (2019) A photoactivatable crosslinking system reveals protein interactions in the Toxoplasma gondii inner membrane complex. *PLoS biology* **17**, e3000475
360. Sinai, A. P. (2014) Chapter 11 - The Toxoplasma gondii Parasitophorous Vacuole Membrane: A Multifunctional Organelle in the Infected Cell. in *Toxoplasma Gondii (Second Edition)* (Weiss, L. M., and Kim, K. eds.), Academic Press, Boston. pp 375-387
361. Boothroyd, J. C., Black, M., Bonnefoy, S., Hehl, A., Knoll, L. J., Manger, I. D., Ortega-Barria, E., and Tomavo, S. (1997) Genetic and biochemical analysis of development in Toxoplasma gondii. *Philos Trans R Soc Lond B Biol Sci* **352**, 1347-1354
362. Dubey, R., Staker, B. L., Foe, I. T., Bogyo, M., Myler, P. J., Ngô, H. M., and Gubbels, M. J. (2017) Membrane skeletal association and post-translational allosteric regulation of Toxoplasma gondii GAPDH1. *Mol Microbiol* **103**, 618-634
363. Yang, J., Yang, C., Qian, J., Li, F., Zhao, J., and Fang, R. (2020) Toxoplasma gondii α-amylase deletion mutant is a promising vaccine against acute and chronic toxoplasmosis. *Microb Biotechnol* **13**, 2057-2069
364. Ralton, J. E., Sernee, M. F., and McConville, M. J. (2021) Evolution and function of carbohydrate reserve biosynthesis in parasitic protists. *Trends Parasitol* **37**, 988-1001
365. TeSlaa, T., Bartman, C. R., Jankowski, C. S., Zhang, Z., Xu, X., Xing, X., Wang, L., Lu, W., Hui, S., and Rabinowitz, J. D. (2021) The Source of Glycolytic Intermediates in Mammalian Tissues. *Cell Metabolism* **33**, 367-378. e365
366. Rajendran, E., Clark, M., Goulart, C., Steinhöfel, B., Tjhin, E. T., Gross, S., Smith, N. C., Kirk, K., and van Dooren, G. G. (2021) Substrate-mediated regulation of the arginine transporter of Toxoplasma gondii. *PLOS Pathogens* **17**, e1009816
367. Ferguson, D. J., Birch-Andersen, A., Siim, J. C., and Hutchison, W. M. (1979) An ultrastructural study on the excystation of the sporozoites of Toxoplasma gondii. *Acta Pathol Microbiol Scand B* **87**, 277-283
368. Nakai, Y., and Ogimoto, K. (1987) Relationship between amylopectin and infectivity of Eimeria tenella sporozoite. *Nihon Juigaku Zasshi* **49**, 447-452
369. Sinai, A. P., Knoll, L. J., and Weiss, L. M. (2020) Bradyzoite and sexual stage development. in *Toxoplasma gondii*, Elsevier. pp 807-857

370. King, E. F., Cobbold, S. A., Uboldi, A. D., Tonkin, C. J., and McConville, M. J. (2020) Metabolomic Analysis of Toxoplasma gondii Tachyzoites. in *Toxoplasma gondii*, Springer. pp 435-452
371. Dubey, J. P. (2008) The history of Toxoplasma gondii--the first 100 years. *J Eukaryot Microbiol* **55**, 467-475

# VITA

## Robert Daniel (Bobby) Murphy

### Education

Bachelor of Science in Biochemistry and Molecular Biology — May 2012
Bellarmine University, Louisville, KY

### Professional Experience

PGXL, Louisville, KY — 2012-2015
Clinical Lab Technician

### Honors

Centers for Disease Control and Prevention — 2022-2024
Laboratory Leadership Service Fellowship

Department of Molecular and Cellular Biochemistry Summer Retreat — 2019
Best Seminar Presentation in 2018-2019 academic year

Graduate Student Congress — 2019
Pillar Award for Belonging and Engagement

Office of Institutional Diversity — 2019
Inclusive Excellence Grant

University of Louisville, College of Business — 2018
Finalist, Cardinal Challenge

Kentucky Cabinet for Economic Development, Office of Entrepreneurship — 2018
Regional finalist, Idea State U

National Science Foundation — 2017-2022
Graduate Research Fellowship, Grant No: 1247392

American Society for Biochemistry and Molecular Biology — 2017
Travel Award

University of Kentucky — 2015-2017
Daniel Reedy Fellowship

### Publications

1) **Murphy RD**[#], Chen T[#], He R, Lin J, Wu L, Pearson CR, Vander Kooi CD, Sinai AP, Zhang ZY, Vander Kooi CW, and Gentry MS. The *Toxoplasma* glucan phosphatase, TgLaforin, utilizes a distinct functional mechanism enabling inhibitor identification. *Under review at J Biol Chem (02/2022).* [#]These authors contributed equally to this work.
2) Place BC, Troublefield CA, **Murphy RD**, Sinai AP, and Patwardhan A (2021). High throughput classification of mitochondrial morphology in Toxoplasma gondii bradyzoites using multivariate logistic regression. Submitted. *Submitted, IEEE Trans Biomed Eng (04/2022).*

3) **Murphy RD**, Troublefield CA, Young LEA, Sun RC, Brizzee CO, Dhara A, Gentry MS, Sinai AP (2022). An unexpected role for amylopectin in Toxoplasma gondii tachyzoites and their impact in the chronic infection revealed by the disruption of the glucan phosphatase TgLaforin. *In preparation.*
4) Troublefield CA, **Murphy RD**, Sinai AP. Factors influencing tissue cyst yield in the murine model of chronic toxoplasmosis. *In preparation*.
5) Troublefield CA, Place BC, McConnell SB, **Murphy RD**, Patwardhan A, Sinai AP (2022). A bespoke application to quantify the diversity of mitochondrial morphologies within ex vivo encysted Toxoplasma gondii bradyzoites reveal a high degree of functional heterogeneity. *In preparation.*
6) Dhara A, McConnell SB, **Murphy RD**, Sinai AP (2022). TgOTUD5, a phosphorylation-dependent cell cycle regulated deubiqitinase regulates distinct aspects of membrane trafficking and homeostasis in Toxoplasma gondii. *In preparation*.
7) Place BC, Troublefield CT, **Murphy RD**, Sinai AP, Patwardhan A. (2022) Computer Aided Image Processing to Facilitate Determination of Congruence in Manual Classification of Mitochondrial Morphologies in Toxoplasma gondii Tissue Cysts. *Annu Int Conf IEEE Eng Med Biol Soc* **2021**, 3509-3513.
8) Young LEA, Brizzee CO, Macedo JKA, **Murphy RD**, Contreras CJ, DePaoli-Roach AA, Roach PJ, Gentry MS, Sun RD. (2020) Accurate and sensitive quantitation of glucose and glucose phosphates derived from storage carbohydrates by mass spectrometry. *Carbohydr Polym* **230**, 115651.
9) Sinai A.P, Watts E.A., Dhara A., **Murphy R.D.**, Gentry M.S., & Patwardhan A. (2016) Reexamining Chronic Toxoplasma gondii Infection: Surprising Activity for a "Dormant" Parasite. *Curr Clin Micro Rpt* **3** (4), 175-185.
10) Huff MO, Todd SL, Smith AL, Elpers JT, Smith AP, **Murphy RD**, Bleser-Shartzer AS, Hoerter JE, Radde BN, Klinge CM. (2016) Arsenite and Cadmium Activate MAPK/ERK via Membrane Estrogen Receptors and G-Protein Coupled Estrogen Receptor Signaling in Human Lung Adenocarcinoma Cells. *Toxicol Sci* **152** (1), 62-71.